Construction of Heterospin Molecule-based Magnets

村島, 健介

https://doi.org/10.15017/1654815

Construction of Heterospin Molecule-based Magnets

Thesis

Submitted to the Graduate School of Pharmaceutical Sciences, Kyushu University
for the Degree of Doctor of Science

Kensuke Murashima

March, 2016

Contents

Chapter1. Introduction

Section1. Molecular magnetism

For a long time, molecular magnetism[1] have been expected to be one of the most attractive topics for a lot of researchers because of its extremely high potentiality in various research fields including the quantum-computing[2], molecular memory devices[3], and external stimuli responsive molecular switches[4] and so on. Generally, magnetism has its origin almost on the electron spin of the metal ion. The unpaired electron has the spin angular momentum (*S*) derives from its rotation movement and often has the orbital angular momentum (*L*) originated from its orbital movement around the atomic nucleus (Figure 1-1). As a result, the magnetic property of each compound is strongly affected by the spin state of the metal ion along with the crystal field effect of the first-coordinated environment surrounding the paramagnetic center.

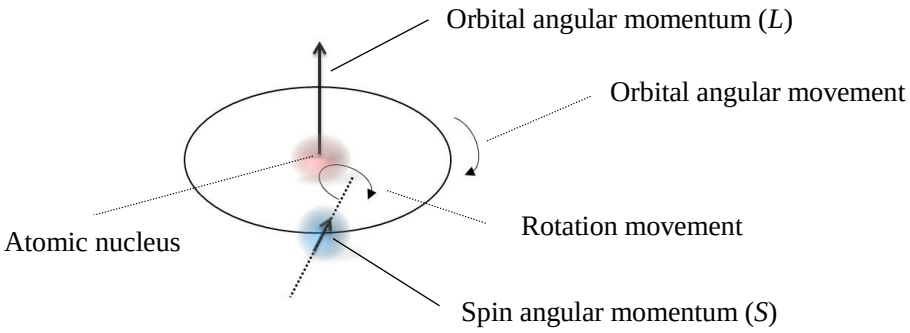

Figure 1-1. Schematic drawing of the magnetic momentum originated from unpaired electron

Such paramagnetic species can magnetically interact each other sometimes through bonds (for example, magnetic exchange coupling, J_{ex}/k_B) and at the other time through space (for instance, magnetic dipole interaction, J_{dipole}/k_B). In any cases mainly two types of magnetic interactions are well known, so-called “ferromagnetic interaction” and “antiferromagnetic interaction” (Figure. 1-2). The former interaction between two or more paramagnetic sources easily induces the higher spin state because of the parallel orientation of the magnetic momentum. On the other hand, the latter interaction often lead the lower degree of magnetic momentum due to the anti-parallel orientation nature. Controlling the magnetic interaction between magnetic sources is considerably important for the construction of molecule-based magnets.

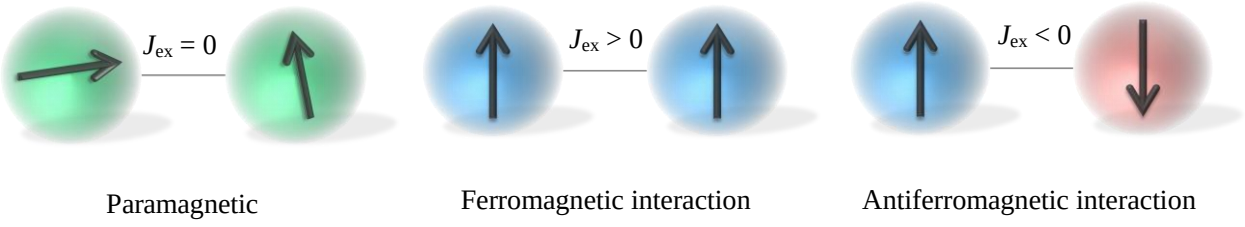

Figure 1-2. Schematic models of magnetic interaction between two unpaired electrons

Section.2　Molecule-based magnets with organic radicals

Organic radical compounds also act as paramagnetic spin sources because of their unpaired electrons. In 1991, Kinoshita et.al reported that doublet species, *p*-NPNN, behaved as a ferromagnet under the ferromagnetic transition temperature, T_c = 0.65 K, in the crystalline solid state[5]. This report revealed the high possibilities of organic radicals for the controlling of magnetism in the molecular levels.

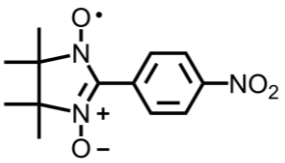

p-NPNN

(*p*-nironylphenyl nitronyl nitroxide)

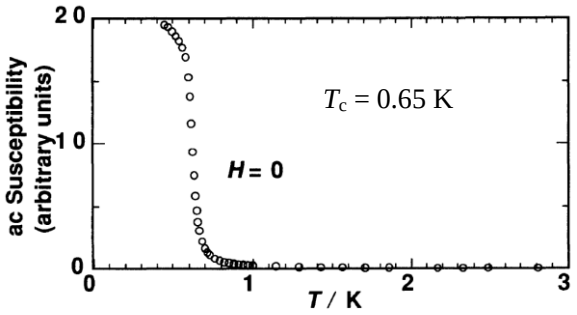

Figure 1-3. Molecular structure of *p*-NPNN and its temperature dependence of ac magnetic properties

Furthermore, Iwamura et.al successfully prepared various kinds of photo-responsive radical compounds with extremely high-spin ground state by using carbenes coupled by *m*-phenylene backbones[6]. Like this, introduction of the organic spins into the molecular magnetism gives us the opportunity to construct various kinds of magnets with interesting chemical properties.

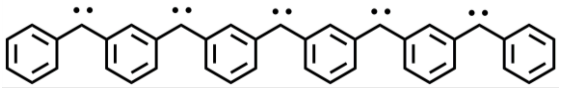

Pentakis carbene compound

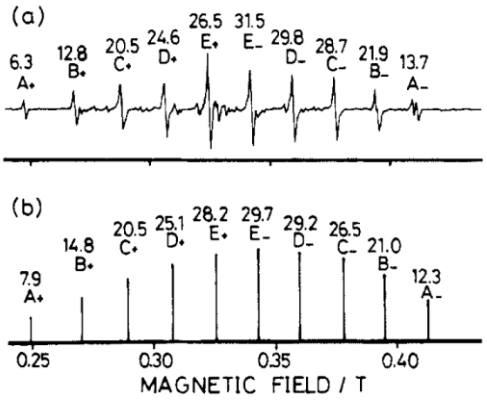

Figure 1-4. Molecular structure of pentakis carbene compound and its EPR spectra in the diluted crystalline solid state

Section.3 Molecule- based magnets in the heterospin systems

From an early period, Gatteschi et. al focused on using the heterospin molecule based magnets consisted of the combination of 3d transition metal spins and 2p organic spins. The mixing of the nitronyl nitroxide derivatives with $M(hfac)_2$ (M = Mn, Fe, Co, Ni, and Cu) gave various kinds of heterospin molecular magnets affected by the magnetic exchange coupling between 3d spins and 2p spins. The combination of $Ni(hfac)_2$ and phenyl-substituted nitronyl nitroxide (NITPh) gave a mononuclear complex formulated as $Ni(hfac)_2(NITPh)_2$ [7]. In this system, organic radicals were coupled with 3d spins of Ni ion very strongly ($J_{ex}/k_B \approx -400\ cm^{-1}$) (Figure 1-5).

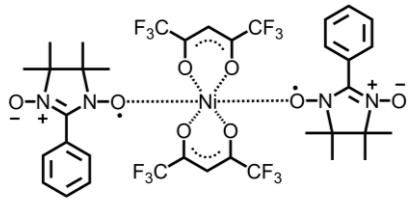

$Ni(hfac)_2(NITPh)_2$

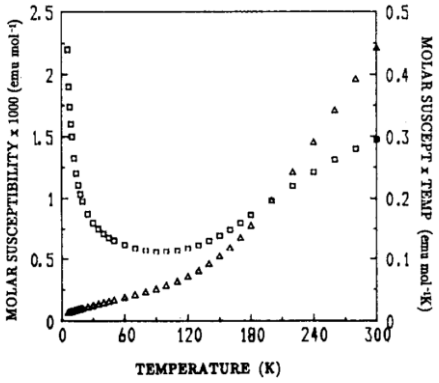

Figure 1-5. Molecular structure of $Ni(hfac)_2(NITPh)_2$ and its temperature dependence of dc magnetic properties

When they used the combination of $Ni(hfac)_2$ and methyl-substituted nitronyl nitroxide (NITMe), one dimensional chain complex formulated as $[Ni(hfac)_2(NITMe)]_n$ was obtained. In this chain compound, extremely large magnetic interaction through the chain ($J_{ex}/k_B \approx -426\ cm^{-1}$) induced the large uncompensated magnetic momentum at the low temperature, suggesting the high usability of organic radical compound in the one dimensional system thanks to its superior magnetic coupling nature with other paramagnetic center (Figure 1-6).

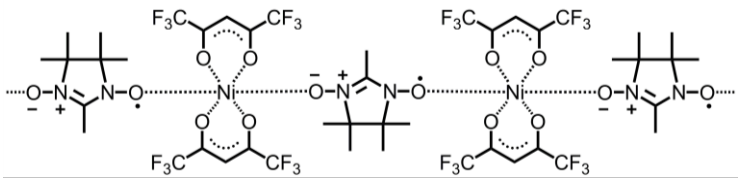

$[Ni(hfac)_2(NITMe)]_n$

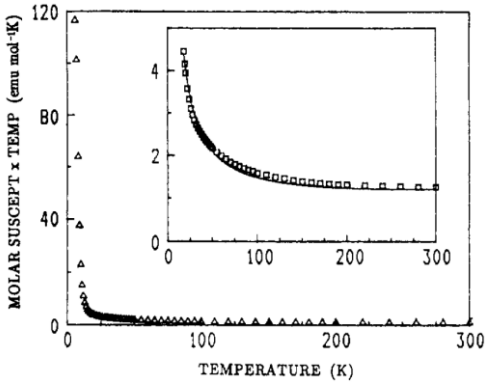

Figure 1-6. Molecular structure of $[Ni(hfac)_2(NITMe)]_n$ and its temperature dependence of dc magnetic properties

Section.4 Single-molecule magnet (SMM)

In recent years, especially among a lot of molecule-based magnets, "single-molecule magnets"[8] (SMM) have been fascinating uncountable number of researchers thanks to their unique magnetic behaviors originated from the curious quantum nature. Mn12 cluster is reported for the first compound as a SMM by Gatteschi et. al in 1991[8b]. Mn ions in this complex showed the relatively strong magnetic interaction each other, resulted the very high spin ground state (S = 20/2) for one molecule. Interestingly enough, Mn12 cluster showed the "frequency depended slow relaxation of magnetization" along with the "quantum tunneling magnetization" at the extremely low temperature. These phenomena clearly suggest the presence of the thermal magnetic relaxation pathway along with the frequency-independent relaxation regime at the same time. In summary, Mn12 exhibited as a magnet with a relatively long lifetime by only twelve paramagnetic spin centers in the crystal state.

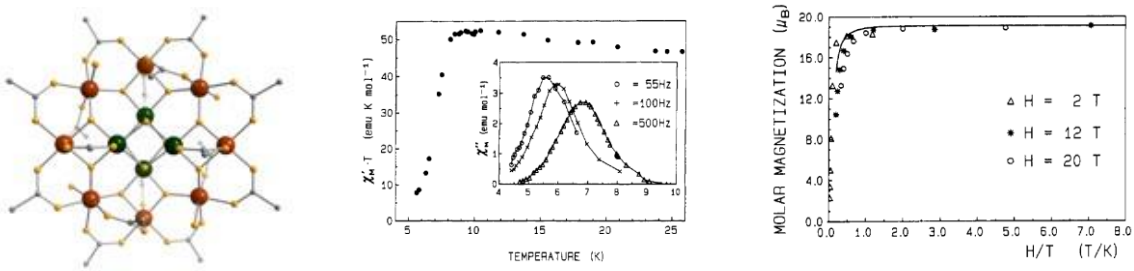

Figure 1-5. Molecular structure of Mn12 cluster and its magnetic properties

Up to date, various kinds of SMMs have been reported and the origins of their unique relaxation mechanisms have also been clarified. Nowadays it is well established that SMM behavior requires following three rules, 1) more than one magnetic center should have highly axial magnetic anisotropy, D, 2) large number of spin ground state S for one molecule, 3) intermolecular magnetic interaction must be much weaker than intramolecular magnetic interaction. When satisfying these regulations, such complex obtains the SMM behavior with activation barrier for the spin reorientation, U, defined by the following equation, $U = |D|S^2$. Although the quantum tunneling magnetization regime is attractive because of the possibility of quantum computing materials, it is not preferred for the observation of SMM behavior (SMMs often lose their magnetic momentum through the fast relaxing pathway of the quantum tunneling). Several approaches for the depression of quantum tunneling magnetization regime are explored (including the dilution method, external dc field method, isotope method, and so on) but there aren't any promising strategies up to now.

Almost all of researches exploring SMMs with high activation barriers and with high blocking temperatures focused on the 3d spins of transition metal ions, on the other hand, Ishikawa et al. had

been already had much attention to the possibilities of 4f spins of lanthanide ions from an early period. In general, lanthanide ions can posses very high spin ground state for each metal center along with the extremely large magnetic anisotropy. Ishikawa et. al cleverly designed the high symmetrical Ln complexes with extremely high activation barrier by using various substituted phthalocyanine derivatives (Figure 1-6)[8g,8h]. This report encouraged large number of researchers about the significant potentialities of lanthanide based molecule-based magnet, and a lot of 4f ion-based SMM and SCMs are well known today[9], although the small distribution of 4f orbital usually avoids the effective magnetic coupling with other paramagnetic centers.

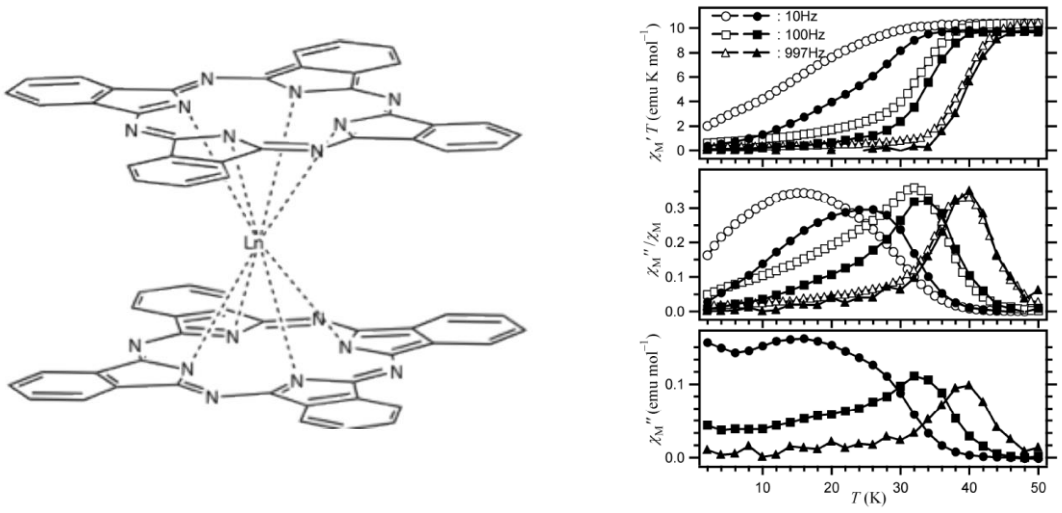

Figure 1-6. Molecular structure of Tb-phthalocyanine complex and its ac magnetic properties

Section.5 Single-chain magnet (SCM)

11 years after the discovery of SMMs, Clerac and Miyasaka et al. reported a new type of 1-D molecule-based magnet showing the slow magnetic relaxation, so called "single-chain magnet"[10] (SCM) in 2002 (Figure 2-1). The almost restricted alignment of the direction of the magnetic anisotropy of metal ion through the 1-D chain complex produced the additional barrier for the spin reorientation given by Δ_ξ ($4JS^2$ in finite regime, and $8JS^2$in infinite regime). As a result, SCM often showed relatively higher activation barrier compared to that of SMM. Up to date, numerous kinds of SCMs have been constructed by using various bridging ligands including cyanide, azide, carboxylate, bipyridine, and so on.

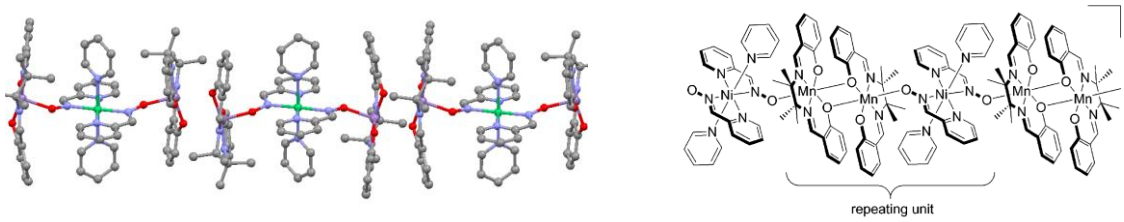

$[Mn(saltmen)_2Ni(pao)_2(py)_2(ClO_4)_2)]_n$

Magnetic hysteresis

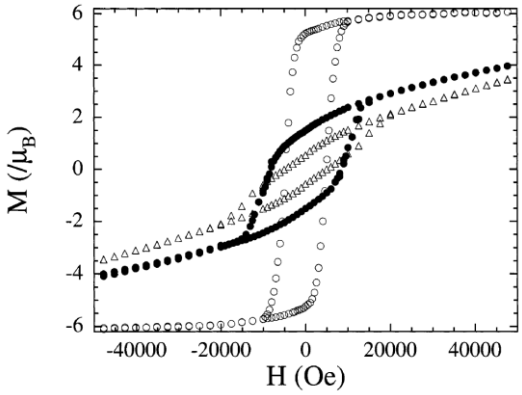

Slow magnetic relaxation

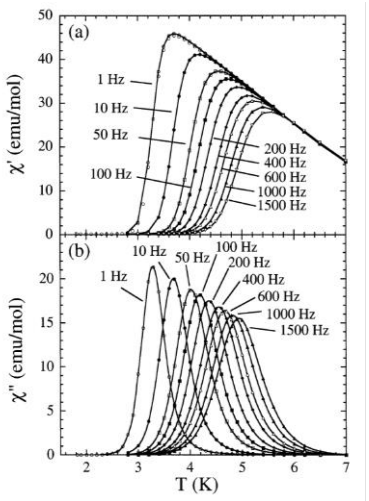

Figure 1-7. Molecular structure of heterometallic single chain magnet consisted of $Mn_2(saltmen)_2$ dimer and $Ni(pao)_2py_2$ unit and its magnetic properties reported in 2002.

Section.6 SMM in 3d-2p heterospin systems

Organic spins also had crucial roles for the construction of 3d metal based SMM and SCM mainly due to their relatively large exchange coupling nature with another spin sources originated from its wide distribution of electron spins compared to those of metal ions. In this line, we have developed various kinds of 2p-3d heterospin magnets previously[11]. In these studies, we mainly focused on two types of organic spin sources. At first, the aminoxyl radical was very useful for the fundamental investigation of the exchange coupling nature with the metal ions thanks to its relatively high stability even in the ambient conditions. The aminoxyl was interacted with 3d spin of metal ion through pyridine moiety sometimes ferromagnetically, and the other time antiferromagnetically. Kanegawa revealed that the combination of $Co(NCO)_2$ and the stable aminoxyl with bulky substituents, TBPNOpy, in 1 : 4 ratio gave mononuclear complex formulated as $[Co(NCO)_2(TBPNOpy)_4]$ (Figure1-8). This complex showed the intramolecular ferromagnetic interaction between Co^{II} ion and aminoxyl (J_{ex}/k_B = 16 K), giving S_{total} = 5/2 state for each molecule and also showed the slow magnetic relaxation typical to the SMM in the ac magnetic property measurement[12a].

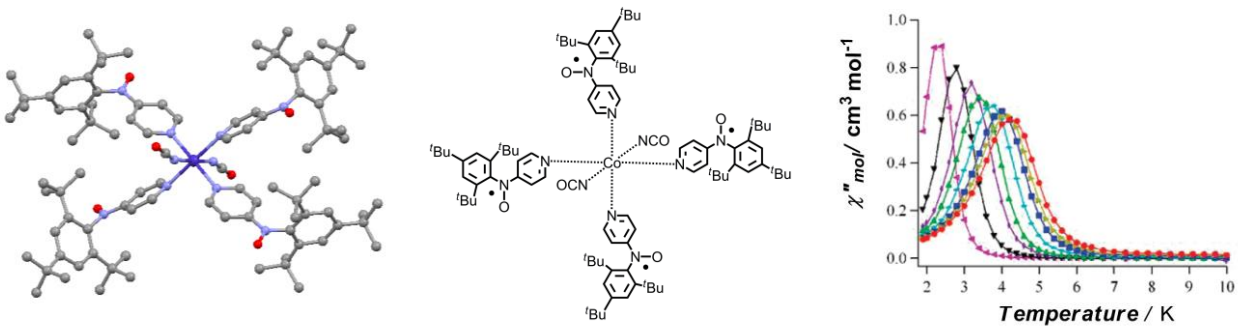

Figure 1-8. Molecular structure of heterospin $[Co(NCO)_2(TBPNOpy)_4]$ complex and its SMM behavior

Secondly, carbene compound was very useful for the establishing of photoresponsive heterospin molecule magnets with very high spin ground state. Though the carbene is magnetically less stable than aminoxyl, we can easily control the spin multiplicity of molecular magnets by the photo-irradiation under the extremely low temperature range. Yoshihara mixed the $Co(hfpip)_2$ derivatives with the photoresponsive diazo ligand carrying two pyridine units, BPBD, gave the single crystal of dinuclear Co^{II} complex formulated as $[Co(hfpip\text{-}R)_2(BPBD)_2]$ (Figure 1-9). After irradiation in the solid state at extremely low temperature, resulting carbene species ferromagnetically interacted with 3d spins of Co^{II} ions through the π conjugation system. The

activation barrier for the spin re-orientation, U_{eff}/k_B, was very large and the 10 kOe of coercive field at 1.9 K was the world record at that time[12b].

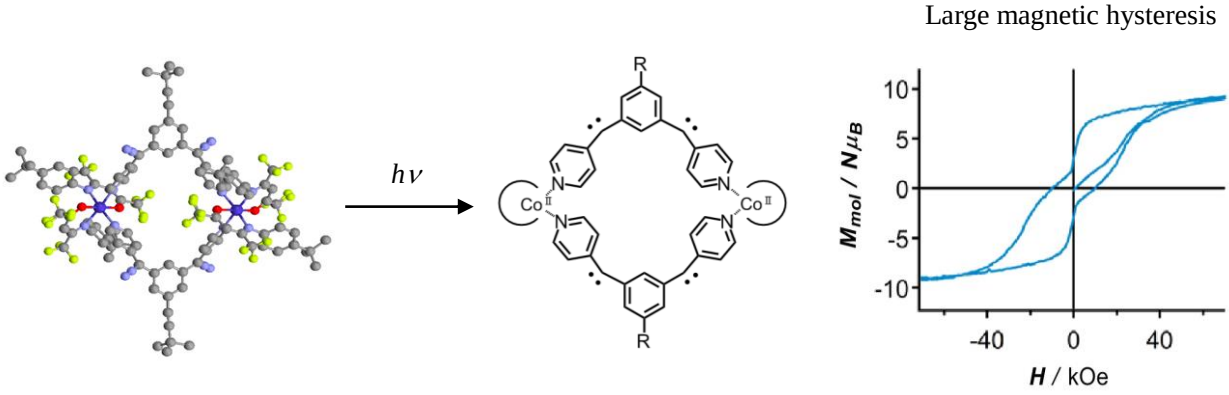

Figure 1-9. Molecular structure of photoresponsive single molecule magnet [Co(hfpip-R)$_2$(BPBD)$_2$] and its field dependence of magnetic susceptibility

As mentioned, introduction of organic radical compound into the molecule based magnet is one of the most promising strategies for the construction of SMMs with high blocking temperature. Although, in spite of the high possibility of 2p spins in the molecular magnetism, it is still challenging to control the magnetic interaction between metal spins and organic spins deliberately even in the 3d-2p heterospin system. In addition, construction and the magnetic investigation of novel 4f-2p heterospin compounds is the most impressive and challenging work for a lot of researchers though only a limited number of 4f –2p based molecule magnets are reported up to date compared to those of 3d-2p ones mainly because of the difficulty of the preparation of the effective magnetic coupler for the 4f-2p systems. In this line, in this report, I will discuss about the construction of novel heterospin complexes mainly focusing on the seeking of newly designed magnetic couplers (Figure 1-10). In chapter 2 and chapter 3, **NOpy$_2$**, as a stable aminoxyl bridging ligand, will be prepared and its polymeric 1-D 3d complexes will be crystallographically and magnetically investigated. It is noteworthy that controlling the spin exchange coupling between the paramagnetic units is one of the most important topics in the molecular magnetism. In chapter 4, and chapter 5, two types of diazo(carbene)-Ln complexes will be constructed for the development of novel 2p-4f heterospin systems. In chapter 6, **D1(pyO)$_2$**, which contains two pyridine-*N*-oxide units and one diazo unit, will be designed for the 2p-4f molecule-based magnets with 1-D chain structures. In these chapters, designing and the preparation of paramagnetic couplers and their novel Ln complexes are very valuable.

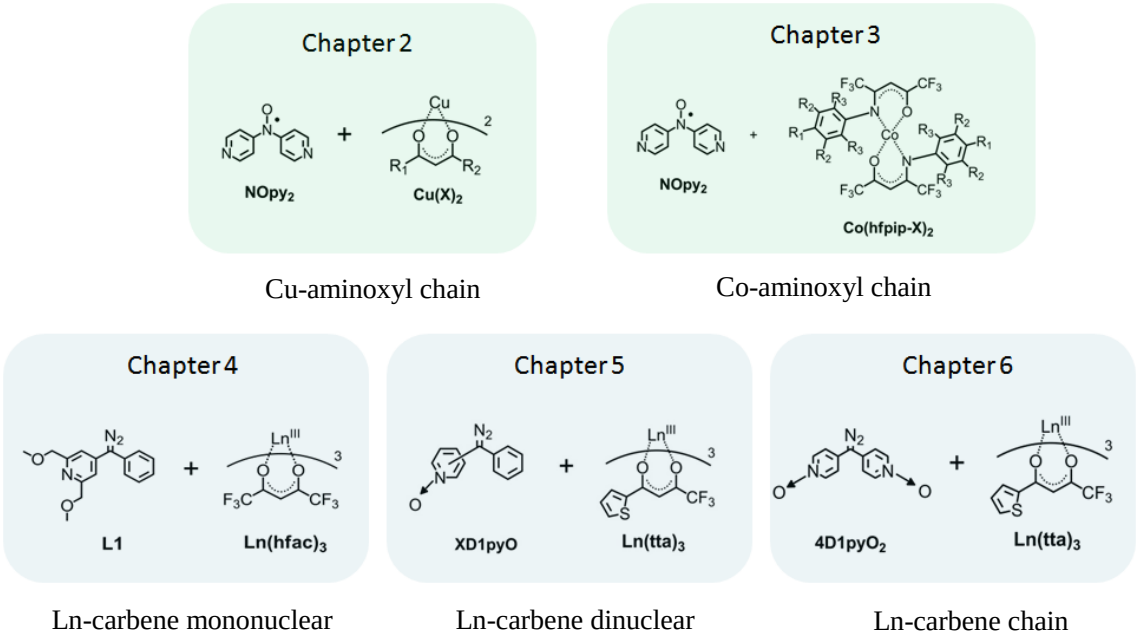

Figure 1-10. Schematic chapter introduction of this thesis

Chapter 2

~Construction of 1-D heterospin Cu(II) complexes~

Section1. Heterospin molecule based magnets with 1-D chain structures

Construction of 1-D chain complexes is one of the most attractive topics from the viewpoint of magneto-structural correlation studies. For the construction of 3d-2p heterospin molecule-based magnet in the 1-D chain system, we have already developed the diazo-pyridine based photoresponsive ligand as a magnetic coupler. **C1py$_2$**, the photo product of **D1py$_2$**, could magnetically connect the neighboring 3d metal ions by its both sides of pyridine units[13] (Figure 2-1).

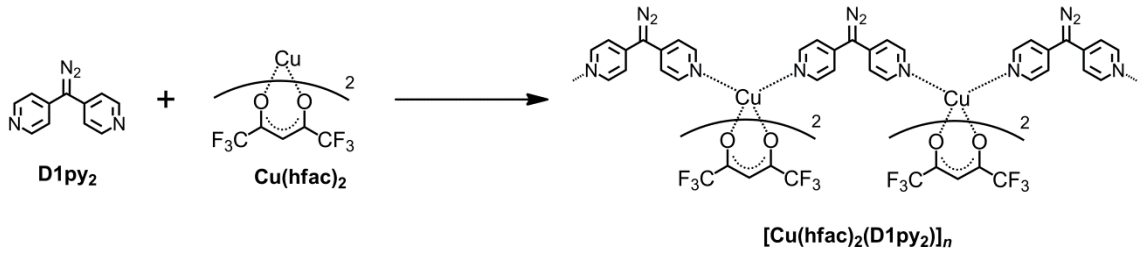

Figure 2-1. Molecular structure of heterospin 3d-2p chain complexes by the combination of Cu^{II} ion and the diazo-pyridine bridging ligand, **D1py$_2$**.

In the case of $[Cu(hfac)_2(D1py_2)]_n$ reported by Iwamura et.al in 1997, after irradiation, 2p spin of carbene was ferromagnetically interacted with 3d spin of Cu^{II} ion through the pyridine moiety. This heterospin system was similar to that of $[Cu(hfac)_2(NITMe)]_n$ reported by Gatteschi et. al although was exactly different in the point that spin center of **C1py$_2$** was indirectly connected to the metal ion but through π conjugation of pyridine rings. Introduction of the photo reactivity into the magnetic materials was very attractive, though the correct discussion about the magnetic exchange coupling between 3d and 2p spins were still inactive because of the difficulties of the quantitative analyses for 3d metal- 2p carbene based magnetic systems. As mentioned in the introduction chapter, controlling and the evaluation of the magnetic coupling nature are the most important topics in the molecular magnetism. Hence in this section, for the construction of novel 3d-2p heterospin chain complexes and the quantitative evaluation of the spin exchange parameters in heterospin chain systems, the stable aminoxyl radical carrying two pyridine moieties were used as an effective magnetic coupler, and its polymeric Cu complexes were investigated in detail.

Section 2. Preparation and the crystal structures of $[Cu(X)_2\mathbf{NOpy_2}]_n$ (**1a**, **1b**, and **1c**)

The aminoxyl radical carrying two pyridine rings, **NOpy₂**, was designed as an effective magnetic coupler for the construction of novel heterospin complexes by Kanegawa[14]. It was expected that **NOpy₂** might be able to magnetically connect the neighboring metal ions by its both sides of the pyridine moieties, giving the 1-D magnetically conjugated heterospin complexes. **NOpy₂** was successfully prepared as a reddish colored crystal in six steps from pyridine-*N*-oxide and 4-aminopyridine according to the Kanegawa's method.

Then, in order to examine the fundamental magnetic property of **NOpy₂** as a magnetic coupler for the heterospin complexes, the small anisotropic Cu(II) ion with three types of *β*-diketonato ligand was used for the determination of spin exchange coupling of 2p and 3d spin. The fluorine substituted acetylacetonato derivatives were selected for the chelating ligands of Cu ions to investigate the effect of Lewis basicities of the diamagnetic units. Generally, the more the number of fluorine substituents increased, the more the stability of the metal *β*-diketonato complex decreased because of the low charge density on the oxygen atoms. The drastic differences of the molecular structures particularly around the metal center were expected.

Mixing the **NOpy₂** with $Cu(\mathbf{X})_2$ in 1 : 1 ratio in the organic solvents gave the green-colored single crystals suitable for the X-ray analysis (Scheme 2-1).

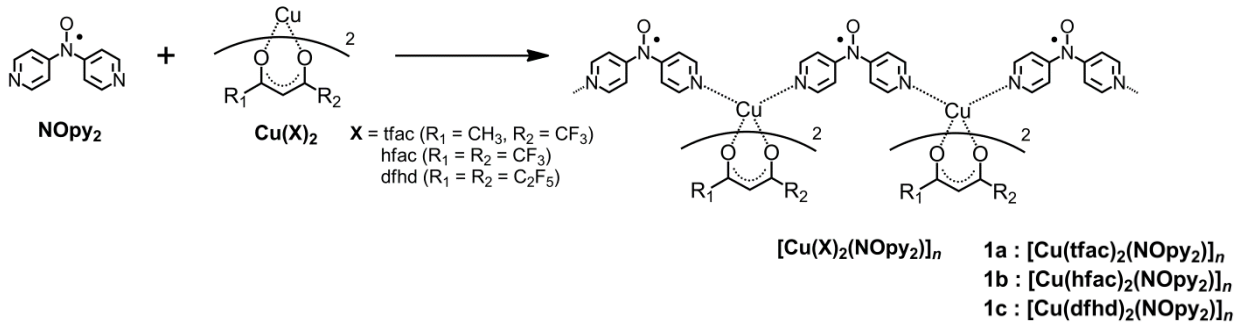

Scheme 2-1. Synthesis of $[Cu(X)_2(NOpy_2)]_n$

X-ray crystal analyses were performed at -183 °C for $[Cu(tfac)_2(\mathbf{NOpy_2})]_n$ (**1a**), at -180 °C for $[Cu(hfac)_2(\mathbf{NOpy_2})]_n$ (**1b**), and at -150 °C for $[Cu(dfhd)_2(\mathbf{NOpy_2})]_n$ (**1c**) using single crystals obtained above.

(i) $[Cu(tfac)_2(\mathbf{NOpy_2})]_n$ (**1a**)

The existence of 1-D chain complex formulated as $[Cu(tfac)_2(\mathbf{NOpy_2})]_n$ was revealed by the X-ray structure analysis. **1a** crystallized in the monoclinic *C*2/*c* (No.15) space groups and the inversion center was located on the metal center, indicating the existence of one crystallographically independent Cu ion and the tfac anion, and the pyridine unit. The local coordination geometry was six-coordinated octahedron arising from the four oxygen atoms of two tfac anions and the two nitrogen atoms of **NOpy$_2$** units in the *trans* configuration, resulted in giving the pseudo-linear *trans* type 1-D chain structures. The dihedral angle between pyridine plane (defined by C1, C2, C3, C4, C5, N1) and the aminoxyl plane (defined by C3, C4, and N2) and between the pyridine planes were 33.35 °and 61.08 °, respectively. The bond length of Cu-N1 was 2.398(4) Å and was much longer than that of Cu-O2 (1.972 (4) Å), and Cu-O3 (1.966 (3) Å), indicating the highly elongated octahedral geometry. In the crystal packing, the chain was crystallographically aligned to $a + 3c$ axis. The shortest interchain contact between **NOpy$_2$** moieties were found at the oxygen atom of aminoxyl and the β carbon atom of pyridine unit ($r_{O\text{-}C}$ = 3.27 Å). The shortest distances of Cu-Cu and NO-NO within the chain were 11.9, and 11.1 Å, respectively indicating the insignificant direct magnetic interaction between spin centers. The ORTEP drawings of the local structures and the crystal packings in the ball and sticks model were depicted in Figure 2-2, and the main crystallographic parameters are summarized in the Table 2-1.

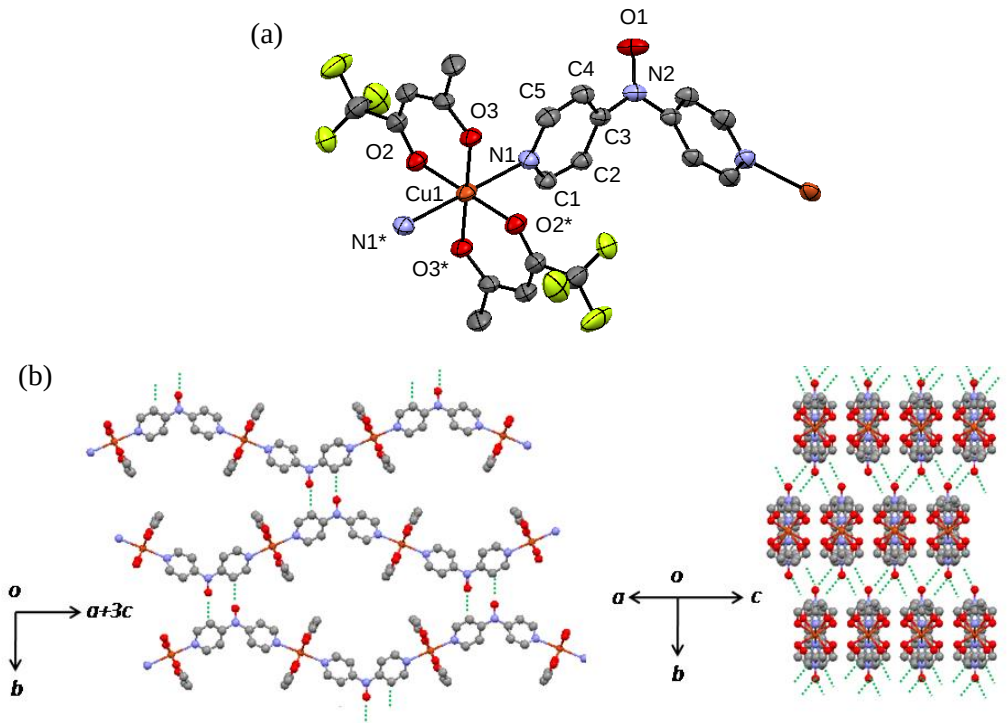

Figure 2-2. (a) ORTEP drawings of $[Cu(tfac)_2(\mathbf{NOpy_2})]_n$ (**1a**). The thermal ellipsoids are set at a 50% probability level, and the hydrogen atoms are omitted for the sake of clarity. (b) Crystal packings with the ball and stick model (C; gray, O; red, N; blue) for **1a** projecting from the shown directions. Hydrogen atoms, CH_3 groups and CF_3 groups are omitted for sake of clarity. Short contacts are indicated by the green dotted lines.

(ii) $[Cu(hfac)_2(\mathbf{NOpy_2})]_n$ (**1b**)

$[Cu(hfac)_2(\mathbf{NOpy_2})]_n$ was crystallized in the orthogonal *Ibam* space groups (No. 72) and had the inversion center on the Cu ion. The local coordination geometry was six-coordinated octahedron similar to **1a**, though it was worth noting that **1b** showed the unique molecular structure expressed as a "static disorder"[15] of the *cis* and *trans* configurations of pyridine rings. The dihedral angle between pyridine plane and the aminoxyl plane, and between the pyridine planes were 34.18 °and 60.08 °, respectively. The bond lengths of Cu-N1, Cu-O2, and Cu-O3 were 2.173 (13), 2.139(4), and 1.972(10) Å, respectively hence the local coordination structure was expressed as a distorted octahedral structure compressed to the O3-Cu-O3 direction. The shorter bond length of Cu-N compared to that of **1a** implied the stronger magnetic interaction between the aminoxyl and the Cu ion in **1b**. In the crystal packing, the shortest interchain contact between $\mathbf{NOpy_2}$ moieties were found at the oxygen atom of aminoxyl and the β carbon atom of pyridine unit ($r_{O\text{-}C}$ = 3.53 Å). The shortest distances of Cu-Cu and NO-NO within the chain were 11.3, and 14.4 Å, respectively suggesting the negligible direct magnetic interaction between spin centers. The ORTEP drawings of the local structures and the crystal packings in the ball and sticks model were depicted in Figure 2-3, and the main crystallographic parameters are summarized in the Table 2-1.

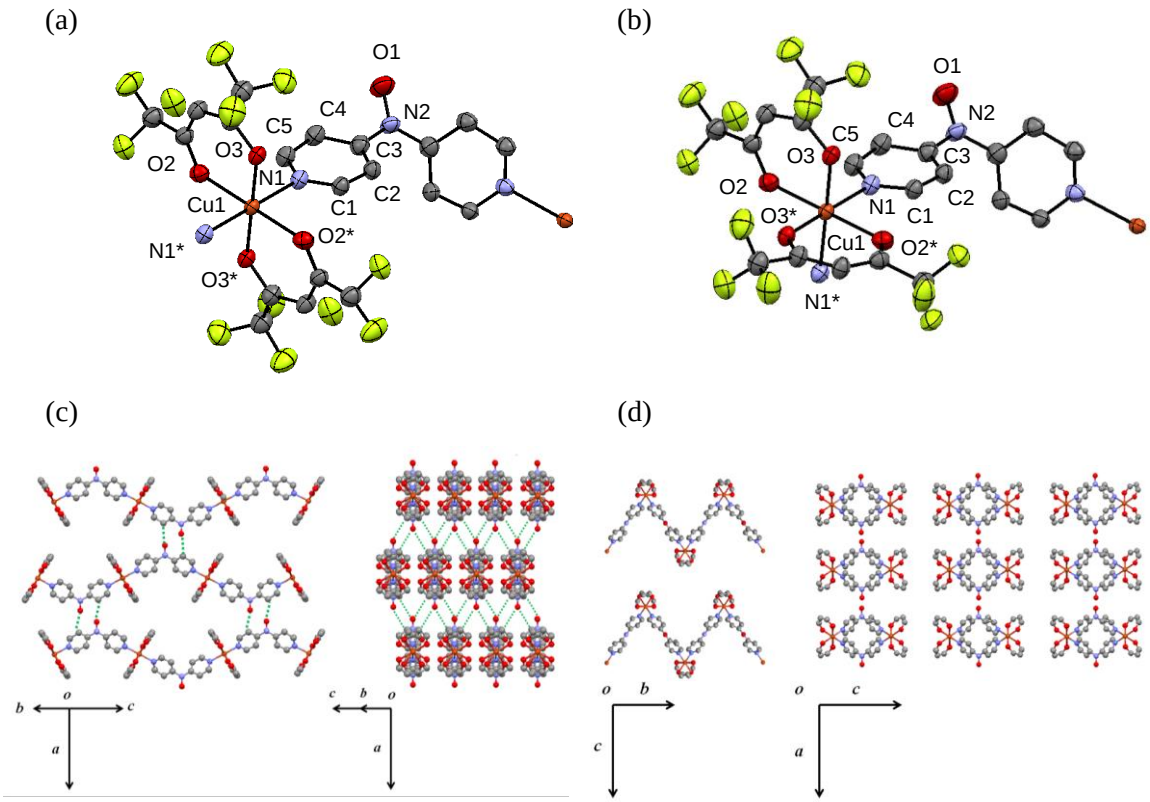

Figure 2-3. (a), (b) ORTEP drawings of $[Cu(hfac)_2(\mathbf{NOpy_2})]_n$ (**1b**) in *trans* and *cis* configuration respectively. The thermal ellipsoids are set at a 50% probability level, and the hydrogen atoms are omitted for the sake of clarity. (c), (d) Crystal packings with the ball and stick model (C; gray, O; red, N; blue) for **1b** projecting from the shown directions. Hydrogen atoms and CF_3 groups are omitted for sake of clarity. Short contacts are indicated by the green dotted lines.

(iii) $[Cu(dfhd)_2(\mathbf{NOpy_2})]_n$ (**1c**)

$[Cu(dfhd)_2(\mathbf{NOpy_2})]_n$ was crystallized in the triclinic *P*-1 space groups (No. 2), and there were crystallographically one $Cu(dfhd)_2$ unit and the one $\mathbf{NOpy_2}$ unit. The local coordination geometry was similar to those of **1a**, and **1b**. The dihedral angles between pyridine plane and the aminoxyl plane, and between the pyridine planes were 25.47, 29.96 °and 60.08 °, respectively. The bond lengths of Cu1-N1, Cu2-N3, were 2.021 (6), 2.015(15), respectively. The local coordination structure was expressed as a distorted octahedral structure elongated to the O2-Cu1-O2* and O4-Cu2-O4* direction. The shortest bond length of Cu-N in **1c** among the three chain complexes suggested the strongest magnetic interaction between the aminoxyl and the Cu ion. In the crystal packing, the shortest interchain contact between $\mathbf{NOpy_2}$ moieties were found at the oxygen atom of aminoxyl and the β carbon atom of pyridine unit ($r_{O\text{-}C}$ = 3.19 Å). The shortest distances of Cu-Cu and NO-NO within the chain were 14.0, and 13.6 Å, respectively. The ORTEP drawings of the local structures and the crystal packings in the ball and sticks model were depicted in Figure 2-4, and the main crystallographic parameters are summarized with those of **1a** and **1b** in the Table 2-1.

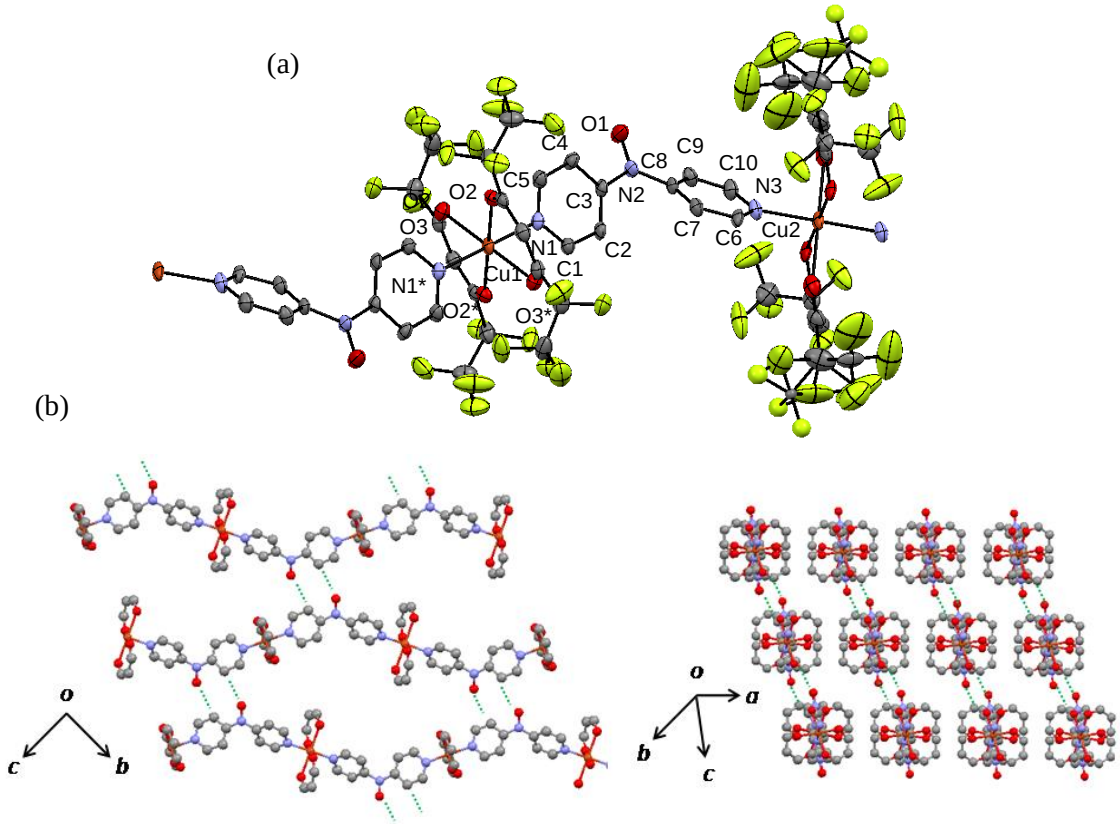

Figure 2-4. (a) ORTEP drawings of $[Cu(dfhd)_2(\mathbf{NOpy_2})]_n$ (**1c**). The thermal ellipsoids are set at a 50% probability level, and the hydrogen atoms are omitted for the sake of clarity. (b) Crystal packings with the ball and stick model (C; gray, O; red, N; blue) for **1c** projecting from the shown directions. Hydrogen atoms and C_2F_5 groups are omitted for sake of clarity. Short contacts are indicated by the green dotted lines.

Table 2-1. Crystallographic Data Collection and Structural Refinement Information for copper complexes, $[Cu(X)_2(\mathbf{NOpy_2})]_n$; X = tfac (**1a**), hfac (**1b**), and dfhd (**1c**).

	1a	**1b**	**1c**
empirical formula	$C_{20}H_{16}N_3O_5F_6Cu$	$C_{20}H_{10}N_3O_5F_{12}Cu$	$C_{24}H_{10}N_3O_5F_{20}Cu$
formula weight	555.90	663.85	863.89
crystal class	monoclinic	orthorhombic	triclinic
space group	*C*2/*c* (no. 15)	*Ibam* (no. 72)	*P*-1 (no. 2)
a /Å	17.580 (9)	19.955 (2)	8.906 (5)
b / Å	18.965 (10)	6.6544 (87)	10.561 (8)
c / Å	7.028 (4)	17.7348 (19)	17.544 (14)
α /deg	90	90	91.30 (3)
β /deg	104.369 (7)	90	101.41 (3)
γ /deg	90	90	106.88 (2)
V / Å^3	2270 (2)	2354.98	1542.2 (19)
μ /mm^{-1}	1.048	1.063	0.872
Z	4	4	2
crystal size /mm	0.20 × 0.20 × 0.10	0.07 × 0.05 × 0.02	0.20 × 0.10 × 0.10
D_{calc} /gcm^{-3}	1.626	1.872	1.862
F (000)	1120.00	1312.00	848.00
radiation	Mo-Kα	Mo-Kα	Mo-Kα
T /K	90.0	93.0	123.0
no. reflections measured	1838	1087	5621
no. unique reflections	1407	795	3730
no. parameters	204	191	506
R_1 [a)]	0.0452 ($I > 2.00\sigma(I)$)	0.0429 ($I > 2.00\sigma(I)$)	0.0884 ($I > 2.00\sigma(I)$)
wR_2 [a)]	0.11.99	0.1050	0.2867
GOF	1.097	1.046	1.094

[a)] $R_1 = \Sigma\ ||F_0|-|F_c||/\ \Sigma\ |F_0|$; $wR_2 = \{\ \Sigma\ w(F_0^2-F_c^2)^2/\ \Sigma\ w(F_0^2)^2\}^{1/2}$

Table 2-2. Selected Bond Lengths (Å) and Dihedral Angles (°) for **1a**, **1b**, and **1c**

1a		**1b**		**1c**	
Bond Lengths (Å)					
Cu(1)-O(2)	1.972 (4)	Cu(1)-O(2)	2.139 (4)	Cu(1)-O(2)	1.990 (5)
Cu(1)-O(3)	1.966 (3)	Cu(1)-O(3)	1.972 (10)	Cu(1)-O(3)	2.272 (6)
Cu(1)-N(1)	**2.398 (4)**	Cu(1)-N(1)	**2.173 (13)**	Cu(2)-O(4)	1.990 (6)
				Cu(2)-O(5)	2.265 (5)
				Cu(1)-N(1)	**2.021 (6)**
				Cu(2)-N(3)	**2.015 (7)**
Dihedral Angles (°) between Pyridine Ring and Aminoxyl Plane					
C(3)N(2)O(1)-C(7) C(9)N(3)	33.35	C(3)N(2)O(1)-C(7) C(9)N(3)	34.18	C(3)N(2)O(1)-C(7) C(9)N(3)	25.47
				C(8)N(2)O(1)-C(2) C(4)N(1)	29.96
Dihedral Angles (°) between the Pyridine Rings					
C(2)C(4)N(1)-C(7) C(9)N(3)	61.08	C(2)C(4)N(1)-C(7) C(9)N(3)	60.08	C(2)C(4)N(1)-C(7) C(9)N(3)	55.79
Interchain distances (Å)					
O(1)-C(4)’	3.274	O(1)-C(4)’	3.530	O(1)-C(4)’	3.189

Section 3. Magnetic properties of $[Cu(X)_2\mathbf{NOpy_2}]_n$ (**1a**, **1b**, and **1c**)

Temperature dependence of direct current magnetic properties were measured using the microcrystalline samples of **1a**, **1b**, and **1c** at a constant dc field of 5 kOe between 300-2 K. The plots of $\chi_{mol}T$ vs. *Temperature* is shown in Figure 2-5. The $\chi_{mol}T$ value at 300 K were 0.76, 0.81, and 0.85 $cm^3mol^{-1}K$ for **1a**, **1b**, and **1c**, respectively. The obtained values were nearly consistent with those calculated by a spin-only equation with isolated aminoxyl radical (0.375 $cm^3mol^{-1}K$) and Cu(II) ions with $S = 1/2$ spin ground state. Upon lowering the temperature, the $\chi_{mol}T$ values for **1a** remained almost unchanged until 12 K and then decreased rapidly below the temperature. This phenomenon indicated the negligible scale of magnetic interaction between aminoxyl and the Cu(II) ion. On the other hand, the temperature dependence of the $\chi_{mol}T$ in the **1b** and **1c** were quite different. The $\chi_{mol}T$ values for **1b** gradually increased when lowering the temperature, reaching a maximum value of 3.3 $cm^3mol^{-1}K$ at 3.5 K, and then steeply decreased. Similarly, those for **1c** gradually increased and reached a maximum of 1.2 $cm^3mol^{-1}K$ at 35 K. The increments of $\chi_{mol}T$ values on cooling were well assigned to the ferromagnetic interaction within the 2p-4f heterospin chain complexes. The observed decrease in complex **1c** below 35 K suggested that an interchain antiferromagnetic interaction might be strong, as implied by the short contacts between the chains in the crystal packing (Figure 2-4b).

For the quantitative evaluation of the magnetic exchange interaction between the aminoxyl and the Cu ion, a ferromagnetic chain model[16], $H = -J\Sigma S_i \cdot S_{i+1}$, was applied to the spin systems for three complexes. The best-fitting results gave the spin exchange coupling parameters J/k_B = 5.7, 32, and 55 K, zJ'/k_B = -7.5, -0.33, and -14.4 K for **1a**, **1b**, and **1c**, respectively. The obtained parameters are summarized in Table 2-3 together with the distances of $r_{Cu\text{-}N}$ and $r_{O(1)\text{-}C(4)}$, and those values for $[Cu(hfac)_2(\mathbf{4NOpy})_2]$ reported in the previous work[8].

The magnitude of the exchange coupling constant, J/k_B values, obviously depended on the diamagnetic chelating ligand of Cu(II) complexes and increased in the order **1a**, **1b**, and **1c**. This order was consistent with that of the bond lengths of $r_{Cu\text{-}Npy}$ (the bond lengths for **1a**, **1b**, and **1c**, were 2.40, 2.14, and 2.02 Å, respectively). The obtained J/k_B values for **1** – **3** together with $[Cu(hfac)_2(\mathbf{4NOpy})_2]$ were plotted as the function of the bond distance between the Cu ion and the nitrogen atoms of pyridines in Figure 2-5b. The J/k_B value increased almost linearly according the decrements of the bond distances ($r_{Cu\text{-}N}$). These results suggested that the bond length of $r_{Cu\text{-}N}$ strongly affected to the magnitude of J/k_B. From the comparison of the dihedral angles between the pyridine ring and the aminoxyl plane with the J/k_B value, the dihedral angle was also suggested to affect the J/k_B value. The values of zJ'/k_B, indicating interchain antiferromagnetic interaction, decreased in the order **1b**, **1a**, **1c**, which was also consistent with the order of short distances between the chains, **1b** > **1a** > **1c**.

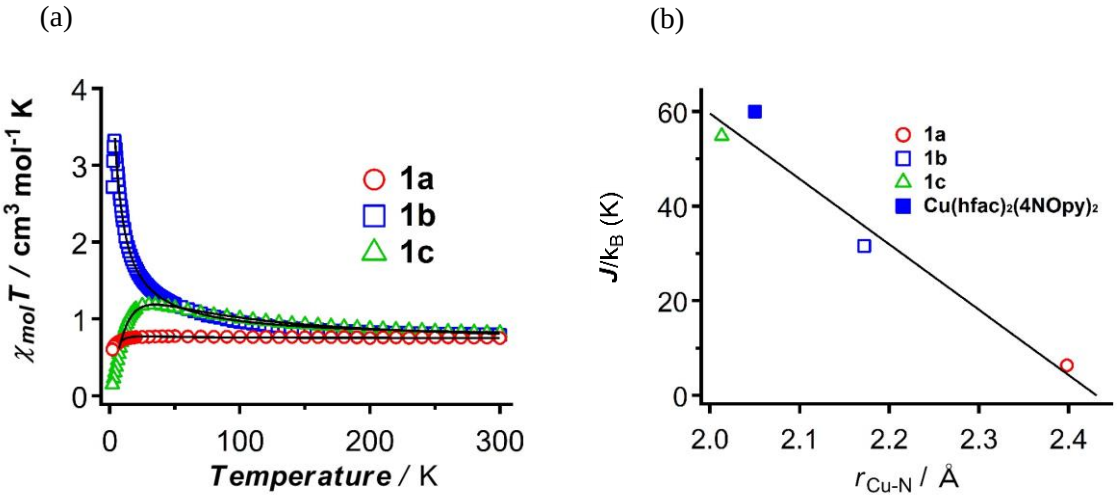

Figure 2-5. (a) The plot of $\chi_{mol}T$ vs. *Temperature* of **1a** (red open circle), **1b** (blue open square), and **2c** (green open triangle), respectively. The black solid lines represent the best-fit results obtained according to the 1-D ferromagnetic chain model (see the text). (b) The plots of exchange coupling constant, J/k_B, vs. the bond lengths of Cu(II) ion and the nitrogen atom of pyridine, r_{Cu-N}.

Table 2-3. Values of J/k_B, zJ'/k_B, r_{Cu-N}, $r_{O(1)-C(4)'}$, and dihedral angles for **1a**, **1b**, and **1c** together with those for [Cu(hfac)$_2$(**4NOpy**)$_2$]

	1a	**1b**	**1c**	[Cu(hfac)$_2$(**4NOpy**)$_2$][8]
J/k_B (K)	5.7	32	55	60
zJ'/k_B (K)	-7.5	-0.33	-14.4	
r_{Cu-N} (Å)	2.40	2.14	2.02, 2.02	2.05
Dihedral angle (°)[b)]	33.4	34.2	25.5, 20.0	10
$r_{O(1)-C(4)'}$ (Å)	3.27	3.53	3.19	

Section 4. Chapter conclusion

NOpy$_2$, for the detailed investigation of the magnetic interaction with the 3d spins of transition metal ions, was successfully prepared and its polymeric Cu^{II} β-diketonato complexes were obtained and crystallographically identified. In the polymeric Cu complexes, 3d spins of Cu ions were magnetically connected through the 2p spin of **NOpy$_2$** unit, resulted in giving the ferromagnetic correlations within the chain structures. The bond lengths of the Cu-N_{py} strongly depended on the number of fluorine atoms of diamagnetic chelating ligands **X** (2.40 Å for tfac, 2.14 Å for hfac, and 2.02 Å for dfhd). In the SQUID measurements, the exchange coupling parameters for **1a**-**1c** were clearly defined by the ferromagnetic chain model. The J/k_B values increased in the order of **1a** (5.7 K), **1b** (32 K), and **1c** (55 K) indicated that controlling the basicities of ligand **X** was the effective strategy for the modulation of the basic magnetic properties in the 3d-2p heterospin complexes.

As a summary of this chapter, we were able to obtain the further insight about the magnetic coupling in the 3d-2p heterospin chain complexes by using the quantitative organic spin coupler, **NOpy$_2$**.

Chapter 3

~ Construction of 1-D heterospin Co(II) complexes ~

Section 1. 1-D chain complexes with high anisotropic metal ions.

In the chapter 2, **NOpy$_2$** was revealed to act as an effective magnetic coupler for the construction of 3d-2p heterospin 1-D chain system. Herein this chapter, Co(II) ion with high magnetic anisotropy was used for the construction of 1-D chain complex showing the slow relaxation of magnetization. As prior information, mononuclear Co-aminoxyl complex, [Co(hfpip-^{t}Bu)$_2$(**4NOpy**)$_2$], showed the SMM behavior thanks to the ferromagnetic interaction within the mononuclear unit[17a].

Section 2. Preparation and the crystal structures of [Co(hfpip-X)$_2$(**NOpy$_2$**)]$_n$ (**2a - 2h**)

Co(hfpip-X)$_2$ (hfpip = 1,1,1,5,5,5-hexafluoro-4-(phenylimino)-2-pentanonate[17], X = H, F, F_3,F_5,Cl, Cl_3, Br, and I) was chosen for the 3d spin source as a highly anisotropic magnetic center. Mixing **NOpy$_2$** with Co(hfpip-X)$_2$ in the solution in 1 :1 ratio gave the reddish colored single crystals of these complexes (Scheme 3-1).

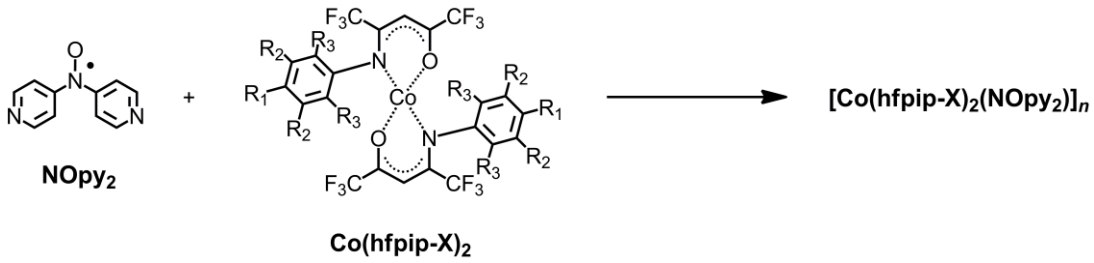

Scheme 3-1. Synthesis of Cu-**NOpy$_2$** chain complexes.

complex No.	X	R_1	R_2	R_3
2a	**H**	H	H	H
2b	**F**	F	H	H
2c	**F_3**	F	F	H
2d	**F_5**	F	F	F
2e	**Cl**	Cl	H	H
2f	**Cl_3**	Cl	Cl	H
2g	**Br**	Br	H	H
2h	**I**	I	H	H

Crystal structures of $[Co(hfpip\text{-}X)_2(\mathbf{NOpy_2})]_n$ (X = H, F, F_3,F_5,Cl, Cl_3, Br, and I)

X-ray crystal analyses were performed at -126 °C for **2d** (X = F_5), and at -183 °C for **2a** (X = H), **2b** (X = F), **2c** (X = F_3), **2e** (X = Cl), **2f** (X = Cl_3), **2g** (X = Br), **2h** (X = I), respectively using single crystals obtained above. The local structures, crystal packings, the crystallographic data, and the selected parameters are summarized in Figure 3-1, 3-2, and Table 3-1, 3-2, respectively.

(i)**2a**, (ii)**2b**, (iii)**2c**, and (iv)**2d** : *trans* chain

As results of X-ray analyses, all complexes showed the 1-D Co-aminoxyl chain structures formulated as $[Co(hfpip\text{-}X)_2(\mathbf{NOpy_2})]_n$ and had no crystal solvents. **2a**, **2b**, **2c**, and **2d** were crystallized in the monoclinic $P2_1/n$, triclinic P-1, monoclinic $C2/c$, and monoclinic $C2/c$, respectively. Each Co(II) was surrounded by two oxygen atoms and two nitrogen atoms arising from two chelated hfpip-X ligand, and two nitrogen atoms of $\mathbf{NOpy_2}$ were coordinated in *trans* configuration. **2b**, **2c**, and **2d** had their intrachain crystallographic symmetry on the Co(II) ions, while **2a** had a symmetrical center between neighboring chains. **2a** had one crystallographically independent Co ion and two independent pyridine rings (A, and B) resulted in giving the "…A-B, Co, A-B…" connected mode. **2b** had two Co ions and two pyridines crystallographically, gave "…A-B, Co1, B-A, Co2, A-B…" connected mode. **2c** and **2d** had one Co ion and one pyridine rings, hence the chain structure was given by "…A-A, Co, A-A…". The local structures of **2a**-**2d** were described as six-coordinated octahedrons compressed to the O-Co-O directions. The bond lengths of Co-O (2.01-2.03 Å) were slightly shorter than those of Co-N ranging from 2.18-2.19 Å in **2a**-**2c**, though the Co-N bond length in **2d** (2.242 Å) was somehow longer than those of **2a**-**2c**, suggesting the weak magnetic interaction between 3d spins of Co(II) ion and aminoxyl. This difference might be caused by the steric repulsion originated from of fluorine atoms on the 2-position of the phenyl ring in **2d**.

The dihedral angle between pyridine plane and XY plane (defined by four nitrogen atoms around Co ion) in **2c** were 55.6° and was slightly smaller than those of **2a**, **2b**, and **2d** (72.4-83.4°). Hence the magnetic coupling within the chain in **2c** might be weak compared to those of other complexes. The dihedral angle between pyridine plane and NO planes were 16.0-31.8°, suggested the effective magnetic interactions. In these complexes, the *z* axes, defined by the shortest O-Co-O directions, were largely tilted to the chain direction of *b* axes (61-69 °). In the viewpoint of the crystal packing, **2a** and **2b** showed the short contact between the aminoxyl and neighboring β carbon atoms of pyridine moieties (3.25 and 3.26 Å) formed 2D sheet structures. **2a** had the intermolecular contact between the aminoxyl and the fluorine atom (3.29 Å), on the other hand, **2d** merely had the interchain short contact around the NO moiety.

(v)**2e**, (vi)**2f**, (vii)**2g**, and (viii)**2h** : *cis* chain

All complexes crystallized in the monoclinic $P2_1/n$ space group for **2e**, **2g**, **2h** and $P2_1/c$ space group for **2f**, respectively (No.14) and had crystal solvents formulated as $[Co(hfpip\text{-}X)_2(\mathbf{NOpy_2})]_n$ *m solvent* (*m* = 0.5 for **2e**, 1 for **2f**-**2h**). Each Co(II) was surrounded by two oxygen atoms and two nitrogen atoms arising from two chelated hfpip-X ligand, and two nitrogen atoms of $\mathbf{NOpy_2}$ coordinated in *cis* configuration to form helical chains. **2e**-**2h** had their symmetrical centers between neighboring chains. All four complexes had one crystallographically independent Co ion and two independent pyridine rings as well as **2a**, resulted in giving the "…A-B, Co, A-B…" connected mode. The local structures of **2e**-**2h** were described as six-coordinated octahedrons compressed to the O-Co-O directions. The bond lengths of Co-O (2.02-2.03 Å) were slightly shorter than those of Co-N ranging from 2.16-2.21 Å. The dihedral angle between pyridine plane and XY plane (defined by four nitrogen atoms around Co ion) were 54.4-70.2° and were somehow smaller than those of **2a**, **2b**, and **2d** (72.4-83.4°). The dihedral angle between pyridine plane and NO planes were 16.0-41.8°, suggested the effective magnetic interactions. In these complexes, the *z* axes, defined by the shortest O-Co-O directions, were largely tilted to the chain direction of *b* axes (63-68 °). In the crystal packing, **2e**, **2g**, and **2h** had the intermolecular contact between the aminoxyl and the halogen atom (3.62-3.68 Å), on the other hand, **2f** had no short contacts within 4 Å. The local structures, crystal packings, the crystallographic data, and the selected parameters are summarized in Figure 3-1, 3-2, and Table 3-1, 3-2, respectively.

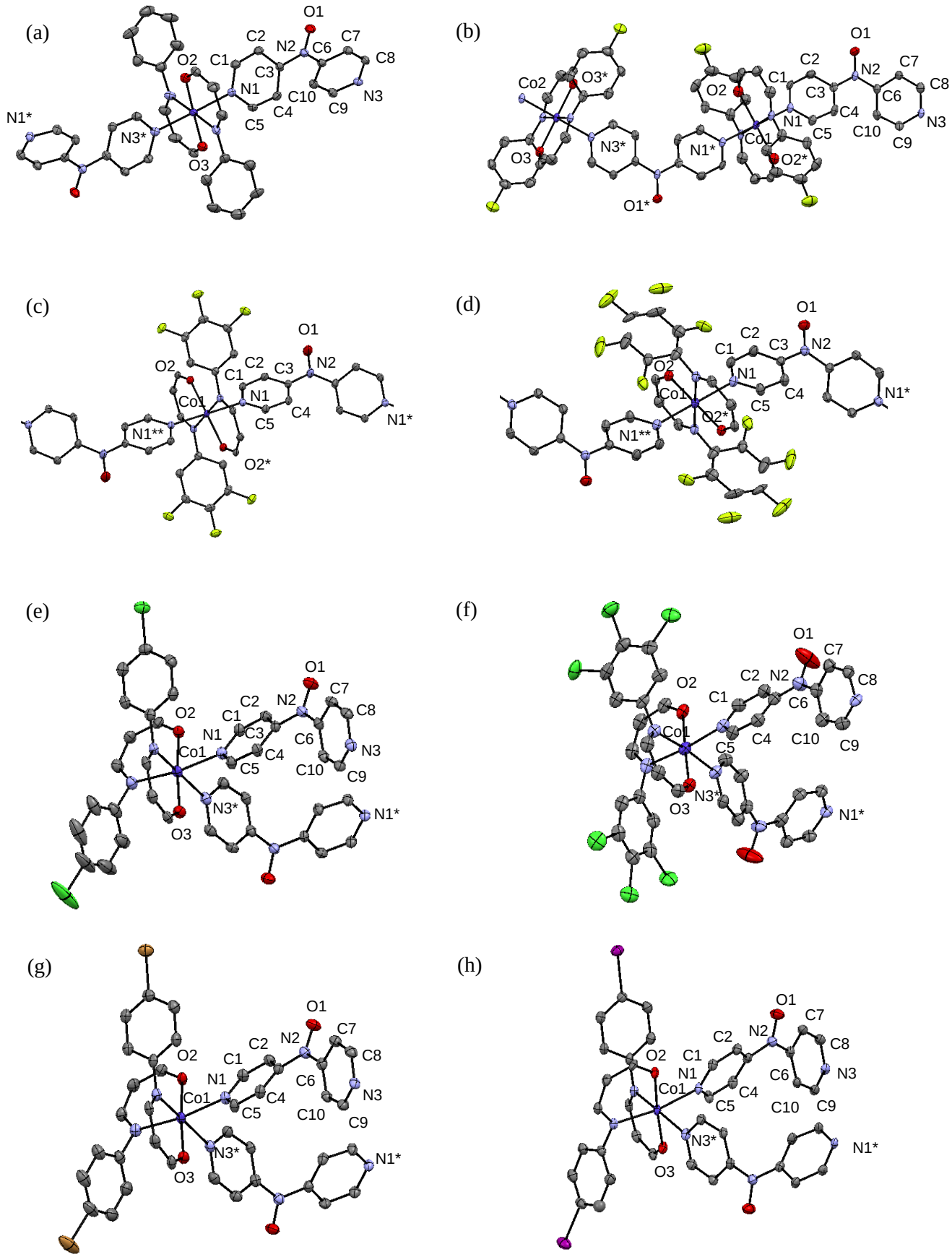

Figure 3-1. (a) ORTEP drawings of $[Co(hfpip\text{-}X)_2NOpy_2]_n$ for (a)**2a**, (b)**2b**, (c)**2c**, (d)**2d**, (e)**2e** ,(f)**2f**, (g)**2g**, and (h)**2h**. The thermal ellipsoids are set at a 50% probability level, and the hydrogen atoms and CF_3 groups are omitted for the sake of clarity

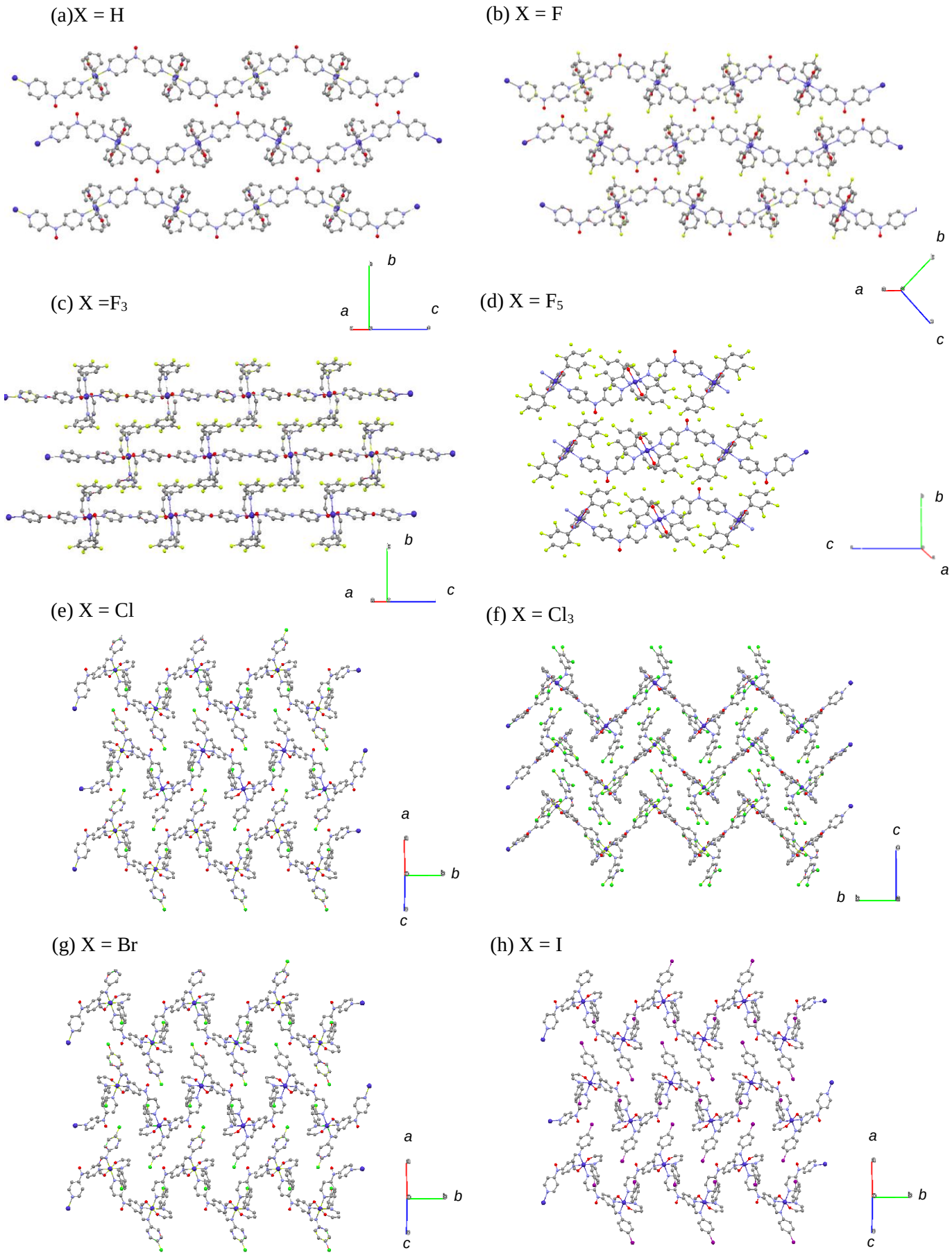

Figure 3-2. (a) Crystal packings with the ball and stick model (C; gray, O; red, N; blue) for (a)**2a**, (b)**2b**, (c)**2c**, (d)**2d**, (e)**2e** ,(f)**2f**, (g)**2g**, and (h)**2h** projecting from the shown directions. Hydrogen atoms and CF_3 groups are omitted for sake of clarity

Table 3-1. Crystallographic Data Collection and Structural Refinement Information for cobalt complexes, $[Co(hfpip\text{-}X)_2(\mathbf{NOpy_2})]_n$; X = H (**2a**), F (**2b**), F_3 (**2c**), F_5 (**2d**), Cl (**2e**), Cl_3 (**2f**), Br (**2g**), and I (**2h**).

	2a	**2b**	**2c**	**2d**
empirical formula	$C_{32}H_{20}N_5O_3F_{12}Co$	$C_{32}H_{18}N_5O_3F_{14}Co$	$C_{32}H_{14}N_5O_3F_{18}Co$	$C_{32}H_{10}N_5O_3F_{22}Co$
formula weight	809.46	845.44	917.40	989.36
crystal class	monoclinic	triclinic	monoclinic	monoclinic
space group	$P2_1/n$ (no. 14)	P-1 (no. 2)	$C2/c$ (no. 15)	$C2/c$ (no. 15)
a /Å	9.539 (5)	9.616 (4)	19.079 (12)	9.9481 (4)
b / Å	18.791 (10)	12.934 (6)	9.6024 (6)	16.9809 (5)
c / Å	18.602 (10)	13.637 (6)	18.6000 (11)	22.1984 (8)
α /deg		91.961 (6)		
β /deg	104.519 (7)	95.844 (6)	103.2390 (10)	111.500 (2)
γ /deg		105.413 (6)		
V / Å^3	3228 (2)	1623.3 (13)	3317.1 (4)	3489.0 (2)
μ /mm^{-1}	0.645	0.654	0.664	0.655
Z	4	2	4	4
crystal size /mm	0.20 × 0.10 × 0.05	0.10 × 0.08 × 0.05	0.20 × 0.10 × 0.05	0.50 × 0.20 × 0.20
D_{calc} /gcm^{-3}	1.666	1.730	1.837	1.883
F (000)	1624.00	844.00	1816.00	1944.00
radiation	Mo-Kα	Mo-Kα	Mo-Kα	Mo-Kα
T /K	90.0	93.0 (2)	90.0	146.0
no. reflections measured	6811	5960	3614	3968
no. unique reflections	4321	3897	3273	2933
no. parameters	479	475	270	378
R_1	0.0607 ($I > 2.00\sigma(I)$)	0.0895 ($I > 2.00\sigma(I)$)	0.0264 ($I > 2.00\sigma(I)$)	0.0484 ($I > 2.00\sigma(I)$)
wR_2	0.1754	0.2778	0.0707	0.1445
GOF	1.027	1.040	1.044	0.924

[a] $R_1 = \Sigma\ ||F_0|-|F_c||/\ \Sigma\ |F_0|$; $wR_2 = \{\ \Sigma\ w(F_0^2-F_c^2)^2/\ \Sigma\ w(F_0^2)^2\}^{1/2}$

	2e	**2f**	**2g**	**2h**
empirical formula	$C_{32}H_{18}N_5$ $O_3F_{12}Cl_2Co/0.5CHCl_3$	$C_{32}H_{14}N_5$ $O_3F_{12}Cl_6Co/CH_3CN$	$C_{32}H_{18}N_5$ $O_3F_{12}Br_2Co/acetone$	$C_{32}H_{18}N_5$ $O_3F_{12}I_2Co/CHCl_3$
formula weight	938.03	1057.18	1025.33	1180.63
crystal class	monoclinic	monoclinic	monoclinic	monoclinic
space group	$P2_1/n$ (no. 14)	$P2_1/c$ (no. 14)	$P2_1/n$ (no. 14)	$P2_1/n$ (no. 14)
a /Å	15.294 (8)	12.124 (12)	15.582 (6)	16.338 (5)
b / Å	13.850 (7)	16.469 (15)	13.914 (5)	14.020 (4)
c / Å	18.514 (9)	20.811 (20)	18.507 (7)	18.562 (5)
α /deg				
β /deg	110.744 (7)	94.210 (12)	110.901 (4)	110.931 (3)
γ /deg				
V / Å^3	3668 (3)	4144 (7)	3748 (3)	3971.0 (20)
μ /mm^{-1}	0.827	0.898	2.704	2.288
Z	4	4	4	4
crystal size /mm	0.20 × 0.10 × 0.05	0.20 × 0.10 × 0.05	0.10 × 0.10 × 0.05	0.20 × 0.10 × 0.05
D_{calc} /gcm^{-3}	1.699	1.694	1.671	1.975
F (000)	1868.00	2096.00	2024.00	2272.00
radiation	Mo-Kα	Mo-Kα	Mo-Kα	Mo-Kα
T /K	90.0	90.0	90.0	90.0
no. reflections measured	7651	7141	8191	8658
no. unique reflections	4691	4841	6248	7225
no. parameters	525	557	540	513
R_1	0.0670 ($I > 2.00\sigma(I)$)	0.0687 ($I > 2.00\sigma(I)$)	0.0516 ($I > 2.00\sigma(I)$)	0.0510 ($I > 2.00\sigma(I)$)
wR_2	0.1612	0.1960	0.1462	0.1566
GOF	1.020	1.049	1.048	1.025

[a] $R_1 = \Sigma\ ||F_0|-|F_c||/\ \Sigma\ |F_0|$; $wR_2 = \{\ \Sigma\ w(F_0^2-F_c^2)^2/\ \Sigma\ w(F_0^2)^2\}^{1/2}$

Table 3-2. Selected Bond Lengths (Å) and Dihedral Angles (°), Distance between the Spin Centers (Å), Angles between the *z* and the Given Axes (°), and Interchain Distances (Å) for $[Co(hfpip\text{-}X)_2(\mathbf{NOpy_2})]_n$; X = H (**2a**), F (**2b**), F_3 (**2c**), F_5 (**2d**), Cl (**2e**), Cl_3 (**2f**), Br (**2g**), and I (**2h**).

2a		**2b**		**2c**		**2d**	
			Bond Lengths (Å)				
Co(1)-N(1)	2.187	Co(1)-N(1)	2.183	Co(1)-N(1)	2.175	Co(1)-N(1)	2.242
Co(1)-N(3)	2.190	Co(1)-N(4)	2.216	Co(1)-N(3)	2.167	Co(1)-N(3)	2.154
Co(1)-N(4)	2.215	Co(1)-O(2)	2.005	Co(1)-O(2)	2.026	Co(1)-O(2)	2.015
Co(1)-N(5)	2.185	Co(2)-N(3)	2.179				
Co(1)-O(2)	2.016	Co(2)-N(5)	2.220				
Co(1)-O(3)	2.008	Co(2)-O(3)	2.005				
			Dihedral Angles (°) between Pyridine Ring and XY Plane				
N(1)N(3)N(4)N(5)-C(1)C(3)C(5)	83.43	N(1)N(4)N(1)*N(4)*-C(1)C(3)C(5)	75.22	N(1)N(3)N(1)**N(3)*-C(1)C(3)C(5)	55.57	N(1)N(3)N(1)**N(3)*-C(1)C(3)C(5)	81.12
N(1)N(3)N(4)N(5)-C(6)C(8)C(10)	72.38	N(3)N(5)N(3)*N(5)*-C(6)C(8)C(10)	80.27				
			Dihedral Angles (°) between Pyridine Ring and Aminoxyl Plane				
C(3)*N(2)O(1)-C(7)C(9)N(3)	27.55	C(3)N(2)O(1)-C(7)C(9)N(3)	19.30	C(3)N(2)O(1)-C(2)*C(4)*N(1)*	25.26	C(3)N(2)O(1)-C(2)*C(4)*N(1)*	31.78
C(8)N(2)O(1)-C(2)*C(4)*N(1)*	15.99	C(8)N(2)O(1)-C(2)C(4)N(1)	23.35				
			Dihedral Angles (°) between Pyridine Ring and Pyridine Ring				
C(2)*C(4)*N(1)*-C(7)C(9)N(3)	38.58	C(2)C(4)N(1)-C(7)C(9)N(3)	36.95	C(2)C(4)N(1)-C(2)*C(4)*N(1)*	47.99	C(2)C(4)N(1)-C(2)*C(4)*N(1)*	53.22
			Angles between the *Z* and the given Axes (°)				
∠*z*-(*a* – *c*)	64	∠*z*-(*b* + *c* - *a*)	63, 65	∠*z*-(*a* + *c*)	69	∠*z*-*c*	61
z - *b*	29	z – (*a* – *2b*)	18, 37	z - *b*	22	*z* - *b*	39
z – (*b* + *c*)	83	z - *a*	56, 68	z – (*a* – *c*)	86	z - a	56
			Interchain distances between chains (Å)				
O(1)-C(9)’	3.251	O(1)-C(2)’	3.259	O(1)-F(1)’	3.080	O(1)-C(11)*	3.114
O(1)-H(2)	2.646	O(1)-F(1)’’	2.899	C(2)-C(6)’	3.292	O(1)-F(7)**	3.432

2e		**2f**		**2g**		**2h**	
Bond Lengths (Å)							
Co(1)-N(1)	2.207	Co(1)-N(1)	2.172	Co(1)-N(1)	2.192	Co(1)-N(1)	2.196
Co(1)-N(3)	2.209	Co(1)-N(3)*	2.152	Co(1)-N(3)	2.193	Co(1)-N(3)	2.207
Co(1)-N(4)	2.186	Co(1)-N(4)	2.177	Co(1)-N(4)	2.179	Co(1)-N(4)	2.168
Co(1)-N(5)	2.182	Co(1)-N(5)	2.193	Co(1)-N(5)	2.160	Co(1)-N(5)	2.198
Co(1)-O(2)	2.013	Co(1)-O(2)	2.028	Co(1)-O(2)	2.030	Co(1)-O(2)	2.027
Co(1)-O(3)	2.022	Co(1)-O(3)	2.031	Co(1)-O(3)	2.023	Co(1)-O(3)	2.036
Dihedral Angles (°) between Pyridine Ring and XY Plane							
N(1)N(3)N(4)N(5)-C(1)C(3)C(5)	76.22	N(1)N(3)*N(4)N(5)-C(1)C(3)C(5)	85.13	N(1)N(3)N(4)N(5)-C(1)C(3)C(5)	75.65	N(1)N(3)N(4)N(5)-C(1)C(3)C(5)	76.13
N(1)N(3)N(4)N(5)-C(6)C(8)C(10)	69.27	N(1)N(3)*N(4)N(5)-C(6)*C(8)*C(10)*	65.38	N(1)N(3)N(4)N(5)-C(6)C(8)C(10)	67.64	N(1)N(3)N(4)N(5)-C(6)C(8)C(10)	70.22
Dihedral Angles (°) between Pyridine Ring and Aminoxyl Plane							
C(3)N(2)O(1)-C(7)*C(9)*N(3)*	19.50	C(3)N(2)O(1)-C(7) C(9)N(3)	31.18	C(3)N(2)O(1)-C(7)*C(9)*N(3)*	20.76	C(3)N(2)O(1)-C(7)*C(9)*N(3)*	20.66
C(8)*N(2)O(1)-C(2)C(4)N(1)	32.89	C(8) N(2)O(1)-C(2)C(4)N(1)	15.99	C(8)*N(2)O(1)-C(2)C(4)N(1)	31.33	C(8)*N(2)O(1)-C(2)C(4)N(1)	29.23
Dihedral Angles (°) between Pyridine Ring and Pyridine Ring							
C(2)C(4)N(1)-C(7)*C(9)*N(3)*	46.09	C(2)C(4)N(1)-C(7)C(9)N(3)	45.25	C(2)C(4)N(1)-C(7)*C(9)*N(3)*	45.56	C(2)C(4)N(1)-C(7)*C(9)*N(3)*	43.28
Angles between the *Z* and the given Axes (°)							
∠*z-b*	63	∠*z-b*	69	∠*z-b*	63	∠*z-b*	65
z-a	39	*z-a*	39	*z-a*	39	*z-a*	38
z-c	81	*z-c*	64	*z-c*	86	*z-c*	87
Interchain distances between chains (Å)							
O(1)-C(14)’	3.199	O(1)-F(8)’	2.743	O(1)-C(14)’	3.246	O(1)-C(14)’	3.405
O(1)-Cl(1)’	3.621	O(1)-F(5)’’	3.031	O(1)-Br(1)’	3.637	O(1)-I(1)’	3.684

Section 3. Magnetic properties of $[Co(hfpip\text{-}X)_2(\mathbf{NOpy_2})]_n$ (X = H, F, F_3,F_5,Cl, Cl_3, Br, and I)

(i) $\chi_{mol}T$ vs. *Temperature* plots

The temperature dependence of dc magnetic properties for **2a**-**2h** were measured using the pulverized samples of these complexes in the range of 300-1.9 K (Figure 3-3). The $\chi_{mol}T$ values at 300 K were 2.96, 2.87, 3.28, 3.15, 3.07, 3.21, 3.19, and 3.27 $cm^3\ mol^{-1}$ K, respectively. The g_{Co} values, calculated by the $\chi_{mol}T$ values at 300 K were in the range of 2.25-2.46. On cooling, The $\chi_{mol}T$ values were nearly constant around 300-100 K, gradually increased below 100 K, steeply increased below 40 K, reached maxima, then rapidly decreased. In **2a** – **2d**, the $\chi_{mol}T$ values showed different thermal profiles in the temperature region below 40 K. **2a** – **2d** had maximum $\chi_{mol}T$ values of 15.3, 5.46, 7.57, and 15.2 $cm^3\ mol^{-1}$ K at 7.5, 12.0, 7.0, and 2.6 K, respectively, while **2e** – **2h** showed similar thermal profiles of the $\chi_{mol}T$ values but with different maximum $\chi_{mol}T$ values of 18.7, 18.0, 14.9, and 11.1 cm^3Kmol^{-1} at 6.0, 5.5, 7.5, and 8.0 K, respectively. All maximum $\chi_{mol}T$ values were larger than the theoretical ones (2.4 cm^3Kmol^{-1}) calculated by the spin-only equation with isolated cobalt ion ($\chi_{mol}T$ of 2.0 $cm^3mol^{-1}K$ for $Co(hfpip)_2$ with an effective spin quantum number, S_{eff}, = 1/2 and g = 4) and aminoxyl (S = 1/2 and g = 2.00). The increments of the $\chi_{mol}T$ products below 40 K indicated that ferromagnetic interactions within the chain operated and the correlation length became longer with decreasing temperature. The decrements of the $\chi_{mol}T$ products at extremely low temperature suggested the antiferromagnetic interaction between chains along with the effects of the zero-field splitting associated with the spin-orbit couplings of high spin Co(II) ions. For the quantitative estimation of the magnetic coupling parameter between Co ion and aminoxyl (J_{intra}/k_B), the branched chain model[18] was applied to the thermal magnetic profiles. The obtained J_{intra}/k_B were 8.5-14.4 K. The J_{intra}/k_B in **2c** and **2d** were somehow smaller than those of others, indicating the weaker intrachain magnetic interactions because of the small dihedral angle of XY plane-pyridine plane in **2c** and the relatively long bond length of Co-N in **2d**, respectively.

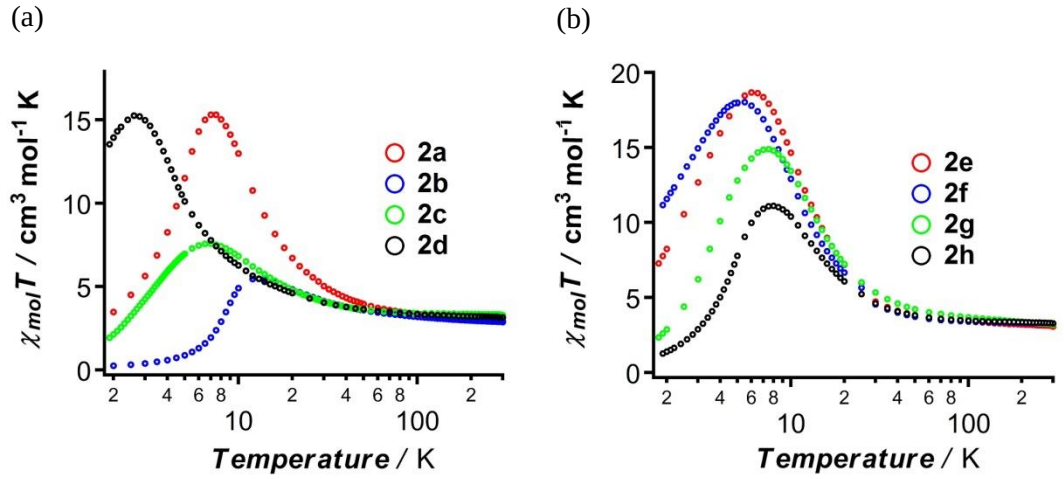

Figure 3-3. The plot of (a) $\chi_{mol}T$ vs. *T*emperature of **2a**-**2d** and (b) $\chi_{mol}T$ vs. *T*emperature of **2a**-**2d**.

(ii) $M_{mol}/N\mu_B$, vs. H, and dM/dH vs. H plots

The field dependence of dc magnetic properties for **2a-2h** were measured with the same samples used above (Figure 3-4). In the $M_{mol}/N\mu_B$, vs. H plot, except for complex **2d**, the $M_{mol}/N\mu_B$ values firstly gradually increased and then steeply increased, resulted in the "*S* shaped" sigmoid curves. The $M_{mol}/N\mu_B$ values at 50 kOe and at 1.9 K for **2a-2h** were 2.56, 2.41, 2.45, 2.79, 2.43, 2.84, 2.44, and 2.56, respectively. The larger values for **2d**, and **2f** implied that weaker antiferromagnetic interactions existed. In the dM/dH vs. H plots, except for, **2d**, all other complexes showed peak tops (H_{cr}) around 2.2, 8.0, 2.4, 1.0, 0.6, 1.5, and 2.4 kOe, respectively for **2a**, **2b**, **2c**, **2e**, **2f, 2g**, and **2h**. These observations were clearly attributed to the metamagnet behaviors affected by the interchain antiferromagnetic interactions. The temperature dependence of H_{cr} for each complex, the peak top temperatures in the χ_{mol} vs. *Temperature* plots, and the frequency independent peak in the χ''_{mol} vs. *Temperature* plots were combined and the (*T, H*) phase diagram for each complex was depicted in Figure 3-5. Since the observed magnetic behaviors were metamagnet-like because of the interchain antiferromagnetic interaction[19], the values of the antiferromagnetic coupling parameter, $|zJ'|$, can be estimated by the equation; $g_{//}\mu_B SH_{cr} = 2|zJ'|S^2$, where $g_{//}$ and z are the parallel g value and the number of the coupled chains, respectively[20]. The $g_{//}$ value was estimated from $C \approx C_{eff} = N\mu_B{}^2 g_{//} S^2/3k$. The obtained $|zJ'|$ values for **2a**−**2c** and **2e**−**2h** are listed in the Table 3-3 together with the T_c, H_{cr}, and $g_{//}$ values.

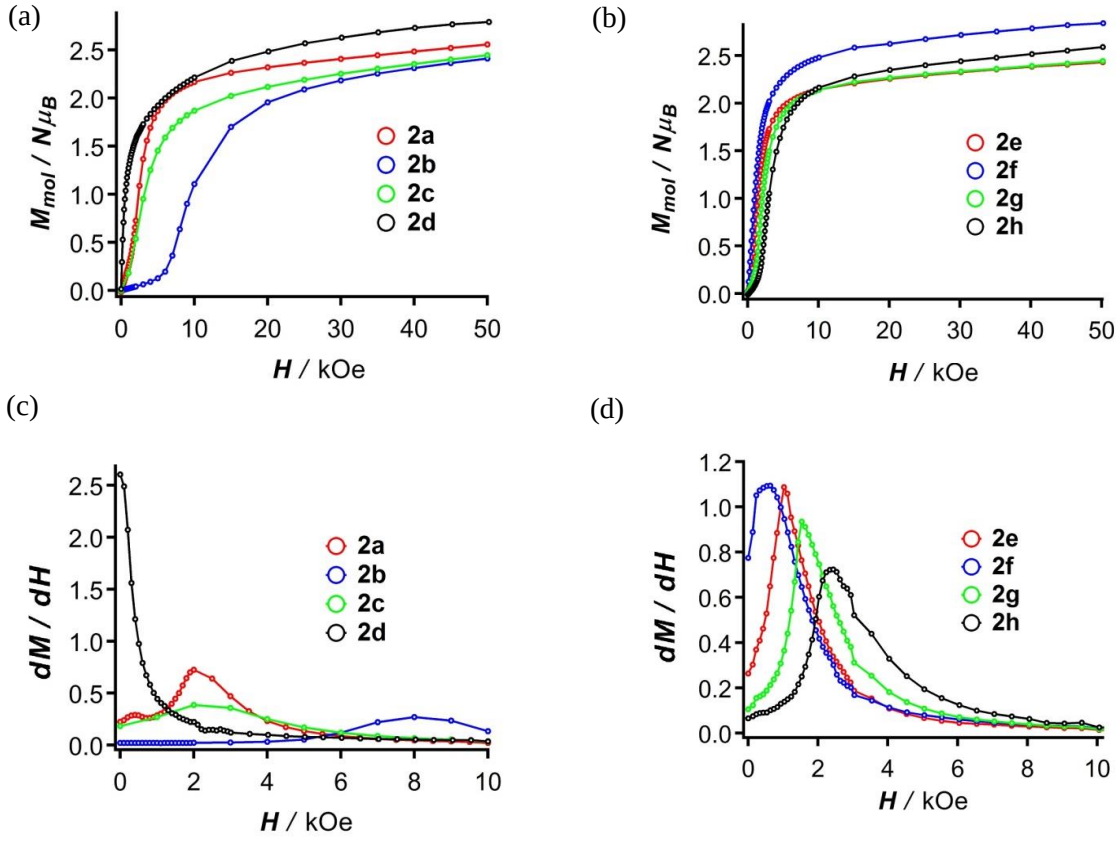

Figure 3-4. The plot of (a),(b) M_{mol} vs. H for **2a-2d**, and **2e-2h** (c),(d) dM/dH vs.H for **2a-2d**, and **2e-2h**, respectively. The solid lines are guides for eyes.

Table 3-3. Values of T_c, H_{cr}, and $|zJ'|/k_B$ for **2a-2h**

	2a	**2b**	**2c**	**2d**	**2e**	**2f**	**2g**	**2h**
T_c (K)	5.5				4.0		4.2	6.2
H_{cr} (kOe)	0.4, 2.2	8.0	2.4		1.0	0.6	1.5	2.4
$\|zJ'\|/k_B$	0.35	1.26	0.41		0.16	0.10	0.25	0.41
$g_{\parallel}$ [a]	4.8	4.7	5.1	5.1	4.9	5.0	5.0	5.1

[a] $g_{\parallel}$ value was estimated from $C \approx C_{eff} = N\mu_B{}^2 g_{\parallel} S^2/3k$.

(iii) The plots of ZFC-FC-REM

In order to understand the detailed magnetic properties at extremely low temperatures, ZFC-FC-REM measurements were performed at the 4.7 Oe of static dc field (Figure 3-5,6). In complex **2a**, **2e**, **2g**, and **2h**, the large discrepancies of ZFC and FC were observed, indicating the long-ranged magnetic ordering into the spin canted 2D or 3D antiferromagnets below the critical temperatures[21]. In contrast, **2b**, **2c**, **2d**, and **2f**, didn't show the differences between ZFC and FC above 1.9 K, suggested the absence of magnetic ordering. In particular, **2d** showed the discrepancy at temperature ranges around 1.0 K, assigned to the blocking temperature, T_B. In summary, **2a**, **2e**, **2g**, and **2h** were the antiferromagnetically interacted canted magnets, **2b**, **2c**, and **2f** were ferromagnetic chain with antiferromagnetic interactions, and **2d** was a ferromagnetic chain with a negligible interchain antiferromagnetic interaction. The reason why the complexes **2b**, **2c**, and **2f** didn't undergo the spin canting was probably due to the fact that crystallographic inversion centers between the chains canceled the total magnetic momentum of these complexes. Also **2a**, **2e**, **2g**, and **2h** had the inversion centers between chains, though the interchain antiferromagnetic interaction in **2a** was active in "non-inversion related chains", and in **2e**, **2g**, and **2h**, were active between "*P*-, and *M*-helical chains". These subtle differences of the crystal packings drastically affected to the magnetic properties in the extremely low temperature ranges.

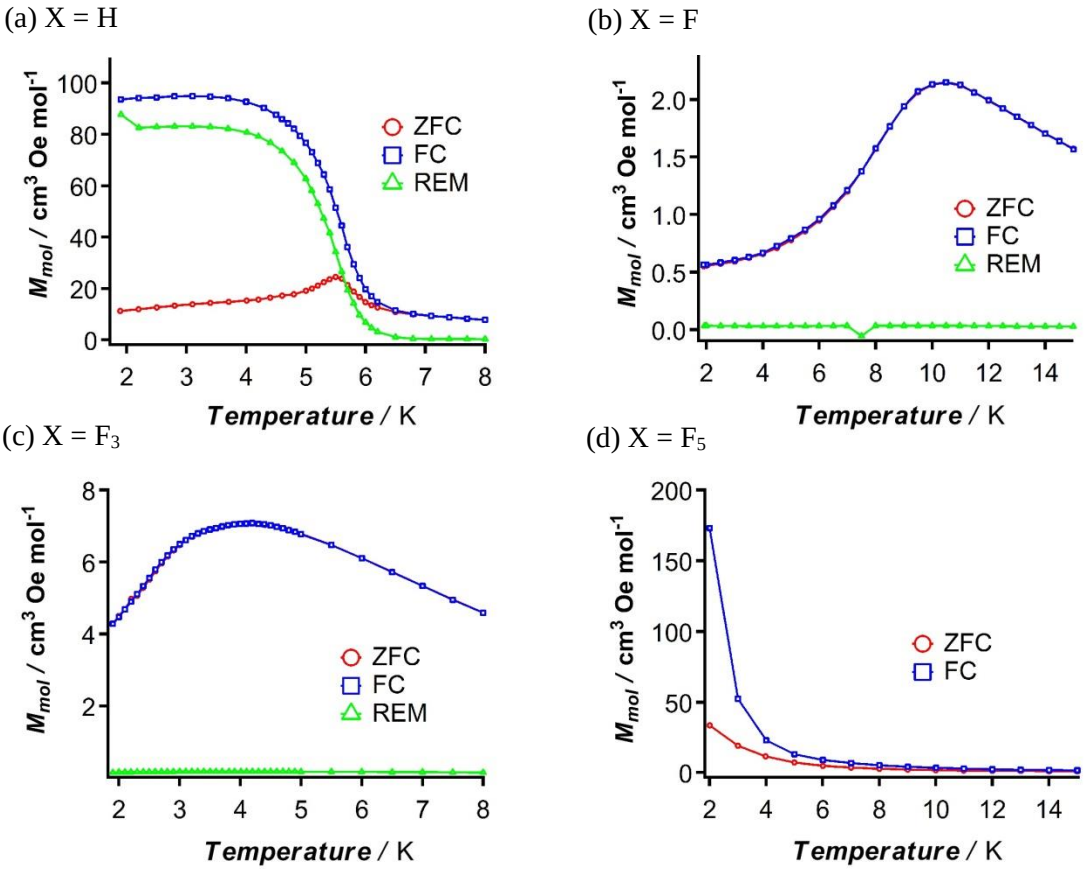

Figure 3-5. The plots of ZFC-FC-REM vs. *Temperature* for (a)**2a**, (b)**2b**, (c)**2c**, (d)**2d**. The solid lines are guides for eyes

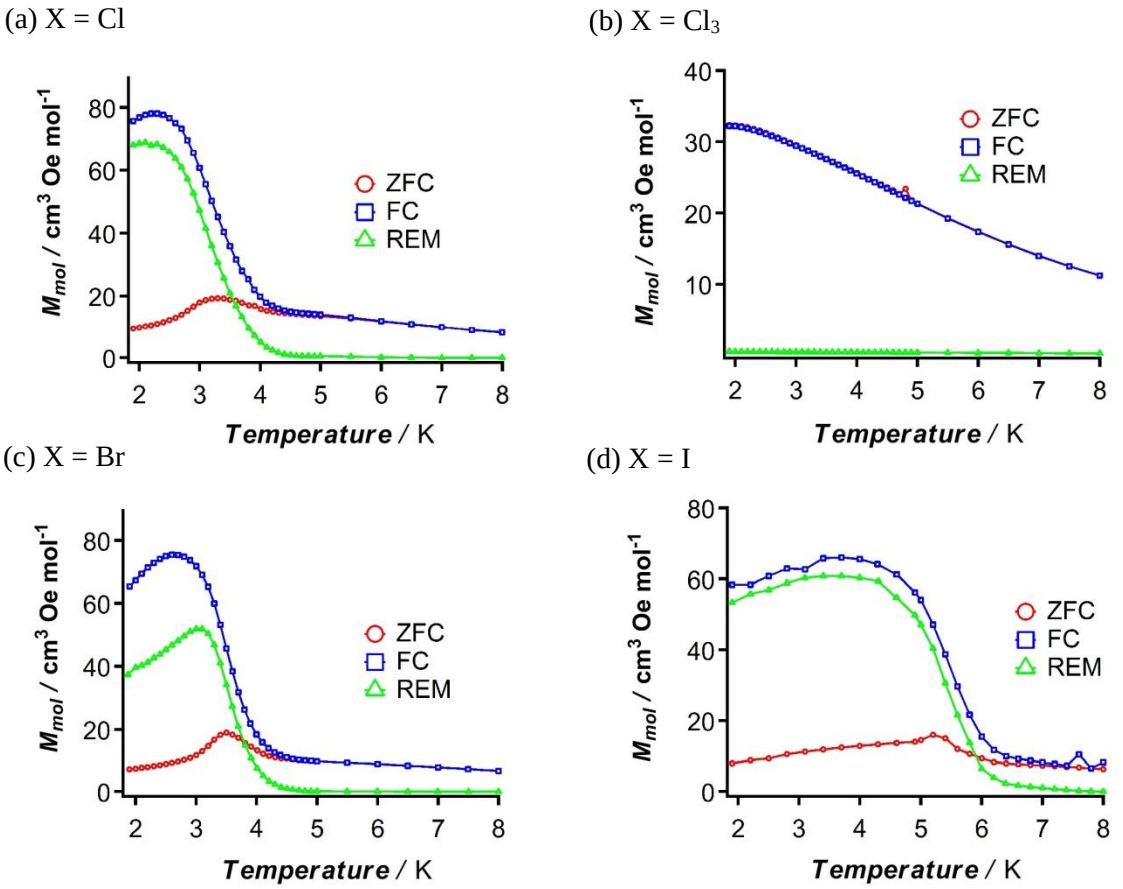

Figure 3-6. The plots of ZFC-FC-REM vs. *Temperature* for (a)**2e**, (b)**2f**, (c)**2g**, (d)**2h**. The solid lines are guides for eyes

(iv) Magnetic phase diagram of **2a**

As mentioned, complex **2a** showed unique magnetic phase transition under the critical temperature and the critical magnetic field. Thus, *Field* vs. *Temperature* phase diagram was plotted in Figure 3-7.

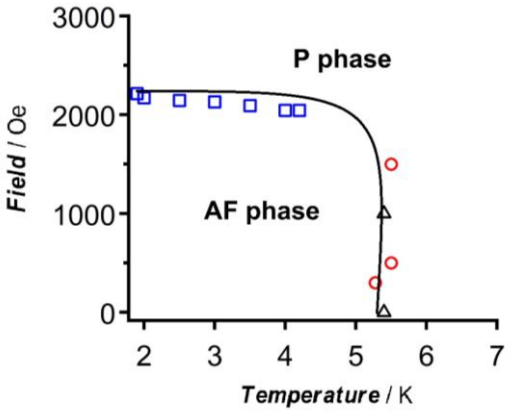

Figure 3-7. *Field* vs. *Temperature* phase diagram of **2a** ; the data from the *dM/dH* vs *Temperature* plot at various temperatures (open blue square), from the χ_{mol} vs *Temperature* plots at constant dc fields of 0.3, 0.5, and 1.5 kOe (open red circle), and from ac susceptibility experiments (open black triangle). The solid line is a guide for eyes

(v) Magnetic properties of aligned single crystal sample of **2f**

For the investigation of the magnetic axes in the single crystalline state, angular dependence of the magnetization for 2f was measured using the ten-pieces of relatively large-sized single crystals (c.a. 0.1 mg) mounted onto a sample holder (Figure3-8). Angular dependence of magnetization was measured in the *ac*, and *ab* plane with the crystal rotating around *b*, and *c* axis, respectively. Because the **2f** crystallized in the monoclinic space group, *a** axis was slightly tilted to *a* axis, and the *b* axis was one of magnetic axes and the other two would exist in the plane perpendicular to the *b* axis[22]. As a result of the measurement, the magnetic axes were determined to be *a**, *b*, and *c* directions. Particularly, the magnetic easy axis lay on the *a** axis close to the *a* direction, suggested the discrepancy of the easy axis with the chain direction, *b*, nor the *z* axis defined by O-Co-O direction.

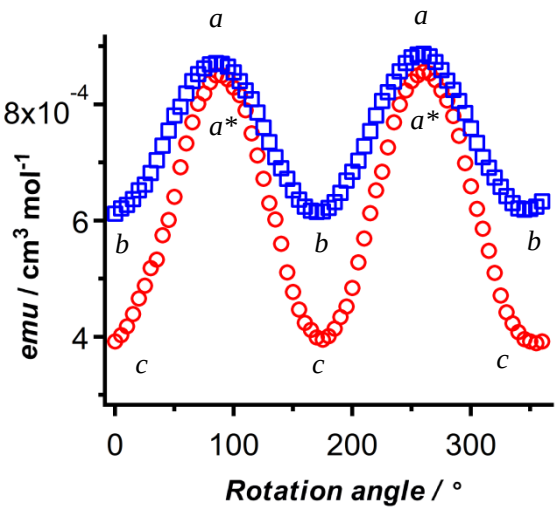

Figure 3-8. Angular dependence of direct current magnetization of aligned single crystal samples of **2f**.

AC Magnetic properties of $[Co(hfpip\text{-}X)_2(\mathbf{NOpy_2})]_n$ (X = H, F, F_3,F_5,Cl, Cl_3, Br, and I)

(i)**2a**

The ac magnetic properties for **2a** were recorded under 0, 1.0, and 2.2 kOe of external DC field in order to investigate the effect of antiferromagnetic interaction. In the χ''_{mol} vs. *Temperature* plots, two maxima at 5.6 K and below 4.0 K were observed. The former and latter are assigned to phase transition to the antiferromagnet and the slow relaxation of magnetization, respectively. Applying the 1.0, and 2.2 kOe of dc field suppressed the phase transition, lead the evidently clear slow magnetic relaxation below 5 K (Figure 3-9).

(ii) ~ (iv)**2b-2d**

The complexes **2b**, and **2c** didn't show the slow magnetic relaxation in the absence of additional dc field. When applying the external dc field, the peak tops were observed in theχ''_{mol} vs. *Temperature* plots, suggesting the existence of antiferromagnetic interactions between heterospin chains. On the other hand, though the antiferromagnetic interaction might be weak, the peak top of the χ''_{mol} signals were not found neither absence nor presence of additional dc field in **2d**. Hence, **2d** was considered to have peak top temperature below 1.9 K.

(ii) ~ (iv)**2e-2h**

In the χ''_{mol} vs. *Temperature* plots at H_{dc} = 0 kOe for **2e**, **2g**, and **2h**, the thermal profiles of χ''_{mol} signals were similar to that of **2a**. The intensities of the χ''_{mol} signals at the peak-top temperature decreased with decreasing frequency. Additional temperature-independent peaks were also observed at 3.6, 4.6, and 5.5 K for **2e**, **2g**, and **2h**, respectively, which were also in good agreement with the T_c values observed from ZFC, FC, and RM measurements. The changes of the χ'_{mol}- and χ''_{mol} vs. *Temperature* plots for **2e**, **2g**, and **2h** by applied-dc field of 1.0, 1.5, and 2.4 kOe, respectively, were similar to that for **2a**. When the dc fields, H_{dc}, were applied, the additional maximum peaks of the χ'_{mol} and χ''_{mol} signals disappeared and the shapes of both χ'_{mol}- and χ''_{mol} vs. *Temperature* plots were close to the typical ones for SMM, and SCM. Complex **2f** showed no large difference of the χ''_{mol} vs. *Temperature* plot between the absence and presence 0.6 kOe of dc field. Somehow an increase of the maximum χ''_{mol} signal in the low temperature region was observed (Figure 3-10).

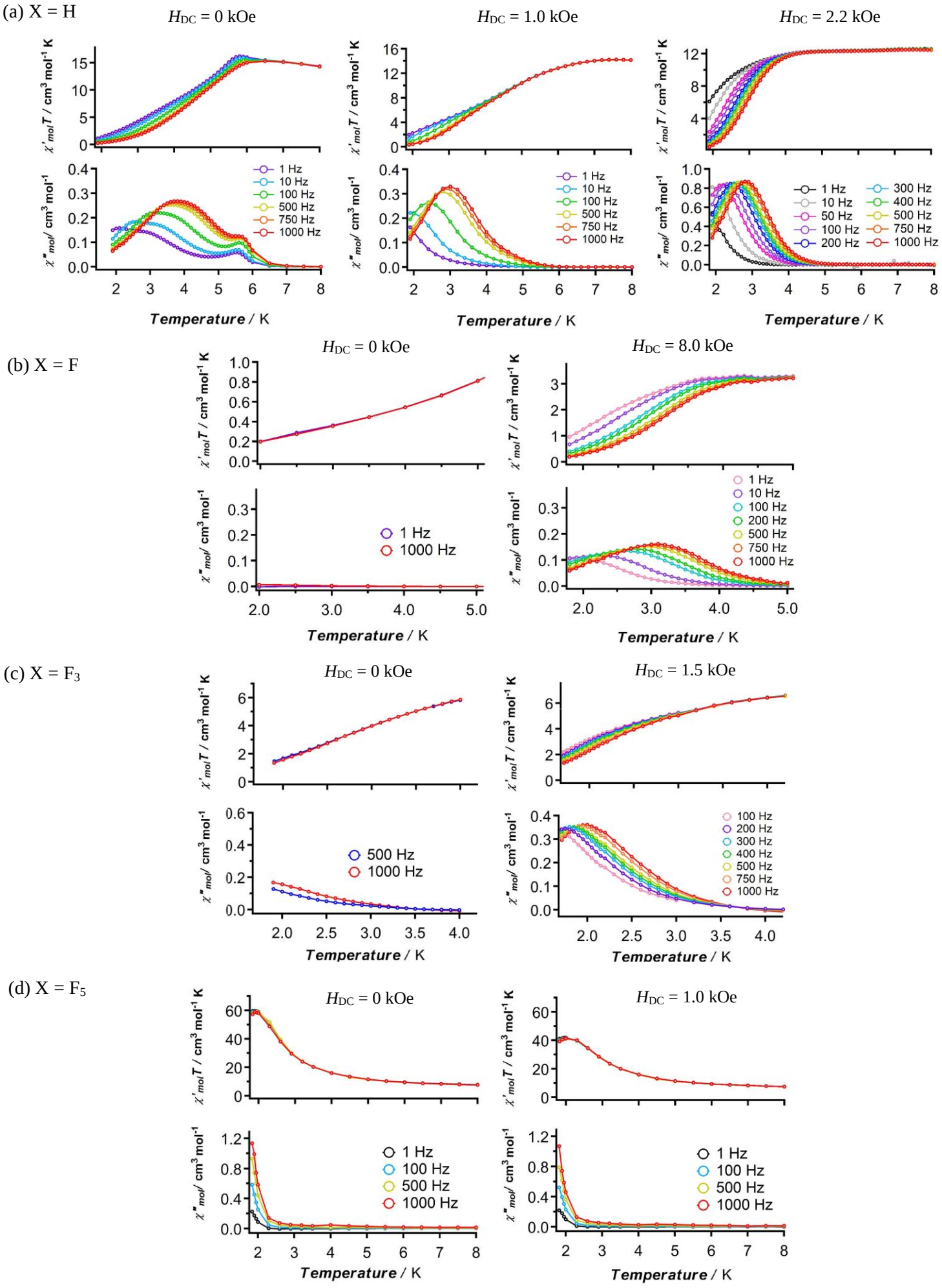

Figure 3-9. The plots of $\chi'T$ vs. *Temperature* and χ'' vs. *Temperature* for (a)**2a**, (b)**2b**, (c)**2c**, (d)**2d**. The solid lines are guides for eyes

(a) X = Cl

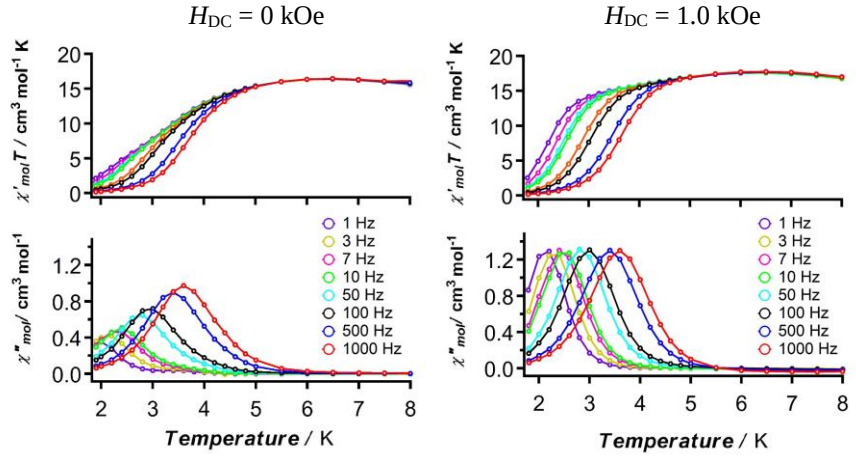

(b) X = Cl_3

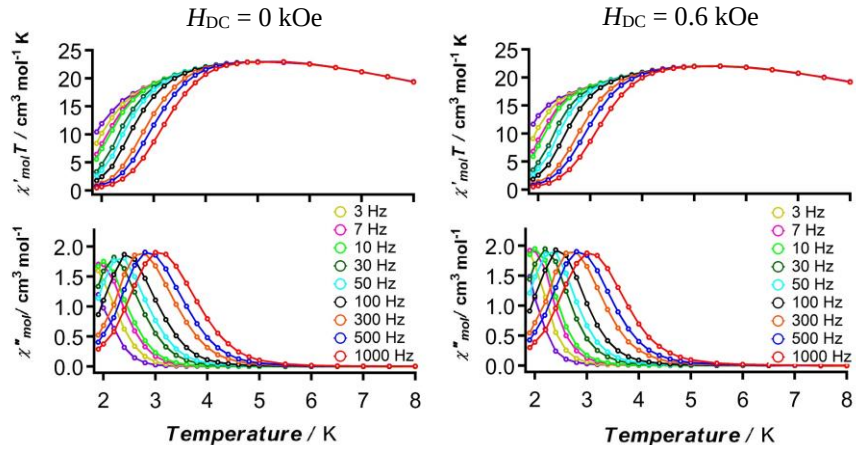

(c) X = Br

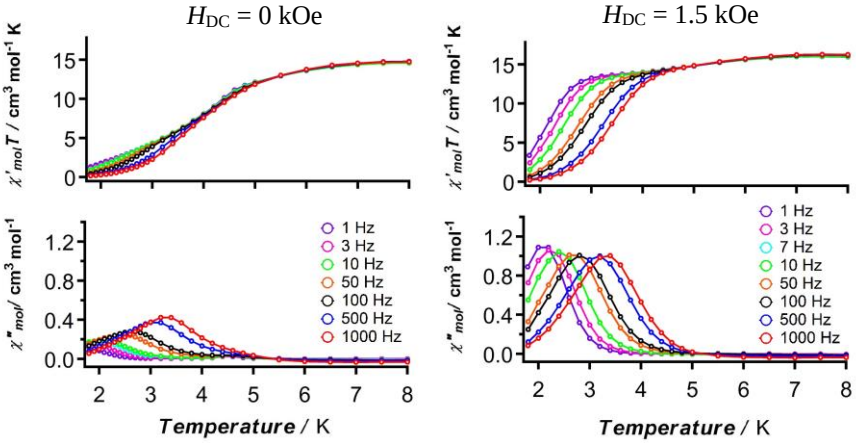

(d) X = I

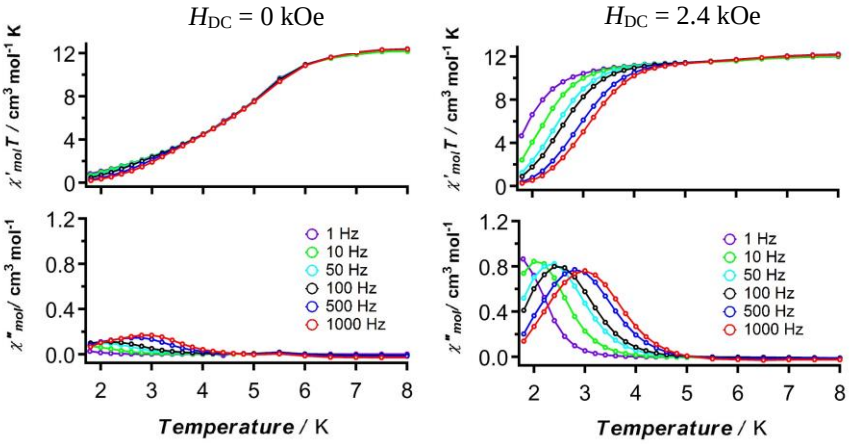

Figure 3-10. The plots of $\chi'T$ vs. *Temperature* and χ'' vs. *Temperature* for (a)**2e**, (b)**2f**, (c)**2g**, (d)**2h**. The solid lines are guides for eyes

The relationship between the relaxation time and the temperature were plotted according to the Arrhenius law. The thermal activation barrier for the spin reorientation, Δ_{eff}/k_B, and the pre-exponential factor, τ_0, are summarized in Table 3-4.

The obtained Δ_{eff} for complexes **2a**-**2h** except **2d** were 25-39 K, and the τ_0 ranged more than 10^{-10} sec. orders, excluding the spin-glass relaxation regime, hence these magnetic relaxation derived from the SMM or SCM behaviors. On the other hand, the Δ_{eff}/k_B of 25-39 K were comparable to that of mononuclear [Co(hfpip)$_2$(**4NOpy**)$_2$] (U_{eff}/k_B = 29 K), implying the less effective contribution of the additional activation barrier arising from the magnetic correlation within the chains. The reason why the activation energies in chain complexes were not so large might be due to the discrepancy of the direction of the chain axis and the local ion anisotropy of Co(II) ion, suggested by the determination of the local magnetic anisotropy using the aligned single crystal samples of **2f**.

Table 3-4. Values of Δ_{eff}/k_B and τ_0 in the absence and presence of dc field

	Presence of dc Field (H_{dc}/kOe)		
	H_{dc}/kOe	Δ_{eff}/K	τ_0/sec
2a	0	56.4	6.8×10^{-11}
	1.0	28.8	1.1×10^{-8}
	2.2	27.4	1.1×10^{-8}
2b	0	n.e	n.e.
	8.0	39.0	4.0×10^{-10}
2c	0	n.e.	n.e.
	1.5	24.5	2.7×10^{-10}
2d	n.e	n.e	n. e.
2e	0	24.5	5.4×10^{-7}
	1.0	36.3	7.4×10^{-9}
2f	0	39.6	1.2×10^{-8}
	0.6	26.9	2.8×10^{-8}
2g	0	23.9	1.3×10^{-7}
	1.5	39.2	1.2×10^{-9}
2h	0	18.4	2.9×10^{-7}
	2.4	31.2	5.0×10^{-9}

n. e.; not estimated,

(a)X = H

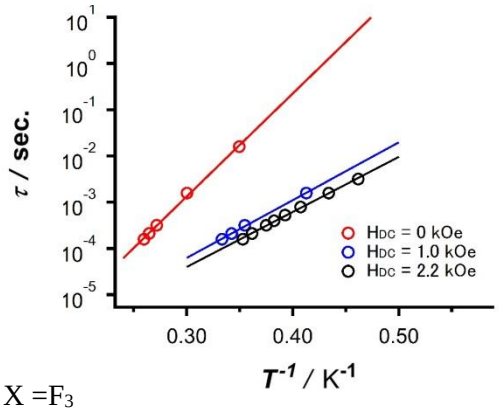

(b) X = F

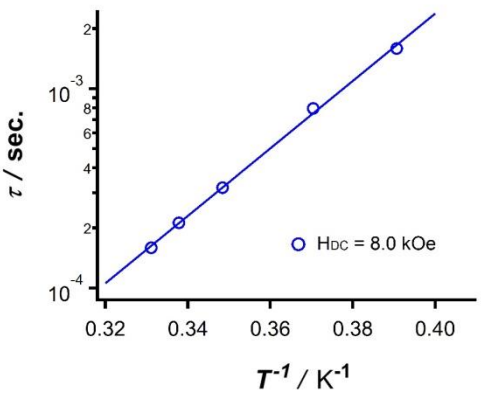

(c) X =F_3

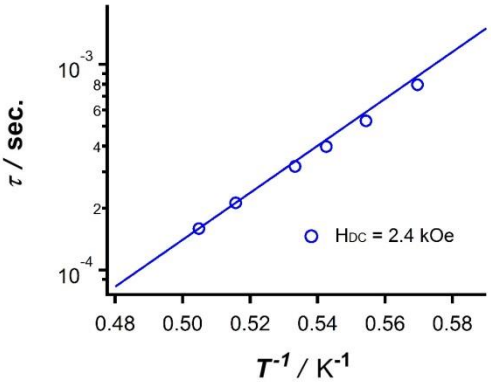

(d) X = Cl

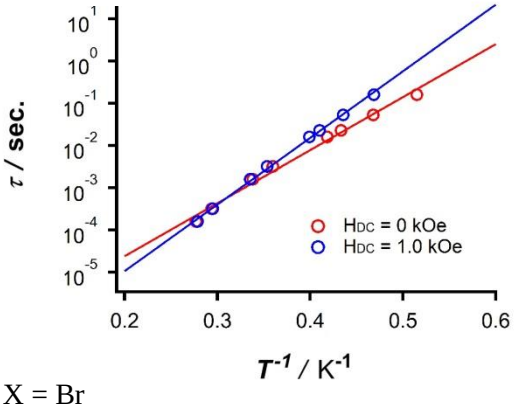

(e) X = Cl_3

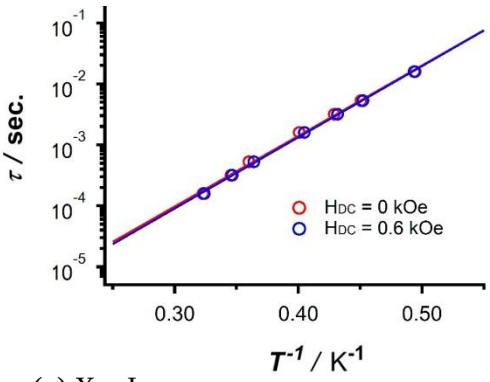

(f) X = Br

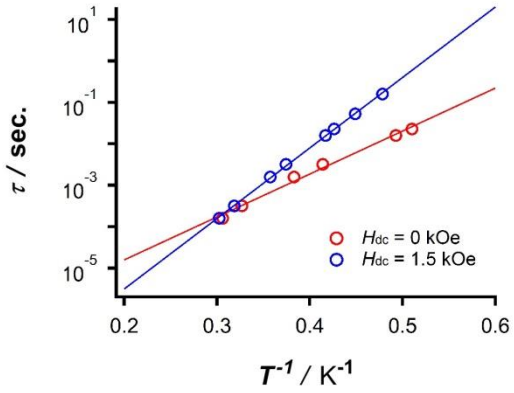

(g) X = I

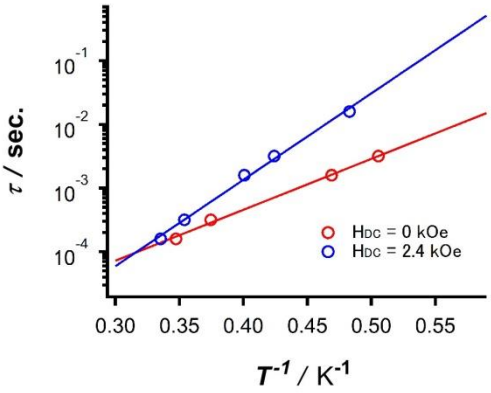

Figure 3-11. Arrhenius plots for (a)**2a**, (b)**2b**, (c)**2c**, (d)**2e**, (e)**2f**, (f)**2g**, and (g)**2h**. The solid lines are best fit results obtained according to the Arrhenius law.

Section 4. Chapter conclusion

For the purpose of further exploring of the usability of **NOpy$_2$** and the construction of 1-D 3d-2p heterospin chain magnet with thermal relaxation activities, Co(hfpip)$_2$ derivatives with high magnetic anisotropies were combined to **NOpy$_2$**, resulted in giving Co^{II}-**NOpy$_2$** alternating chain complexes **2a**-**2h** in the crystalline states. As well as the Cu^{II}-**NOpy$_2$** complexes, 3d spins of Co^{II} ions were ferromagnetically interacted with the 2p spins of **NOpy$_2$**, gave the magnetic correlation through the chains. The magnetic exchange coupling constant between Co^{II} ions and aminoxyl were estimated to be 8.5-14.4 K by the branched chain model.

The subtle differences of the crystal packings and the interchain magnetic interaction pathways drastically affected to the whole magnetisms of these complexes (i.e. **2a**, **2e**, **2g**,and **2h** underwent the spin canted phase transitions under the critical temperatures, though the complexes **2b**, and **2c** didn't.). Complex **2d** did not show the obvious short contact between chains in the crystal structure analysis, led the less effective antiferromagnetic interaction with the neighboring chains, though the magnetic interaction within the chain was insignificant because of the relatively long bond length of Co-N. As a result, only complex **2f** had both the efficient magnetic correlation in the chain and the negligible magnetic contribution of antiferromagnetic interaction.

The Δ_{eff}/k_B of 25-39 K were comparable to that of mononuclear [Co(hfpip)$_2$(**4NOpy**)$_2$] (U_{eff}/k_B = 29 K), implying the less effective contribution of the additional activation barrier arising from the magnetic correlation within the chains. This result might derive from the discrepancy of the direction of the chain axis and the local ion anisotropy of Co(II) ion, suggested by the determination of the local magnetic anisotropy using the aligned single crystal samples of **2f** (Figure 3-12).

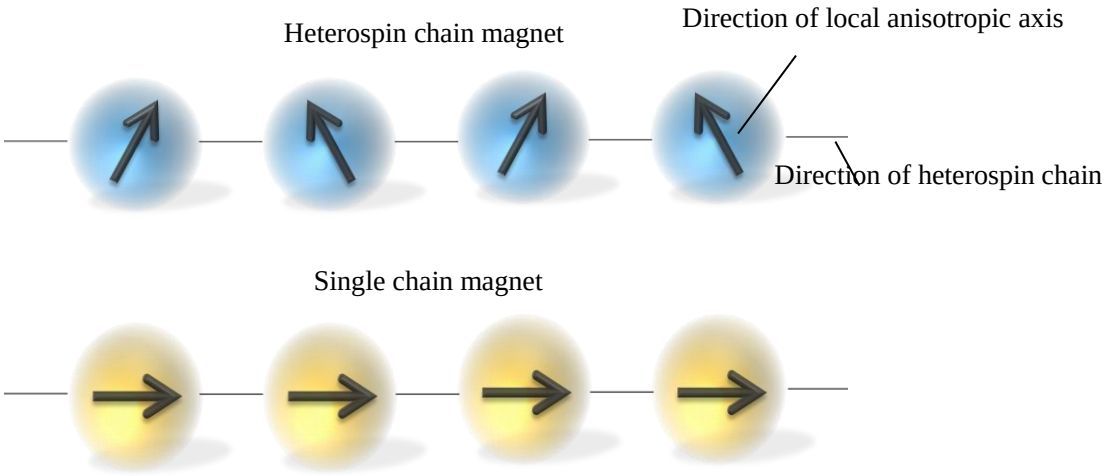

Figure 3-12. Schematic drawings of the relationships of local anisotropic axis and the chain axis in heterospin chain magnets (upper) and single chain magnets (down).

In summary, though it was difficult to obtain the SCMs or SMMs with a high thermal activation barrier, **NOpy$_2$** also acted as an extremely useful magnetic coupler for the formation of novel 3d-2p chain systems. The design and the preparation of a new magnetic coupler for the control of magnetic anisotropy and the chain directions are strongly demanded and now under investigating.

Chapter 4

~ Construction of mononuclear Ln(III) complexes in 4f-2p heterospin system ~

Section 1. Single molecule magnet in 4f ion based complex

The most recently 4f-2p heterospin systems gathered much attention because of their high possibility for the high temperature stable SMM or SCM thanks to the high spin ground state and large magnetic anisotropy of 4f ion and the effective magnetic coupling nature of 2p organic spin. Long et. al reported the 4f-2p dinuclear complexes with record blocking temperature(T_B = 14 K) by the combination of Tb ion and the N_2^{3-} radical. These complexes showed extremely strong magnetic interaction within the molecule as the 4f ion based complexes, showing the intrinsic usability of organic radicals[23] in the molecular magnetism. On the other hand, up to now, only a limited number of 4f-2p complexes with SMM behaviors were reported compared to those of 3d-2p[7,24] ones mainly because the effective magnetic coupler for 4f-2p spin systems has not been well established yet. Accordingly, the exploring and the production of novel magnetic coupler for the 4f-2p spin system is extra strongly demanded over the world.

Hence, herein, I will focus on the seeking of novel magnetic couplers for the 4f-2p heterospin systems and on the evaluation of molecular structures and magnetic properties of their lanthanide complexes. The gadolinium (III), terbium (III), and dysprosium (III) ions as 4f spin sources as well as the carbene (photoproduct of the diazo compound) carrying various types of pyridine derivatives as the 2p spin source were chosen for the investigation.

Section 2. Preparation of diazo-pyridine chelating ligand **L1** and its Ln(III) complexes

It is well known that simple pyridine ring does not connect to the Ln(III) ions so strongly because of the relatively soft basic nature of the nitrogen atom. In fact, we haven't yet successfully obtained the Ln-pyridine complexes as single crystals in our laboratory. In this line, for the construction of Ln complexes directly combine to the pyridine-diazo component, tridentate chelating ligand **L1** carrying one diazo moiety at the 4-position of 2,6-bis(methoxymethyl)pyridine was newly designed and prepared according to the procedure shown in the next page (Scheme 4-1). 4-bromo2,6-bis(methoxylmethyl)pyridine was coupled with benzaldehyde by the Grignard reaction, and then oxidized to the ketone derivative by the activated MnO_2. Resulted ketone was firstly hydrazonated by the hydrazine anhydrous, and then oxidized to the diazo compound.

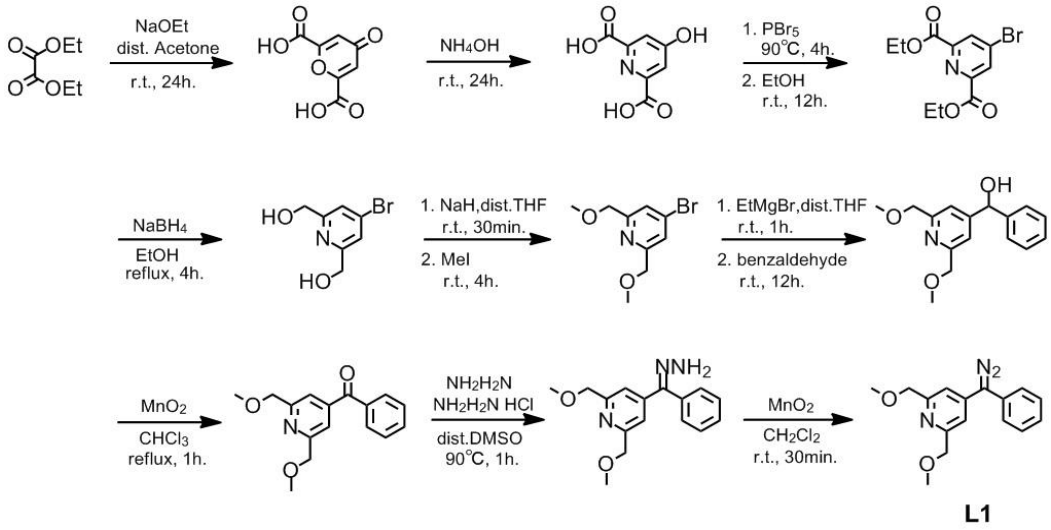

Scheme 4-1. Synthesis of diazo-pyridine chelating ligand **L1**.

L1 was obtained as reddish colored oily product through 9 steps from the diethyloxalate and dry acetone. Mixing the solution of **L1** to the Ln(hfac)$_3$ 2H$_2$O (Ln = Gd, Tb, and Dy ; hfac = 1,1,1,5,5,5-hexafluoroacetylacetonate) in 1 : 1 ratio in chloroform/*n*-heptane gave the reddish-orange colored single crystals (Scheme 4-2).

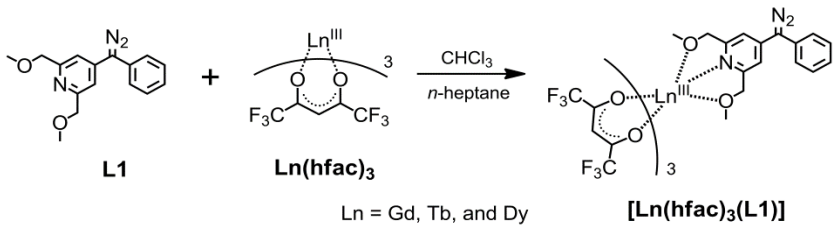

Scheme 4-2. Synthesis of Ln-**L1** complexes.

Section 3. UV-vis. absorption spectra of **L1** and **3a**.

UV-vis. absorption spectra of **L1** and **3a** were recorded using the solid samples and the 10 mM toluene solutions at room temperature (Figure 4-3). **L1** showed the specific absorptions attributed to the *n*-π* transition of diazo component at 500 nm both in solid state and solution state.

3a showed absorptions attributed to the *n*-π* transition of diazo component at 485 nm in solid state and at 480 nm in solution state. Hence, it was expected that the local structure in the solution state was very similar to that of crystalline solid state. The blue shift of the absorption peaks indicated the electronic interaction of diazo moiety with Ln ion in both cases.

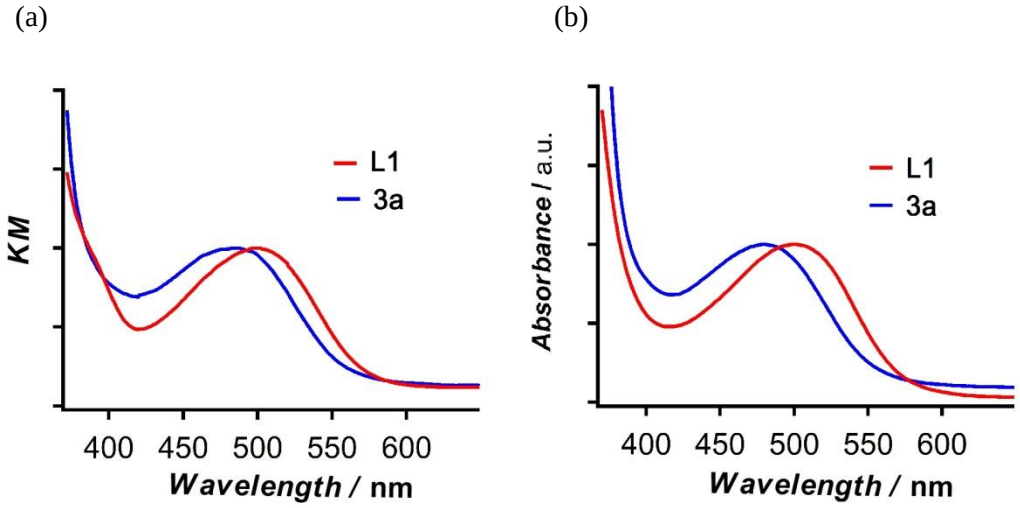

Figure 4-3.
(a)Solid-state and (b)solution state absorption spectra of **L1** and **3a**.

Section 4. ^{1}H-NMR spectra of **L1** and [Y(hfac)$_3$(**L1**)].

In order to obtain further insight into the local structure of [Ln(hfac)$_3$(**L1**)] in the toluene solution, ^{1}H-NMR spectra of **L1** and its Yttrium complex, [Y(hfac)$_3$(**L1**)] were measured in the 10 mM of toluene-d$_8$ solution (Figure 4-4). Herein, [Y(hfac)$_3$(**L1**)] was prepared by the similar manner to the other Ln complexes.

L1 showed the methylene and methyl peaks at 4.5 and 3.2 ppm, respectively. On the other hand, in [Y(hfac)$_3$(**L1**)], these two peaks completely disappeared and shifted to 4.1 and 3.5 ppm, respectively. These results suggested the stable complexation of Y(hfac)$_3$ unit and **L1** even in the solution state. Further addition of one equivalent of **L1** to the [Y(hfac)$_3$(**L1**)] solution caused the broadenings of these peaks, though the chemical shift were not changed (Figure 4-4c). This phenomenon implied that only one equivalent of **L1** was able to combine to the Y(hfac)$_3$ complex as seen in the single crystalline state. Some chemical shifts were also found in the aromatic region though the aromatic proton peaks of residual toluene solution prevented the detailed investigation.

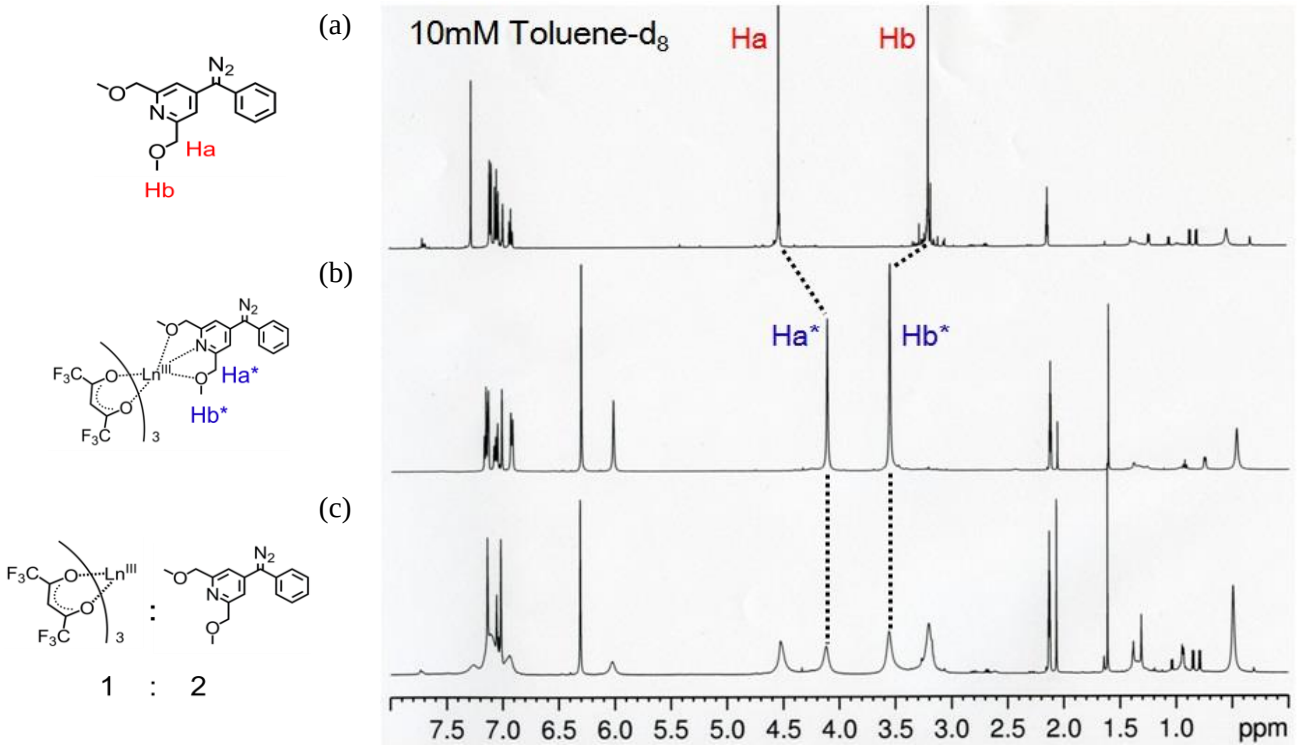

Figure 4-4.
^{1}H-NMR spectra of (a) **L1** and (b) [Y(hfac)$_3$(**L1**)] and (c) [Y(hfac)$_3$(**L1**) : **L1** = 1 : 1 in the 10 mM of toluene-d$_8$ solution.

Section 5. Crystal structures of [Ln(hfac)$_3$(**L1**)] (Ln = Gd : **3a**, Tb : **3b**, and Dy : **3c**)

X-ray crystal analyses were performed at -183 °C for Gd, and Dy complexes and at -153 °C for Tb complex using single crystals obtained above.

(i) ~ (iii) [Ln(hfac)$_3$(**L1**)] (**3a**~**3c**)

All three complexes crystallized in the same monoclinic $P2_1/c$ (No.14) space group and had isostructures. Hence herein the detailed description was given only about the Gd complex, **1a**. When the Gd ion ($^8S_{7/2}$, S = 7/2, L = 0) was used as 4f spin source, one **L1** molecule was ligated to the one Gd(hfac)$_3$ giving the mononuclear Gd complex formulated as [Gd(hfac)$_3$(**L1**)]. In this complex one crystallographically independent Gd center was existed. Gd ion was surrounded by six oxygen atoms of three hfac anions and two oxygen atoms and one nitrogen atom of **L1** resulting the nine-coordinated local structures. The Gd-O$_{\mathbf{L1}}$ bond length were 2.491(7) and 2.509 (6) Å, which were slightly longer than the Gd-O$_{hfac}$ bond length ranging from 2.363 (8) to 2.436 (8) Å. The dihedral angle between the pyridine plane (defined by C1, C2, C3, C4, C5, and N1) and diazo plane (defined by C3, C6, and N2) was 16.30°, indicating the effective delocalization of 2p spins on the pyridine ring after the generation of carbenes. ORTEP drawings of **1a**, **1b**, and **1c** are shown in Figure 4-5.

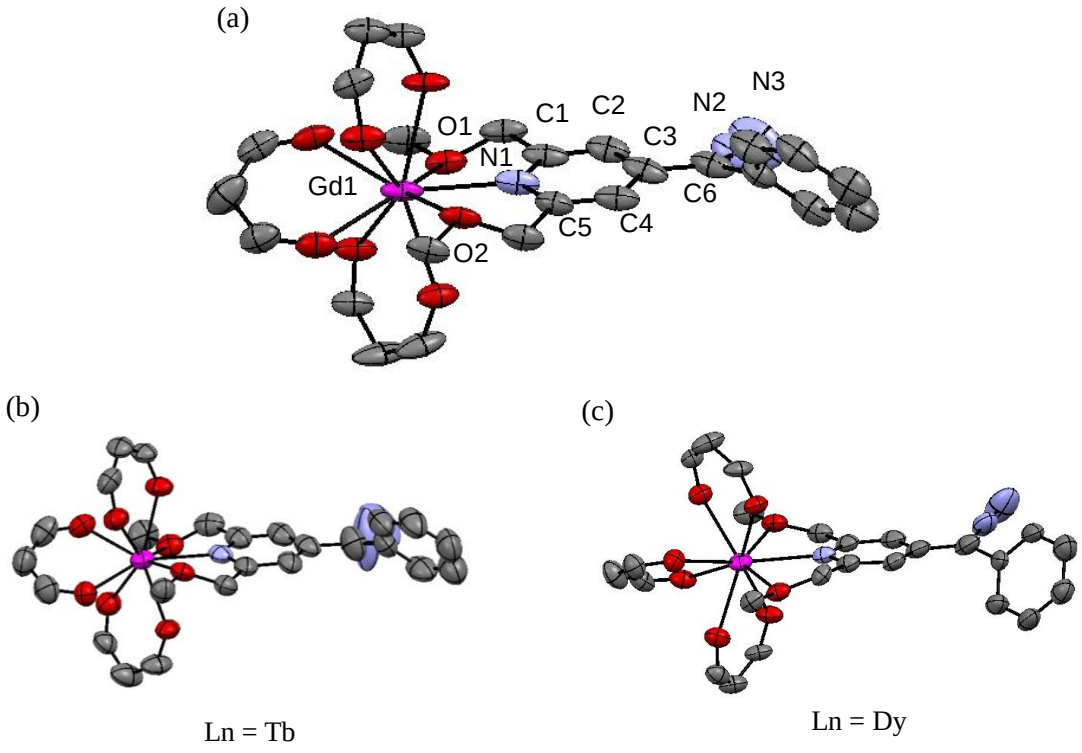

Figure 4-5. ORTEP drawings of (a) [Gd(hfac)$_3$(**L1**)], (b) [Tb(hfac)$_3$(**L1**)],and (c) [Dy(hfac)$_3$(**L1**)], respectively. The thermal ellipsoids are set at a 50% probability level, and the hydrogen atoms , and the CF_3 groups are omitted for the sake of clarity.

From the viewpoint of crystal packings, mononuclear complexes were aligned along the *a* axis intermolecularly to form the pseudo 1-D head-to-tail configurations (Figure 4-6). Short intermolecular contacts were found between the nitrogen atom of diazo component of **L1** and the carbon atom of methyl group (3.317 Å), and the carbon atom of hfac anion and carbon atom of **L1** (4.017 Å). Intermolecular Gd centers were well separated and that distance was 8.998 Å, suggesting the insignificant intermolecular magnetic interactions between the Gd centers.

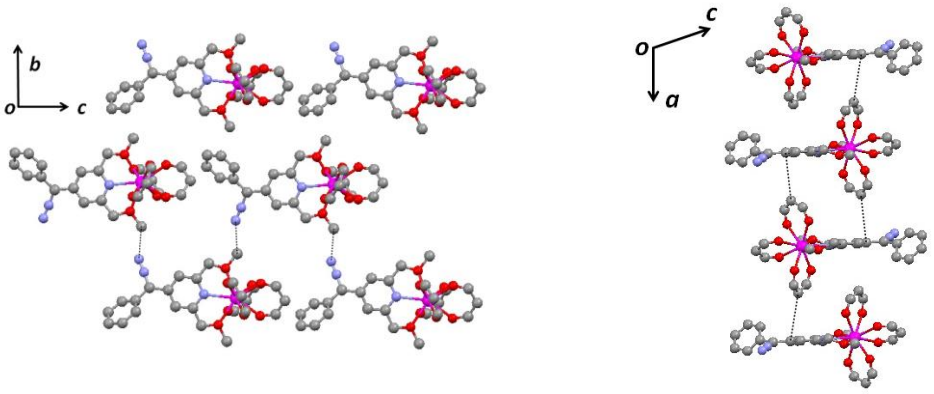

Figure 4-6. Crystal packings of [Gd(hfac)$_3$(**L1**)] projecting from the shown directions. Intermolecular short distances are depicted as black dotted lines.

The calculation of the degree of deviation for the coordination polyhedron from the ideal nine-vertex Gd structure by using the continuous shape measure theory and SHAPE[25] software indicated the low values for mono-capped square antiprism and tri-capped trigonal prism (Table 4-1).

Table 4-1. The SHAPE analyses for [Ln(hfac)$_3$(**L1**)]. (Ln = Gd, Tb, and Dy)

	[Gd(hfac)$_3$(**L1**)] (**3a**)	[Tb(hfac)$_3$(**L1**)] (**3b**)	[Dy(hfac)$_3$(**L1**)] (**3c**)
Monocapped square antiprism	**1.419**	**1.233**	**1.250**
Tricapped-trigonal prism	1.854	1.599	1.407

Main crystallographic parameters for these complexes and the selected bond lengths, bond angles are summarized in the Table 4-2, and Table 4-3, respectively.

Table 4-2. Crystallographic Data Collection and Structural Refinement Information for [Ln(hfac)$_3$(**L1**)]. (Ln = Gd, Tb, and Dy)

	[Gd(hfac)$_3$(**L1**)] (**3a**)	[Tb(hfac)$_3$(**L1**)] (**3b**)	[Dy(hfac)$_3$(**L1**)] (**3c**)
empirical formula	$C_{31}H_{20}F_{18}O_8N_3Gd$	$C_{31}H_{20}F_{18}O_8N_3Tb$	$C_{31}H_{20}F_{18}O_8N_3Tb$
formula weight	2302.74	2306.09	2313.24
crystal class	monoclinic	monoclinic	monoclinic
space group	$P2_1/c$ (no. 14)	$P2_1/c$ (no. 14)	$P2_1/c$ (no. 14)
a /Å	15.600 (3)	15.868 (4)	15.667 (4)
b / Å	16.609 (3)	16.187 (4)	16.586 (4)
c / Å	15.710 (3)	15.932 (4)	15.705 (4)
α /deg			
β /deg	108.622 (2)	107.835 (3)	108.058 (2)
γ /deg			
V / Å^3	3857.2 (11)	3895.6 (17)	3880.1 (15)
μ /mm^{-1}	1.862	1.952	2.066
Z	4	4	4
crystal size /mm	0.30 × 0.20 × 0.20	0.30 × 0.30 × 0.20	0.30 × 0.30 × 0.20
D_{calc} /gcm^{-3}	1.828	1.813	1.826
F (000)	2268.00	2272.00	2076.00
radiation	Mo-Kα	Mo-Kα	Mo-Kα
T /K	90.0	120	90.0
no. reflections measured	20459	21238	41892
no. unique reflections	8326	8831	9101
no. parameters	550	552	550
R_1 [a]	0.0883 ($I > 2.00\sigma(I)$)	0.0591 ($I > 2.00\sigma(I)$)	0.0611 ($I > 2.00\sigma(I)$)
wR_2 [a]	0.2562	0.1830	0.1448
GOF	1.015	1.386	1.176

[a] $R_1 = \Sigma \, ||F_0|-|F_c|| \, / \, \Sigma \, |F_0|$; $wR_2 = \{\Sigma \, w(F_0^2-F_c^2)^2 \, / \, \Sigma \, w(F_0^2)^2\}^{1/2}$

Table 4-3. Selected bond lengths, dihedral angles, and intermolecular Ln^{III}-Ln^{III} distances for [Ln(hfac)$_3$(**L1**)]. (Ln = Gd, Tb, and Dy)

	[Gd(hfac)$_3$(**L1**)] (**3a**)	[Tb(hfac)$_3$(**L1**)] (**3b**)	[Dy(hfac)$_3$(**L1**)] (**3c**)
	Bond lengths (Å)		
Ln(1)-N(1)	2.509 (6)	2.512 (6)	2.498 (4)
Ln(1)-O(1)	2.491 (7)	2.482 (5)	2.482 (5)
Ln(1)-O(2)	2.509 (6)	2.500 (4)	2.499 (6)
Ln(1)-O(3)	2.363 (8)	2.348 (4)	2.351 (6)
Ln(1)-O(4)	2.374 (10)	2.346 (5)	2.343 (5)
Ln(1)-O(5)	2.393 (8)	2.374 (4)	2.380 (4)
Ln(1)-O(6)	2.426 (6)	2.432 (4)	2.418 (6)
Ln(1)-O(7)	2.406 (6)	2.426 (4)	2.364 (5)
Ln(1)-O(8)	2.436 (8)	2.403 (4)	2.415 (4)
	Dihedral angles (°)		
C(2)C(4)N(1)-C(3)C(6)N(2)	16.17	17.22	13.52
	Intermolecular Ln^{III}-Ln^{III} distances (Å)		
Ln(1)-Ln(1)’	8.689	9.090	8.757

Section 6. Magnetic properties of [Ln(hfac)$_3$(**L1**)] (**3a-3c**) in the solid state.

Magnetic properties measurements of [Ln(hfac)$_3$(**L1**)] were performed on the microcrystalline sample of each complex using the SQUID systems.

(i) [Ln(hfac)$_3$(**L1**)] (**3a**~**3c**): before irradiation

Temperature dependence and field dependence of direct current magnetic properties of the [Ln(hfac)$_3$(**L1**)] (**3a**~**3c**) were performed on the 1.83 mg (1.73×10^{-6} mol), 1.41 mg (1.36×10^{-6} mol), and 1.55 mg (1.45×10^{-6} mol) of pulverized crystalline samples of **3a**, **3b**, and **3c** between the temperature range of 90-1.9 K (5 kOe) and field range of 0-50 kOe (1.9-5.0 K), respectively. In the temperature dependent magnetic properties measurement, the molar magnetic susceptibility, $\chi_{mol}T$, at 90 K were 7.18 cm^3 mol^{-1} K, 9.05 cm^3 mol^{-1} K, and 14.3 cm^3 mol^{-1} K, respectively. They were somehow smaller than the expected value of 7.88 cm^3 mol^{-1} K for the free Gd^{III} ion (g = 2.0, S = 7/2), 11.8 cm^3 mol^{-1} K for Tb^{III} ion (g_J = 3/2, $^7F_6$, S = 3, L = 3), and 14.2 cm^3 mol^{-1} K for Dy^{III} ion (g_J = 4/3, $^6H_{15/2}$, S = 5/2, L = 5), respectively. On cooling, the $\chi_{mol}T$ value was nearly constant from 90 K to 10 K and then steeply decreased until 1.9 K (Fig 4-7). The observed decreasing of $\chi_{mol}T$ values below 10 K might be due to the antiferromagnetic interaction between the Ln ions and/or the magnetic saturation effect because of the relatively high (probably insufficient) DC field for these measurements in addition to the thermal depopulation of low-lying crystal field states except for **3a**.

In the field dependent magnetic properties measurement, molar magnetic susceptibility per bohr magneton, $M_{mol}/N\mu_B$, at 1.9 K and at 50 kOe were 6.31, 3.92, and 5.44 and were relatively smaller than the expected saturation values of 7.0,9.72, and 10.65.

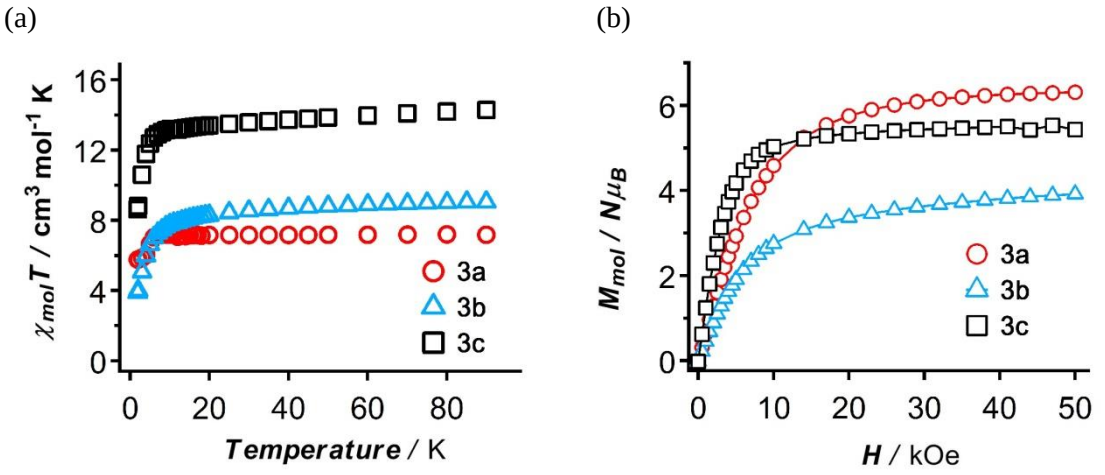

Figure 4-7. The plot of (a) $\chi_{mol}T$ vs. *T*emperature and (b) M_{mol} vs. H of [Ln(hfac)$_3$(**L1**)] (**3a**–**3c**). Solid lines are guide for eyes.

3a and **3b** didn't show the slow magnetic relaxation in the ac magnetic properties measurements, on the other hand, in the complex **3c**, $\chi'_{mol}T$ and χ''_{mol} weakly depended on both temperature and frequencies at low temperature, although the activation barrier for the spin re-orientation was not evaluated because of the loss of the peak-top temperature of χ''_{mol} signals (Figure 4-8).

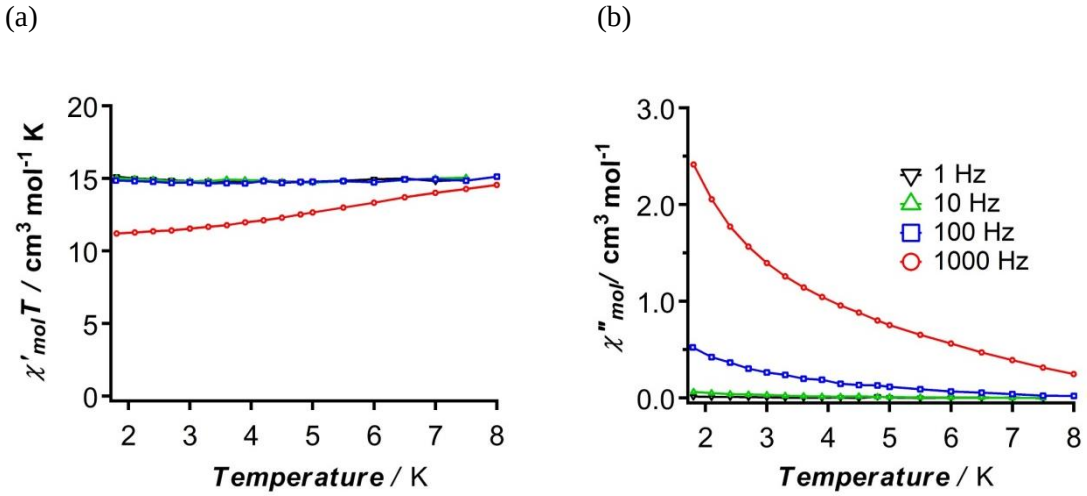

Figure 4-8. The plot of (a) $\chi'_{mol}T$ vs. *T*emperature, and (b) χ''_{mol} vs. *T*emperature of **3c**. Solid lines are guide for eyes.

Then, photo-irradiation for these complexes were performed in the SQUID systems. The detailed procedures and conditions for the photolysis of diazo component were summarized in the experimental sections. Particular in these complexes, "photolysis method A" was used for the production of carbenes.

It was very difficult and failed to photolyze effectively the Ln-diazo complexes, [Ln(hfac)$_3$(**L1**)] to Ln-carbene complexes, [Ln(hfac)$_3$(**L1'**)] (**3a'** – **3c'**) in the crystalline solid state. The photo-conversion ratios were estimated to be 10-50 % from the decrement of the 2061 cm^{-1} of IR absorption band typical to the diazo moieties after 2 days of irradiation. As results, no obvious changes of magnetic properties were observed after irradiation state for **3b**, and **3c**. Hence herein, we will briefly discuss about the magnetic properties of **3a** after irradiation.

(ii) [Gd(hfac)$_3$(**L1**)] (**3a**): after irradiation

After the irradiation of 2240 minutes for **3a**, the value of the $\chi_{mol}T$ product at 90 K and at 5 kOe was 7.26 cm^3 mol^{-1} K. It was slightly larger than the one observed before irradiation, indicating the occurrence of carbene by the photolysis. As lowering the temperature, the $\chi_{mol}T$ value decreased more rapidly compared to before irradiation state and reached 5.23 cm^3 mol^{-1} K at 1.9 K. This rapid decrement of $\chi_{mol}T$ product below around 40 K weakly suggests the antiferromagnetic interaction between the 4f spins of Gd ion and the 2p spins of carbene. For the quantitative evaluation of the magnitude of magnetic exchange interaction between 2p and 4f spins, the Heisenberg model fitting was tentatively performed between 90 - 10 K according to the following equation, $H = -J_{Gd\text{-}carbene}(S_{Gd}\ S_{carbene})$[26]. (detailed description is shown in the experimental sections) The best fit result gave g = 1.82 and $J_{Gd\text{-}carbene}/k_B$ = -0.67 K, respectively. The obtained $J_{Gd\text{-}carbene}/k_B$ was much smaller than the ones estimated in 3d-2p heterospin systems[21]. $M_{mol}/N\mu_B$ values at 1.9 K and at 50 kOe decreased from 6.31μ_B to 5.66μ_B through the irradiation, also supported the antiferromagnetic coupling within the 2p-4f complex.

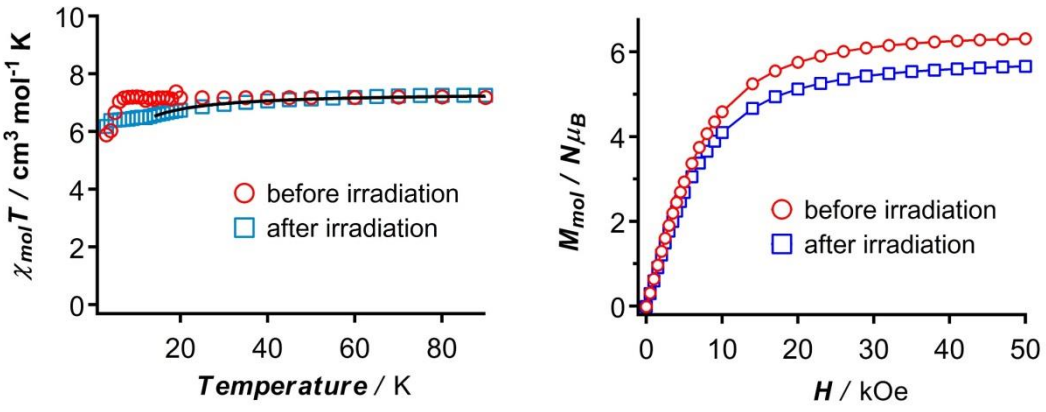

Figure 4-9. The plot of $\chi_{mol}T$ vs. *T*emperature (left) and M_{mol} vs. H (right) of [Gd(hfac)$_3$(**L1**)] after irradiation of 2240 min..The black solid lines in the plot of $\chi_{mol}T$ vs. *T*emperature indicate the best fit result.

Section. 7 Magnetic properties of [Ln(hfac)$_3$(**L1**)] (**3a**-**3c**) in the solution state

For the effective photo-conversion of the diazo moiety of the [Ln(hfac)$_3$(**L1**)] complex to carbene, their magnetic properties were recorded using the 10 mM of toluene solution in the SQUID system. Photo-irradiation for these complexes was performed in the SQUID systems using 10 mM of toluene samples. The "photolysis method A" was used for the production of carbenes.

On the photolysis, the $\chi_{mol}T$ values steeply decreased and reached to the saturation after irradiation about one day. The yields of photolysis of **3a**-**3c** were c.a. 100 % determined by the decrements of the IR absorption bands at 2061 cm^{-1} originated from the diazo components in these complexes after SQUID measurements.

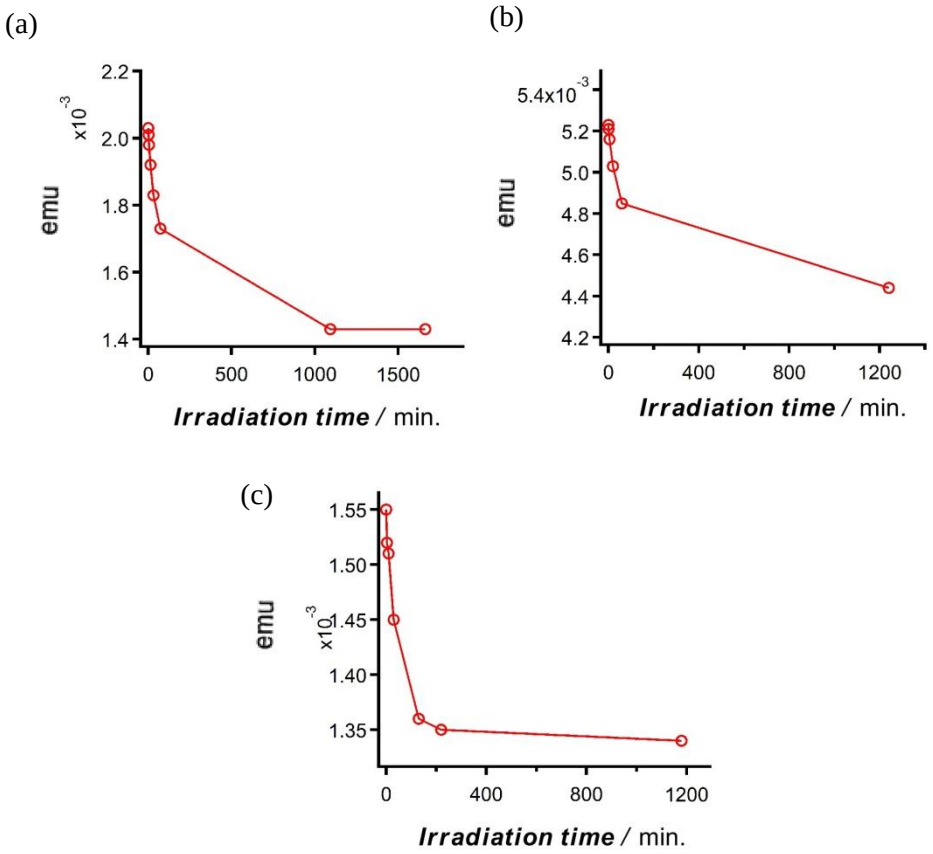

Figure 4-10. Plots of emu vs. Irradiation time for (a) [Gd(hfac)$_3$(**L1**)], (b) [Tb(hfac)$_3$(**L1**)], (c) [Dy(hfac)$_3$(**L1**)] in 10mM of toluene solution.

In advance to mention, the magnetic properties of these complexes in toluene solutions before irradiation were very similar to those of solid states except for the ac properties of the Dy complex.

(i) [Ln(hfac)$_3$(**L1**)] (**3a**~**3c**): before irradiation, solution state

As mentioned, the temperature dependence and field dependence of direct current magnetic properties were very similar to those of crystalline solid states. Their magnetic properties are depicted as $\chi_{mol}T$ vs. *T*emperature plot and M_{mol} vs. H plot in Figure 4-11.

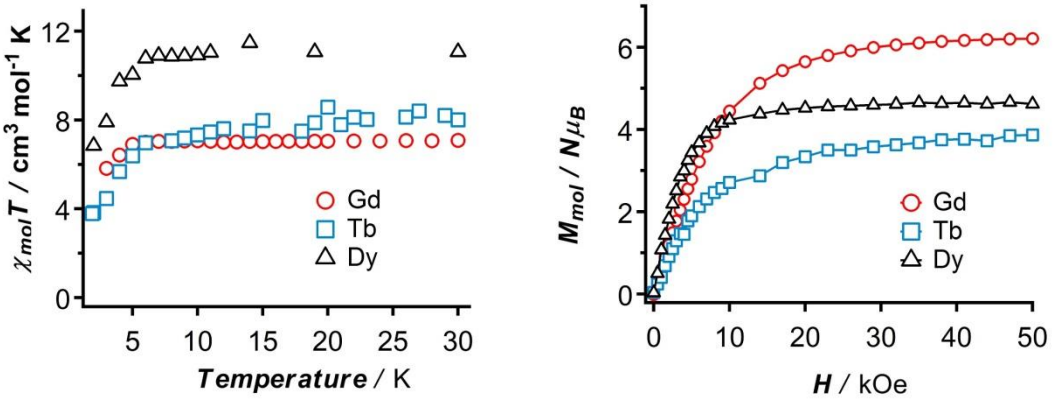

Figure 4-11. The plot of (a) $\chi_{mol}T$ vs. *T*emperature and (b) M_{mol} vs. H of [Ln(hfac)$_3$(**L1**)] (**3a**–**3c**) in the 10mM of toluene solution. Solid lines are guide for eyes.

Contrary to the ac magnetic properties in the solid state, **3c** clearly showed the SMM behavior without external dc field. This result indicated that well-separated intermolecular configuration in the solution state lead the negligible magnetic contribution of the dipole interaction that might enhance the quantum tunneling relaxation pathway. The activation barrier for the spin re-orientation, U_{eff}/k_B, and the pre-exponential factor, τ_0, were estimated to be 19.5 K and 3.5 x 10^{-7} sec., respectively from the $\chi''_{mol}T$ vs. T plot. The extended Debye's fitting results also gave the U_{eff}/k_B value of 23.9 K and the τ_0 value of 4.3 x 10^{-6} sec., from the χ''_{mol} vs. ν plot and the $\chi''_{mol}T$ vs. ν plot. The α values extracted by the extended Debye's equation and by the generalized Debye's equation in Cole-Cole plot ranged from 0.21-0.71, suggesting wide distribution of spin relaxation particular in the extremely low temperature might be due to the residual quantum tunnelling regime. The extracted magnetic parameters are summarized in Table 1-4 to1-6.

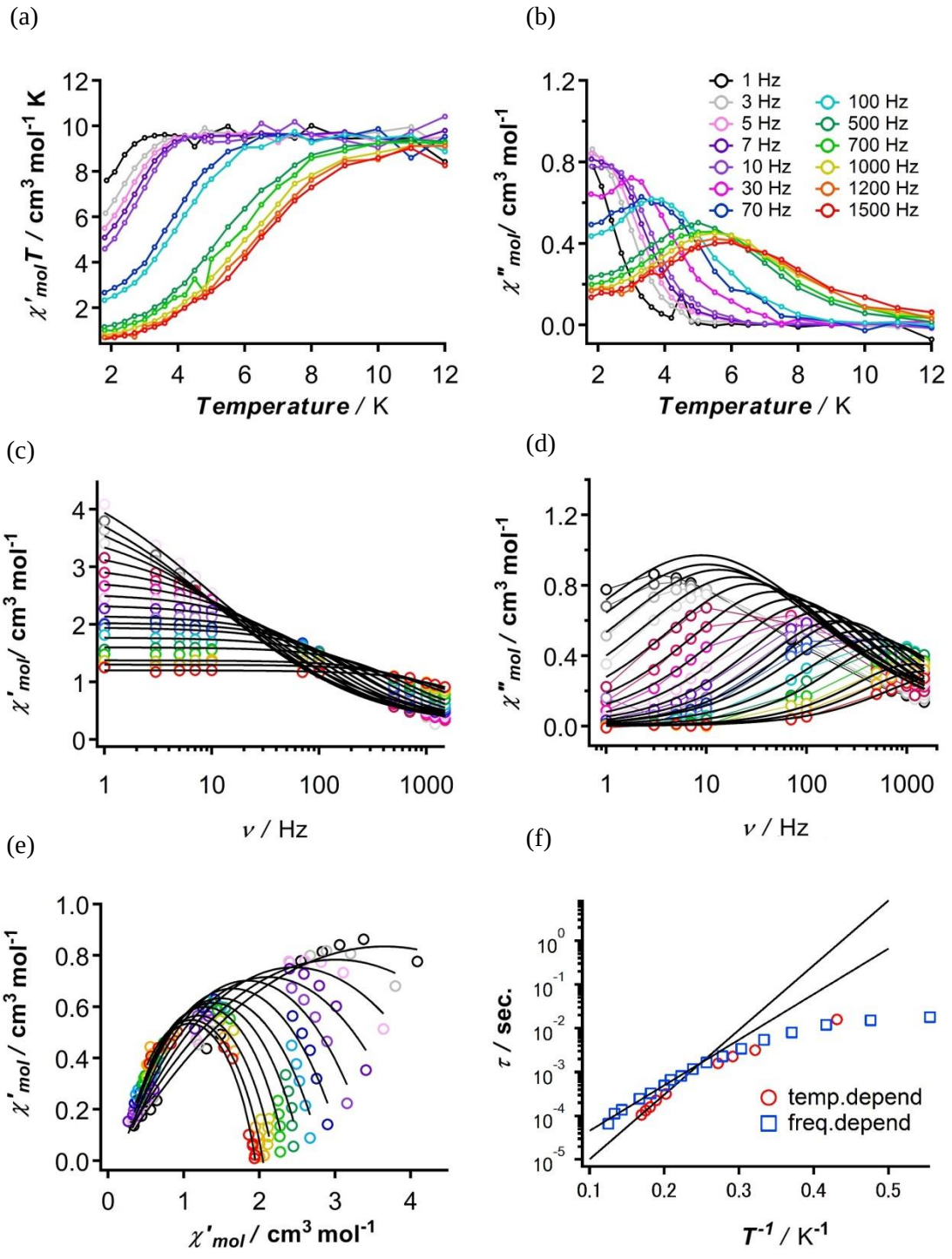

Figure 4-12. The plot of (a) $\chi'_{mol}T$ vs. *T*emperature, (b) χ''_{mol} vs. *T*emperature, (c) $\chi'_{mol}T$ vs. ν, (d) χ''_{mol} vs. ν, (e) Cole-Cole diagram, and (f) Arrhenius law of **3c** in 10 mM of toluene solution. The black bold lines in (c), and (d) show the fitting lines obtained from the extended Debye's model. In (e), black lines represent the best-fit results of generalized Debye's equation. The solid lines in (f) indicate the best fit result extracted from the Arrhenius law.

Table 4-4. The extracted peak top temperature for each frequency in the plot of χ''_{mol} vs. *T*emperature.

Frequency (Hz)	**10**	**50**	**70**	**100**	**500**
Temp.(K)	2.32	3.11	3.43	3.68	4.95
T^{-1} (K^{-1})	0.431034	0.321543	0.291545	0.271739	0.20202
τ (sec.)	0.0159236	0.0031847	0.0022748	0.0015924	0.0003185
Frequency (Hz)	**700**	**1000**	**1200**	**1500**	
Temp.(K)	5.29	5.53	5.71	5.91	
T^{-1} (K^{-1})	0.189036	0.180832	0.175131	0.169205	
	0.0002275	0.0001592	0.0001327	0.0001062	

Table 4-5. The extracted parameters for selected temperatures by the extended Debye's fitting in the plot of χ'_{mol} vs. ν, and χ''_{mol} vs. ν.

***Temp.*(K)**	**1.8**	**2.1**	**2.4**	**2.7**	**3.0**	**3.3**	**3.6**	**3.9**	**4.2**
χ_S (cm^3mol^{-1})	0.194638	0.20152	0.203642	0.206428	0.243289	0.236764	0.236798	0.287719	0.279518
χ_T (cm^3mol^{-1})	5.06157	4.86455	4.19624	3.75522	3.35732	3.03999	2.77393	2.53917	2.34073
τ (sec.)	0.112824	0.094962	0.075022	0.050411	0.034119	0.021556	0.014421	0.010484	0.007365
α	0.516937	0.503746	0.466977	0.432869	0.390463	0.365002	0.341709	0.305407	0.283879
***Temp.*(K)**	**4.5**	**4.8**	**5**	**5.5**	**6.0**	**7.0**	**7.5**	**8.0**	
χ_S (cm^3mol^{-1})	0.283716	0.111	0.246451	0.263598	0.353848	0.416601	0.481806	0.396442	
χ_T (cm^3mol^{-1})	2.1535	2.016	1.95069	1.77388	1.60205	1.37635	1.30075	1.2025	
τ (sec.)	0.005158	0.00432	0.003119	0.002079	0.001565	0.000872	0.000714	0.000418	
α	0.276094	0.2223	0.280744	0.262697	0.200009	0.195053	0.174245	0.208938	

Table 4-6. The extracted parameters for selected temperatures by the generalized Debye's fitting in the plot of χ''_{mol} vs. χ'_{mol} (Cole-Cole plot).

***Temp.*(K)**	**1.8**	**2.1**	**2.4**	**2.7**	**3.0**	**3.3**
χ_S (cm^3mol^{-1})	0.0938	0.0783	0.1378	0.1332	0.1761	0.1597
χ_T (cm^3mol^{-1})	7.2124	5.9426	4.7761	4.0878	3.5105	3.1325
α	0.7067	0.6676	0.6000	0.5579	0.4929	0.4604
***Temp.*(K)**	**3.6**	**3.9**	**4.2**	**4.5**	**4.8**	**5.0**
χ_S (cm^3mol^{-1})	0.1436	0.2059	0.2042	0.2051	0.1629	0.2214
χ_T (cm^3mol^{-1})	2.8409	2.5751	2.3602	2.1901	2.0469	1.9452
α	0.4415	0.3904	0.3544	0.3409	0.3291	0.2934

(ii) [Ln(hfac)$_3$(**L1**)] (**3a**~**3c**): after irradiation, solution state

Although the photolysis were underwent almost completely in all complexes, the obvious changes of the temperature dependence of molar magnetic susceptibilities were found only in the **3a** (Figure 4-13). In the $\chi_{mol}T$ vs. *T*emperature plot of **3a**, the $\chi_{mol}T$ product at 90 K and at 5 kOe was 7.57 cm^3 6the occurrence of 2p carbene spin by the irradiation. As decreasing the temperature the $\chi_{mol}T$ product decreased more clearly compared to that of solid state and reached 4.56 cm^3 mol^{-1} K at 1.9 K. This indubitable decrement of $\chi_{mol}T$ product below 30 K certainly indicates the antiferromagnetic interaction between the 4f spins of Gd ion and the 2p spin of carbene as suggested in the solid state. The magnetic exchange coupling constant $J_{Gd\text{-}carbene}/k_B$ was estimated to be -1.1 K (g = 1.88) according to the following Heisenberg fitting, H = - $J_{Gd\text{-}carbene}$ (S_{Gd} $S_{carbene}$). The unchanged temperature dependence of magnetization in **3b'**, and **3c'** by the irradiation suggests the negligible scale of magnetic interaction within the 4f-2p systems in these complexes. In **3a**, $M_{mol}/N\mu_B$ values at 1.9 K and at 50 kOe decreased from 6.21μ_B to 5.09μ_B through the irradiation, also strongly indicated the antiferromagnetic interaction within the complex. Unlike the temperature dependence plot, **3b'**, and **3c'** also showed the different magnetic properties compared to those of before irradiation states.

3a' nor **3b'** did not show the frequency dependence in the ac magnetic susceptibility measurement even after irradiation, on the other hand, **3c'** retained its SMM behavior even after irradiation (Figure 4-14). However, the peak tops of the χ''_{mol} signals shifted to lower temperature through irradiation, preventing the estimation of U_{eff}/k_B, and τ_0 from the χ''_{mol} vs. T plot. Hence, the U_{eff}/k_B, and τ_0, were extracted from the χ''_{mol} vs. ν plot and χ''_{mol} vs. ν plot , and was determined to be 10.3 K and 2.4 x 10^{-7} sec., respectively. The somehow small value of activation barrier for the spin inversion after photolysis suggest the decreasing of spin ground state S_{total} and/or of the magnitude of single ion magnetic anisotropy of Dy center because of the exchange coupling with another paramagnetic species. The α values extracted by the extended Debye's equation and by the generalized Debye's equation in Cole-Cole plot ranged from 0.21-0.52, still suggesting wide distribution of spin relaxation particular in the extremely low temperature. The extracted magnetic parameters are summarized in Table 4-7, 4-8.

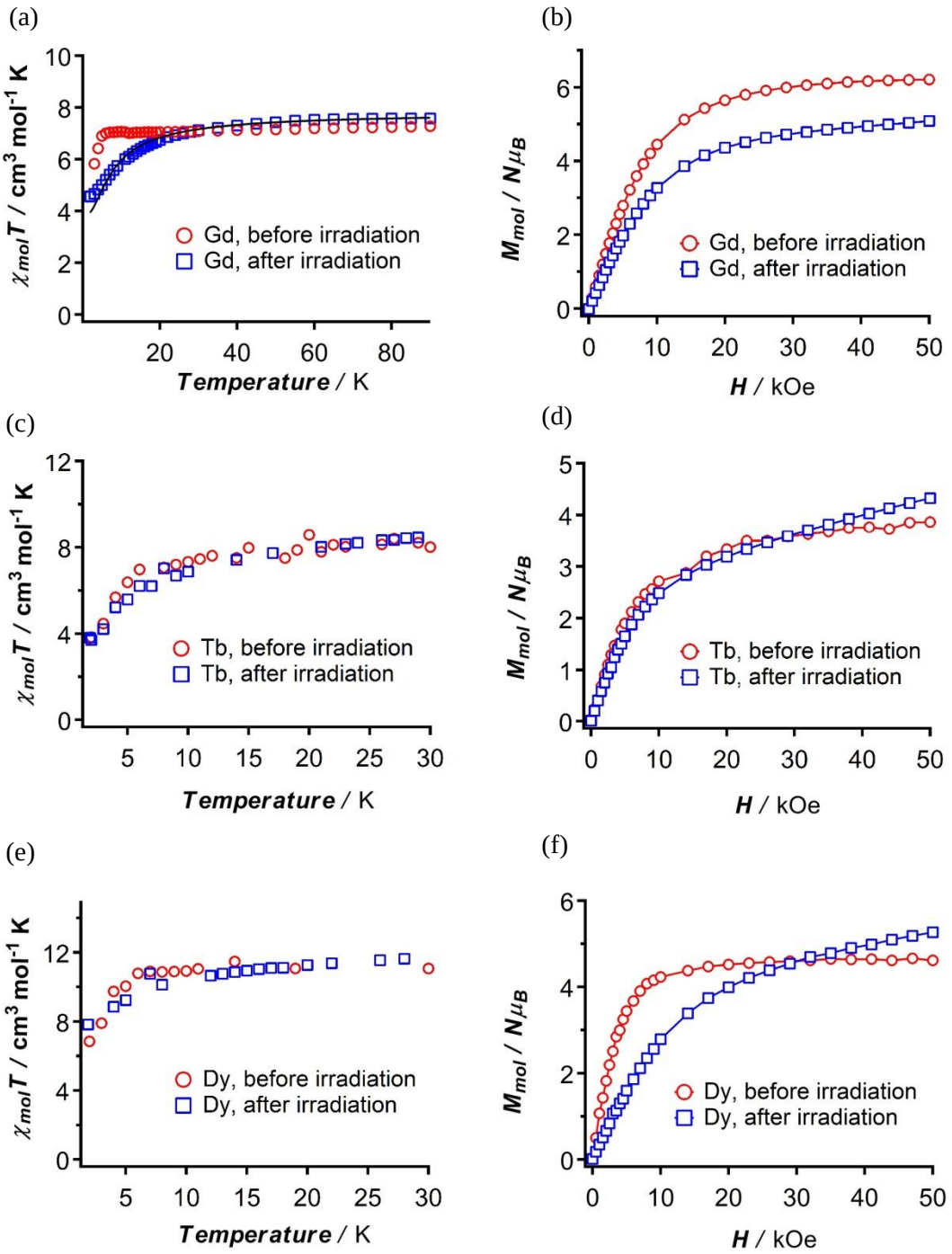

Figure 4-13. (a),(c),(e)The plot of $\chi_{mol}T$ vs. *T*emperature of **3a**, **3b**, and **3c**, respectively. The black solid line in (a) shows the best fit results obtained according to the Heisenberg model (see text). (b),(d),(f) The plot of M_{mol} vs. *H* of **3a**, **3b**, and **3c**, respectively in the 10 mM of toluene solution. The solid lines are guide for eyes.

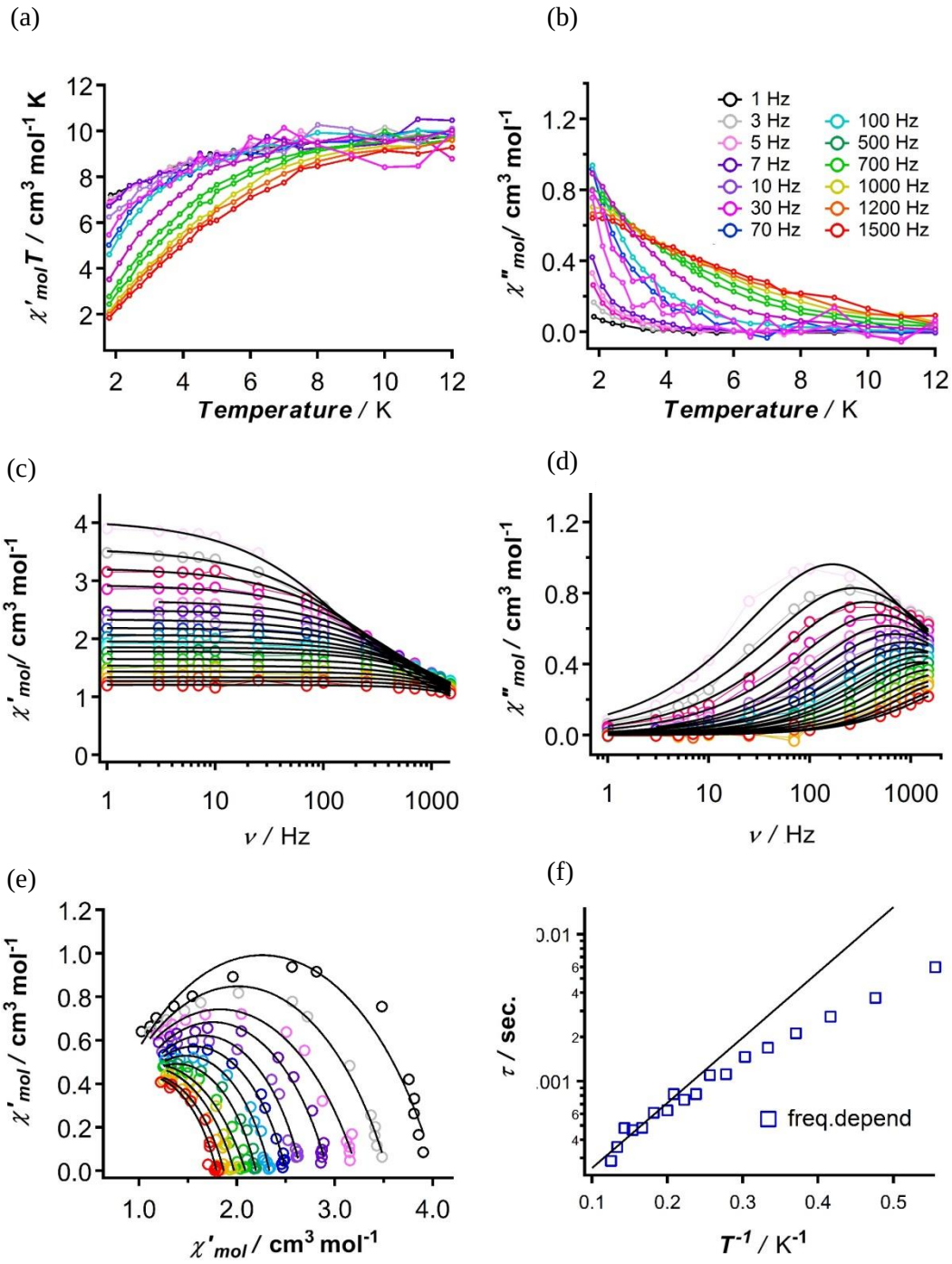

Figure 4-14. The plot of (a) $\chi'_{mol}T$ vs. *T*emperature, (b) χ''_{mol} vs. *T*emperature, (c) $\chi'_{mol}T$ vs. ν, (d) χ''_{mol} vs. ν, (e) Cole-Cole diagram, and (f) Arrhenius law of **3c** in 10 mM of toluene solution after irradiation. The black bold lines in (c), and (d) show the fitting lines obtained from the extended Debye's model. In (e), black lines represent the best-fit results of generalized Debye's equation. The solid lines in (f) indicate the best fit result extracted from the Arrhenius law.

Table 4-7. The extracted parameters for selected temperatures by the extended Debye's fitting in the plot of χ'_{mol} vs. ν, and χ''_{mol} vs. ν.

***Temp.*(K)**	**1.8**	**2.1**	**2.4**	**2.7**	**3.0**	**3.3**	**3.6**	**3.9**	**4.2**
χ_S (cm^3mol^{-1})	0.464275	0.441069	0.505445	0.572867	0.621991	0.622546	0.561822	0.657103	0.556238
χ_T (cm^3mol^{-1})	4.06051	3.56741	3.2293	2.93302	2.65913	2.5024	2.33816	2.19057	2.07215
τ (sec.)	0.005977	0.003693	0.002755	0.002115	0.001689	0.001463	0.001116	0.001100	0.000819
α	0.516937	0.503746	0.466977	0.432869	0.390463	0.365002	0.341709	0.305407	0.283879
***Temp.*(K)**	**4.5**	**4.8**	**5**	**5.5**	**6.0**	**7.0**	**7.5**	**8.0**	
χ_S (cm^3mol^{-1})	0.61169	0.709466	0.624123	0.667649	0.615286	0.654933	0.698099	0.61799	
χ_T (cm^3mol^{-1})	1.9562	1.85457	1.78248	1.6518	1.53573	1.43526	1.33797	1.27403	
τ (sec.)	0.000749	0.000817	0.000635	0.000609	0.000483	0.000465	0.000479	0.000356	
α	0.276094	0.2223	0.280744	0.262697	0.200009	0.195053	0.174245	0.208938	

Table 4-8. The extracted parameters for selected temperatures by the generalized Debye's fitting in the plot of χ''_{mol} vs. χ'_{mol} (Cole-Cole plot).

***Temp.*(K)**	**1.8**	**2.1**	**2.4**	**2.7**	**3.0**	**3.3**
χ_S (cm^3mol^{-1})	0.4962	0.482762	0.428123	0.582418	0.657199	0.629484
χ_T (cm^3mol^{-1})	4.02029	3.53743	3.23105	2.92752	2.65409	2.49874
α	0.347391	0.354386	0.379796	0.327621	0.290151	0.30052
***Temp.*(K)**	**3.6**	**3.9**	**4.2**	**4.5**	**4.8**	**5.0**
χ_S (cm^3mol^{-1})	0.634266	0.586249	0.215991	0.270521	0.344285	0.334155
χ_T (cm^3mol^{-1})	2.33191	2.19457	2.0864	1.97305	1.86753	1.79293
α	0.289927	0.301092	0.386332	0.35308	0.333099	0.312095

Section 8. Chapter conclusion

Newly designed magnetic coupler for the construction of novel 4f-2p heterospin complex was successfully prepared. The tridentate pyridine ligand **L1** carrying diazo component on the 4-position of pyridine ring could combine to the $Ln(hfac)_3$ in 1:1 ratio. The crystal structure analysis revealed that these complexes had isostructure formulated as [$Ln(hfac)_3$(**L1**)]. Each metal ion was surrounded by six oxygen atoms of three hfac anions and two oxygen atoms and one nitrogen atom of **L1**, resulted in giving the nine-coordinated structure. The local coordination geometry was determined to be the intermediate state between the mono-capped square antiprism and the tri-capped trigonal prism. The Ln-N bond lengths were 2.498(4)-2.512(6) Å, which were much longer than those of 3d-2p complex generally observed.

In the solid states SQUID measurements, the carbenes were not efficiently produced by the photolysis of 532 nm DPSS laser, prevented us from investigating the detailed magnetic interaction between 4f spins of Ln ions and the 2p spins of carbenes. The magnetic property measurement in the liquid state was performed using the 10 mM of toluene solution for each complex. After irradiation, antiferromagnetic interaction of 4f spin and the 2p spin through pyridine moiety was clearly suggested by the dc magnetic susceptibility measurement. Interestingly, the SMM behavior of Dy complex was strongly affected by the existence of organic radical, though the value of U_{eff}/k_B decreased after irradiation (23.9 K to 10.3 K).

In conclusion, by introducing the diazo component to the 4f Ln complex through pyridine unit, we were able to construct a new type of photo-responsive molecule based magnet. The SMM with high activation barrier was not established might be due to the antiferromagnetic nature of their interactions and/or the extremely weak coupling constant. Hence in the next chapter, we will investigate the different type of magnetic coupler using the same diazo component aiming at the realization of ferromagnetic coupling between 4f and 2p spins.

Chapter 5

~ Construction of dinuclear Ln(III) complexes in 4f-2p heterospin system ~

Section 1.

Preparation of diazo-pyridine-*N*-oxide ligands **4D1pyO** and **3D1pyO**, and their Ln(III) complexes

In the former mononuclear complexes, 4f spins of Ln ions could be combined antiferromagnetically with 2p spins of carbenes through the π conjugation systems of pyridine moieties. However, generally in our heterospin molecule-based magnets, the ferromagnetic interaction is more preferred than the antiferromagnetic interaction for the construction of SMMs and SCMs because the plus sign of the magnetic exchange interaction can easily lead the higher spin ground state, S_{total}, for each magnetic unit. In this line, novel magnetic couplers **4D1pyO** and **3D1pyO**, carrying diazo components on 4- and 3- positions of pyridine-*N*-oxide, and their Ln complexes were designed. As prior information, it was known that 1) R-pyO (R = H, or CN ; pyO = pyridine-*N*-oxide) could make dinuclear complexes with $Ln(X)_3\ 2H_2O$ (X = hfac, and tta ; thenoyl trifluoroactonate) formulated as $[Ln(X)_3(R\text{-}pyO)_2]_2$-*solvent*[27,28] and was reported that 2) orthogonality between the pyridine plane and the first coordinated O-Ln-O plane preferred the ferromagnetic interactions between 2p-4f spins[29].

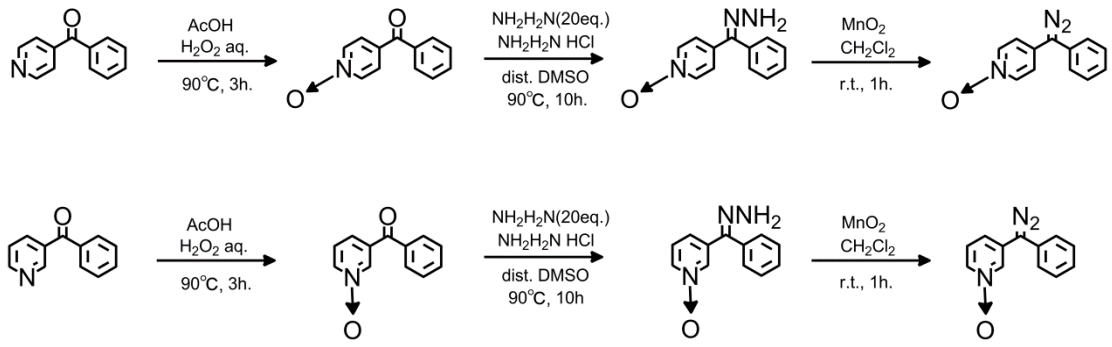

Scheme 5-1. Synthesis of diazo-pyridine-*N*-oxide ligand, **4D1pyO**, and **3D1pyO**

4D1pyO and **3D1pyO** were obtained as reddish-purple colored crystalline solid and reddish colored oily product respectively by three steps from 4- or 3-benzoylpyridine (Scheme 5-1). Then **4D1pyO** and **3D1pyO** were mixed with $Ln(hfac)_3\ 2H_2O$ (Ln = Gd, Tb, and Dy) in the various combinations of organic solvents, but only oily products were obtained so that it was difficult to determine the local structures of these compounds. Hence $Ln(tta)_3\ 2H_2O$, which were also known to be able to make complexes with R-pyO[28] were used as 4f spin sources instead of $Ln(hfac)_3\ 2H_2O$.

Mixing the **4D1pyO** or **3D1pyO** with $Ln(tta)_3\ 2H_2O$ in the chloroform/*n*-heptane gave the reddish-orange colored single crystals (Scheme 5-2).

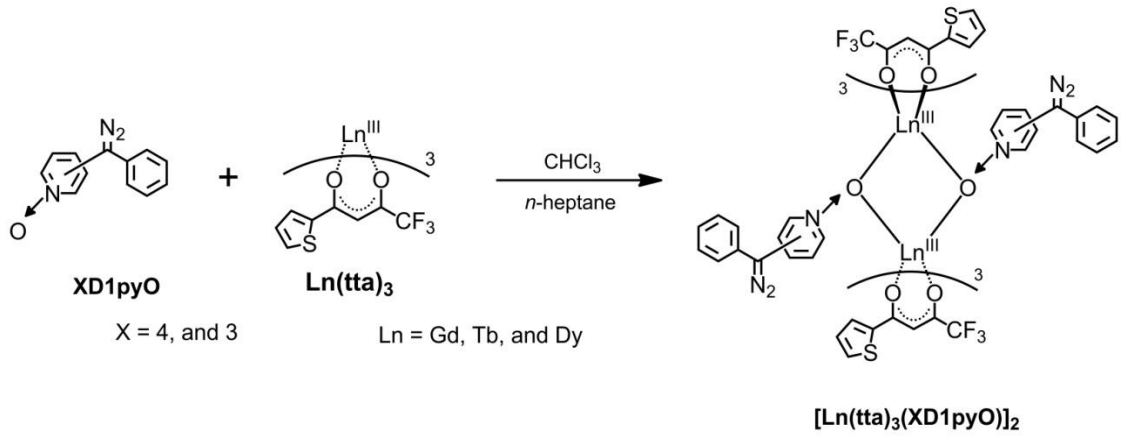

Scheme 5-2. Synthesis of Ln-XD1pyO complexes.

Section 2. UV-vis. absorption spectra of **4D1pyO** and **3D1pyO**, and their Ln(III) complexes.

UV-vis. absorption spectra of **4D1pyO** and **3D1pyO** were recorded using the 10 mM chloroform solutions at room temperature. **4D1pyO** and **3D1pyO** showed the specific absorptions attributed to the *n*-π* transition of diazo component at 528 nm (ε = 167) and 507 nm (ε = 90), respectively. This difference of the absorption wavelength suggests the larger conjugation systems of **4D1pyO** compared to **3D1pyO**, and also **4D1py** previously reported (497 nm, ε = 200)[30].

Solid state diffuse reflection measurements for Ln complexes were performed using the solid samples diluted by KBr at room temperature. The obtained data were converted to absorption spectra by the KM function. In the solid state spectra, $[Gd(tta)_3(\mathbf{4D1pyO})]_2$ $2CHCl_3$ (**4a**), $[Tb(tta)_3(\mathbf{4D1pyO})]_2$ $2CHCl_3$ (**4b**), and $[Dy(tta)_3(\mathbf{4D1pyO})]_2$ $2CHCl_3$ (**4c**) showed the very similar absorption band. The wavelengths of maxima for the broad bands are 472 nm in all three complexes, while $[Tb(tta)_3(\mathbf{3D1pyO})]_2$ $4CHCl_3$ (**4d**) had its peak top at 502 nm (Figure 5-1). The blue shift of the absorption band of *n*-π* transition of diazo component through complexation in **4a**-**4c** (528 nm to 472 nm) implying a certain electronic interaction between the Ln complexes and **4D1pyO**, although that of **4d** is limited (507 nm to 502 nm).

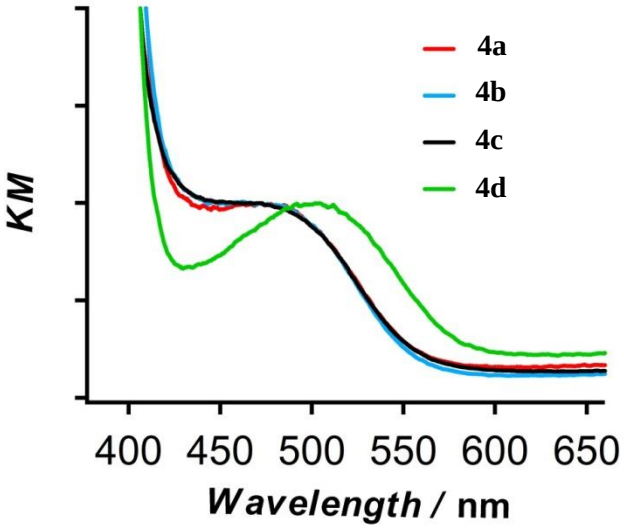

Figure 5-1.
Solid-state absorption spectra of $[Ln(tta)_3(\mathbf{4D1pyO})]_2$ (**4a**-**4c**), and **4d**

Section 3. Calculation of spin density of **4C1pyO** and **3C1pyO** using DFT method

To obtain some information about the spin polarization of **4C1pyO** and **3C1pyO**, DFT calculation was performed using the model compounds with doublet spin ground state, **4NOpyO** and **3NOpyO** (Figure 5-2). In **4NOpyO**, relatively large α spin density was found on the oxygen atom of pyridine-*N*-oxide unit. In contrast, **3NOpyO** clearly showed the β spin distribution on the pyridine-*N*-oxide unit. This result suggested that **4C1pyO** and **3C1pyO** might be regioselectively interacted with 4f spin of Ln ions in the heterospin complexes.

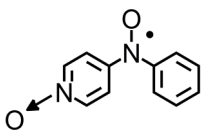

4NOpyO

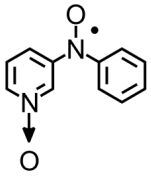

3NOpyO

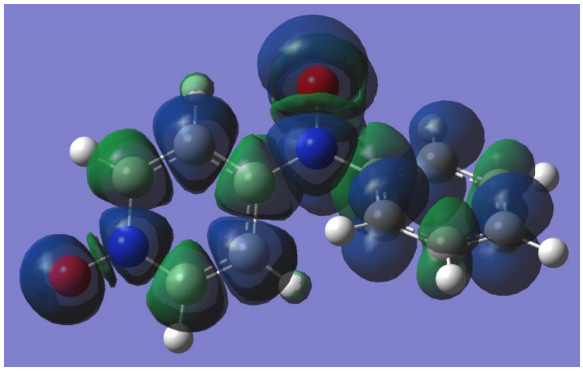

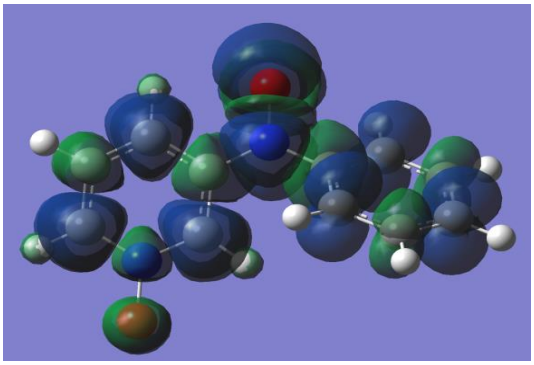

Method : Ground state, DFT, Unrestricted, B3LYP, Basis set : 6-31G, +, d, Charge 0, spin : doublet

Figure 5-2. Spin density calculation of **4NOpyO** (left) and **3NOpyO** (right). Blue and green areas represent the α spin and β spin distribution, respectively.

Section 4. EPR spectra of **4D1pyO** and **3D1pyO** in the rigid solution (before and after irradiation).

The electron paramagnetic resonance spectra were measured for **4D1pyO** and **3D1pyO** before and after irradiation using the 5mM of distilled MTHF solution at cryogenic temperature (3.7 K for **4D1pyO** and 4.4 K for **3D1pyO**, respectively). Before the irradiation of 532 nm of DPSS laser, no resonant signals (except for the impurity signal around 310-320 mT ; g = 2.00) were found around the field range of 0-800 mT (Figure 5-3). On the photolysis of **4D1pyO** and **3D1pyO**, four resonant signals typical to the triplet carbenes, **4C1pyO** and **3C1pyO** were observed in both cases. In **4C1pyO**, the resonant peaks at 44, 436, 503, and 693 mT corresponded to the –z, x, y, and z transitions appeared and increased during the irradiation. The zero-field splitting parameters, $|D|$/hc and $|E|$/hc, were estimated to be 0.35 and 0.017 cm^{-1}, respectively from the spectrum. On the other hand, **3C1pyO** had its resonant peaks at 118, 455, 536, and 762 mT and the zero-field splitting parameters, $|D|$/hc and $|E|$/hc, were estimated to be 0.41 and 0.020 cm^{-1}. The smaller $|D|$/hc value of **4C1pyO** than that of **3C1pyO** and of the corresponding pyridine ligand, **4C1py** ($|D|$/hc and $|E|$/hc, were 0.434 and 0.020 cm^{-1}, respectively) strongly suggests the more extended pi conjugation systems (larger distribution of 2p spins) in **4C1pyO** than the other two compound. This result implies larger spin density on oxygen atom and more effective magnetic interaction between 4f spins of Ln ions and the 2p spins of **4C1pyO** than that of **3C1pyO** . The $|E|/|D|$ rations for **4C1pyO** and **3C1pyO** were ca. 0.05, which were comparable with those for the parent **4C1py** reported previously.

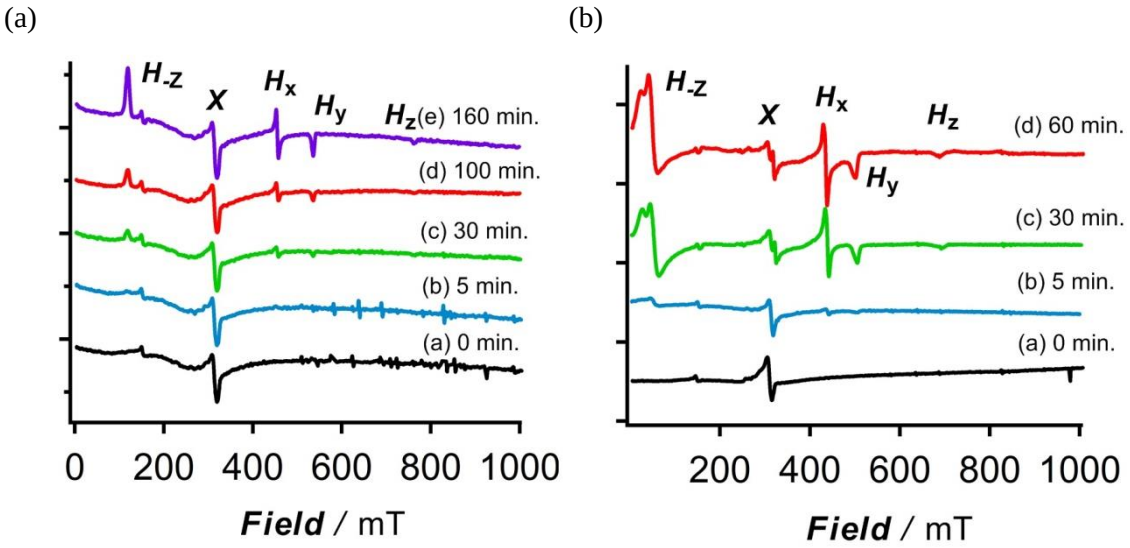

Figure 5-3.

ESR spectra (9.0 GHz) before and after irradiation of (a) **4-D1pyO** and (b) **3-D1pyO**

Section 5. Crystal structures of **4D1pyO** and $[Ln(tta)_3(\mathbf{4D1pyO})]_2$ $2CHCl_3$ (Ln = Gd : **4a**, Tb : **4b**, and Dy : **4c**), and $[Tb(tta)_3(\mathbf{3D1pyO})]_2$ $4CHCl_3$: **4d**

X-ray crystal analyses were performed at -183 °C for $[Ln(tta)_3(\mathbf{4D1pyO})]_2$ $2CHCl_3$ (Ln = Gd : **4a**, Tb : **4b**, and Dy : **4c**), and $[Tb(tta)_3(\mathbf{3D1pyO})]_2$ $4CHCl_3$: **4d** using single crystals obtained above.

(i) **4D1pyO**

4D1pyO crystallized in the monoclinic $P2_1/c$ (No. 14) space group. The bond length of N-O is 1.317 Å, and the dihedral angle between pyridine plane (defined by C1, C2, C3, C4, C5, and N1) and diazo plane (defined by C3, C6, and N2) was 10.4°. The ORTEP drawing of **4D1pyO** is shown in Figure 5-4.

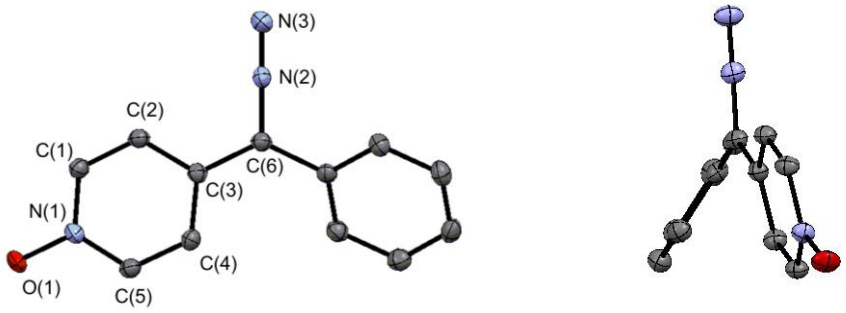

Figure 5-4. ORTEP drawings of diazo-pyridine-*N*-oxide ligand, **4D1pyO**. The thermal ellipsoids are set at a 50% probability level, and the hydrogen atoms are omitted for the sake of clarity.

(ii) $[Gd(tta)_3(\mathbf{4D1pyO})]_2$ $2CHCl_3$ (**4a**)

When using the combination of **4D1pyO** and Gd ion, dinuclear Gd complex formulated as $[Gd(tta)_3(\mathbf{4D1pyO})]_2$ $2CHCl_3$ was obtained. This complex crystallized in the monoclinic $P2_1/n$ (No.14) space group and had two chloroform molecules as crystal solvents. Two Gd ions were bridged by the oxygen atom of the **4D1pyO** in a μ_2 coordination mode to form a dinuclear complex. Two Gd ions were crystallographically equivalent due to the inversion center within the molecule. Each Gd ion was surrounded by eight oxygen atoms arising from three tta anions and two **4D1pyO**. The calculation of the degree of deviation for the Gd coordination polyhedron from the ideal eight-vertex Gd structure by using the continuous shape measure theory and SHAPE[25] software, indicated the low values for square antiprism (0.993, D_{4d}), triangular dodecahedron (1.021, D_{2d}). Therefore, the coordination geometry was expected to be in the intermediate state between these structures.

The Gd-$O_{\mathbf{4D1pyO}}$ bond lengths were 2.411, and 2.422 Å. These were slightly longer than the Gd-O_{tta} bond lengths ranging from 2.324 to 2.400 Å. Gd-Gd and $O_{\mathbf{4D1pyO}}$-$O_{\mathbf{4D1pyO}}$ distances were 4.129 and 2.510 Å, respectively. Regarding the **4D1pyO** moiety, N-O bond length was 1.355 Å and was relatively longer than the value obtained for uncomplexed **4D1pyO** (1.317 Å). The pyridine plane was almost perpendicular to the Gd-$O_{\mathbf{4D1pyO}}$-Gd-$O_{\mathbf{4D1pyO}}$ plane (the dihedral angle between these planes was 89.06 °) and that might lead the ferromagnetic interaction between 4f and 2p spins after irradiation. **4D1pyO** moiety had the crystallographic disorder due to the rotation of the phenyl ring. The shortest interdimer Gd-Gd distance was 12.05Å and was almost same value for the one previously been reported, indicating that the direct interaction of spin centers was insignificant. Intermolecular CH-π interaction between phenyl rings of two **4D1pyO** was expected, but it was difficult to mention the accurate interaction mode because of the rotation disorder of phenyl moieties. The ORTEP drawings, local structure, and the crystal packings are shown in Figure 5-5.

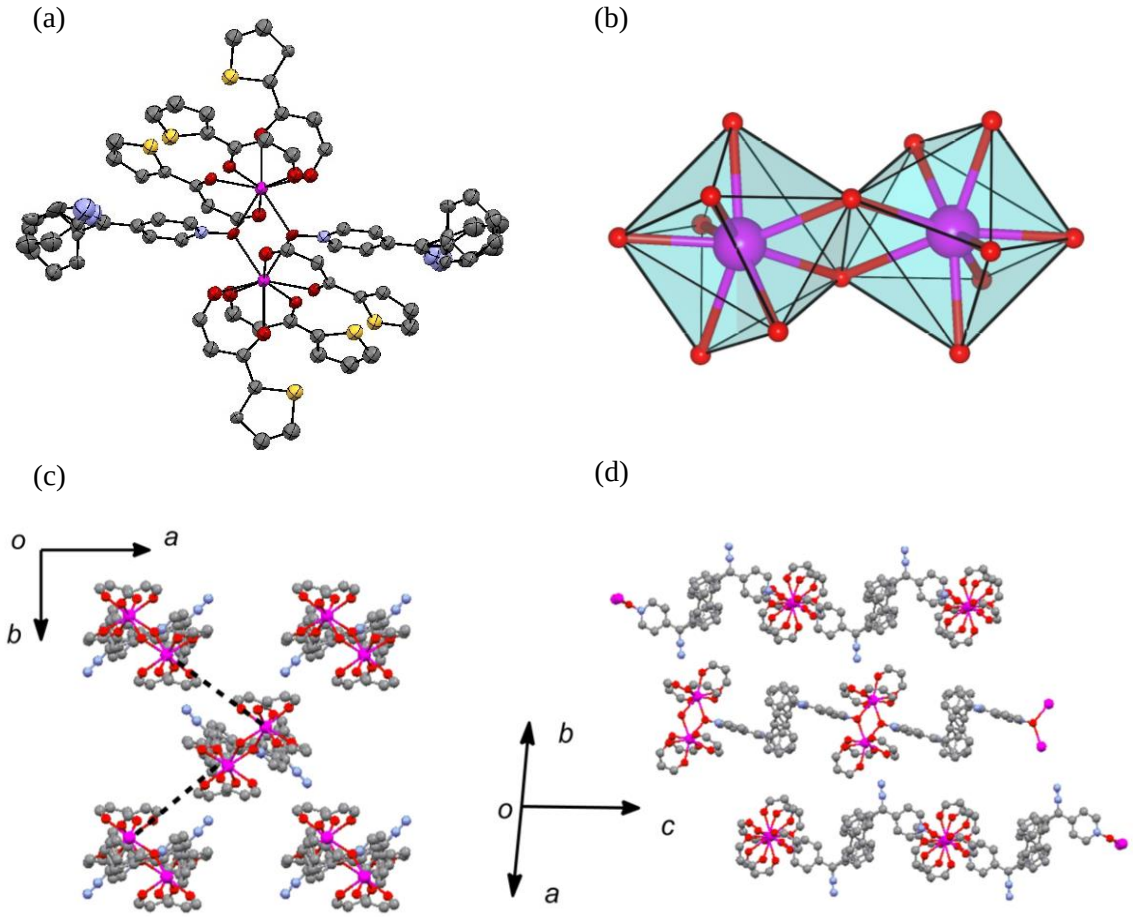

Figure 5-5. (a) ORTEP drawings of $[Gd(tta)_3(\mathbf{4D1pyO})]_2$ $2CHCl_3$. The thermal ellipsoids are set at a 50% probability level, and the hydrogen atoms and CF_3 groups, and solvent molecules are omitted for the sake of clarity. (b) Schematic drawing of local coordination structures of Ln ions (red : O atoms, pink : Gd atoms). (c), (d) Crystal packings of dinuclear complexes projecting from the shown directions. Intermolecular short distances between metal centers are depicted as black dotted lines.

(iii) $[Tb(tta)_3(\mathbf{4D1pyO})]_2$ $2CHCl_3$ (**4b**), and (iv) $[Dy(tta)_3(\mathbf{4D1pyO})]_2$ $2CHCl_3$ (**4c**)

The other derivatives (Ln = Tb, and Dy) also crystallized in the same monoclinic $P2_1/n$ (No.14) space group and had isostructures to the Gd complex though the thermal disordering of thiophen rings were found in these cases. Main crystallographic parameters for these complexes are summarized in the Table 5-1 and ORTEP drawings of **4b** and **4c** are shown below (Figure 5-6).

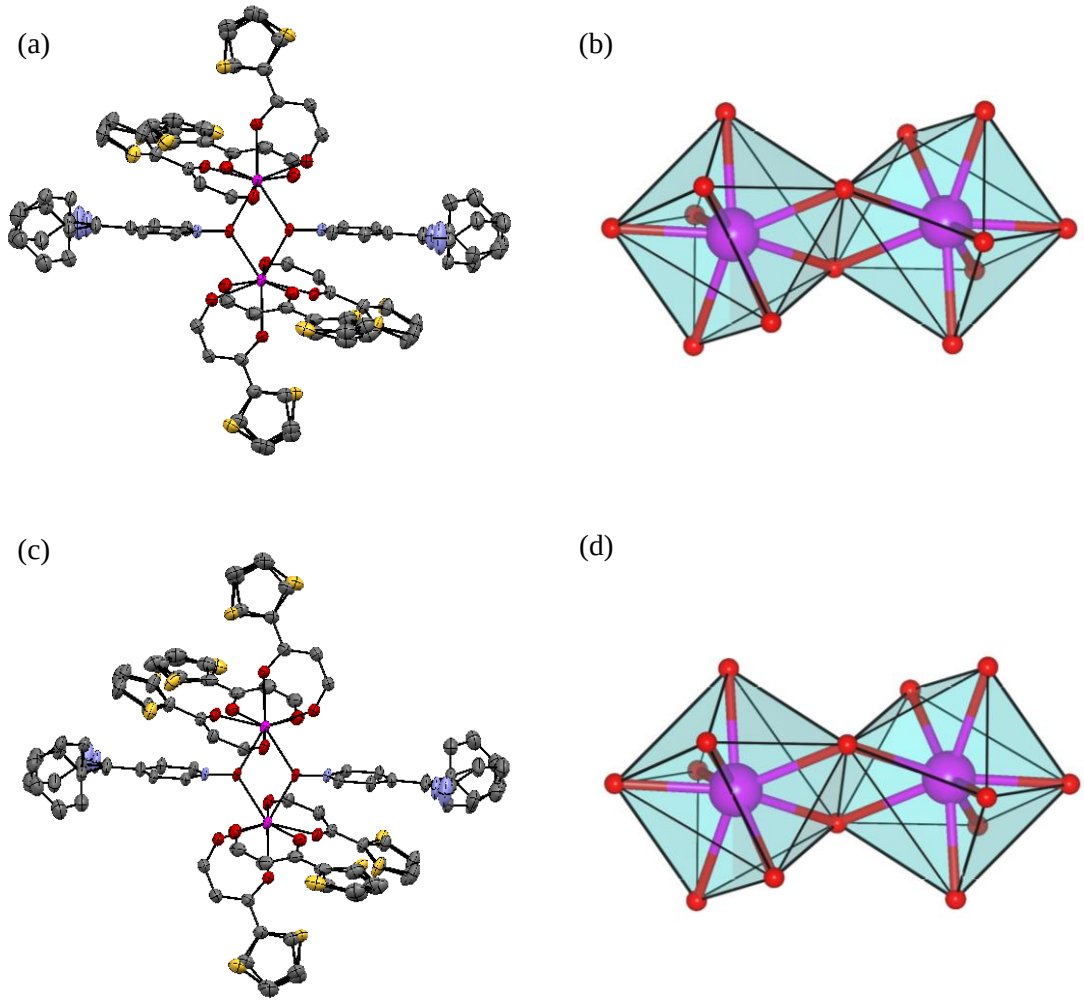

Figure 5-6. (a), (c) ORTEP drawings of $[Tb(tta)_3(\mathbf{4D1pyO})]_2$ $2CHCl_3$, and $[Dy(tta)_3(\mathbf{4D1pyO})]_2$ $2CHCl_3$, respectively. The thermal ellipsoids are set at a 50% probability level, and the hydrogen atoms and CF_3 groups, and solvent molecules are omitted for the sake of clarity. (b), (d) Schematic drawings of local coordination structures of Ln ions (red : O atoms, pink : Tb atoms in (b), and Dy atoms in (d)).

(v) $[Tb(tta)_3(\mathbf{3D1pyO})]_2$ $4CHCl_3$ (**4d**)

Using the combination of $Tb(tta)_3$ and **3D1pyO** instead of **4D1pyO** gave the reddish-orange colored compound formulated as $[Tb(tta)_3(\mathbf{3D1pyO})]_2$ $4CHCl_3$. This dinuclear complex crystallized in the triclinic *P*-1 (No.2) space group and had four chloroform molecules as crystal solvents although the local structure of Tb ions were similar to those of **4b**. Each Tb ion was surrounded by six oxygen atoms of tta anions and two oxygen atoms of pyridine-*N*-oxide moieties. The SHAPE software analysis indicated much lower values for square antiprism (0.691, D_{4d}) than triangular dodecahedron (1.708, D_{2d}), suggesting the subtle differences of the local coordination geometries compared to **4a**-**4c**. The main bond lengths and dihedral angles are summarized in Table 5-2. $O_{\mathbf{4D1pyO}}$-$O_{\mathbf{4D1pyO}}$ distances, $r_{O\text{-}O}$ and the dihedral angle between pyridine plane (defined by C1, C2, C3, C4, C5, and N1) and diazo plane (defined by C3, C6, and N2) were 2.537 Å and 16.2°, respectively. These values were slightly longer and larger in each than those of **4a**-**4c** (2.483-2.510 Å, and 3.70-5.79 °). The shortest inter-molecular Tb-Tb distance was 9.733 Å observed along *a* axis, suggesting the negligible magnetic interactions between dimer complexes. The ORTEP drawings, local structure, and the crystal packings are shown in Figure 5-7.

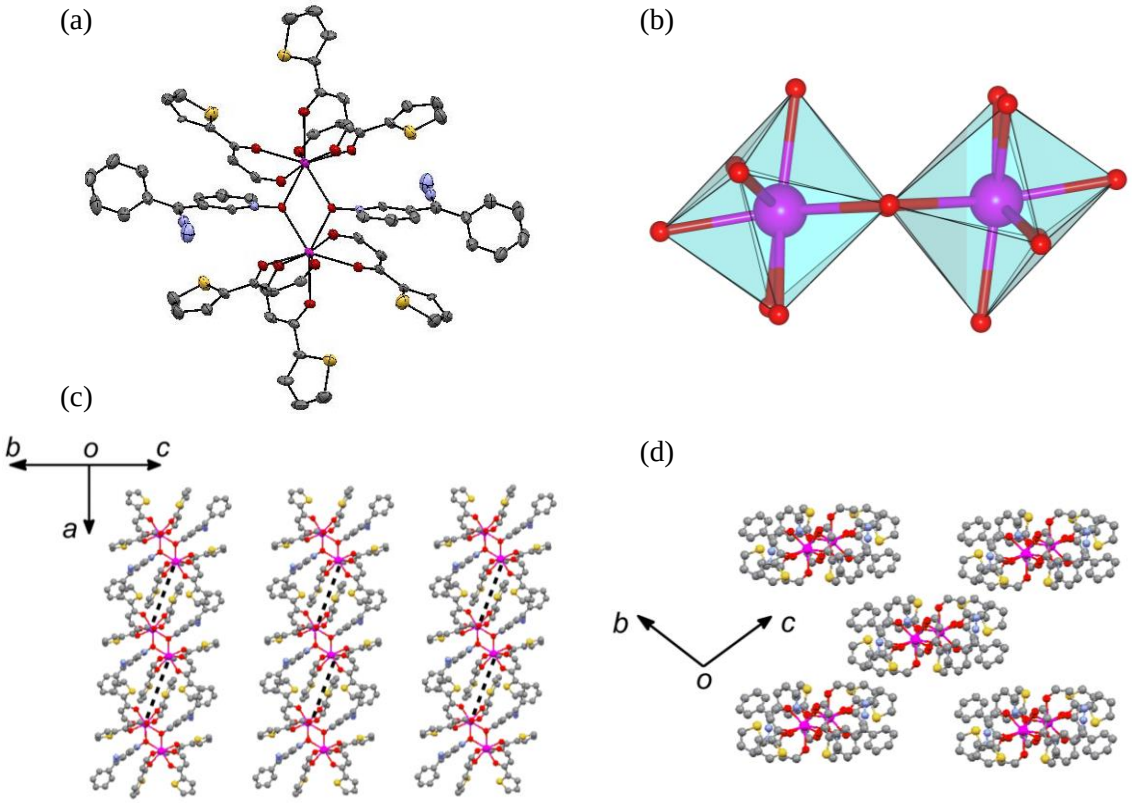

Figure 5-7. (a) ORTEP drawings of $[Tb(tta)_3(\mathbf{3D1pyO})]_2$ $4CHCl_3$. The thermal ellipsoids are set at a 50% probability level, and the hydrogen atoms and CF_3 groups, and solvent molecules are omitted for the sake of clarity. (b) Schematic drawing of local coordination structures of Ln ions (red : O atoms, pink : Tb atoms). (c), (d) Crystal packings of dinuclear complexes projecting from the shown directions. Intermolecular short distances between metal centers are depicted as black dotted lines.

Table 5-1. Crystallographic Data Collection and Structural Refinement Information for **4D1pyO**, $[Ln(tta)_3(\mathbf{4D1pyO})]_2$ $2CHCl_3$ (Ln = Gd : **4a**, Tb : **4b**, and Dy : **4c**), and $[Tb(tta)_3(\mathbf{3D1pyO})]_2$ $4CHCl_3$: **4d**

	D1pyO	**4a**	**4b**	**4c**	**4d**
empirical formula	C_{12} H_9 N_3 O_1	$C_{74}H_{44}N_6O_{14}F_{18}$ Cl_6Gd_2	$C_{74}H_{44}N_6O_{14}F_{18}$ $S_6Cl_6Tb_2$	$C_{74}H_{44}N_6O_{14}F_{18}$ $S_6Cl_6Dy_2$	$C_{76}H_{46}N_6O_{14}F_{18}$ $S_6Cl_{12}Tb_2$
formula weight	211.22	2302.74	2306.09	2313.24	2552.00
crystal class	monoclinic	monoclinic	monoclinic	monoclinic	triclinic
space group	$P2_1/c$ (no. 14)	$P2_1/n$ (no. 14)	$P2_1/n$ (no. 14)	$P2_1/n$ (no. 14)	P-1 (no. 2)
a /Å	9.582(4)	14.9824 (14)	14.9961 (9)	14.9627 (13)	12.697(3)
b / Å	11.591(5)	16.7219 (15)	16.7164 (10)	16.7262 (15)	13.700(3)
c / Å	9.149(4)	17.1700 (16)	17.1809 (10)	17.1610 (15)	13.882(3)
α /deg	90				100.957(3)
β /deg	100.212(5)	96.0760(11)	96.1740(7)	96.0290(11)	101.137(3)
γ /deg	90				93.548(3)
V / Å^3	1000.0(8)	4276.7(7)	4281.9(4)	4271.1(7)	2313.8(8)
μ /mm^{-1}	0.94	1.979	2.072	2.177	2.186
Z	4 (1)	2	2	2	1
crystal size /mm	0.50 × 0.20 × 0.20	0.30 × 0.20 × 0.20	0.30 × 0.30 × 0.20	0.30 × 0.30 × 0.20	0.30 × 0.30 × 0.20
D_{calc} /gcm^{-3}	1.403	1.788	1.788	1.799	1.831
F (000)	440.00	2260.00	2264.00	2268.00	1250.00
radiation	MoKα	Mo-Kα	Mo-Kα	Mo-Kα	
T /K	90.0	90.0	90.0	90.0	90.0
no. reflections measured	5322	7935	7976	9246	9588
no. unique reflections	2158	7108	7204	8026	7786
no. parameters	181	636	747	741	604
R_1 [a]	0.0439 ($I > 2.00\sigma(I)$)	0.0509 ($I > 2.00\sigma(I)$)	0.0377 ($I > 2.00\sigma(I)$)	0.0433 ($I > 2.00\sigma(I)$)	0.0715 ($I > 2.00\sigma(I)$)
wR_2 [a]	0.1198	0.1341	0.0987	0.1127	0.1918
GOF	1.032	1.028	1.086	1.037	1.058

[a] $R_1 = \Sigma \, ||F_0|-|F_c|| \, / \, \Sigma \, |F_0|$; $wR_2 = \{\Sigma \, w(F_0^2-F_c^2)^2 \, / \, \Sigma \, w(F_0^2)^2\}^{1/2}$

Table 5-2. Selected bond lengths, bond angles, dihedral angles, and intermolecular Ln^{III}-Ln^{III} distances for $[Ln(tta)_3(\mathbf{4D1pyO})]_2$ $2CHCl_3$ (Ln = Gd : **4a**, Tb : **4b**, and Dy : **4c**), and $[Tb(tta)_3(\mathbf{3D1pyO})]_2$ $4CHCl_3$: **4d**

	4a	**4b**	**4c**	**4d**
		Bond lengths (Å)		
Ln(1)-O(1)	2.411 (3)	2.40616 (9)	2.38526 (13)	2.390 (5)
Ln(1)-O(1)*	2.421 (3)	2.40780 (10)	2.40132 (14)	2.456 (5)
Ln(1)-O(2)	2.318 (3)	2.30492 (10)	2.28988 (14)	2.321 (5)
Ln(1)-O(3)	2.376 (3)	2.37195 (10)	2.36048 (15)	2.357 (5)
Ln(1)-O(4)	2.378 (3)	2.59997 (11)	2.34780 (14)	2.335 (5)
Ln(1)-O(5)	2.382 (3)	2.37168 (10)	2.35075 (13)	2.363 (6)
Ln(1)-O(6)	2.350 (4)	2.30492 (10)	2.31550 (13)	2.331 (5)
Ln(1)-O(7)	2.397 (3)	2.38435 (10)	2.37776 (14)	2.335 (5)
N(1)-O(1)	1.355 (5)	1.34693 (7)	1.35983 (10)	1.365 (8)
Ln(1)-Ln(1)*	4.129	4.111	4.092	4.129
O_{pyO}-O_{pyO}	2.510	2.504	2.483	2.537
		Bond angle (°)		
O_{pyO}-Ln- O_{pyO}	62.58	62.70	62.49	63.10
Ln- O_{pyO}-Ln	117.42	117.30	117.51	116.90
		Dihedral angles (°)		
C(2)C(4)N(1)-C(3)C(6)N(2)	4.44	5.79	3.70	16.21
$LnO_{pyO}Ln$-C(2)N(1)C(4)	89.06	89.76	89.20	89.31
		Intermolecular Ln^{III}-Ln^{III} distances (Å)		
Ln(1)-Ln(1)’	12.05	12.07	12.07	9.733

Table 5-3. The SHAPE analyses for $[Ln(tta)_3(\mathbf{4D1pyO})]_2$ $2CHCl_3$ (Ln = Gd : **4a**, Tb : **4b**, and Dy : **4c**), and $[Tb(tta)_3(\mathbf{3D1pyO})]_2$ $4CHCl_3$: **4d**

	4a	**4b**	**4c**	**4d**
		Bond lengths (Å)		
Square antiprism	0.993	0.931	0.977	**0.697**
Triangular dodecahedron	1.021	1.050	0.991	1.708

Section 6. Powder states X-ray diffraction measurements of **4a**-**4c**

PXRD spectra of **4a**-**4c** were recorded at room temperature. Each compound was firstly washed by small amount of chloroform and then dried under the atmospheric condition for five minutes. Relatively larger size of crystal was pulverized before the measurement in advance.

The recorded spectra of **4a**-**4c** were quite similar to the ones simulated by single crystal X-ray diffraction data at low temperatures (Figure 5-8). Strong diffraction peaks at 7.4° (*h, k ,l* = 0, 1 , 1) and 22° (*h, k ,l* = 2, 3, -2) in simulated pattern were found at 7.3-7.7° and 21-22° in measured spectra, respectively. This result indicated that these complexes almost retained its original crystal lattice even in the ambient conditions. Notably, the elemental analysis revealed that Dy complex sustained 1.5 molecules of chloroform as crystal solvents after the one hour of drying under the reduced pressure.

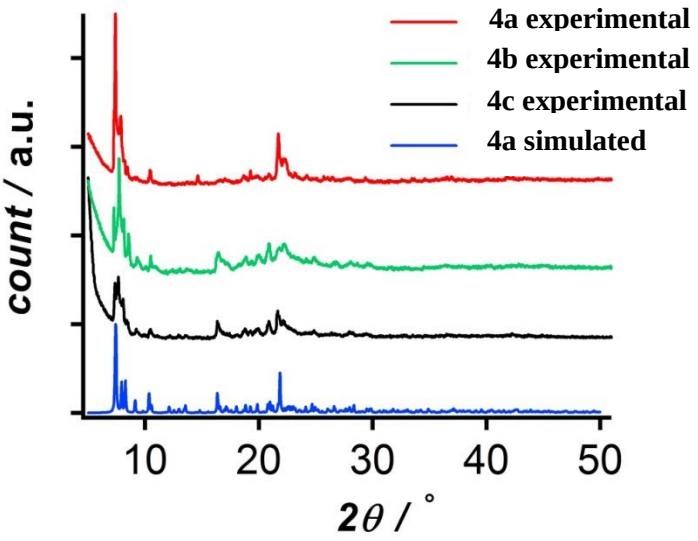

Figure 5-8.

Powder states X-ray diffraction spectra of $[Ln(tta)_3(\mathbf{4D1pyO})]_2$ (Ln = Gd, Tb, and Dy).

Section 7. Magnetic properties of **4a-4d** before irradiation

Magnetic properties measurements of **4a-4d** were performed using the two types of microcrystalline samples of each complex in the SQUID systems. (sample A ; c.a. 10 mg, for the quantitative analysis between 300-1.8 K and sample B ; 1.45 mg , for the photolysis under 30 K)

(1-1) $[Gd(tta)_3(\mathbf{4D1pyO})]_2$ (**4a**) : before irradiation, sample A

Temperature dependence of direct current magnetic property was measured using sample A between 295-1.8 K (10-1 kOe). The $\chi_{mol}T$ value at 295 K was 15.8 $cm^3\,mol^{-1}\,K$. It was corresponding to the expected value of 15.8 $cm^3\,mol^{-1}\,K$ for two Gd ions (g = 2.0, S = 7/2). No obvious change of the $\chi_{mol}T$ values was found during the cooling from 295 K to 30 K, but gradual decrement of the $\chi_{mol}T$ values was found under 30 K until reaching to 12.1 $cm^3\,K\,mol^{-1}$ at 1.9 K (Figure 5-9a). Interdimer magnetic interaction was expected to be very small in this system expected from the single crystal analysis so that the decrease of the $\chi_{mol}T$ values at lower temperature was attributed to the antiferromagnetic coupling between the Gd ions within the dimer. For the quantitative evaluation of the magnetic interaction in this compound, the least-square fitting considering the Heisenberg Hamiltonian ($H = -J_{Gd\text{-}Gd}(S_{Gd1}\,S_{Gd2})$) was performed. The $J_{Gd\text{-}Gd}/k_B$ value was estimated to be -0.082 K and which lay in the same order compared to the ones previously been reported[27a,28b] and the minus sign of $J_{Gd\text{-}Gd}/k_B$ indicated a certain antiferromagnetic interaction in this compound.

(1-2) $[Gd(tta)_3(\mathbf{4D1pyO})]_2$ (**4a**) : before irradiation, sample B

Temperature dependence and field dependence of direct current magnetic properties were measured using sample B between 30-1.9 K (10-1 kOe) and 0-50 kOe (1.9-7.0 K), respectively. The $\chi_{mol}T$ vs. *Temperature* plot was very similar to that of sample A in the corresponding temperature regions.

The $M_{mol}/N\mu_B$, at 1.9 K and at 50 kOe was 13.9. It was almost corresponding to the expected saturation value of 14.0 for the two Gd ions. The plots of reduced field (HT^{-1}) dependency of the magnetization showed the superimposition to the single mater curve (Figure 5-9b). This result indicated the negligible uniaxial magnetic anisotropies for each Gd ion.

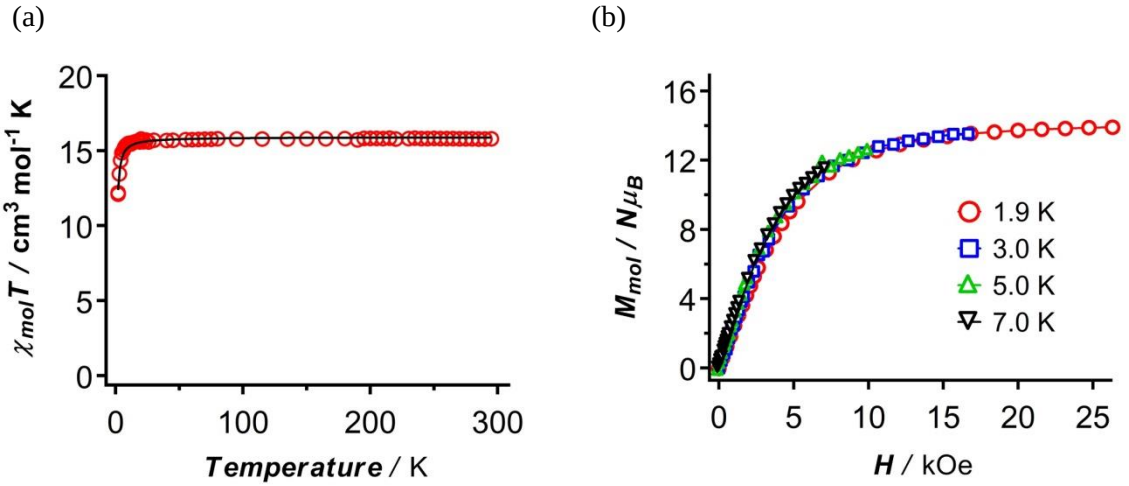

Figure 5-9. The plot of (a) $\chi_{mol}T$ vs. *T*emperature using sample A and (b) M_{mol} vs. *H* using sample B of $[Gd(tta)_3(\mathbf{4D1pyO})]_2$. The black solid line in the left figure represents the best-fit results obtained according to the Gd dimer spin model (see the text).

(2-1) $[Tb(tta)_3(\mathbf{4D1pyO})]_2$ (**4b**) : before irradiation, sample A

Temperature dependence of direct current magnetic properties was measured using sample A between 300-1.8 K (10-1 kOe) (Figure 5-10a). The $\chi_{mol}T$ value at 300 K was 21.8 $cm^3\,mol^{-1}\,K$. It was slightly smaller than the expected value of 23.6 $cm^3\,mol^{-1}\,K$ for two isolated Tb ions (g_J = 3/2, $^7F_6$, S = 3, L = 3). As lowering the temperature the $\chi_{mol}T$ value remained nearly constant around 300-200 K and then gradually decreased to 16.2 $cm^3\,mol^{-1}\,K$ at 1.9 K. This decrement was attributed to both the thermal depopulation of low-lying crystal field states and the antiferromagnetic interaction between two Tb ions as observed in Gd complex.

(2-2) $[Tb(tta)_3(\mathbf{4D1pyO})]_2$ (**4b**) : before irradiation, sample B

Temperature dependence and field dependence of direct current magnetic properties were measured using sample B between 30-1.9 K (10-1 kOe) and 0-50 kOe (1.9-7.0 K), respectively. The $\chi_{mol}T$ vs. *Temperature* plot was very similar to that of sample A in the corresponding temperature regions.

The $M_{mol}/N\mu_B$, at 1.9 K and at 50 kOe was 8.2. It was smaller than the expected saturation value of 19.4 for the two Tb ions. The plots of reduced field (HT^{-1}) dependency of the magnetization did not show the superimposition onto the single mater curve, confirming the presence of non-negligible uniaxial magnetic anisotropies and/or low-lying excited states, though the magnetic hysteresis was not observed above 1.9 K at the field dependence of the magnetization plots(Figure 5-10b).

In the alternative current magnetic properties measurements, no frequency and temperature dependent peaks were observed between 8.0-2.0 K under zero external DC field (Figure 5-10c,d). This result indicated that $[Tb(tta)_3(\mathbf{4D1pyO})]_2$ did not behave as a SMM probably due to the fast quantum tunneling relaxing rate and /or the small magnetic anisotropy of each Tb ion.

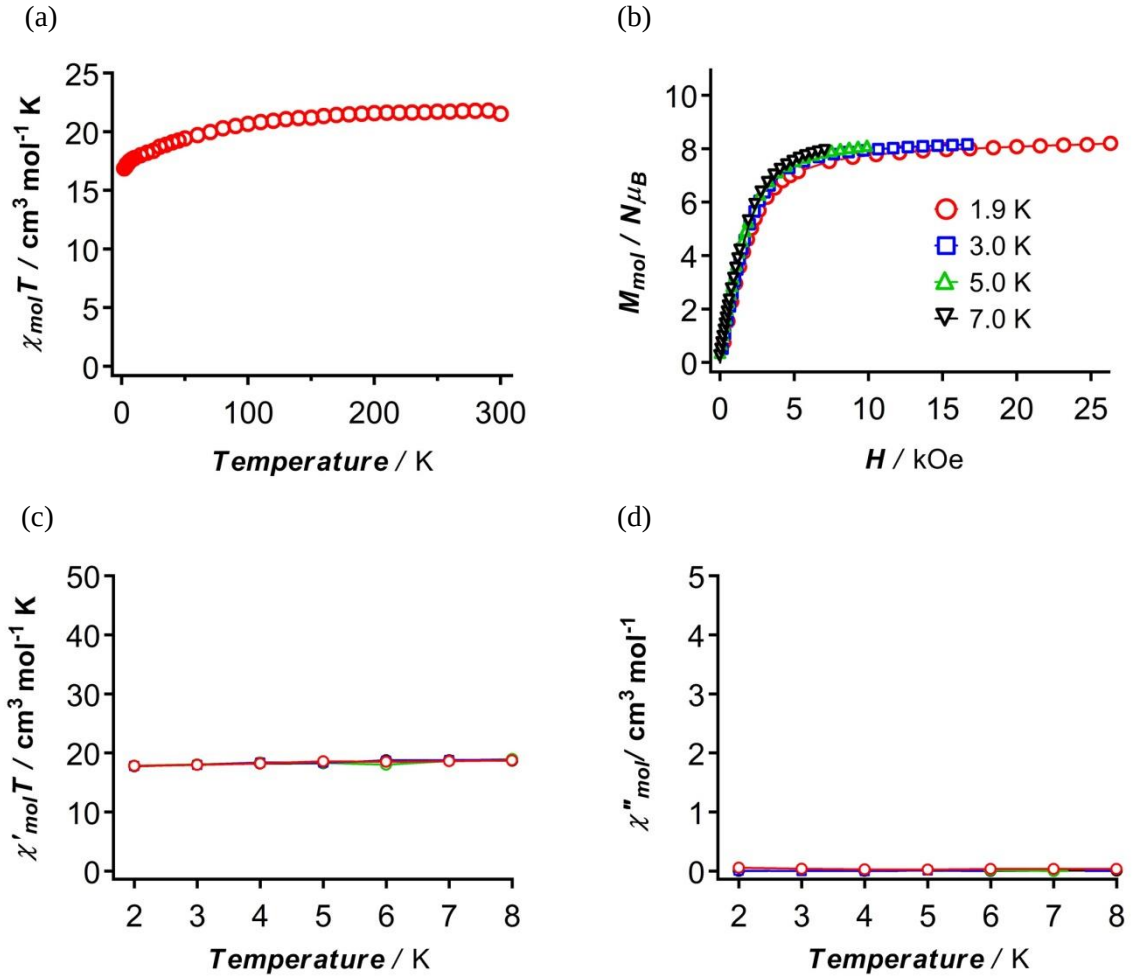

Figure 5-10. The plot of (a) $\chi_{mol}T$ vs. *T*emperature, (b) M_{mol} vs. H (c) $\chi'_{mol}T$ vs. *T*emperature, and (d) χ''_{mol} vs. *T*emperature of [Tb(tta)$_3$(**4D1pyO**)]$_2$.

(3-1) $[Dy(tta)_3(\mathbf{4D1pyO})]_2$ (**4c**) : before irradiation, sample A

Temperature dependence of direct current magnetic properties was measured using sample A between 300-1.9 K (10-1 kOe) (Figure 5-11a). The $\chi_{mol}T$ value at 300 K was 27.3 $cm^3\,mol^{-1}\,K$. It was slightly smaller than the expected value of 28.3 $cm^3\,mol^{-1}\,K$ for two isolated Dy ions (g_J = 4/3, $^6H_{15/2}$, S = 5/2, L = 5). As lowering the temperature the $\chi_{mol}T$ value remained nearly constant around 300-50 K and then gradually decreased to 12.8 $cm^3\,mol^{-1}\,K$ at 1.9 K. This decrement was attributed to both the thermal depopulation of low-lying crystal field states and the antiferromagnetic interaction between 4f spins of two Dy ions.

(3-2) $[Dy(tta)_3(\mathbf{4D1pyO})]_2$ (**4c**) : before irradiation, sample B

Temperature dependence and field dependence of direct current magnetic properties were measured using sample B between 30-1.9 K (10-1 kOe) and 0-50 kOe (1.9-7.0 K), respectively. The $\chi_{mol}T$ vs. *Temperature* plot was very similar to that of sample A in the corresponding temperature regions.

The $M_{mol}/N\mu_B$, at 1.9 K and at 50 kOe was 9.3. It was smaller than the expected saturation value of 21.3 for the two Dy ions. The plots of reduced field (HT^{-1}) dependency of the magnetization did not show the superimposition onto the single mater curve, confirming the presence of non-negligible uniaxial magnetic anisotropies and/or low-lying excited states, though the magnetic hysteresis was not observed above 1.9 K at the field dependence of the magnetization plots(Figure 5-11b).

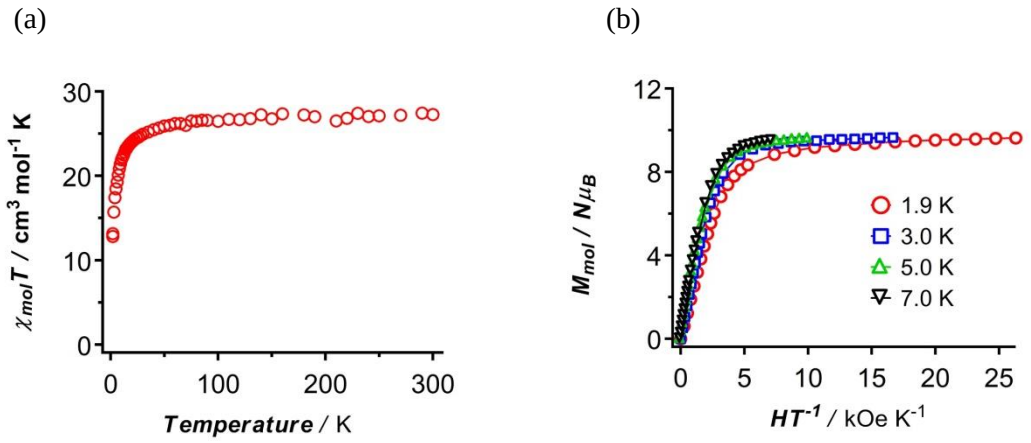

Figure 5-11. The plot of (a) $\chi_{mol}T$ vs. *T*emperature, and (b) M_{mol} vs. H of $Dy(tta)_3(\mathbf{4D1pyO})]_2$.

The temperature and frequency dependence of the χ'_{mol} and the χ''_{mol} signals in AC magnetic properties were found between the temperature ranges of 20-1.8 K under zero external DC field(Figure 5-12). The activation barrier for the spin re-orientation, U_{eff}/k_B, and the pre-exponential factor, τ_0, were estimated to be 97.8 K and 5.8 x 10^{-8} sec., respectively from the $\chi''_{mol}T$ vs. *Temperature* plot. The extended Debye's fitting results gave the U_{eff}/k_B value of 102 K and the τ_0 value of 5.7 x 10^{-8} sec., from the χ'_{mol} vs. ν plot and the $\chi''_{mol}T$ vs. ν plot. Notably, the obtained U_{eff}/k_B value was similar to that previously reported[28]. The α values extracted by the extended Debye's equation and by the generalized Debye's equation in Cole-Cole plot ranged from 0.15-0.29, suggesting relatively narrow distribution of spin relaxation. The extracted magnetic parameters are summarized in Table 5-4 to 5-6.

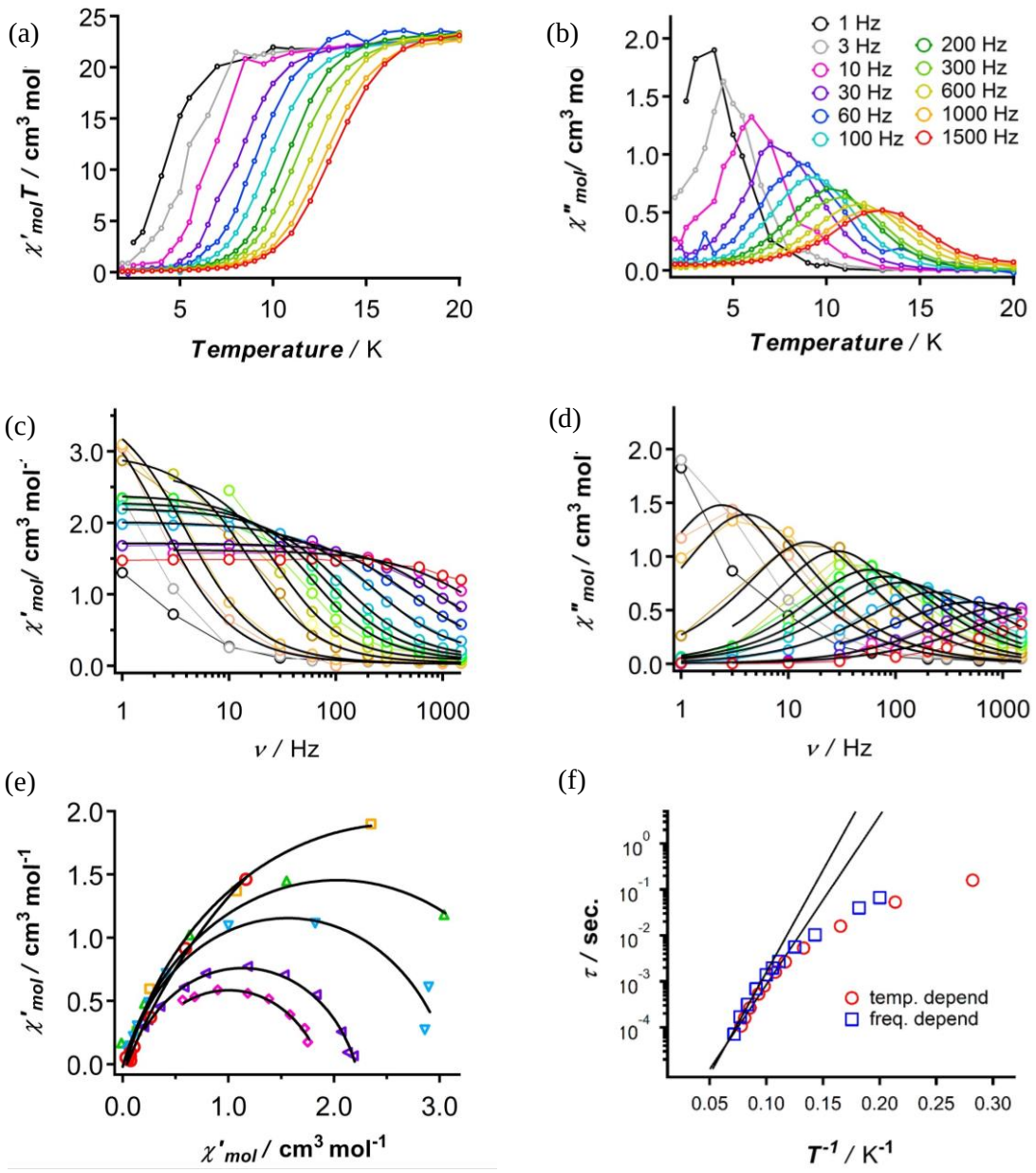

Figure 5-12. The plot of (a) $\chi'_{mol}T$ vs. *T*emperature, (b) χ''_{mol} vs. *T*emperature, (c) $\chi'_{mol}T$ vs. ν, (d) χ''_{mol} vs. ν, (e) Cole-Cole diagram, and (f) Arrhenius law of $[Dy(tta)_3(\mathbf{4D1pyO})]_2$. The black bold lines in (c), and (d) show the fitting lines obtained from the extended Debye's model. In (e), black lines represents the best-fit results of generalized Debye's equation. The solid lines in (f) indicate the best fit result extracted from the Arrhenius law.

Table 5-4.

The extracted peak top temperature for each frequency in the plot of χ''_{mol} vs. *T*emperature.

Frequency (Hz)	**1**	**3**	**10**	**30**	**60**	**100**
Temp.(K)	3.546	4.678	6.047	7.525	8.570	9.268
T^{-1} (K^{-1})	0.2820	0.2138	0.1654	0.1329	0.1167	0.1079
τ (sec.)	0.159	0.0531	0.0159	0.00531	0.00265	0.00159

Frequency (Hz)	**200**	**300**	**600**	**1000**	**1500**
Temp.(K)	10.20	10.74	11.69	12.37	12.87
T^{-1} (K^{-1})	0.0984	0.0931	0.0855	0.0808	0.0777
τ (sec.)	0.00796	0.000531	0.000265	0.000159	0.000107

Table 5-5.

The extracted parameters for selected temperatures by the extended Debye's fitting in the plot of χ'_{mol} vs. ν, and χ''_{mol} vs. ν.

***Temp.*(K)**	**5.0**	**5.5**	**7.0**	**8.0**	**9.0**	**9.5**
χ_S (cm^3mol^{-1})	0.0228	0.0714	0.0203	0.0333	0.0623	0.0773
χ_T (cm^3mol^{-1})	3.963	2.727	3.733	2.972	2.394	2.291
τ (sec.)	0.06662	0.039736	0.010324	0.005608	0.00274	0.001958
α	0.1802	0.1477	0.1808	0.1627	0.1794	0.1929

***Temp.*(K)**	**10.0**	**11.0**	**12.0**	**13.0**	**14.0**
χ_S (cm^3mol^{-1})	0.0765	0.111	0.101	0.245	0.111
χ_T (cm^3mol^{-1})	2.208	2.016	1.897	1.717	1.623
τ (sec.)	0.001394	0.000688	0.000316	0.000169	0.0000707
α	0.2134	0.2223	0.2727	0.2142	0.2659

Table 5-6.

The extracted parameters for selected temperatures by the generalized Debye's fitting in the plot of χ''_{mol} vs. χ'_{mol} (Cole-Cole plot).

***Temp.*(K)**	**2.5**	**4.0**	**5.0**	**7.0**	**10.0**	**12.0**
χ_S (cm^3mol^{-1})	0.04067	0.03121	0.007167	0.03047	0.06793	0.1301
χ_T (cm^3mol^{-1})	8.364	5.202	4.056	3.092	2.204	1.876
α	0.2871	0.1940	0.2068	0.1772	0.2130	0.2489

(4-1) $[Tb(tta)_3(\mathbf{3D1pyO})]_2$ (**4d**): before irradiation, sample B

Temperature dependence and field dependence of direct current magnetic properties were measured using sample B between 30-1.9 K (10-1 kOe) and 0-50 kOe (1.9-7.0 K), respectively. The $\chi_{mol}T$ vs. *Temperature* plot and the $M_{mol}/N\mu_B$ plot were very similar to that of $[Tb(tta)_3(\mathbf{4D1pyO})]_2$ (Figure 5-13a,b).

In the alternative current magnetic properties measurements, no frequency and temperature dependent peaks were observed between 8.0-1.9 K under zero external DC field similar to the case of $[Tb(tta)_3(\mathbf{4D1pyO})]_2$ (Figure 5-12c,d).

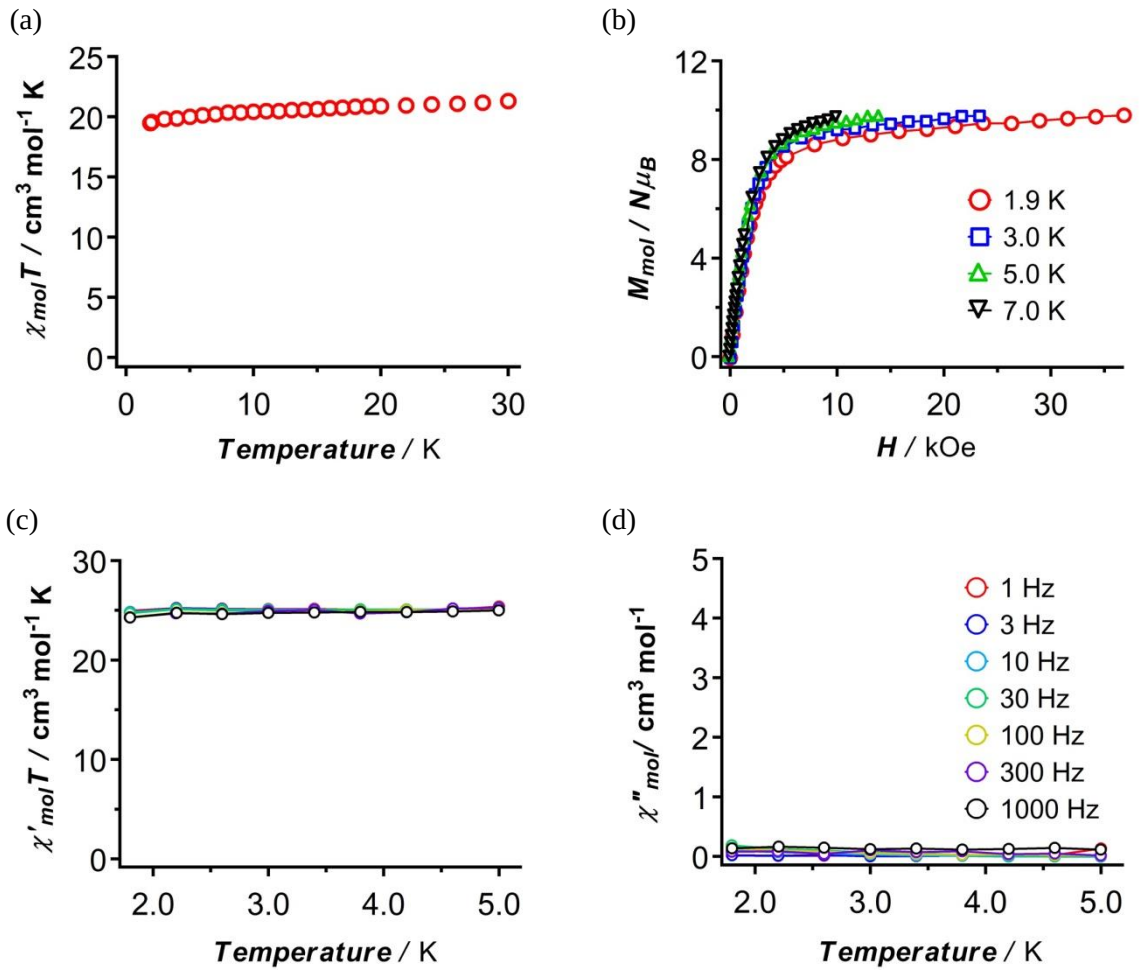

Figure 5-13. The plot of (a) $\chi_{mol}T$ vs. *T*emperature, (b) M_{mol} vs. H (c) $\chi'_{mol}T$ vs. *T*emperature, and (d) χ''_{mol} vs. *T*emperature of $[Tb(tta)_3(\mathbf{3D1pyO})]_2$.

Section 7. Magnetic properties of **4a**-**4d** after irradiation

Photo-irradiation of **4a**-**4d**

Then, photo-irradiation for these complexes was performed in the SQUID systems using sample B. The detailed procedures and conditions for the photolysis of diazo component were summarized in the experimental sections. Particular in these dinuclear complexes, "photolysis method A" was used for the production of carbenes.

On the photolysis, the $\chi_{mol}T$ values steeply increased and reached to the saturation after irradiation 1-2 days (Figure 5-14). The yields of photolysis of **4a**-**4d** were determined to be ca. 72-91 % by the decrements of the IR absorption bands at 2049 cm^{-1} for **4a**-**4c** and 2053 cm^{-1} for **4d** originated from the diazo components in these complexes after SQUID measurements.

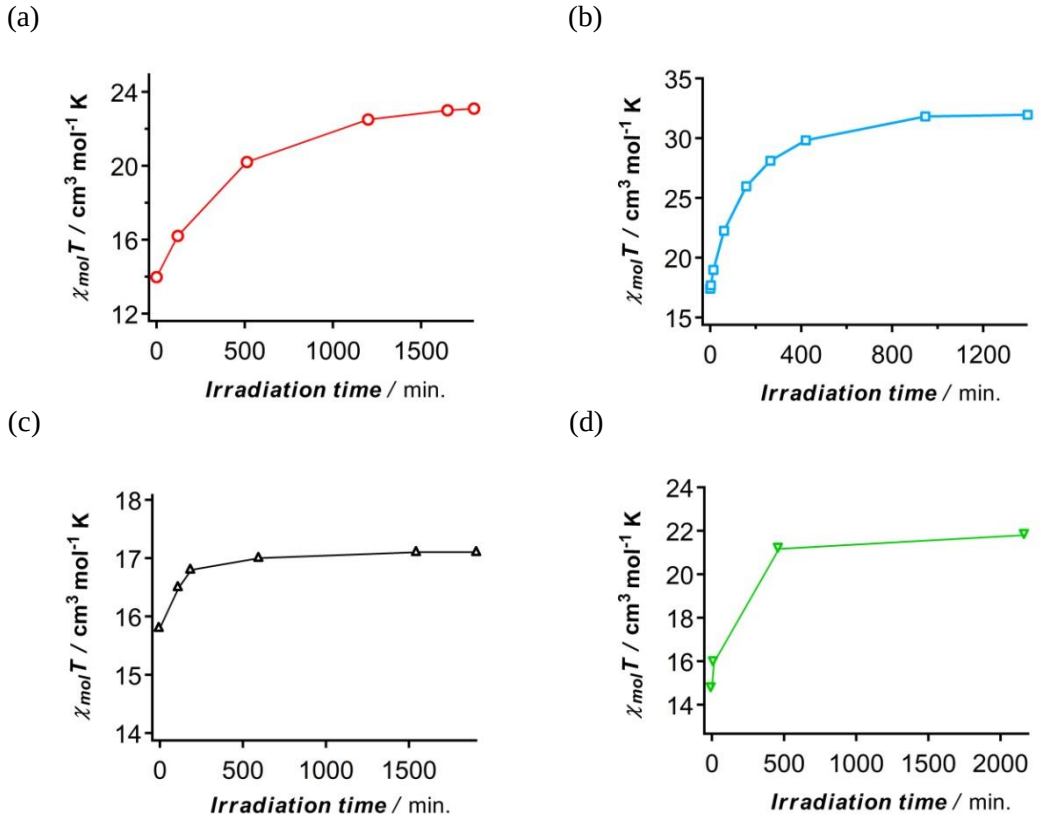

Figure 5-14.

Plots of $\chi_{mol}T$ vs. Irradiation time for (a)[Gd(tta)$_3$(**4D1pyO**)]$_2$, (b)[Tb(tta)$_3$(**4D1pyO**)]$_2$, (c)[Gd(tta)$_3$(**4D1pyO**)]$_2$, and (d)[Tb(tta)$_3$(**3D1pyO**)]$_2$

(1-1) $[Gd(tta)_3(\mathbf{4C1pyO})]_2$ (**4a'**): after irradiation, sample B

The $\chi_{mol}T$ value at 30 K was 18.7 $cm^3\,mol^{-1}\,K$. It was slightly larger than the value of 17.8 expected for two isolated Gd ions (g = 2.0, S = 7/2) and two isolated triplet carbenes (g = 2.0, S = 2/2). On cooling temperature, the $\chi_{mol}T$ value gradually increased and reached to 30.1 $cm^3\,mol^{-1}\,K$ at 1.9 K (Figure 5-15a). This increment of $\chi_{mol}T$ product clearly demonstrated the non-negligible ferromagnetic interactions between 4f spins of Gd ions and 2p spins of triplet carbenes within the dinuclear complex. Surprisingly, the $\chi_{mol}T$ product showed almost the same value between the temperature ranges of 100-150 K (17.1-17.2 $cm^3\,mol^{-1}\,K$). This result implied the relatively high thermal stability of **4C1pyO** in this spin system. Continuous heating induced the rapid decrement of $\chi_{mol}T$ value around 150-200 K , indicating the decomposition of triplet carbenes.

For the evaluation of $J_{car\text{-}car}/k_B$ and $J_{Gd\text{-}car}/k_B$, which were the exchange coupling constants between the carbenes with the O-O through-space interaction and between the carbene and the Gd ion with through-bond interaction, respectively, a rhombic four-spin system; $H = -J_{Gd\text{-}Gd}\,(S_{Gd1}\,S_{Gd2}) - J_{car\text{-}car}\,(S_{car\,1}\,S_{car\,2}) - J_{Gd\text{-}car}\,(S_{Gd1}\,S_{car1} + S_{Gd1}\,S_{car2} + S_{Gd2}\,S_{car1} + S_{Gd2}\,S_{car2})$, was applied to this spin system. To estimate these parameters, *FIT-MART* program[31] was applied to the data in the range of 2-150 K. The best fit gave $J_{Gd\text{-}Gd}/k_B$ = -0.082 K (fixed in order to avoid over-parameterization), $J_{carbene\text{-}carbene}/k_B$ = -8.9 K, and $J_{Gd\text{-}carbene}/k_B$ = 2.4 K, respectively. The estimsted $J_{Gd\text{-}carbene}$ value was somehow small that might be due to the relatively long Gd-O_{D1pyO} bond length and/or elongated N-O bonds of the pyO moieties, though the plus sign of $J_{Gd\text{-}car}/k_B$ strongly supported the ferromagnetic interaction between 4f and 2p spins.

The $M_{mol}/N\mu_B$, at 1.9 K and at 50 kOe was 16.0. It was corresponding to the expected saturation value of 16.0 for the two Gd ions and two triplet carbenes. The plots of reduced field (HT^{-1}) dependency of the magnetization showed the superimposition to the single master curve, indicating the negligible uniaxial magnetic anisotropies for Gd ions (Figure 5-15b).

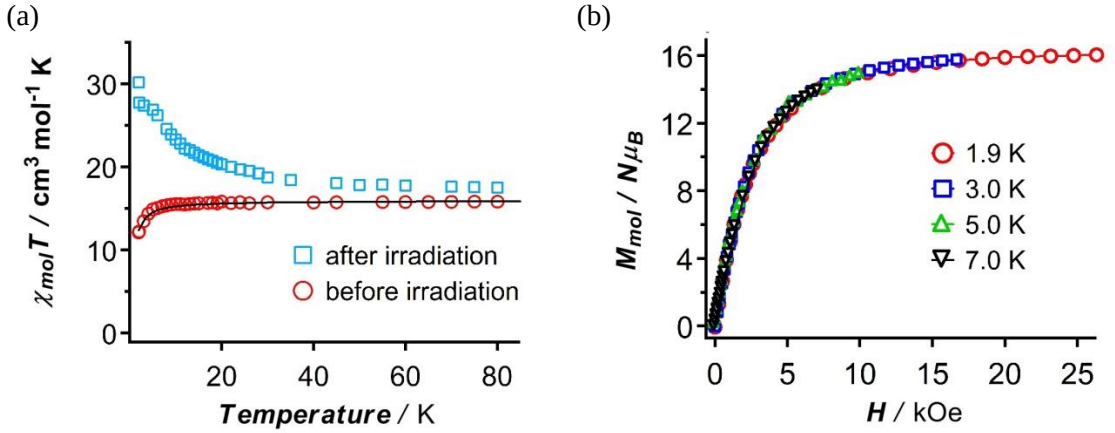

Figure 5-15. The plot of (a) $\chi_{mol}T$ vs. *T*emperature using sample A and (b) M_{mol} vs. H using sample B of $[Gd(tta)_3(\mathbf{4C1pyO})]_2$ (**4a'**). The black solid line in the left figure represents the best-fit results obtained according to the Heisenberg spin Hamiltonian before irradiation (see the text).

(2-1) $[Tb(tta)_3(\mathbf{4D1pyO})]_2$ (**4b'**): after irradiation, sample B

The $\chi_{mol}T$ value at 30 K was 23.9 $cm^3\ mol^{-1}$ K. It was slightly larger than the value of 20.2 calculated by a spin-only equation of two isolated triplet carbenes (g = 2.0, S = 2/2) and two Tb ions (before irradiation, the $\chi_{mol}T$ value at 30 K for two Tb ions was 18.2). On cooling, the $\chi_{mol}T$ value gradually increased and reached the maximum value of 41.6 $cm^3\ mol^{-1}$ K at 4.0 K, and then decreased below 4.0 K. This increment of $\chi_{mol}T$ product clearly indicated a certain ferromagnetic interactions between 4f spins of Tb ions and 2p spins of triplet carbenes within the dinuclear complex, and the decrement below 4.0 K might suggest the antiferromagnetic interactions and/or the thermal depopulation of low-lying crystal field states (Figure 5-16a).

The $M_{mol}/N\mu_B$, at 1.9 K and at 50 kOe was 10.4. It was smaller than the expected saturation value of 23.4 for the two Tb ions and two triplet carbenes, but was larger than that of before irradiation ($8.2\mu_B$). The plots of reduced field (HT^{-1}) dependency of the magnetization did not show the superimposition to the single master curve, indicating the presence of uniaxial magnetic anisotropies of Tb ions (Figure 5-16b).

As mentioned above, before irradiation, no frequency and temperature dependent peaks were observed between 8.0-2.0 K under zero external DC field in the alternative current magnetic properties measurements. On the other hand, alternative current magnetic properties after irradiation clearly depended on both frequency and temperature between the temperature ranges of 6.0-1.8 K under zero external DC field (Figure 5-17). In the $\chi'_{mol}T$ vs. *Temperature* plot, the $\chi'_{mol}T$ values gradually increased as cooling the temperature below 6.0 K, indicating that the $\chi'_{mol}T$ values in this temperature range were still affected by the population of the thermally excited state resulting from the ferromagnetic interaction of the carbene and Tb ion. In the χ''_{mol} vs. *Temperature* plot the peak top for each frequency was extracted according to the Gaussian distribution, and the obtained relaxation time, τ, and the temperature (T^{-1}) was plotted in accordance with the Arrhenius law (Figure 5-17). The activation barrier for the spin re-orientation, U_{eff}/k_B, and the pre-exponential factor, τ_0, was estimated to be 32.2 K and 3.5 x 10^{-9} sec., respectively. This magnificent result (observation of SMM behaviour in dinuclear Tb complex) clearly supported the crucial role of organic spin for the construction of Ln based SMMs, particular might be in the depressing of spin relaxation pathway due to the quantum tunnelling magnetization (QTM). Similarly, the relaxation time, τ, and the distribution factor of the spin relaxation, α, was extracted in both the χ''_{mol} vs. ν plot and the χ''_{mol} vs. ν plot using the extended Debye's model. The obtained values of χ_s, χ_T, τ, and α were summarized in Table 5-8. The U_{eff}/k_B, and τ_0, was estimated to be 30.4 K and 9.3 x 10^{-9} sec., respectively and were similar to that extracted from χ''_{mol} vs. *Temperature* plot. The α values, 0.16-0.50 between the temperature ranges of 4.0-1.8 K suggested the wide distribution of spin relaxation, especially at the extremely low temperature. In fact, at high frequencies over 300 Hz the

second increase of χ''_{mol} signal was observed below 2.1 K in the χ''_{mol} vs. *Temperature* plot, though the presence of two species of relaxation components were unclear in this stage. The second relaxation component might be attributed to the another spin relaxation pathway of carbene-Tb systems in the exited state and/or the intrinsic relaxation mechanism of Tb ion because of the weak interaction with the carbene. Then, 1.5 kOe of external DC filed was applied in the AC measurement, but no obvious change was found (U_{eff}/k_B, and τ_0, was estimated to be 30.8 K and 5.9 x 10^{-9} sec., respectively from the χ''_{mol} vs. *T* plot) compared to the absence case, indicating that ferromagnetic interaction between 4f-2p spins certainly affected to the depressing of QTM. The Cole-Cole plot at the selected temperature was fitted by the generalized Debye's model (Figure5-17e), and the obtained parameters were noted in Table 5-7 to 5-9.

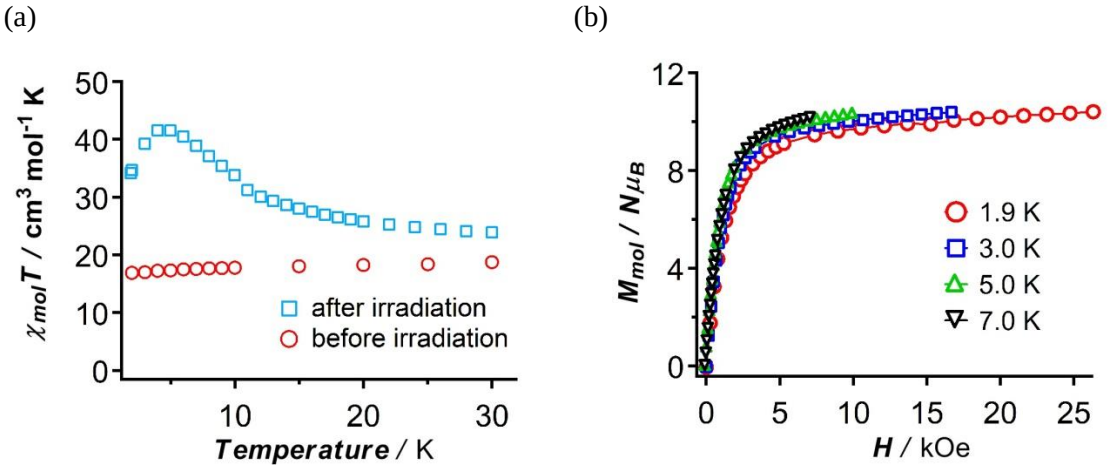

Figure 5-16. The plot of (a) $\chi_{mol}T$ vs. *T*emperature and (b) M_{mol} vs. *H* of [Tb(tta)$_3$(**4C1pyO**)]$_2$ (**4b'**). The solid lines in the right figure represent the guides for eyes.

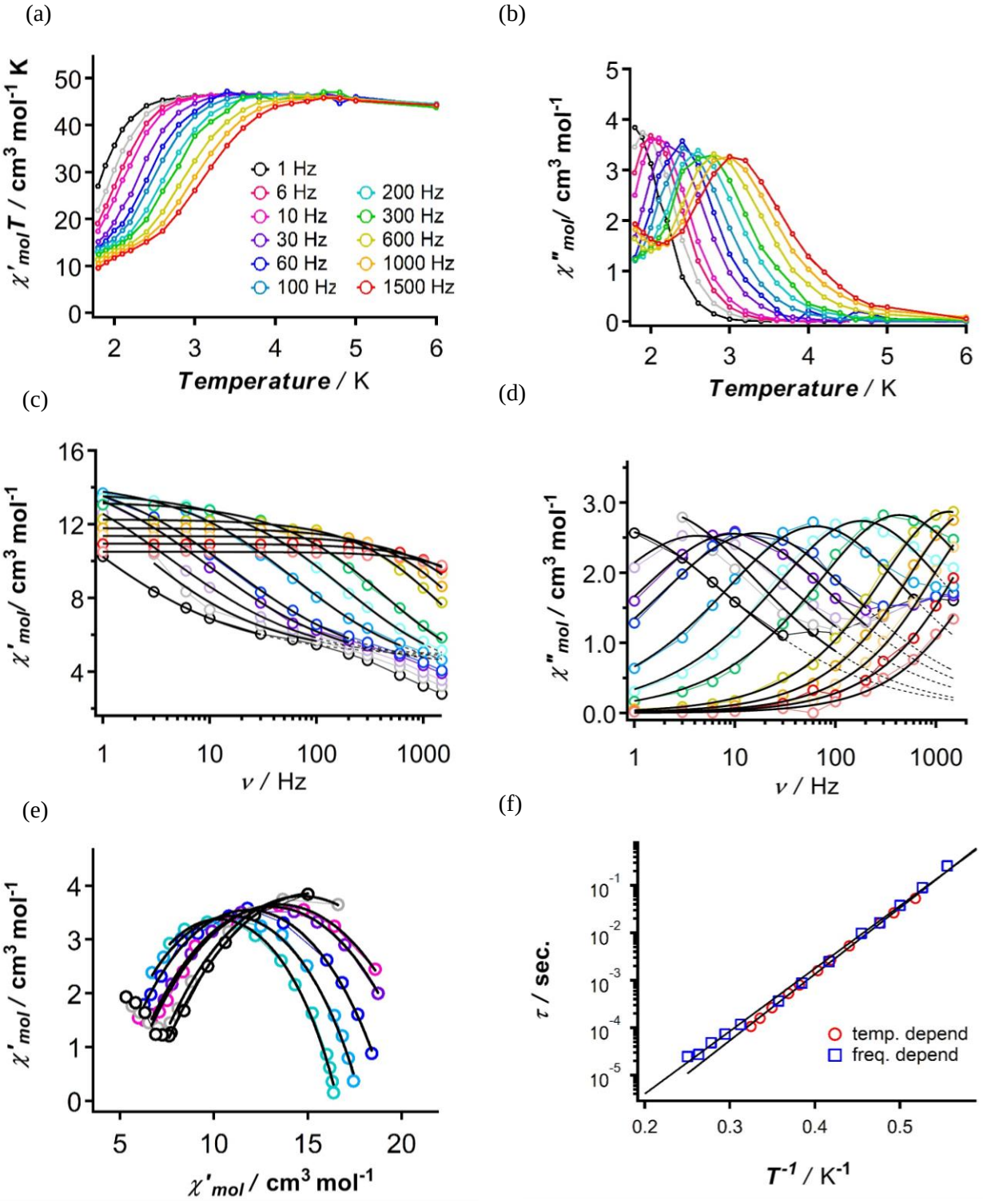

Figure 5-17. The plot of (a) $\chi'_{mol}T$ vs. *T*emperature, (b) χ''_{mol} vs. *T*emperature, (c) $\chi'_{mol}T$ vs. ν, (d) χ''_{mol} vs. ν, (e) Cole-Cole diagram, and (f) Arrhenius law of $[Tb(tta)_3(\mathbf{4C1pyO})]_2$ (**4b'**). The black bold lines in (c), and (d) show the fitting lines obtained from the extended Debye's model. In (e), black lines represents the best-fit results of generalized Debye's equation. The solid lines in (f) indicate the best fit result extracted from the Arrhenius law.

Table 5-7.

The extracted peak top temperature for each frequency in the plot of χ''_{mol} vs. *T*emperature.

Frequency (Hz)	**3**	**6**	**10**	**30**	**60**	**100**
Temp.(K)	1.93	2.03	2.1	2.27	2.39	2.48
T^{-1} (K^{-1})	0.518135	0.492611	0.47619	0.440529	0.41841	0.403226
τ (sec.)	0.053079	0.026539	0.015924	0.005308	0.002654	0.001592

Frequency (Hz)	**200**	**300**	**600**	**1000**	**1500**
Temp.(K)	2.62	2.71	2.86	2.98	3.08
T^{-1} (K^{-1})	0.381679	0.369004	0.34965	0.33557	0.324675
τ (sec.)	0.000796	0.000530	0.000265	0.000159	0.000106

Table 5-8.

The extracted parameters for selected temperatures by the extended Debye's fitting in the plot of χ'_{mol} vs. ν, and χ''_{mol} vs. ν.

***Temp.*(K)**	**1.8**	**1.9**	**2.0**	**2.1**	**2.2**	**2.4**	**2.6**
χ_S (cm^3mol^{-1})	4.7153	4.78687	4.39194	4.17644	4.08357	3.64698	3.29364
χ_T (cm^3mol^{-1})	17.4995	17.1715	15.8956	15.2997	15.0021	14.334	13.7767
τ (sec.)	0.257108	0.090109	0.037866	0.016255	0.009789	0.002478	0.000879
α	0.504361	0.448258	0.472878	0.451552	0.44081	0.411417	0.386945

***Temp.*(K)**	**2.8**	**3.2**	**3.4**	**3.6**	**3.8**	**4.0**
χ_S (cm^3mol^{-1})	3.00268	3.46688	3.58046	3.78817	2.99412	4.45017
χ_T (cm^3mol^{-1})	13.2457	12.27	11.7888	11.3659	10.9476	10.5091
τ (sec.)	0.000368	0.000119	0.0000737	0.0000488	0.0000275	0.0000248
α	0.358451	0.264284	0.225182	0.195324	0.195845	0.158905

Table 5-9.

The extracted parameters for selected temperatures by the generalized Debye's fitting in the plot of χ''_{mol} vs. χ'_{mol} (Cole-Cole plot).

***Temp.*(K)**	**1.8**	**1.9**	**2.1**	**2.2**	**2.4**	**2.6**	**2.8**
χ_S (cm^3mol^{-1})	6.3393	6.10724	5.13416	5.01863	4.40856	4.03885	3.9397
χ_T (cm^3mol^{-1})	24.3356	23.2642	21.8052	21.1585	19.2825	17.8578	16.5896
α	0.48456	0.468714	0.474573	0.465427	0.433509	0.412628	0.376136

(3-1) $[Dy(tta)_3(\mathbf{4D1pyO})]_2$ (**4c'**): after irradiation, sample B

The $\chi_{mol}T$ value at 30 K was 29.7 $cm^3\,mol^{-1}\,K$. It was slightly larger than the value of 26.9 calculated by a spin-only equation of two isolated triplet carbenes (g = 2.0, S = 2/2) and two Dy ions (before irradiation, the $\chi_{mol}T$ value at 30 K for two Dy ions was 24.9) indicating the presence of ferromagnetic interaction. On cooling, the $\chi_{mol}T$ value gradually increased and reached the maximum value of 38.3 $cm^3\,mol^{-1}\,K$ at 4.0 K, and then decreased below 4.0 K (Figure 5-18a). This increment of $\chi_{mol}T$ product also indicated the ferromagnetic interaction between 4f spins of Dy ions and 2p spins of triplet carbenes within the dinuclear complex, and the decrement below 4.0 K might suggest the antiferromagnetic interactions and/or the thermal depopulation of low-lying crystal field states.

The $M_{mol}/N\mu_B$, at 1.9 K and at 50 kOe was 11.0. It was smaller than the expected saturation value of 25.3 for the two Dy ions and two triplet carbenes, but was larger than that of before irradiation ($9.6\mu_B$). The plots of reduced field (HT^{-1}) dependency of the magnetization did not show the superimposition to the single master curve, indicating the presence of uniaxial magnetic anisotropies of Dy ions (Figure 5-18b).

The temperature and frequency dependence of the χ'_{mol} and the χ''_{mol} signals in AC magnetic properties were found between the temperature ranges of 10-1.8 K under zero external DC field (Figure 5-18c,d). The increment of $\chi'_{mol}T$ value below 10 K represented the effect of the population of the thermally excited state resulting from the ferromagnetic interaction of the carbene and Dy ion. The activation barrier for the spin re-orientation, U_{eff}/k_B, and the pre-exponential factor, τ_0, were estimated to be 29.5 K and 2.9 x 10^{-8} sec., respectively from the χ''_{mol} vs. T plot. The extended Debye's fitting results gave the U_{eff}/k_B value of 31.3 K and the τ_0 value of 2.0 x 10^{-8} sec., from the χ''_{mol} vs. ν plot and the χ''_{mol} vs. ν plot. Notably, the obtained U_{eff}/k_B value was much smaller than that estimated before irradiation (97.8 K). This decrease of the effective activation barrier implied that magnetic exchange interaction between 4f and 2p spins might reduce the single ion anisotropy of 4f ion as described in the case of 3d-2p heterospin SMMs, previously. At the same time, weak magnetic coupling between the 4f and 2p spins might enhance the magnetic relaxation through the thermally exited state lying nearly on the spin ground state. The α values extracted by the extended Debye's equation and by the generalized Debye's equation in Cole-Cole plot ranged from 0.31-0.40, suggesting relatively wide distribution of spin relaxation. The extracted magnetic parameters are summarized in Table 5-10 to 5-12.

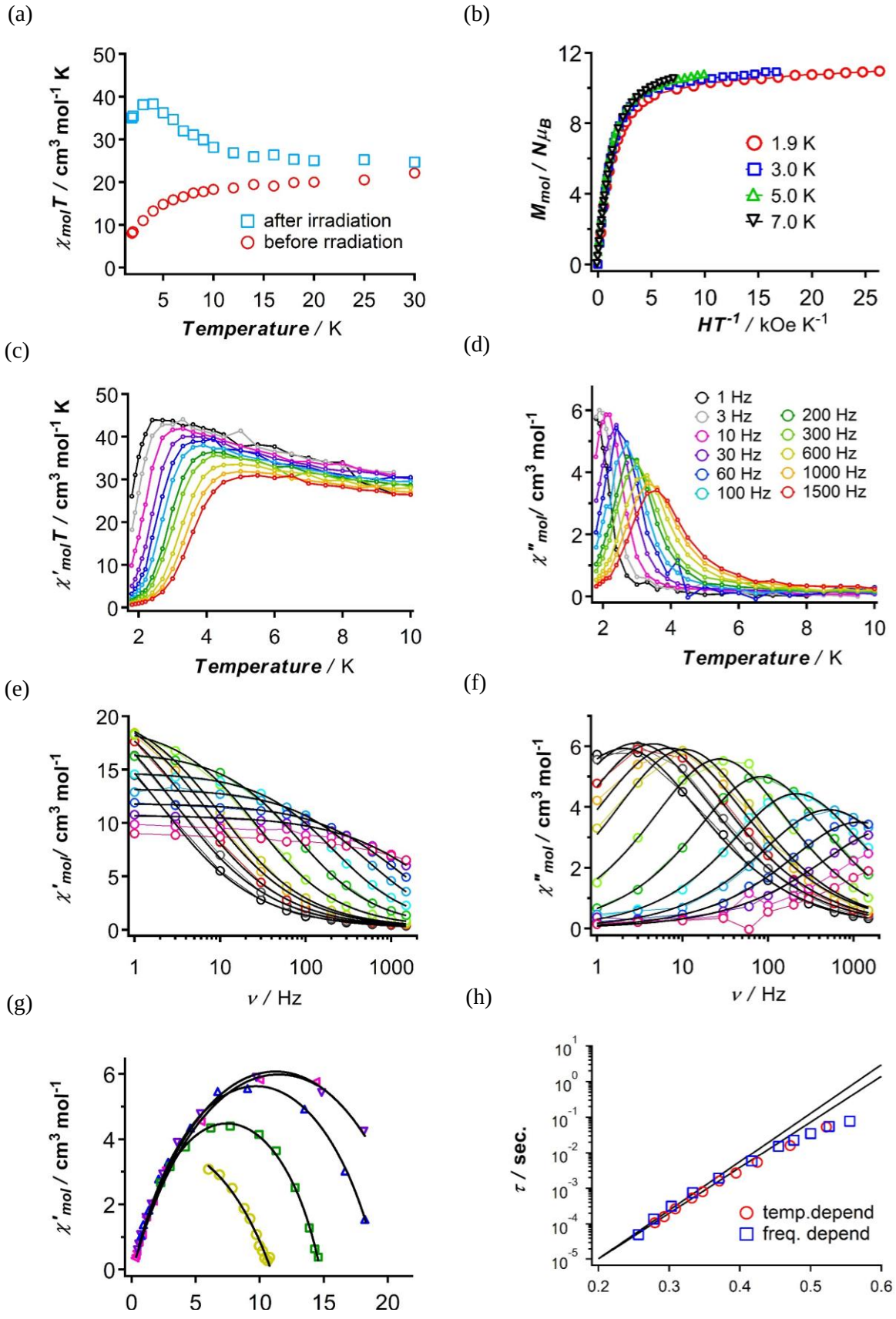

Figure 5-18. The plot of (a) $\chi_{mol}T$ vs. *T*emperature and (b) M_{mol} vs. H , (c) $\chi'_{mol}T$ vs. *T*emperature, (d) χ''_{mol} vs. *T*emperature, (e) $\chi'_{mol}T$ vs. ν, (f) χ''_{mol} vs. ν, (g) Cole-Cole diagram, and (h) Arrhenius law of $[Dy(tta)_3(\mathbf{4C1pyO})]_2$ (**4c'**). The black bold lines in (c), and (d) show the fitting lines obtained from the extended Debye's model. In (e), black lines represents the best-fit results of generalized Debye's equation. The solid lines in (f) indicate the best fit result extracted from the Arrhenius law.

Table 5-10.

The extracted peak top temperature for each frequency in the plot of χ''_{mol} vs. *T*emperature.

Frequency (Hz)	**3**	**10**	**30**	**60**	**100**
Temp.(K)	1.915	2.123	2.356	2.533	2.695
T^{-1} (K^{-1})	0.522193	0.471032	0.424448	0.394789	0.371058
τ (sec.)	0.053076	0.015926	0.005309	0.002659	0.001594

Frequency (Hz)	**200**	**300**	**600**	**1000**	**1500**
Temp.(K)	2.878	3.01	3.24	3.416	3.575
T^{-1} (K^{-1})	0.347464	0.332226	0.308642	0.29274	0.27972
	0.000792	0.000538	0.000264	0.000152	0.000107

Table 5-11.

The extracted parameters for selected temperatures by the extended Debye's fitting in the plot of χ'_{mol} vs. ν, and χ''_{mol} vs. ν.

***Temp.*(K)**	**1.8**	**1.9**	**2.0**	**2.1**	**2.2**	**2.4**
χ_S (cm^3mol^{-1})	0.03668	-0.02474	0.01572	-0.04795	0.08806	0.09676
χ_T (cm^3mol^{-1})	23.10	23.88	23.06	22.53	21.28	19.32
τ (sec.)	0.077287	0.055216	0.034749	0.022632	0.015231	0.005848
α	0.3955	0.3991	0.3817	0.3833	0.3535	0.3303

***Temp.*(K)**	**2.7**	**3.0**	**3.3**	**3.6**	**3.9**
χ_S (cm^3mol^{-1})	0.14887	0.13732	-0.16243	-0.63958	-2.28312
χ_T (cm^3mol^{-1})	16.71	14.76	13.24	11.83	10.72
τ (sec.)	0.001917	0.000745	0.000311	0.000137	0.0000500
α	0.3085	0.3053	0.3273	0.3485	0.3977

Table 5-12.

The extracted parameters for selected temperatures by the generalized Debye's fitting in the plot of χ''_{mol} vs. χ'_{mol} (Cole-Cole plot).

***Temp.*(K)**	**1.8**	**2.1**	**2.4**	**3.0**	**3.9**
χ_S (cm^3mol^{-1})	3.0046	1.8399	2.8065	0.0868	-0.3786
χ_T (cm^3mol^{-1})	26.456	24.930	21.906	14.889	13.022
α	0.39895	0.38822	0.31685	0.30750	0.40237

(4-1) $[Tb(tta)_3(\mathbf{3D1pyO})]_2$ (**4d'**): after irradiation, sample B

In the temperature dependence of DC magnetic property measurement, the $\chi_{mol}T$ value between 1.9- 30 K was shifted parallel upward by 1.8 $cm^3\,mol^{-1}$ K nearly corresponding to two carbene units in contrast to before irradiation(Figure 5-19a). This phenomenon indicated the insignificant magnetic interaction of 2p-4f spins through the pyO units of **3C1pyO** moieties because of the negligible electronic spin densities on oxygen atoms, suggested by the EPR spectra measurement. It is worth noting that 2p spin of **C1pyO** unit regio-selectively interacted with 4f spin of Ln ion (ferromagnetically interacted in **4C1pyO**, while negligibly interacted in **3C1pyO**).

The $\Delta M_{mol}/N\mu_B$ vs. H plot (ΔM is defined by $M_{\text{after irradiation}} - M_{\text{before irradiation}}$) was compared to that of $[Tb(tta)_3(\mathbf{4D1pyO})]_2$. The obtained ΔM was converted to ΔM / ΔM_{50kOe} in Figure 5-19c. In $[Tb(tta)_3(\mathbf{3D1pyO})]_2$, ΔM / ΔM_{50kOe} value gradually increased between 10-50 kOe, while in $[Tb(tta)_3(\mathbf{4D1pyO})]_2$ ΔM / ΔM_{50kOe} steeply increased below 0.2 kOe and marked nearly the same value in the field ranges of 10-50 kOe, indicating the higher spin ground state of $[Tb(tta)_3(\mathbf{4C1pyO})]_2$ compared to that of $[Tb(tta)_3(\mathbf{3C1pyO})]_2$. This difference also supported the more effective ferromagnetic interaction in the case of **4C1pyO** (Figure 5-18c).

Interestingly in the AC susceptibility measurement, no temperature and field dependent signals were found under zero DC field and temperature ranges of 8-2 K (Figure 5-20). No observation of slow relaxation of magnetization in $[Tb(tta)_3(\mathbf{3C1pyO})]_2$ clearly indicated that even weak magnetic interaction had the critical role for the construction of SMM in 4f-2p heterospin systems.

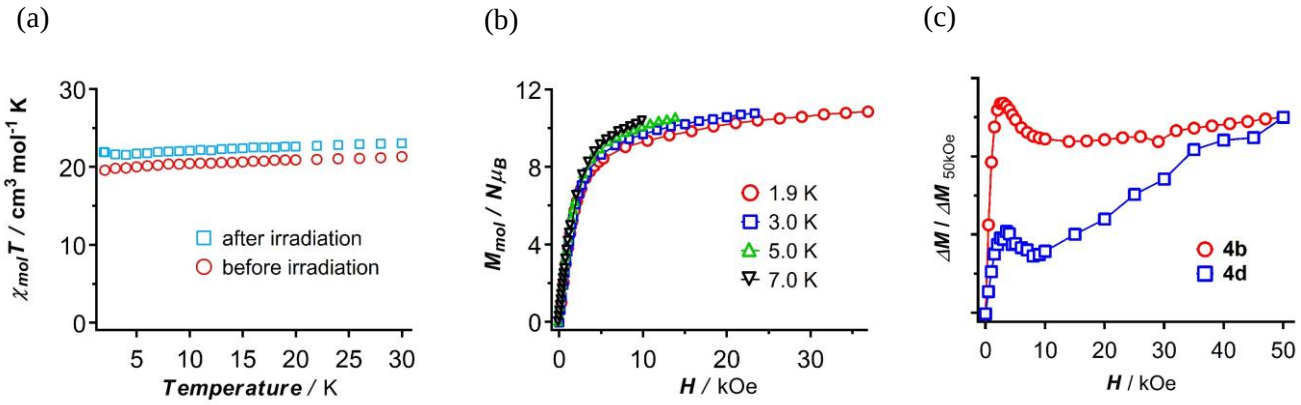

Figure 5-19. The plot of (a) $\chi_{mol}T$ vs. *T*emperature and (b) M_{mol} vs. H and (c)ΔM vs. H of $[Tb(tta)_3(\mathbf{3C1pyO})]_2$ (**4d'**). The solid lines in the right figure represent the guides for eyes.

(a) (b)

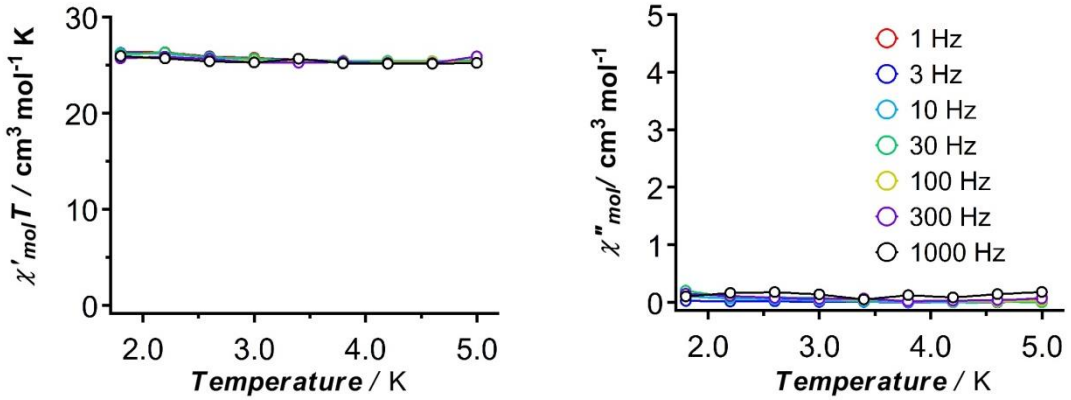

Figure 5-20. The plot of (a) $\chi_{mol}T$ vs. *T*emperature, (b) M_{mol} vs. *H* (c) $\chi'_{mol}T$ vs. *T*emperature, and (d) χ''_{mol} vs. *T*emperature of $[Tb(tta)_3(\mathbf{3C1pyO})]_2$ (**4d'**).

Section 9. Chapter conclusion

In order to construct the ferromagnetically coupled 4f-2p heterospin molecule-based magnets, novel photo-responsive ligands, **4D1pyO** and **3D1pyO** were successfully prepared and spectroscopically characterized. The EPR spectra of these ligands after irradiation at cryogenic temperature revealed that electronic spin of **4C1pyO** widely delocalized over the molecule compared to **3C1pyO**, and **4C1py**, suggesting the higher possibility of **4C1pyO** as an effective spin coupler with the metal ions. Mixing the **XD1pyO** with $Ln(tta)_3$ gave dinuclear complexes formulated as $[Ln(tta)_3(\mathbf{XD1pyO})]_2$ *x* solvent. Each Ln ion was surrounded by eight oxygen atoms and had distorted square-antiprismatic structure.

Two Ln ion was antiferromagnetically interacted each other through the oxygen atoms of pyO units and/or through space. In the Gd complex the magnetic exchange coupling constant, $J_{Gd\text{-}Gd}/k_B$, was estimated to be -0.08 K. Only the Dy complex showed the SMM behavior before irradiation. Hereupon irradiation, resulting carbene did interact ferromagnetically with the 4f spin of Ln ion in case of **4C1pyO** ($J_{Gd\text{-}carbene}/k_B$ = 2.4 K) but didn't in case of **3C1pyO**. $[Tb(tta)_3(\mathbf{4C1pyO})]_2$ showed the slow magnetic relaxation in the AC susceptibility measurement and the U_{eff}/k_B and the τ_0 were estimated to be 32.2 K, and 3.5 x 10^{-9} sec., respectively. $[Dy(tta)_3(\mathbf{4C1pyO})]_2$ still remained its SMM property though the U_{eff}/k_B value reduced from 97.8 K to 29.5 K by the photolysis. On the other hand, $[Tb(tta)_3(\mathbf{3C1pyO})]_2$ was not a SMM. These results clearly supported the extremely magnificent role of magnetic interaction of the organic spin with Ln ions.

In conclusion, magnetic interaction of 2p spin with 4f spin opened up the intrinsic/potential SMM possibility of Ln ion probably due to the depressing of the QTM, although the detailed mechanism was not so clear in this stage.

Chapter 6

~ Construction of 1-D Ln(III) complexes in 4f-2p heterospin system ~

4f-2p heterospin single-chain magnets[32] (SCMs) are one of the most promising candidates for the construction of high-temperature stable molecule-based magnets because of the possibilities of their higher activation barrier for the spin re-orientation compared to those of 4f-2p SMMs. According to this strategy, in this section, bridging ligands carrying a diazo unit along with the pyridine moieties will be prepared and their polymeric 4f metal complexes will be both crystallographically and magnetically investigated.

Section 1. Preparation of diazo-pyridine-*N*-oxide bridging ligands **D1(pyO)$_2$**, and its polymeric Ln(III) chain complexes

D1(pyO)$_2$ was obtained as a reddish colored crystal in five steps from 4-bromopyridine and 4-pyridinecarboxaldehyde (Scheme 6-1). The oxidations of nitrogen atoms of **K1py**$_2$ by per-acetic acid or mCPBA lead the Baeyer-Villiger oxidation[33] on the carbonyl group so that di(4-pyridine)methanol was firstly oxidized by H_2O_2 aq./ H_2WO_4 mixture, and then resulting crude product was oxidized to **K1(pyO)**$_2$ by activated MnO_2. The obtained **K1(pyO)**$_2$ was converted to hydrazon derivatives in methanol, and then oxidized to **D1(pyO)$_2$**.

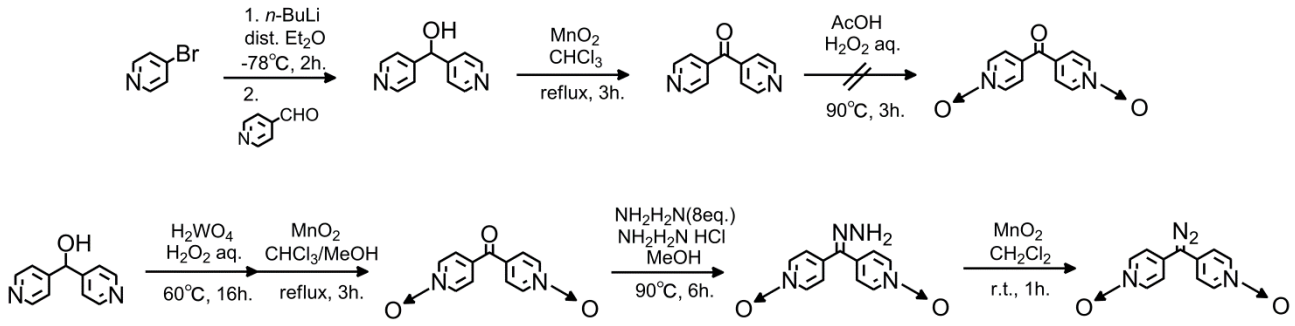

Scheme 6-1. Synthesis of diazo-pyridine-*N*-oxide bridging ligand, **D1(pyO)$_2$**

The obtained **D1(pyO)$_2$** was hardly soluble to dichloromethane, chloroform, although was well soluble to methanol. Then mixing the **D1(pyO)$_2$** with two equivalent of Ln(tta)$_3$ in dichloromethane/methanol/benzonitrile gave orange-yellow colored crystals suitable for the single crystal X-ray structure analysis (Scheme 6-2).

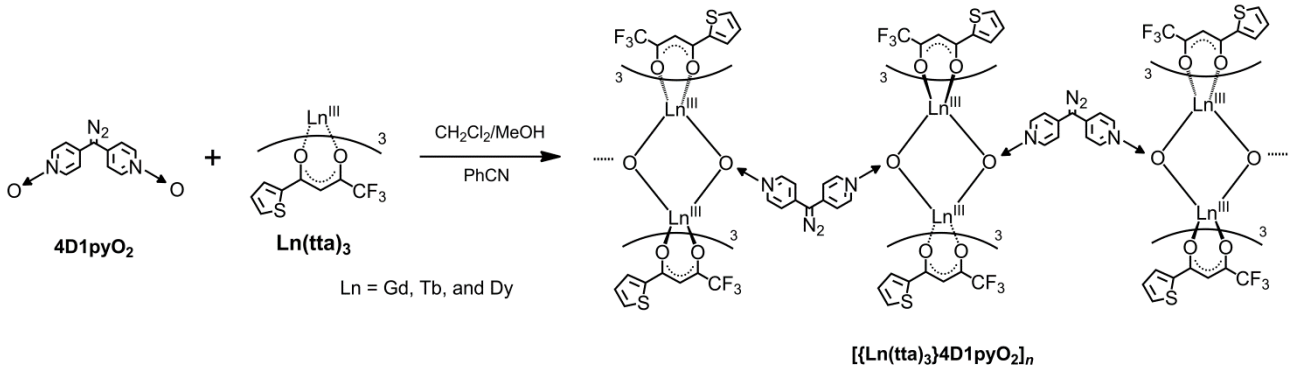

Scheme 6-2. Synthesis of Ln-**D1pyO$_2$** chain complexes.

Section 2. UV-vis. absorption spectra of **D1(pyO)$_2$**, and their Ln(III) complexes.

UV-vis. absorption spectra of **D1(pyO)$_2$** were recorded using the 0.5 mM chloroform solution at room temperature. **D1(pyO)$_2$** showed the typical absorption peak attributed to the n-π* transition of diazo component at 507 nm (ε = 280). This relatively red-shifted absorption wavelength compared to that of **D1py$_2$** previously reported (484 nm) [34] indicated a certain electronic effect of an expansion of conjugation system in **D1(pyO)$_2$**.

Solid state diffuse reflection measurements for Ln complexes were performed using the solid samples diluted by KBr at room temperature. The obtained data were converted to absorption spectra by the KM function (Figure 6-1). In the solid state spectra, [{Gd(tta)$_3$}$_2$(**D1(pyO)$_2$**)]$_n$ (**5a**), [{Tb(tta)$_3$}$_2$(**D1(pyO)$_2$**)]$_n$ (**5b**), and [{Dy(tta)$_3$}$_2$(**D1(pyO)$_2$**)]$_n$ (**5c**) showed similar absorption band. The wavelengths of maxima for the broad bands are around 440-450 nm in all three complexes. The blue shift of the absorption band of n-π* transition of diazo component through complexation in **5a**-**5c** (507 nm to 440-450 nm) implying a certain electronic interaction between the Ln complexes and **D1(pyO)$_2$**.

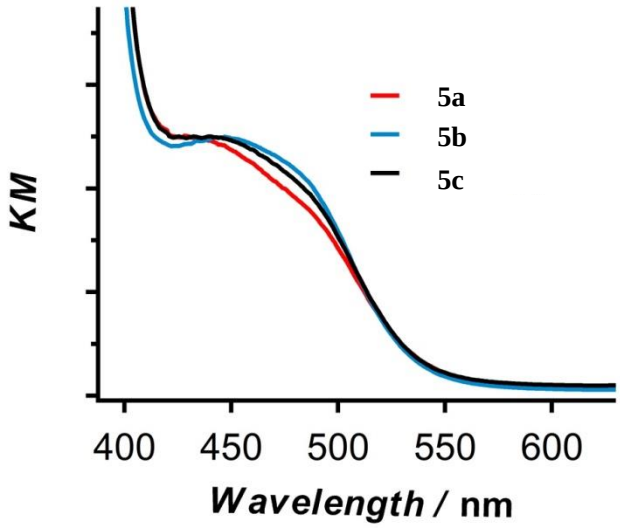

Figure 6-1.
Solid-state absorption spectra of [{Ln(tta)$_3$}$_2$(**D1(pyO)$_2$**)]$_n$ (**5a**-**5c**).

Section 3. Crystal structures of **D1(pyO)$_2$** and [{Ln(tta)$_3$}$_2$(**D1(pyO)$_2$**)]$_n$ nCH$_2$Cl$_2$ nPhCN (Ln = Gd : **5a**, Tb : **5b**, and Dy : **5c**)

X-ray crystal analyses were performed at -183 °C for **D1(pyO)$_2$**, and at -143 °C for Ln complexes using single crystals obtained above.

(i) **D1(pyO)$_2$**

D1(pyO)$_2$ crystallized in the monoclinic *C*2/*c* (No. 15) space group. This compound has an inversion center in the molecule so that one crystallographically independent pyO moiety existed. The bond length of N-O is 1.315 (18) Å, and the dihedral angle between pyridine plane (defined by C1, C2, C3, C4, C5, and N1) and diazo plane (defined by C3, C6, and N2) was 19.3°. The ORTEP drawing of **D1(pyO)2** is shown in Figure 6-2.

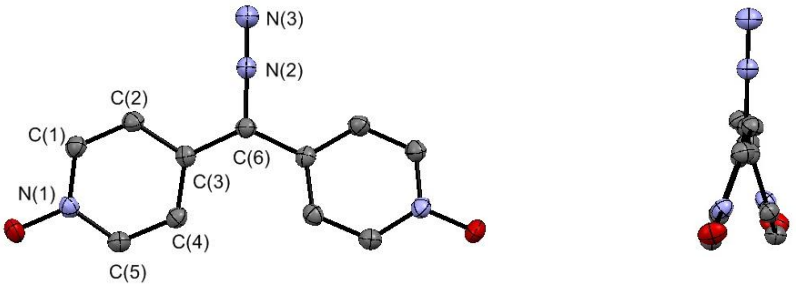

Figure 6-2. ORTEP drawings of diazo-pyridine-*N*-oxide bridging ligand, **D1(pyO)$_2$**. The thermal ellipsoids are set at a 50% probability level, and the hydrogen atoms are omitted for the sake of clarity.

(ii) [{Gd(tta)$_3$}$_2$(**D1(pyO)$_2$**)]$_n$ nCH$_2$Cl$_2$ nPhCN (**5a**)

When using the combination of **D1(pyO)$_2$** and two equivalent of Gd ions, dinuclear Gd chain complex formulated as [{Gd(tta)$_3$}$_2$(**D1(pyO)$_2$**)]$_n$ nCH$_2$Cl$_2$ nPhCN was obtained. This complex crystallized in the triclinic *P*-1 (No.2) space group and had one dichloromethane and one benzonitrile molecule as crystal solvent per one dinuclear unit. Two Gd ions were bridged by two oxygen atoms of both sides of **D1(pyO)$_2$** molecules in a μ_2 coordination mode to form a dinuclear local structure. Two crystallographically independent Gd ions were found in the crystal structure and the inversion center was located on the Gd ions. Gd1 was connected to Gd1* through the pyO moiety of one side of **D1(pyO)$_2$**, on the other hand, Gd2 and Gd2* were bridged by the oxygen atom of the other side of pyO unit. Each Gd ion was surrounded by eight oxygen atoms arising from three

tta anions and two **D1(pyO)$_2$**. The calculation of the degree of deviation for the Gd coordination polyhedron from the ideal eight-vertex Gd structure by using the continuous shape measure theory and SHAPE[25] software, indicated the low values for square antiprism (0.943 for Gd 1, and 1.040 for Gd 2, respectively), and triangular dodecahedron (0.997 for Gd 1, and 0.940 for Gd 2, respectively). Therefore, the coordination geometry was expected to be in the intermediate state between these structures.

The Gd -$O_{\mathbf{D1(pyO)2}}$ bond lengths were 2.416(3) and 2.471(3) Å for Gd 1-O1, and 2.428(3) and 2.463(3) Å for Gd 2-O8, respectively. They were slightly longer than the Gd -O_{tta} bond lengths ranging from 2.312(3) to 2.392(3) Å for Gd 1-O_{tta} and 2.341(3) to 2.389(3) Å for Gd 2-O_{tta}, respectively. Gd 1- Gd 1*, Gd 2- Gd 2* and O1-O1*, O8-O8* distances were 4.117, 4.118 Å and 2.537, 2.558 Å, respectively. Regarding the **D1(pyO)$_2$** moiety, N-O bond lengths were 1.358(3) and 1.351(4) Å and were longer than the value obtained for uncomplexed **D1(pyO)$_2$** (1.315 Å). The dihedral angles between pyridine plane (defined by C1, C2, C3, C4, C5, N1, and C7, C8, C9, C10, C11, N4) and diazo plane (defined by C3, C6, N2, and C9,C6, N2) was 19.48, and 25.49 °, respectively. These values were slightly smaller than those of Co-aminoxyl chain complexes, [Co(hfpip-X)$_2$**NOpy$_2$**]$_n$, suggesting the effective delocalization of 2p spin in the **C1(pyO)$_2$** state compared to **NOpy$_2$**. The pyridine planes were nearly perpendicular to the Gd -$O_{\mathbf{4D1pyO}}$- Gd -$O_{\mathbf{4D1pyO}}$ planes (the dihedral angle between these planes were 86.89, and 81.65 ° for Gd 1, and Gd 2) but showed less orthogonality compared to that of discrete dinuclear complex. As mentioned above, except for the subtle differences of the coordination structure, the local structure of each Gd ion was very similar to that of dinuclear discrete complex, [Gd(tta)$_3$(**4D1pyO**)]$_2$ 2$CHCl_3$ (**4a**).

The shortest interchain Gd - Gd distance was 11.63 Å, indicating that the direct interaction of spin centers between the chains through space was insignificant. The 1-D chain direction was parallel to "*a* + *c* - *b*" axis in the crystal packing. The shortest interchain contact was found between the nitrogen atom of diazo moiety and the carbon atom of tta unit (3.329 Å). Dichloromethane and benzonitrile molecule were located between the four chains, and the benzonitrile molecules formed the dimer structures in a head-to-tail configuration (Figure 6-2). Main crystallographic parameters for these complexes are summarized in the Table 6-1 and the molecular structure of chain complex as the ORTEP drawing, the local structure of each Gd ion, and the crystal packings were depicted in the Figure 6-2.

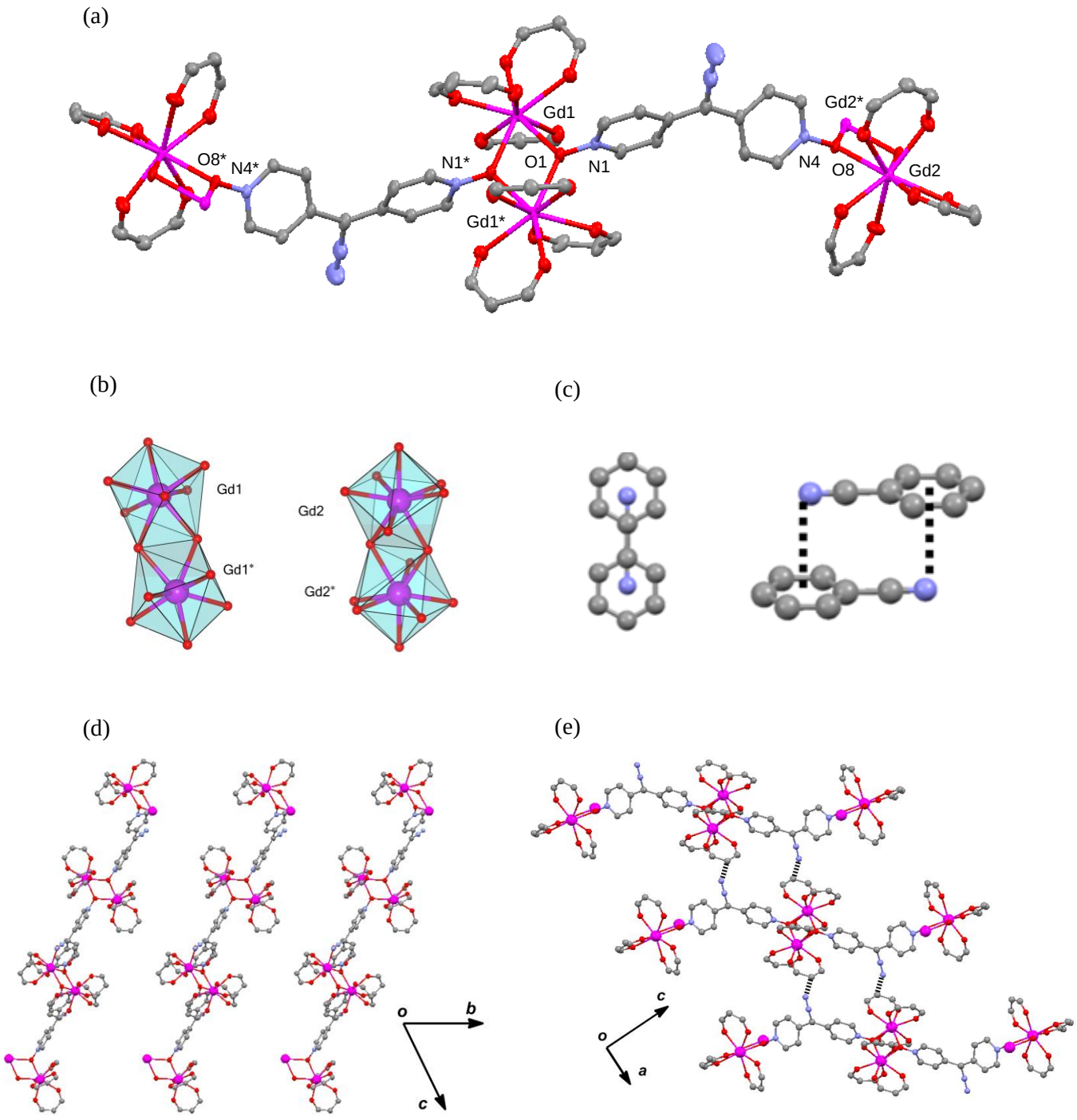

Figure 6-2. (a) ORTEP drawings of $[\{Gd(tta)_3\}_2(\mathbf{D1(pyO)_2})]_n$ $n$$CH_2Cl_2$ nPhCN. The thermal ellipsoids are set at a 50% probability level, and the hydrogen atoms, thiophen rings and CF_3 groups, and solvent molecules are omitted for the sake of clarity. (b) Schematic drawing of local coordination structures of Ln ions (red : O atoms, pink : Gd atoms). (c) Head-to-tail dimer structure of benzonitrile molecule. Black dotted line represents the shortest contact between phenyl ling and the nitrogen atom. (d), (e) Crystal packings of dinuclear chain complexes projecting from the shown directions. Intermolecular short distances are depicted as black dotted lines in (d).

(iii) [{Tb(tta)$_3$}$_2$(**D1(pyO)$_2$**)]$_n$ nCH$_2$Cl$_2$ nPhCN (**5b**), and (iv) [{Dy(tta)$_3$}$_2$(**D1(pyO)$_2$**)]$_n$ nCH$_2$Cl$_2$ nPhCN (**5c**)

The other derivatives (Ln = Tb, and Dy) also crystallized in the same triclinic *P*-1 (No.2) space group and had isostructures to the Gd complex. Main crystallographic parameters for these complexes are summarized in the Table 6-1 and ORTEP drawings and the local coordination mode of [{Tb(tta)$_3$}$_2$(**D1(pyO)$_2$**)]$_n$ nCH$_2$Cl$_2$ nPhCN and (iv) [{Dy(tta)$_3$}$_2$(**D1(pyO)$_2$**)]$_n$ nCH$_2$Cl$_2$ nPhCN are shown below (Figure 6-3).

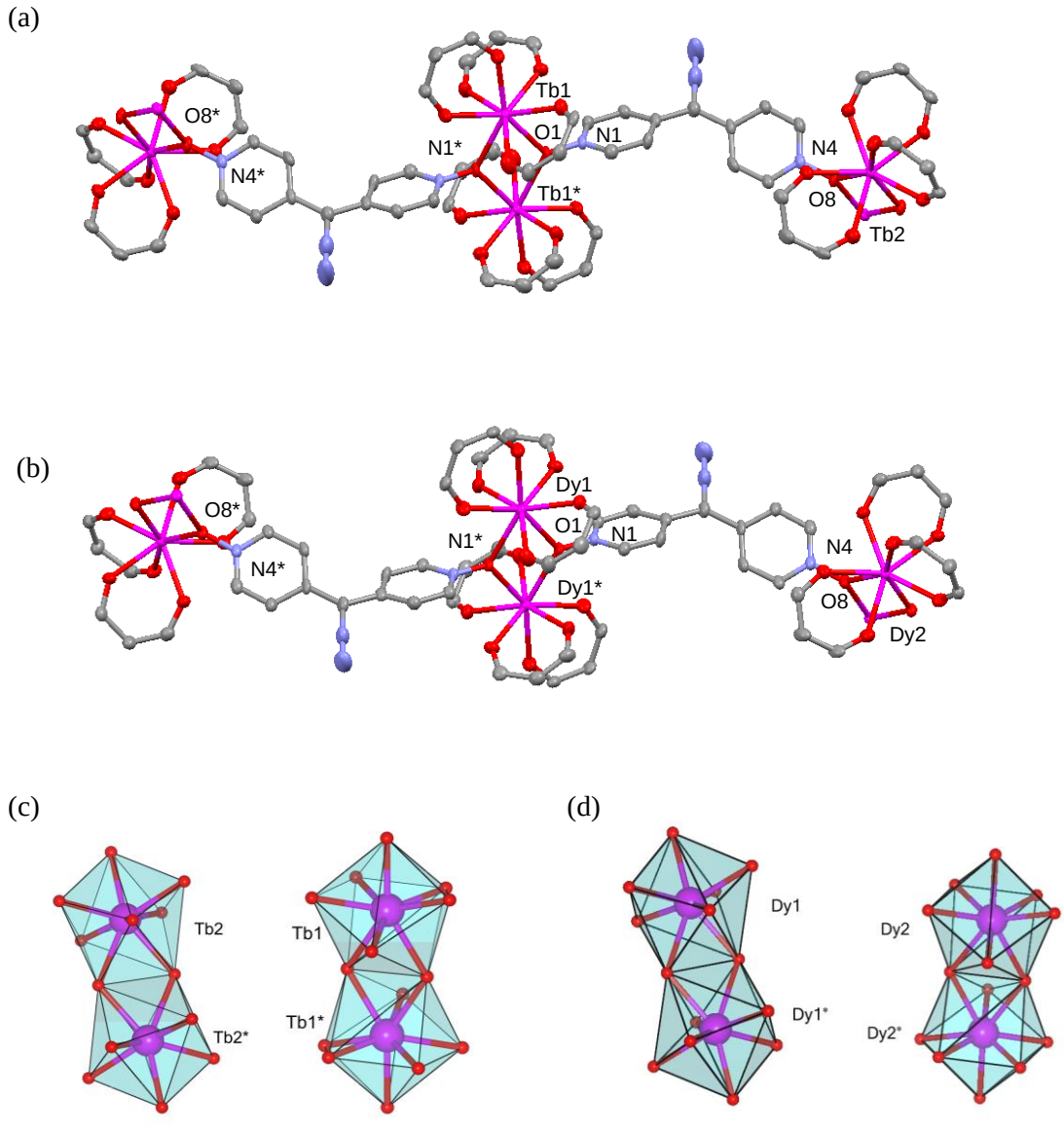

Figure 6-3. (a),(b) ORTEP drawings of [{Tb(tta)$_3$}$_2$(**D1(pyO)$_2$**)]$_n$ nCH$_2$Cl$_2$ nPhCN, and [{Dy(tta)$_3$}$_2$(**D1(pyO)$_2$**)]$_n$ nCH$_2$Cl$_2$ nPhCN, respectively. The thermal ellipsoids are set at a 50% probability level, and the hydrogen atoms, thiophen rings and CF$_3$ groups, and solvent molecules are omitted for the sake of clarity. (c), (d) Schematic drawing of local coordination structures of Ln ions (red : O atoms, pink : Tb, and Dy atoms)

Table 6-1. Crystallographic Data Collection and Structural Refinement Information for **D1(pyO)$_2$**, and [{Ln(tta)$_3$}$_2$(**D1(pyO)$_2$**)]$_n$ *n*CH_2Cl_2 *n*PhCN (Ln = Gd, Tb, and Dy).

	D1(pyO)$_2$	**5a**	**5b**	**5c**
empirical formula	C_{12} $H_8N_4O_2$	$C_{67}H_{39}N_5O_{14}F_{18}$ $S_6Cl_6Gd_2$	$C_{67}H_{39}N_5O_{14}F_{18}$ $S_6Cl_6Tb_2$	$C_{67}H_{39}N_5O_{14}F_{18}$ $S_6Cl_6Dy_2$
formula weight	211.22	2056.84	2058.87	2068.85
crystal class	monoclinic	triclinic	triclinic	triclinic
space group	$P2_1/c$ (no. 14)	P-1 (no. 2)	P-1 (no. 2)	P-1 (no. 2)
a /Å	9.582(4)	12.670 (4)	12.714 (3)	12.591 (3)
b / Å	11.591(5)	15.107 (4)	15.188 (3)	15.096 (4)
c / Å	9.149(4)	20.658 (6)	20.687 (5)	20.580 (5)
α /deg	90	71.199(3)	71.036(2)	108.763(3)
β /deg	100.212(5)	88.419(3)	88.212(3)	91.728(73)
γ /deg	90	89.956(3)	89.848(2)	90.122(3)
V / Å^3	1000.0(8)	3742.0(2)	3775.9(15)	3701.9(15)
μ /mm^{-1}	0.94	2.107	2.204	2.357
Z	4 (1)	2	2	2
crystal size /mm	0.50 × 0.20 × 0.20	0.10 × 0.10 × 0.10	0.10 × 0.10 × 0.10	0.10 × 0.10 × 0.10
D_{calc} /gcm^{-3}	1.403	1.810	1.797	1.856
F (000)	440.00	1980.00	1984.00	2024.00
radiation	Mo-Kα	Mo-Kα	Mo-Kα	Mo-Kα
T /K	90.0	90.0	130.0	90.0
no. reflections measured	5322	40486	33075	38496
no. unique reflections	2158	16115	12715	15912
no. parameters	181	1027	1027	1027
R_1 [a]	0.0439 ($I > 2.00\sigma(I)$)	0.0411 ($I > 2.00\sigma(I)$)	0.0472 ($I > 2.00\sigma(I)$)	0.0619 ($I > 2.00\sigma(I)$)
wR_2 [a]	0.1198	0.1097	0.1855	0.1675
GOF	1.032	0.986	1.578	1.140

[a] $R_1 = \Sigma \, ||F_0|-|F_c|| \, / \, \Sigma \, |F_0|$; $wR_2 = \{\Sigma \, w(F_0^2-F_c^2)^2 \, / \, \Sigma \, w(F_0^2)^2\}^{1/2}$

Table 6-2. Selected bond lengths, bond andgles, dihedral angles, and intermolecular Ln^{III}-Ln^{III} distances for $[\{Ln(tta)_3\}_2(\mathbf{D1(pyO)_2})]_n$ $n$$CH_2Cl_2$ nPhCN (Ln = Gd, Tb, and Dy).

Ln-D1(pyO)$_2$	**5a**	**5b**	**5c**
Bond lengths / Å (estimated standard deviation)			
Ln(1)-O(1)	2.416 (3)	2.419 (4)	2.385 (5)
Ln(1)-O(1)*	2.471 (3)	2.454 (5)	2.448 (5)
Ln(1)-O(2)	2.342 (3)	2.303 (5)	2.294 (5)
Ln(1)-O(3)	2.392 (3)	2.368 (5)	2.351 (5)
Ln(1)-O(4)	2.364 (3)	2.356 (4)	2.314 (5)
Ln(1)-O(5)	2.372 (3)	2.357 (5)	2.353 (5)
Ln(1)-O(6)	2.312 (3)	2.331 (5)	2.334 (5)
Ln(1)-O(7)	2.380 (3)	2.378 (5)	2.339 (5)
N(1)-O(1)	1.358 (4)	1.362 (7)	1.366 (7)
Ln(1)-Ln(1)*	4.155	4.148	4.116
O(1)-O(1)*	2.573	2.559	2.536
Ln(2)-O(8)	2.428 (3)	2.414 (4)	2.399 (4)
Ln(2)-O(8)*	2.463 (3)	2.463 (5)	2.455 (4)
Ln(2)-O(9)	2.341 (3)	2.320 (5)	2.323 (5)
Ln(2)-O(10)	2.360 (3)	2.350 (5)	2.346 (5)
Ln(2)-O(11)	2.347 (3)	2.336 (4)	2.303 (5)
Ln(2)-O(12)	2.355 (3)	2.345 (5)	2.342 (5)
Ln(2)-O(13)	2.365 (3)	2.356 (5)	2.335 (5)
Ln(2)-O(14)	2.389 (3)	2.378 (5)	2.336 (5)
N(4)-O(8)	1.351 (4)	1.356 (6)	1.333 (7)
Ln(2)-Ln(2)*	4.156	4.145	4.119
O(8)-O(8)*	2.580	2.567	2.569
Bond angle / ° (estimated standard deviation)			
O(1)-Ln(1)-O(1)*	63.52 (11)	63.34 (17)	63.24 (18)
Ln(1)-O(1)-Ln(1)*	116.48 (11)	116.66 (17)	116.76 (18)
O(2)-Ln(2)-O(8)*	63.66 (11)	63.57 (16)	63.86 (16)
Ln(2)-O(8)-Ln(2)*	116.34 (10)	116.43 (16)	116.14 (16)

	Dihedral angles (°)		
C(2)C(4)N(1)-C(3)C(6)N(2)	19.48	18.46	17.56
$LnO_{pyO}Ln$-C(2)N(1)C(4)	86.89	86.65	87.40
C(2)C(4)N(1)-C(3)C(6)N(2)	25.49	26.40	26.47
$LnO_{pyO}Ln$-C(2)N(1)C(4)	81.65	82.50	82.38
	Intermolecular Ln^{III}-Ln^{III} distances (Å)		
Ln(1)-Ln(1)’	11.63	11.51	11.89

Table 6-3. The SHAPE analyses for $[\{Ln(tta)_3\}_2(\mathbf{D1(pyO)_2})]_n$ $n$$CH_2Cl_2$ nPhCN (**5a**-**5c**).

Ln-D1(pyO)$_2$	**5a**	**5b**	**5c**
	Gd1, Gd2	Tb1, Tb2	Dy1, Dy2
Square antiprism	1.008, 1.172	**0.943**, 1.040	0.972, 1.168
Triangular dodecahedron	**0.908**, **0.858**	0.997, **0.940**	**0.946**, **0.824**

Section . 4 Magnetic properties of [{Ln(tta)$_3$}$_2$(**D1(pyO)$_2$**)]$_n$ (Ln = Gd : **5a**, Tb : **5b**, and Dy : **5c**) before irradiation.

Magnetic properties measurements of [{Ln(tta)$_3$}$_2$(**D1(pyO)$_2$**)]$_n$ *n*CH_2Cl_2 *n*PhCN (Ln = Gd, Tb, and Dy) were performed using the microcrystalline samples of each complex in the SQUID systems.

(1-1) [{Gd(tta)$_3$}$_2$(**D1(pyO)$_2$**)]$_n$ (**5a**): before irradiation

Temperature dependence of direct current magnetic properties was measured between 90-2.0 K (10-1 kOe) (Figure 6-4a). The $\chi_{mol}T$ value at 90 K was 15.7 $cm^3\,mol^{-1}\,K$. It was close to the expected value of 15.8 $cm^3\,mol^{-1}\,K$ for two Gd ions (g = 2.0, S = 7/2). No obvious change of the $\chi_{mol}T$ values was found during the cooling from 90 K to 20 K, but gradual decrement of the $\chi_{mol}T$ values was found below 20 K until reaching to 13.0 $cm^3\,K\,mol^{-1}$ at 2.0 K. The decrease of the $\chi_{mol}T$ values at lower temperature was attributed to the antiferromagnetic coupling between the Gd ions within the dimer. For the quantitative evaluation of the magnetic interaction in this compound, the least-square fitting considering the Heisenberg Hamiltonian (H = - $J_{Gd\text{-}Gd}$ (S_{Gd1} S_{Gd2})[27a,28b] was performed. The $J_{Gd\text{-}Gd}/k_B$ value was estimated to be -0.052 K and which lay in the same order compared to that of discrete dinuclear complex, [Gd(tta)$_3$(**4D1pyO**)]$_2$ (**4a**).

The $M_{mol}/N\mu_B$, at 1.9 K and at 70 kOe was 14.6. It was close to the expected saturation value of 14.0 for the two Gd ions. The plots of reduced field (HT^{-1}) dependency of the magnetization showed the superimposition to the single mater curve. This result indicated the negligible uniaxial magnetic anisotropy for each Gd ion (Figure 6-4b).

In summary, the DC magnetic properties of Gd chain complex were very similar to those of dinuclear complex, **4a**, before irradiation.

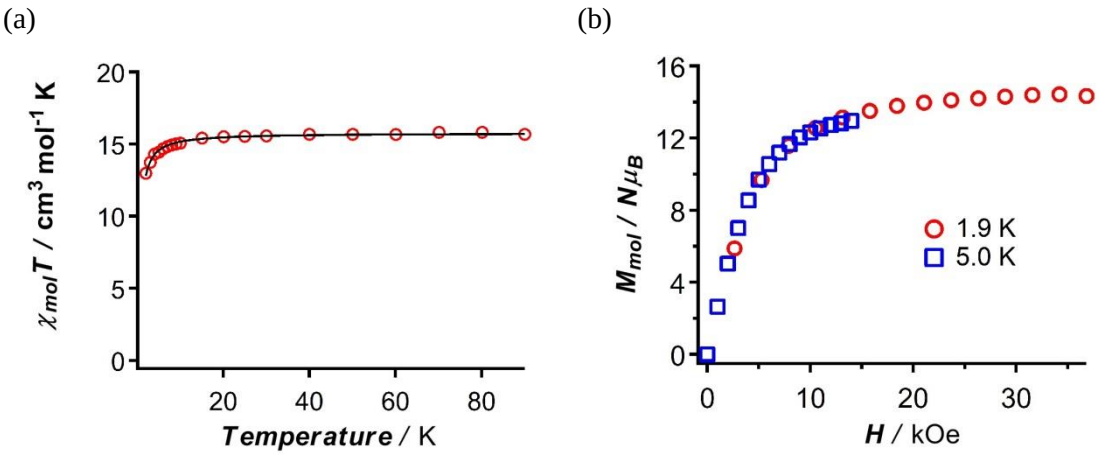

Figure 6-4. The plot of (a) $\chi_{mol}T$ vs. *T*emperature and (b) M_{mol} vs. HT^{-1} of [{Gd(tta)$_3$}$_2$(**D1(pyO)$_2$**)]$_n$. The black solid line in the left figure represents the best-fit results obtained according to the Heisenberg spin Hamiltonian (see the text).

(1-2) [{Tb(tta)$_3$}$_2$(**D1(pyO)$_2$**)]$_n$ (**5b**) : before irradiation

DC and AC magnetic susceptibility measurements were performed using pulverized microcrystalline sample. The magnetic properties of **5b** were very similar to those of [Tb(tta)$_3$(**4D1pyO**)]$_2$ (**4b**). Temperature dependence of direct current magnetic properties was measured between 30-1.8 K under 1 kOe of DC field and the $\chi_{mol}T$ value at 30 K was 21.0 cm^3 mol^{-1} K. It was slightly smaller than the expected value of 23.6 cm^3 mol^{-1} K for two isolated Tb ions (g_J = 3/2, $^7F_6$, S = 3, L = 3). As lowering the temperature the $\chi_{mol}T$ value gradually decreased to 18.4 cm^3 mol^{-1} K at 1.9 K. The smaller value at 30 K and the decrement below 30 K was attributed to both the thermal depopulation of low-lying crystal field states and the antiferromagnetic interaction between two Tb ions within the dinuclear unit (Figure 6-5a).

The field dependence of DC magnetic property was measured at 1.9 and 5.0 K and at field ranges of 0-70 kOe. The $M_{mol}/N\mu_B$ at 1.9 K and at 70 kOe was 9.9. It was smaller than the expected saturation value of 19.4 for the two Tb ions. The plots of reduced field (HT^{-1}) dependency of the magnetization did not show the superimposition onto the single mater curve, confirming the presence of non-negligible uniaxial magnetic anisotropies and/or low-lying excited states, though the magnetic hysteresis was not observed above 1.9 K at the field dependence of the magnetization plots(Figure 6-5b).

No frequency and temperature dependent peaks were observed between 8.0-2.0 K under zero external DC field in the alternative current magnetic properties measurements. This result suggested the fast quantum tunneling relaxing rate and /or the small magnetic anisotropy of each Tb ion similar to the case of [Tb(tta)$_3$(**4D1pyO**)]$_2$ (**4b**).

(a) (b)

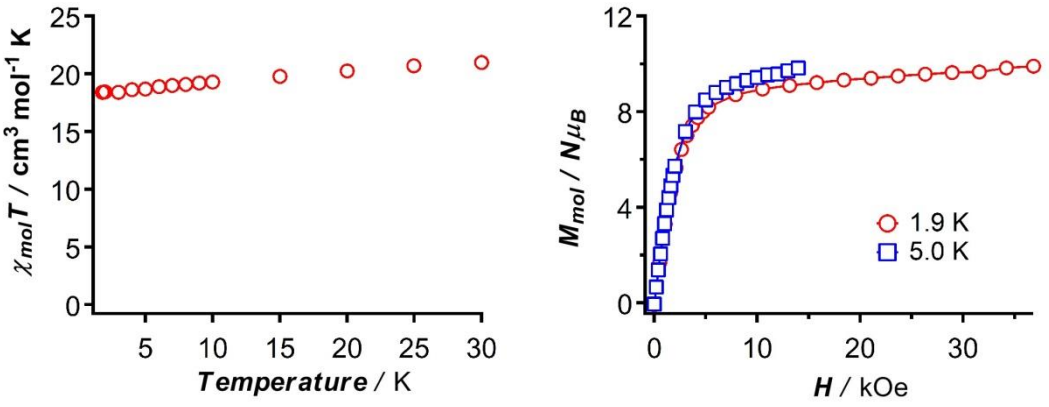

Figure 6-5. The plot of (a) $\chi_{mol}T$ vs. *T*emperature and (b) M_{mol} vs. HT^{-1} of [{Tb(tta)$_3$}$_2$(**D1(pyO)$_2$**)]$_n$.

(1-3) [{Dy(tta)$_3$}$_2$(**D1(pyO)$_2$**)]$_n$ (**5c**) : before irradiation

The magnetic properties of **5c** were very similar to those of [Dy(tta)$_3$(**4D1pyO**)]$_2$ (**4c**). Temperature dependence of direct current magnetic properties was measured between 90-1.8 K under 10-0.1 kOe of DC field. The $\chi_{mol}T$ value at 90 K and at 1.8 K were 25.6 and 13.6 cm^3 mol^{-1} K. (Figure 6-6a).

The field dependence of DC magnetic property was measured at 1.9-7.0 K and at field ranges of 0-70 kOe. The $M_{mol}/N\mu_B$ at 1.9 K and at 70 kOe was 10.3. The plots of reduced field (HT^{-1}) dependency of the magnetization did not show the superimposition onto the single mater curve, confirming the presence of non-negligible uniaxial magnetic anisotropies and/or low-lying excited states (Figure 6-6b).

In the ac magnetic property measurement, slow magnetic relaxation behavior typical to an SMM was observed under 15 K in the absence of external dc magnetic field (Figure 6-7). The activation barrier, Δ_{eff}/k_B, was estimated to be 90.0 K (τ_0 = 8.8 x 10^{-8}), and 76.5 K (τ_0 = 7.3 x 10^{-7}) from the temperature and frequency dependence plots, respectively. The extracted parameters of the magnetic relaxation were summarized in Table 6-4 to Table 6-6.

(a) (b)

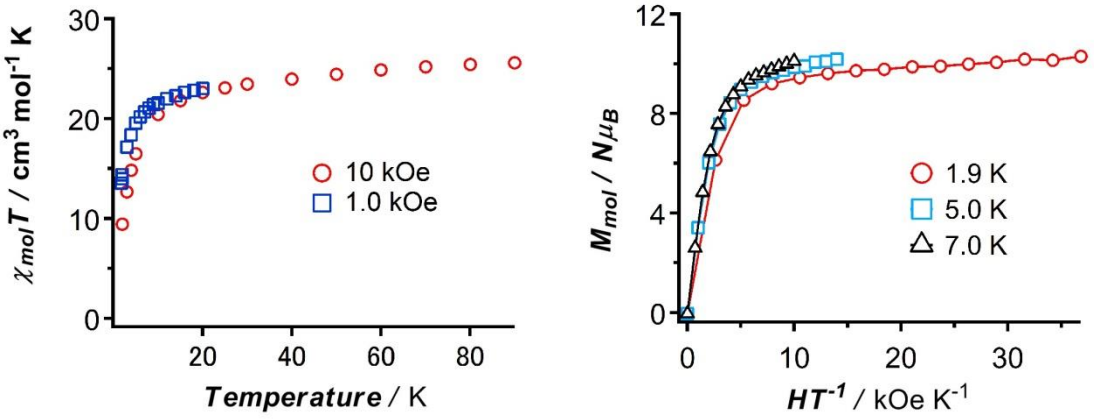

Figure 6-6. The plot of (a) $\chi_{mol}T$ vs. *T*emperature and (b) M_{mol} vs. HT^{-1} of [{Dy(tta)$_3$}$_2$(**D1(pyO)$_2$**)]$_n$.

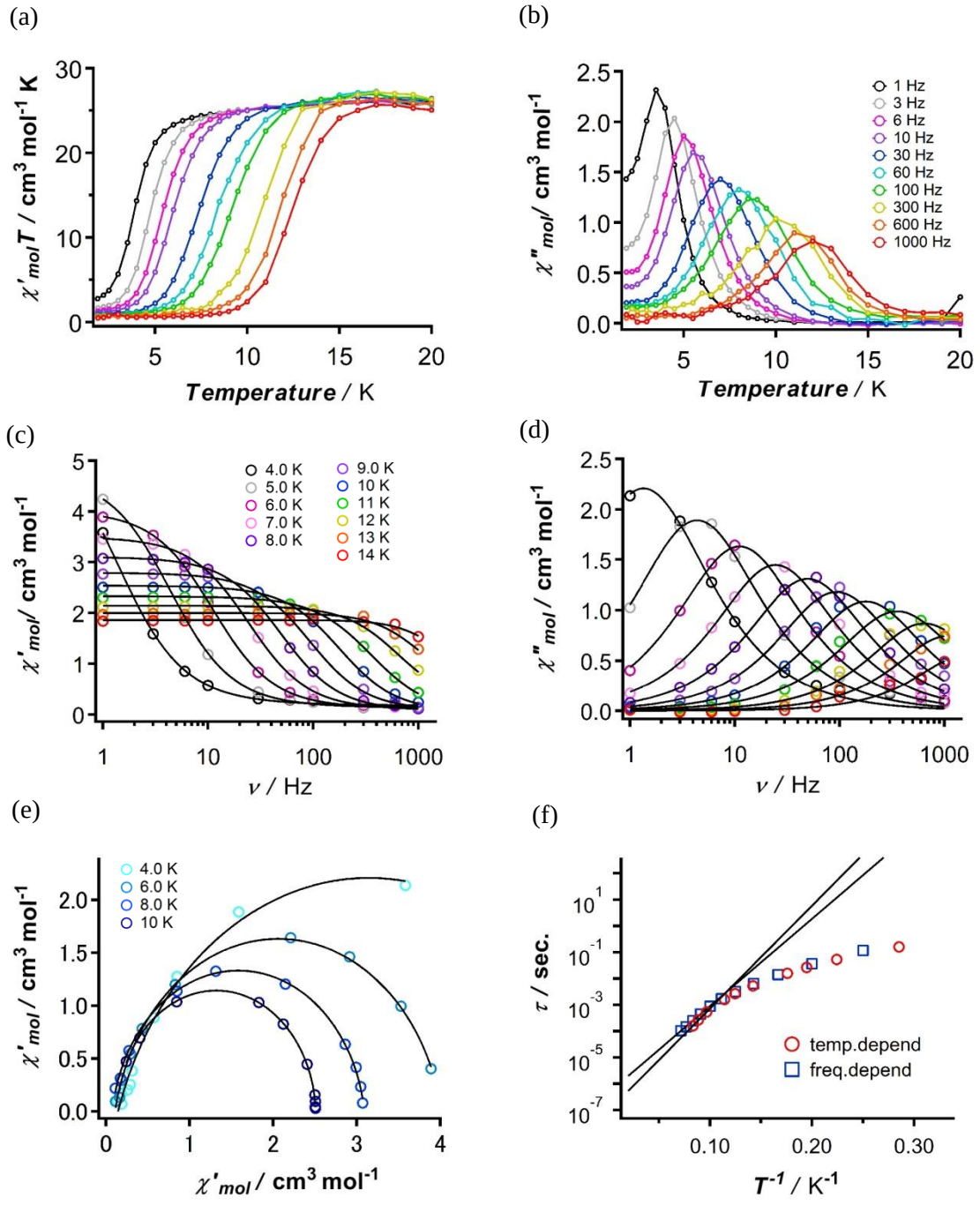

Figure 6-7. The plot of (a) $\chi'_{mol}T$ vs. *T*emperature, (b) χ''_{mol} vs. *T*emperature, (c) $\chi'_{mol}T$ vs. ν, (d) χ''_{mol} vs. ν, (e) Cole-Cole diagram, and (f) Arrhenius law of $[\{Dy(tta)_3\}_2(\mathbf{D1(pyO)_2})]_n$. The black bold lines in (c), and (d) show the fitting lines obtained from the extended Debye's model. In (e), black lines represents the best-fit results of generalized Debye's equation. The solid lines in (f) indicate the best fit result extracted from the Arrhenius law.

Table 6-4.

The extracted peak top temperature for each frequency in the plot of χ''_{mol} vs. *T*emperature.

Frequency (Hz)	**1**	**3**	**10**	**30**	**60**	**100**
Temp.(K)	3.506	4.46	5.136	5.685	7.029	8.016
T^{-1} (K^{-1})	0.285225	0.224215	0.194704	0.175901	0.142268	0.12475
τ (sec.)	0.159	0.0531	0.0159	0.00531	0.00265	0.00159

Frequency (Hz)	**200**	**300**	**600**	**1000**
Temp.(K)	8.753	10.34	11.28	11.99
T^{-1} (K^{-1})	0.114247	0.096712	0.088653	0.083403
τ (sec.)	0.00796	0.000531	0.000265	0.000159

Table 6-5.

The extracted parameters for selected temperatures by the extended Debye's fitting in the plot of χ'_{mol} vs. ν, and χ''_{mol} vs. ν.

***Temp.*(K)**	**4.0**	**5.0**	**6.0**	**7.0**	**8.0**	**9.0**
χ_S (cm^3mol^{-1})	0.177073	0.132006	0.113697	0.0874437	0.0645641	0.0765312
χ_T (cm^3mol^{-1})	5.83321	4.75213	4.03224	3.50843	3.10795	2.79445
τ (sec.)	0.117814	0.0363947	0.0143328	0.006503	0.0032122	0.0017038
α	0.155542	0.125884	0.116467	0.105857	0.0950304	0.0895846

***Temp.*(K)**	**10.0**	**11.0**	**12.0**	**13.0**	**14.0**
χ_S (cm^3mol^{-1})	0.0527389	0.0240085	0.224544	0.431507	0.787832
χ_T (cm^3mol^{-1})	2.53956	2.33059	2.14209	2.00153	1.85932
τ (sec.)	0.0008949	0.0004492	0.0002483	0.0001481	0.0001032
α	0.0864054	0.0980071	0.0629151	0.0338353	-0.013264

Table 6-6.

The extracted parameters for selected temperatures by the generalized Debye's fitting in the plot of χ''_{mol} vs. χ'_{mol} (Cole-Cole plot).

***Temp.*(K)**	**4.0**	**6.0**	**8.0**	**10.0**
χ_S (cm^3mol^{-1})	0.14413	0.108106	0.076745	0.129465
χ_T (cm^3mol^{-1})	6.14535	4.01411	3.09077	2.51018
α	0.192476	0.113878	0.078239	0.025689

Section . 5 Magnetic properties of [{Ln(tta)$_3$}$_2$(**D1(pyO)$_2$**)]$_n$ (Ln = Gd, Tb, and Dy) after irradiation

Photo-irradiation of [{Ln(tta)$_3$}$_2$(**D1(pyO)$_2$**)]$_n$ (Ln = Gd, Tb, and Dy).

Then, photo-irradiation for these complexes was performed in the SQUID systems. The detailed procedures and conditions for the photolysis of diazo component were summarized in the experimental sections. Particular in these chain complexes, "photolysis method **A**" for **5a** and "photolysis method **B**" for **5b** were used for the production of carbenes.

On the photolysis, the $\chi_{mol}T$ values steeply increased and reached to the saturation after irradiation 1 day. The yields of photolysis of [{Ln(tta)$_3$}$_2$(**D1(pyO)$_2$**)]$_n$ (Ln = Gd, Tb and Dy) were determined to be ca. 73, 81, and 92 % by the decrements of the IR absorption bands at 2068 cm^{-1} originated from the diazo components in these complexes after SQUID measurements.

(a) Ln = Gd

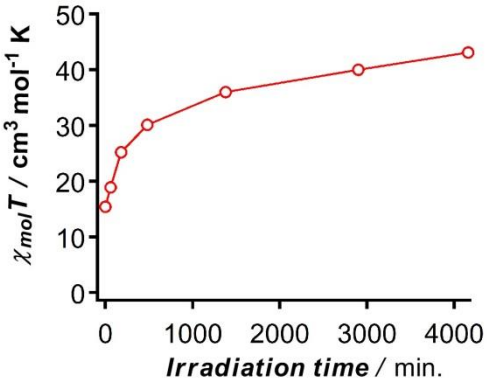

(b) Ln = Tb

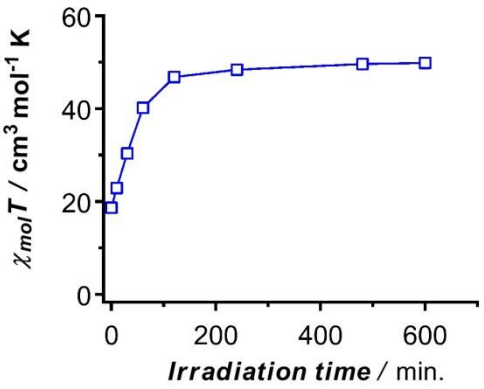

(c) Ln = Dy

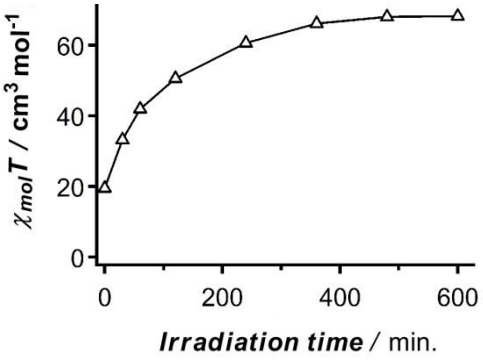

Figure 6-8. Plots of $\chi_{mol}T$ vs. Irradiation time for [{Ln(tta)$_3$}$_2$(**D1(pyO)$_2$**)]$_n$ (Ln = Gd, Tb and Dy)

(2-1) [{Gd(tta)$_3$}$_2$(**C1(pyO)$_2$**)]$_n$ (**5a'**) : after irradiation

The $\chi_{mol}T$ value at 30 K was 18.8 cm^3 mol^{-1} K. It was slightly larger than the value of 17.1 calculated by a sum of the spin-only value of one isolated triplet carbene (g = 2.0, S = 2/2) and two Gd ions (before irradiation, the $\chi_{mol}T$ value at 30 K for two Gd ions was 15.8) (Figure 6-9a). As lowering the temperature, the $\chi_{mol}T$ value gradually increased and reached 90.7 cm^3 mol^{-1} K at 1.8 K, indicating the presence of ferromagnetic correlation within the dinuclear chain complex (the $\chi_{mol}T$ value of 90.7was much larger than that of 30.1 observed in [Gd(tta)$_3$(**4C1pyO**)]$_2$).

The $M_{mol}/N\mu_B$, at 1.9 K and at 70 kOe was 15.8. It was smaller than the expected saturation value of 16.0 for the two Gd ions and one triplet carbene, but was 1.2 larger than that of before irradiation (14.6μ_B).

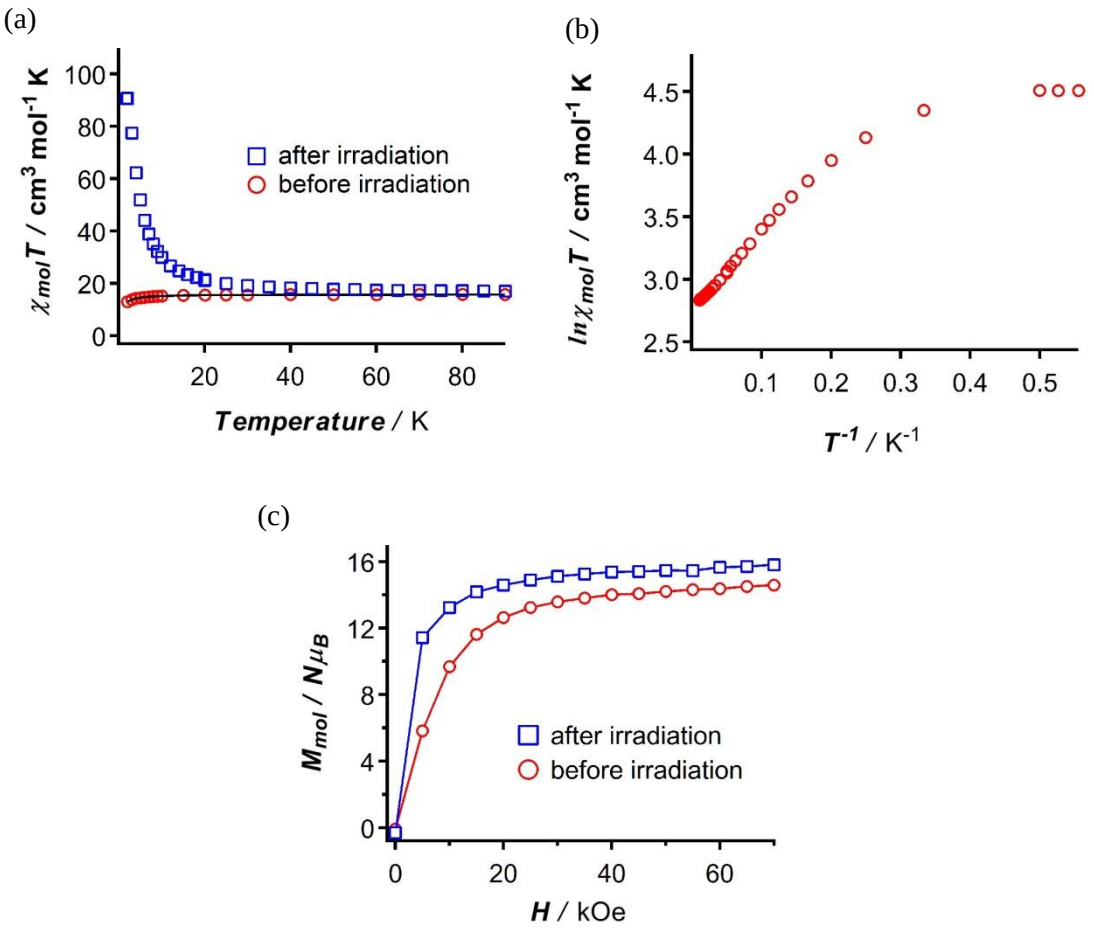

Figure 6-9. (a)The plot of $\chi_{mol}T$ vs. *T*emperature , (b)$ln\chi_{mol}T$ vs. T^{-1} , and (c)M_{mol} vs. H of [{Gd(tta)$_3$}$_2$(**C1(pyO)$_2$**)]$_n$. The black solid line in the Figure (a) represents the best-fit results obtained according to the Heisenberg spin Hamiltonian (see the text).

(2-2) [{Tb(tta)$_3$}$_2$(**C1(pyO)$_2$**)]$_n$ (**5b'**) : after irradiation

The $\chi_{mol}T$ value at 30 K was 26.5 cm^3 mol^{-1} K. It was slightly larger than the value of 22.0 calculated by a sum of the spin-only value of one isolated triplet carbene (g = 2.0, S = 2/2) and two Tb ions (before irradiation, the $\chi_{mol}T$ value at 30 K for two Tb ions was 21.0) (Figure 6-10a). As lowering the temperature, the $\chi_{mol}T$ value gradually increased and reached 90.3 cm^3 mol^{-1} K at 1.9 K, indicating the presence of ferromagnetic correlation within the dinuclear chain complex (the $\chi_{mol}T$ value of 90.3 was much larger than that of 41.6 observed in [Tb(tta)$_3$(**4C1pyO**)]$_2$). The activation barrier for the spin relaxation due to the magnetic correlation, from the $ln\chi_{mol}T$ vs. T^{-1} plot (Figure 6-10b).

The $M_{mol}/N\mu_B$, at 1.9 K and at 70 kOe was 11.6. It was smaller than the expected saturation value of 21.4 for the two Tb ions and one triplet carbene, but was 1.7 larger than that of before irradiation (9.9μ_B). The plots of reduced field (HT^{-1}) dependency of the magnetization did not show the superimposition to the single master curve, indicating the presence of uniaxial magnetic anisotropies of Tb ions. (Figure 6-10c,d)

Interestingly, alternative current magnetic properties after irradiation clearly depended on both frequency and temperature between the temperature ranges of 5.0-1.8 K under zero external DC field (Figure 6-11). In the $\chi'_{mol}T$ vs. *Temperature* plot, the $\chi'_{mol}T$ values gradually increased as cooling the temperature below 5.0 K, indicating the ferromagnetic correlation of the carbene and Tb ion through the heterospin chain. The $\chi'_{mol}T$ value at 2.2 K and at 1 Hz was 152 cm^3 mol^{-1} K. The magnetic correlation lengths, n, was estimated to be 6 using the following equation, $n\chi'T = (g^2/8)\,nS(nS+1)$; g = 2.0, $\chi'T$ =152. In the χ''_{mol} vs. *Temperature* plot the peak top for each frequency was extracted according to the Gaussian distribution, and the obtained relaxation time, τ, and the temperature (T^{-1}) was plotted in accordance with the Arrhenius law. The activation barrier for the spin re-orientation, Δ_{eff}/k_B, and the pre-exponential factor, τ_0, was estimated to be 33.9 K and 2.9 x 10^{-10} sec., respectively. The Δ_{eff}/k_B value was slightly higher than that of [Tb(tta)$_3$(**4C1pyO**)]$_2$, indicating the presence of additional activation energy barrier owing to the magnetic correlation between the dinuclear SMM units. Relatively smaller order of τ_0 value also supported the different relaxation mechanism compared to discrete complex. Similarly, the relaxation time, τ, and the distribution factor of the spin relaxation, α, was extracted in both the χ'_{mol} vs. ν plot and the χ''_{mol} vs. ν plot using the extended Debye's model. The obtained values of χ_s, χ_T, τ, and α were summarized in Table 6-8 and plotted in Figure 6-11c,d. The Δ_{eff}/k_B, and τ_0, was estimated to be 30.4 K and 9.3 x 10^{-9} sec., respectively. The Δ_{eff}/k_B was smaller than that extracted from the temperature dependent plot might be due to the antiferromagnetic interaction between chains observed in the χ''_{mol} vs. *Temperature* plot below 2.2 K. The α values, 0.20-0.48 between the temperature ranges of 2.8-1.8 K suggested the wide distribution of spin relaxation, especially at the extremely low temperature. The Cole-Cole

plot at the selected temperature was fitted by the generalized Debye's model (Figure 6-11e), and the obtained parameters were noted in Table 6-7 to 6-9.

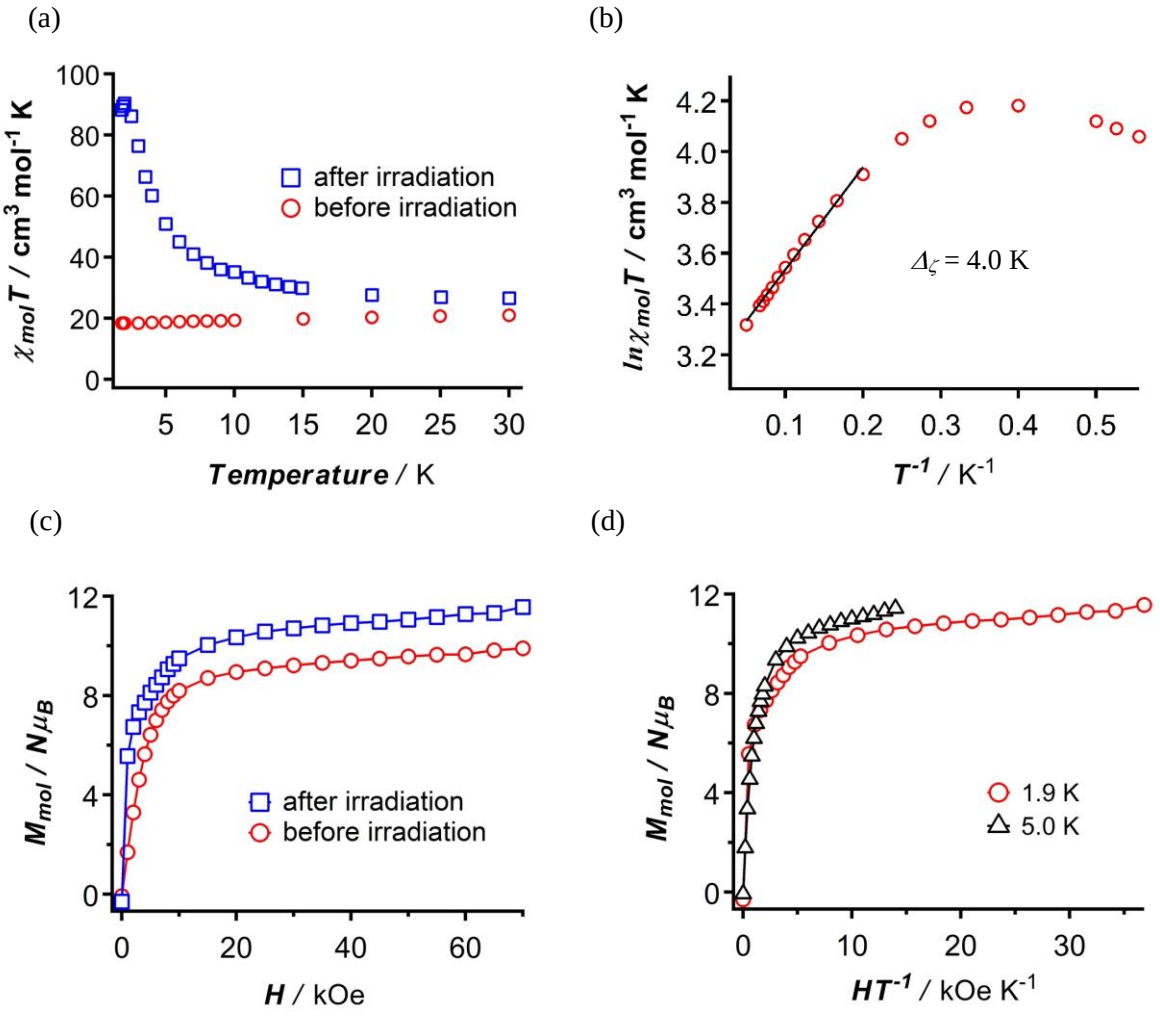

Figure 6-10. (a)The plot of $\chi_{mol}T$ vs. *T*emperature , (b)ln$\chi_{mol}T$ vs. T^{-1} (c)M_{mol} vs. H and (d)M_{mol} vs. HT^{-1} of [{Tb(tta)$_3$}$_2$(**C1(pyO)$_2$**)]$_n$.

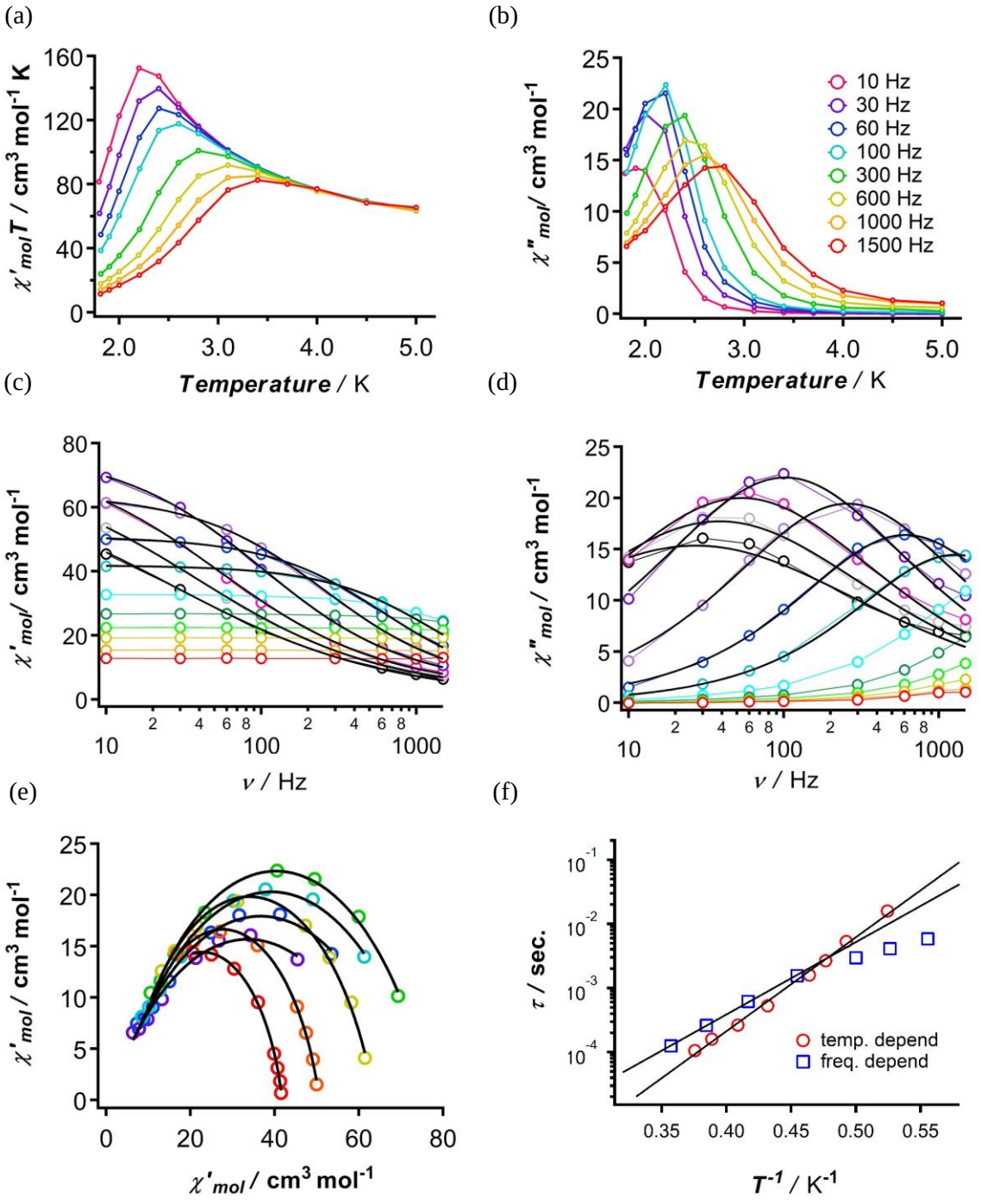

Figure 6-11. The plot of (a) $\chi'_{mol}T$ vs. *T*emperature, (b) χ''_{mol} vs. *T*emperature, (c) χ'_{mol} vs. ν, (d) χ''_{mol} vs. ν, (e) Cole-Cole diagram, and (f) Arrhenius law of $[\{Tb(tta)_3\}_2(\mathbf{C1(pyO)_2})]_n$. The black bold lines in (c), and (d) show the fitting lines obtained from the extended Debye's model. In (e), black lines represent the best-fit results of generalized Debye's equation. The solid lines in (f) indicate the best fit result extracted from the Arrhenius law.

Table 6-7.

The extracted peak top temperature for each frequency in the plot of χ''_{mol} vs. *T*emperature.

Frequency (Hz)	**10**	**30**	**60**	**100**	**300**	**30**
Temp.(K)	1.907	2.03	2.098	2.155	2.316	2.446
T^{-1} (K^{-1})	0.524384	0.492611	0.476644	0.464037	0.431779	0.408831
τ (sec.)	0.015924	0.005308	0.002654	0.001592	0.000531	0.000265

Frequency (Hz)	**1000**	**1500**
Temp.(K)	2.573	2.662
T^{-1} (K^{-1})	0.388651	0.375657
τ (sec.)	0.000159	0.000107

Table 6-8.

The extracted parameters for selected temperatures by the extended Debye's fitting in the plot of χ'_{mol} vs. ν, and χ''_{mol} vs. ν.

***Temp.*(K)**	**1.8**	**1.9**	**2.0**	**2.2**	**2.4**	**2.6**	**2.8**
χ_S (cm^3mol^{-1})	-0.104	1.315	2.369	3.347	3.468	3.349	2.145
χ_T (cm^3mol^{-1})	70.818	73.914	77.555	78.249	64.574	51.059	41.995
τ (sec.)	0.005857	0.004122	0.00296	0.00156	0.000619	0.000261	0.000125
α	0.4802	0.4219	0.3777	0.3239	0.278588	0.233911	0.201592

Table 6-9.

The extracted parameters for selected temperatures by the generalized Debye's fitting in the plot of χ''_{mol} vs. χ'_{mol} (Cole-Cole plot)

***Temp.*(K)**	**1.8**	**1.9**	**2.0**	**2.2**	**2.4**	**2.6**	**2.8**
χ_S (cm^3mol^{-1})	0.572724	1.32577	2.53071	3.54622	4.24529	4.71704	4.09373
χ_T (cm^3mol^{-1})	66.6609	71.9973	75.9174	77.0995	63.7979	50.6621	41.7969
α	0.436189	0.402421	0.356742	0.305534	0.252027	0.20195	0.168842

(2-3) [{Dy(tta)$_3$}$_2$(**C1(pyO)$_2$**)]$_n$ (**5c'**) : after irradiation

DC magnetic properties of **5c'** were similar to those of **5b**'. The $\chi_{mol}T$ value at 90 K was 27.2 cm^3 mol^{-1} K. It was larger than the value of 26.6 calculated by a sum of the spin-only value of one isolated triplet carbene (g = 2.0, S = 2/2) and two Dy ions (before irradiation, the $\chi_{mol}T$ value at 90 K for two Dy ions was 25.6) (Figure 6-12a). As lowering the temperature, the $\chi_{mol}T$ value gradually increased and reached 152 cm^3 mol^{-1} K at 3.0 K, then decreased to 134 cm^3 mol^{-1} K at 1.8 K. This thermal property suggested the presence of ferromagnetic correlation within the dinuclear chain complex along with the antiferromagnetic interaction between chains and the thermal depopulation of the low-lying excited state (the $\chi_{mol}T$ value of 152 was much larger than that of 38.3 observed in the discrete complex, [Dy(tta)$_3$(**4C1pyO**)]$_2$). The activation barrier for the spin relaxation due to the magnetic correlation, Δ_ζ, was expected to be 6.2 K from the $ln\chi_{mol}T$ vs. T^{-1} plot (Figure 6-12b).

The $M_{mol}/N\mu_B$, at 1.9 K and at 70 kOe was 11.8 μ_B. It was smaller than the expected saturation value of 24.3 for the two Dy ions and one triplet carbene, but was 1.5 larger than that of before irradiation (10.3μ_B). The plots of reduced field (HT^{-1}) dependency of the magnetization did not show the superimposition to the single master curve, indicating the presence of uniaxial magnetic anisotropies of Dy ions. (Figure 6-12c,d)

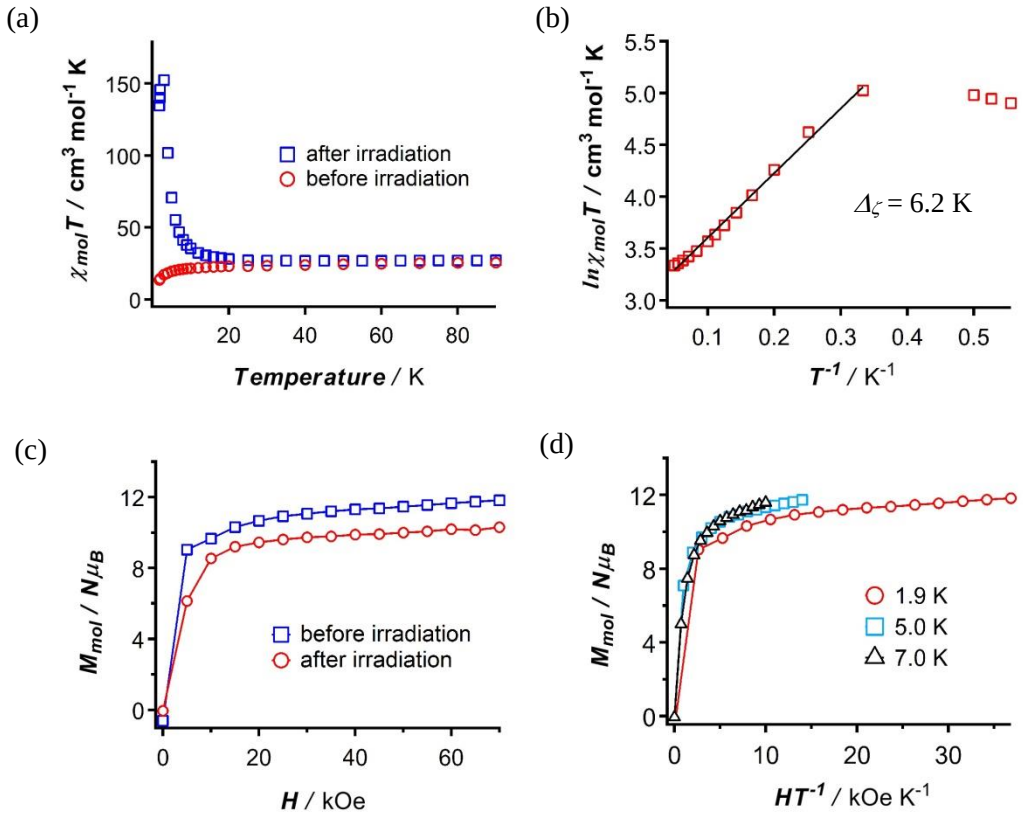

Figure 6-12. (a)The plot of $\chi_{mol}T$ vs. *T*emperature , (b) ln$\chi_{mol}T$ vs. T^{-1} (c) M_{mol} vs. H and (d) M_{mol} vs. HT^{-1} of [{Dy(tta)$_3$}$_2$(**C1(pyO)$_2$**)]$_n$.

The most interestingly, **5c'** showed the magnetic hysteresis in the field dependence of magnetization measurement at 1.8 K (Figure 6-13). The coercive field and the remnant magnetization were expected to be about 0.2 kOe and 2.4 μ_B respectively. It should be mentioned that dinuclear discrete complex, **4c'**, didn't show the magnetic hysteresis even in the same condition. Hence it was proposed that ferromagnetic correlation within the heterospin chain system effectively slowed down the magnetic relaxation mainly by depressing the quantum tunneling pathway. Furthermore, **5c** was crystallized in the triclinic *P*-1 space group so that we probably could exclude the possibility of spin-canted antiferromagnet induced by the antiferromagnetic ordering between the neighboring chains (in chapter 3, **2b** also didn't show the magnetic ordering). In other word, the magnetic hysteresis of **5c'** should be the intrinsic magnetic behavior of nearly isolated SCM.

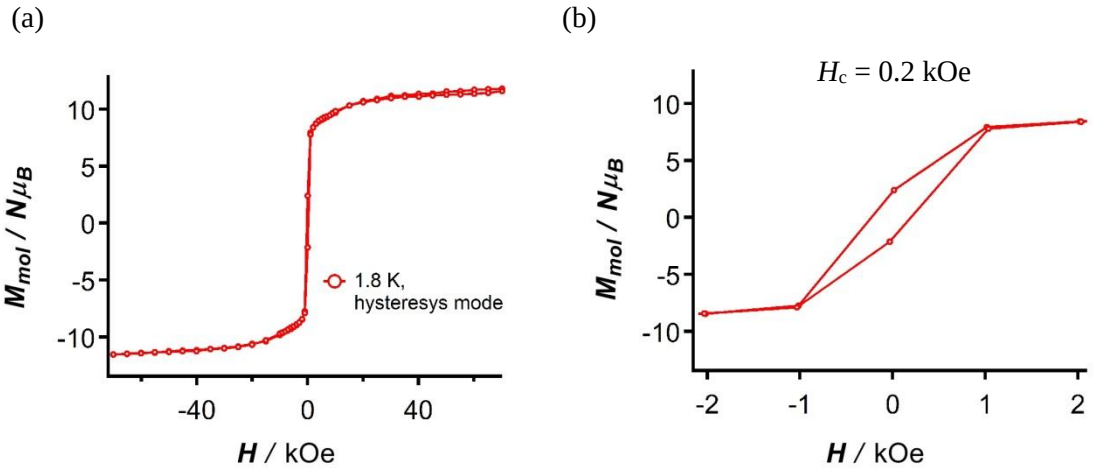

Figure 6-13. (a)The plot of M_{mol} vs. H measured by the hysteresis mode of SQUID system for [{Dy(tta)$_3$}$_2$(**C1(pyO)$_2$**)]$_n$. Figure (b) showed the expanded region of the Figure (a).

Complex **5c'** showed the slow magnetic relaxation behaviour in the ac magnetic property measurement. The peak-top intensities of χ''_{mol} signals were decreased below 6 Hz, suggesting that interchain antiferromagnetic interaction was active at the extremely low temperature as observed in the complex **5b'**. The $\chi'_{mol}T$ value at 3.0 K and at 1 Hz was 287 $cm^3\ mol^{-1}$ K. The magnetic correlation lengths, *n*, was estimated to be 16 using the following equation, $n\chi'T = (g^2 / 8)\ nS(nS+1)$; g = 2.0, $\chi'T$ =287. From the χ''_{mol} vs. *Temperature* plot, Δ_{eff}/k_B, and the pre-exponential factor, τ_0, was estimated to be 44.8 K and 4.3 x 10^{-9} sec., respectively. The Δ_{eff}/k_B value was obviously higher than that of $[Dy(tta)_3(\mathbf{4C1pyO})]_2$ (**4c'** : 29.5 K), clearly indicating the presence of additional activation energy barrier attributed to the magnetic correlation between the dinuclear Dy units. Similarly, the relaxation time, τ, and the distribution factor of the spin relaxation, α, was extracted in both the χ'_{mol} vs. ν plot and the χ''_{mol} vs. ν plot using the extended Debye's model. The obtained values of χ_s, χ_T, τ, and α were summarized in Table 6-10 and plotted in Figure 6-14c,d. The Δ_{eff}/k_B, and τ_0, was estimated to be 37.9 K and 5.0 x 10^{-8} sec., respectively. The Δ_{eff}/k_B was smaller than that extracted from the temperature dependent plot, though 6.6 K higher than that extracted in the frequency dependence plot of **4c'**. The value of 6.6 K showed the good corresponding to the one obtained in the $ln\chi_{mol}T$ vs. T^{-1} plot (Figure 6-12b: Δ_ζ = 6.2 K). The α values, 0.08-0.40 between the temperature ranges of 6.0-1.8 K suggested the wide distribution of spin relaxation at the extremely low temperature. The Cole-Cole plot between the temperature range of 2.2 - 3.3 K was fitted by the generalized Debye's model (Figure 6-14e), and the obtained parameters were listed in Table 6-10 to 6-12.

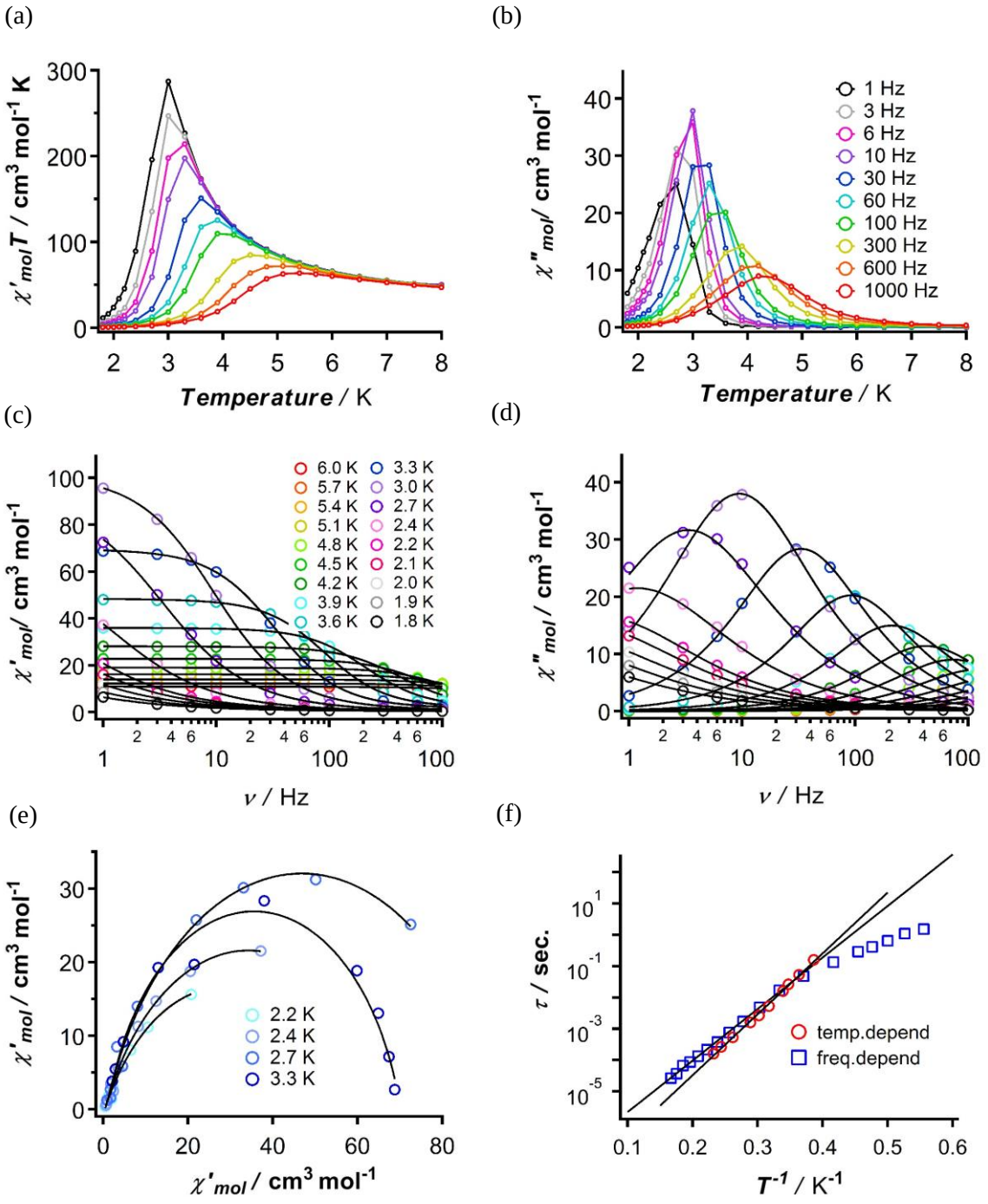

Figure 6-14. The plot of (a) $\chi'_{mol}T$ vs. *T*emperature, (b) χ''_{mol} vs. *T*emperature, (c) χ'_{mol} vs. ν, (d) χ''_{mol} vs. ν, (e) Cole-Cole diagram, and (f) Arrhenius law of $[\{Dy(tta)_3\}_2(\mathbf{C1(pyO)_2})]_n$. The black bold lines in (c), and (d) show the fitting lines obtained from the extended Debye's model. In (e), black lines represent the best-fit results of generalized Debye's equation. The solid lines in (f) indicate the best fit result extracted from the Arrhenius law.

Table 6-10. The extracted peak top temperature for each frequency in the plot of χ''_{mol} vs. Temperature

Frequency (Hz)	**1**	**3**	**6**	**10**	**30**	**60**
Temp.(K)	2.59	2.75	2.88	2.95	3.15	3.31
T^{-1} (K^{-1})	0.3861	0.363636	0.347222	0.338983	0.31746	0.302115
τ (sec.)	0.001592	0.000530	0.000265	0.015924	0.005308	0.002654
Frequency (Hz)	**100**	**300**	**600**	**1000**		
Temp.(K)	3.46	3.82	4.10	4.31		
T^{-1} (K^{-1})	0.289017	0.26178	0.243902	0.232019		
τ (sec.)	0.001592	0.000531	0.000265	0.000159		

Table 6-11. The extracted parameters for selected temperatures by the extended Debye's fitting in the plot of χ'_{mol} vs. ν, and χ''_{mol} vs. ν.

***Temp.*(K)**	**1.8**	**1.9**	**2.0**	**2.1**	**2.2**	**2.4**	**2.7**	**3.0**	**3.3**
χ_s (cm^3mol^{-1})	0.349962	0.307587	0.31422	0.334145	0.407497	0.290956	0.30414	0.636877	1.5399
χ_T (cm^3mol^{-1})	39.6714	46.1488	48.5988	52.9176	56.2495	69.4674	93.601	101.988	69.7866
τ (sec.)	1.52895	1.09361	0.64639	0.413223	0.288661	0.134564	0.04774	0.016805	0.004789
α	0.390099	0.376894	0.357863	0.338851	0.319375	0.291706	0.241113	0.180756	0.116959
***Temp.*(K)**	**3.6**	**3.9**	**4.2**	**4.5**	**4.8**	**5.1**	**5.7**	**5.7**	**6.0**
χ_s (cm^3mol^{-1})	1.88203	2.07279	2.13396	2.28533	2.27669	2.39503	3.28981	1.55546	1.64554
χ_T (cm^3mol^{-1})	48.4403	36.0018	28.1264	22.7812	18.9887	16.1581	13.9822	12.291	10.9258
τ (sec.)	0.001727	0.000756	0.000378	0.000217	0.000132	8.68E-05	6.64E-05	3.67E-05	2.64E-05
α	0.088562	0.079215	0.082840	0.081084	0.088988	0.096673	0.079186	0.148668	0.167739

Table 6-12. The extracted parameters for selected temperatures by the generalized Debye's fitting in the plot of χ''_{mol} vs. χ'_{mol} (Cole-Cole plot)

***Temp.*(K)**	**2.2**	**2.4**	**2.7**	**3.3**
χ_s (cm^3mol^{-1})	0.39131	0.404842	0.553977	1.07112
χ_T (cm^3mol^{-1})	56.7064	68.1098	93.1307	70.0697
α	0.320666	0.277287	0.229133	0.156853

Section 6. Chapter conclusion

For the construction of 4f-2p heterospin SCMs, a novel bridging ligand **D1(pyO)$_2$** carrying one diazo moiety and two pyridine-*N*-oxide units as a magnetic coupler was successfully prepared. Mixing the **D1(pyO)$_2$** with Ln(tta)$_3$ in 1 : 2 ratio gave the 1-D chain complexes consisted of the connection of dinuclear Ln units formulated as [{Ln(tta)$_3$}$_2$(**D1(pyO)$_2$**)]$_n$. The local coordination structure and magnetic property before irradiation were very similar to those of dinuclear complex, [Ln(tta)$_3$(**4D1pyO**)]$_2$. On the other hand, interestingly enough, the optical property, and the magnetization after the photolysis were quite different to those of discrete complexes. Complexation of both sides of pyO moieties of **D1(pyO)$_2$** induced more effective blue shift of absorption band of diazo component (507 nm to 440-450 nm) in the UV-vis. absorption spectra measurements.

In the magnetic property measurement, ferromagnetic correlation within the chain was observed in the temperature dependence of DC magnetic susceptibility measurement after irradiation The correlation lengths estimated from the maximum value of $\chi_{mol}T$ product and the quantum spin number of each dinuclear unit for Gd (S = 16/2), Tb (S = 14/2), and Dy (S = 12/2) chain complexes were 3.3, 6.1, and 16 respectively. [{Tb(tta)$_3$}$_2$(**C1(pyO)$_2$**)]$_n$ and [{Dy(tta)$_3$}$_2$(**C1(pyO)$_2$**)]$_n$ showed the slow magnetic relaxation typical to the SCMs. The obtained activation barrier and pre-exponential factor were somehow higher and smaller than those of [Tb(tta)$_3$(**4C1pyO**)]$_2$, and [Dy(tta)$_3$(**4C1pyO**)]$_2$, clearly indicating a certain, non-negligible effect of the magnetic correlation in the 4f-2p heterospin chain system (Table 6-13). The most interestingly, [{Dy(tta)$_3$}$_2$(**C1(pyO)$_2$**)]$_n$ did show the magnetic hysteresis at 1.8 K though the discrete complex, [Dy(tta)$_3$(**4C1pyO**)]$_2$ didn't.

As mentioned above, combining the SCM strategy to the 4f-2p heterospin systems could have the crucial role for the modulation of both the molecular structure and magnetization, although the local magnetic axis (direction of magnetic anisotropy on the spin ground state) was not investigated in this stage. The determination of the local magnetic anisotropy and the construction of various kinds of additional 1-D heterospin systems for the quantitative analyses (i.e. preparation of aminoxyl bridging ligand with pyO units and its polymeric Ln complexes) are required and now under investigating.

Table 6-13. The activation barrier and the pre-exponential factor estimated from the temperature dependence of ac magnetization plots for Tb, and Dy complexes discussed in chapter 5, and chaper6.

Before irradiation	Tb-dinuclear (**4b**)	Tb-chain (**5b**)	Dy-dinuclear (**4c**)	Dy-chain (**5c**)
U_{eff} / k_B (K)	not estimated	not estimated	97.8	90.0 (Δ_{eff} / k_B)
τ_0 (sec.)	not estimated	not estimated	5.8 x 10^{-10}	8.8 x 10^{-8}
After irradiation	Tb-dinuclear (**4b'**)	Tb-chain (**5b'**)	Dy-dinuclear (**4c'**)	Dy-chain (**5c'**)
U_{eff} / k_B (K)	32.2	33.9 (Δ_{eff} / k_B)	29.5	44.8 (Δ_{eff} / k_B)
τ_0 (sec.)	3.5 x 10^{-9}	2.9 x 10^{-10}	2.9 x 10^{-8}	4.3 x 10^{-9}

Chapter 7. Conclusion Remarks

In this report, at first, **NOpy$_2$** was prepared for the quantitative investigation of exchange coupling in the 2p-3d heterospin chain complexes. Cu ion and aminoxyl ferromagnetically interacted and the $J_{NOpy2\text{-}Cu}/k_B$ value was easily controlled by modulating the Lewis basicities of chelating ligand **L** on Cu ions.

NOpy$_2$ also made complexes with Co(hfpip-X)$_2$ with high magnetic anisotropies. 3d spins of Co ions and 2p spin of aminoxyl ferromagnetically interacted, gave slow magnetic relaxation behavior attributed to the SMMs. The discrepancy of the direction between local magnetic axis and chain axis prevented us giving additional activation barrier for the spin re-orientation derived from the magnetic correlation within the chain system.

For the construction of 4f-2p systems, three types of diazo-pyridine based magnetic couplers were newly designed and successfully obtained. By combining these magnetic couplers with Ln ions, novel heterospin 4f-2p molecule based magnets were prepared and were both crystallographically and magnetically investigated thoroughly.

The tridentate chelating ligand **L1** carrying one diazo moiety on the 4-position of 2,6-bis-(methoxymethyl)pyridine component was coordinated to Ln(hfac)$_3$ in 1:1 ratio, resulted in giving the mononuclear complexes formulated as [Ln(hfac)$_3$(**L1**)]. In these complexes, diazo moieties were connected with the Ln ions through the nitrogen atoms of pyridine rings. After the photoirradiation in the toluene solution, the produced carbene was antiferromagnetically interacted with the 4f spins of Ln ions, provided the lower spin ground state compared to before irradiation. The ac magnetic properties of [Dy(hfac)$_3$(**L1**)] after irradiation was clearly affected by the magnetic interaction between 4f and 2p spins, indicate a certain effect of the conjugated organic spins in the 4f-2p heterospin systems.

4D1pyO and **3D1pyO** formed the dinuclear complexes with Ln(tta)$_3$ in 2:2 ratio, giving the [Ln(tta)$_3$(**4D1pyO**)]$_2$ 2CHCl$_3$, and [Tb(tta)$_3$(**3D1pyO**)]$_2$ 4CHCl$_3$, respectively. The resulted carbenes by the photolysis ferromagnetically interacted with Ln ions through pyridine-*N*-oxide units, resulted in the higher spin ground states. The most interestingly, [Tb(tta)$_3$(**4D1pyO**)]$_2$ was not an SMM, on the other hand, the photoproduct [Tb(tta)$_3$(**4C1pyO**)]$_2$ undoubtedly showed the slow magnetic relaxation behavior typical to the SMM. Considering the fact that [Tb(tta)$_3$(**3C1pyO**)]$_2$ was not an SMM, the magnetic exchange interaction within the 4f-2p heterospin system played a crucial role for the observation of slow relaxation of magnetization. Notably, this complex is the first compound of the external stimuli responsive SMM accompanying the change of spin ground state. By the way, the activation barrier for the spin reorientation of [Dy(tta)$_3$(**4D1pyO**)]$_2$ reduced after irradiation, though the relaxation regime might change through the photoirradiation. The elucidation of the detailed effect of organic spins in 4f-2p systems is now challenging in this stage, but we could indicate the

extremely high possibility of the introduction of organic spins in Ln based molecule magnets.

D1(pyO)$_2$ was prepared in order to explore the further usability of heterospin molecule based magnet in the 1-D chain complexes. **D1(pyO)$_2$** was able to couple neighboring dinuclear Ln units by the both sides of pyridine-*N*-oxide components. After the photoirradiation, its polymeric chain complexes formulated as [{Ln(tta)$_3$}$_2$(**D1(pyO)$_2$**)]$_n$ *n*CH_2Cl_2 *n*PhCN obviously showed the ferromagnetic correlations within the chain structures. [{Tb(tta)$_3$}$_2$(**C1(pyO)$_2$**)]$_n$ and [{Dy(tta)$_3$}$_2$(**C1(pyO)$_2$**)]$_n$, the photoproducts of [{Tb(tta)$_3$}$_2$(**D1(pyO)$_2$**)]$_n$, and [{Dy(tta)$_3$}$_2$(**D1(pyO)$_2$**)]$_n$, respectively showed the SCM behaviors affected by the magnetic correlations through the chain. This noteworthy results opened up the further possibility of carbene based magnetic coupler for the construction of 4f ion based molecule magnets with extremely high blocking temperature and high thermal activation barriers in future.

Though the correct roles of organic spins in the 4f-2p systems are not completely clarified in this report, I was able to show the unprecedented interesting strategy for the construction of newly designed molecular magnets. Further investigation including the examination of the effect of the spin multiplicities of carbenes and the preparation of **NO(pyO)$_2$** for the quantitative analyses in the 4f-2p heterospin chain complexes are undergoing along with the construction of pyridine-*N*-oxide based 3d-2p heterospin magnets (Figure 7-1).

1. Controlling the magnetic properties by changing the spin multiplicity

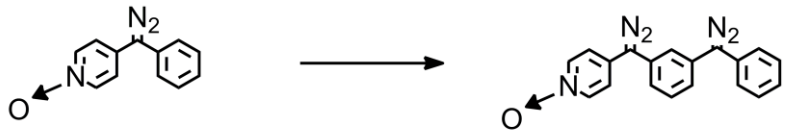

4D1pyO (this work) **4D2pyO**

2. Preparation of **NOpyO$_2$** for the quantitative analyses in the 4f-2p chain complexes

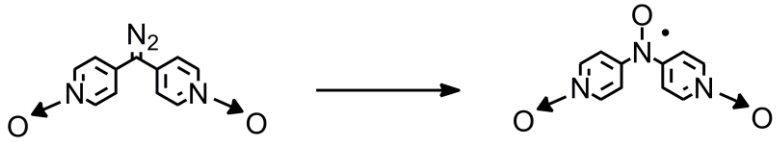

D1(pyO)$_2$ (this work) **NO(pyO)$_2$**

Figure 7-1. The next strategies for the further development of our heterospin molecule based magnet

Chapter 8. Experimental chapter

Section .1 Instrument section

UV-vis. absorption spectrum measurement

UV-vis. absorption spectrum measurement in the solution state was recorded on a JASCO V570 spectrometer in the ambient conditions. All solvents were commercially available. Solid state diffuse reflection measurements for Ln complexes were performed on the same equipment using the solid samples diluted by KBr at room temperature. The obtained data were converted to absorption spectra by the KM function.

IR spectrum measurement

Infrared spectrum was recorded on a JASCO 420 FT-IR spectrometer. All samples were diluted by KBr, and then molded to a thin pellet.

NMR spectrum measurement

^{1}H NMR spectra and ^{13}C NMR spectra were measured on a Bruker Biospin AVANCE III 500 Fourier transform spectrometer using $CDCl_3$ or CD_3OD.

ESI mass spectrum measurement

ESI mass spectra (ESI MS) were recorded on a Bruker Daltonics microTOF spectrometer using MeOH.

X-ray single crystal analysis

X-ray diffraction (XRD) spectra were performed with a BrukerD2PHASER. All the X-ray data were collected on a Bruker APEX-II diffractometer with graphite monochromated MoK_α radiation (0.7107 Å). The refinements were converged using the full-matrix least-squares method of the Crystal Structure software package[35] and SHELX97[36]. All non-hydrogen atoms were refined anisotropically. Hydrogen atoms were included at standard positions (C-H = 0.96 Å, C-C-H = 120 °) and refined isotropically using a rigid model.

Powder state X-ray diffraction measurement (PXRD)

XRD measurements for powder samples were carried out at a 2θ angle of 5–50 ° at 25 °C.

EPR spectrum measurement

EPR measurements were performed using an X band microwave system (JEOL ES-SCEX)

equipped with a continuous He flow type cryostat (Oxford ESR 910) operating down to 5 K.

Elemental Analyse

Elemental Analyses were performed at the Analytical Center of the Faculty of Science of Kyushu University.

Magnetic property measurement

Direct current (dc) and alternating current (ac) magnetic susceptibility data were obtained on a Quantum Design MPMS5S or Quantum Design MPMS7 SQUID magneto/susceptometer, and corrected for the magnetization of the sample holder and capsule, and for diamagnetic contributions to the samples, which were estimated from Pascal's constants. The diazo moieties of the complexes were photolyzed inside the sample room of a SQUID apparatus.

Photolysis method A

For the production of carbene in the SQUID apparatus, each sample was 2 cm separately attached to the top of the glass fibber equipped to the 532 nm of DPSS laser. The irradiation was performed under 10 K in order to avoid the diminishment of resulted carbene by the thermal contribution.

Photolysis method B

514 nm of solid He laser was used alternative to the 532 nm of DPSS laser for the effective photolysis for the Ln-diazo chain complexes.

Section 2. Theoretical section

Evaluation of the magnetic exchange interaction between Cu ion and **NOpy$_2$** : ferromagnetic chain model including the interchain exchange interaction

$$\chi_{chain} = \frac{\chi}{1-\frac{2zJ'\chi}{Ng^2\mu_B{}^2}}$$

with

$$\chi = \frac{4Ng^2\mu_B{}^2}{kT}\left\{\frac{1+5.98x+16.9x^2+29.4x^3+29.8x^4+14.0x^5}{1+2.80x+7.01x^2+8.05x^3+4.57x^4}\right\}^{2/3}, \quad x = J/2kT$$

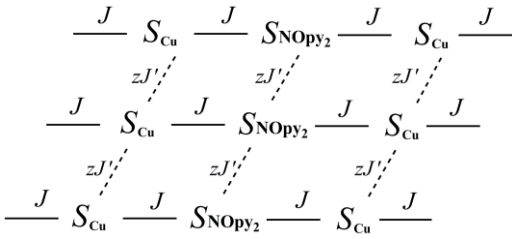

$S_{\mathbf{NOpy2}}$: spin angular momentum of **NOpy$_2$**, S_{Cu} : spin angular momentum of Cu ion

J : exchange interaction between **NOpy$_2$** and Cu ion, zJ' : interchain interacion

Evaluation of the magnetic exchange interaction between Co ion and **NOpy$_2$** : branched chain model

$\chi_{mol} = (Nb^2/kT)\,[u^2a + 2uc + (ua + c)^2/b + d] / (a + b)$

with

$a = (2e^z \cosh 3y + 1)\cosh 6x + (2e^z \cosh y + 1)\cosh 2x$

$b = 2[e^z(\cosh 3y + \cosh y) + 1]$

$c = \{e^z[e^{-3y}(3v - k) + e^{3y}(3v + k)] + 3v\}\sinh 6x + [e^z(e^{-y}(v - k)) + e^{y}(u + k) + v]\sinh 2x$

$d = \{e^z[e^{-3y}(3v - k)^2 + e^{3y}(3v + k)^2] + (3v)^2\}(1+\cosh 6x) + \{e^z[e^{-y}(v-k)^2 + e^{y}(v+k)^2] + v^2\}(1+\cosh 2x)$

and

$u = g_B / 2,\ v = g_A / 2$

and

$x = J/4kT,\ y = -J'/2kT,\ z = -D/kT$

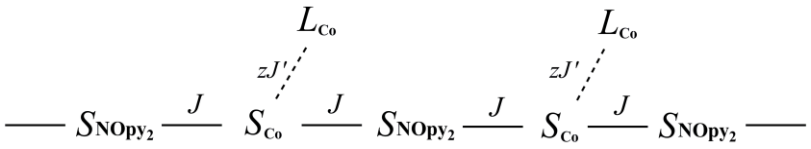

S_{NOpy2} : spin angular momentum of **NOpy$_2$**, S_{Co} : spin angular momentum of Co ion

L_{Co} : orbital angular momentum of Co ion

J : exchange interaction between **NOpy$_2$** and Co, zJ' : spin-orbit interaction of Co ion

Evaluation of the magnetic exchange interaction between Gd ion and carbene in [Gd(hfac)$_3$(**L1**)] after irradiation.

$$\chi_{mol}T = \frac{Ng^2\mu_B{}^2}{3k}\frac{247.5+126e^{9x}+57.5e^{16x}}{10+8e^{9x}+6e^{16x}},\ \chi = -J/kT$$

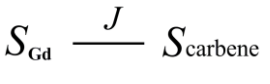

$S_{carbene}$: spin angular momentum of carbene, S_{Gd} : spin angular momentum of Gd ion

J : exchange interaction between carbene and Gd ion

Evaluation of the magnetic exchange interaction between Gd ions in [Gd(tta)$_3$(**xD1pyO**)]$_2$ (x = 3,4) and [{Gd(tta)$_3$}$_2$(**D1(pyO)$_2$**)]$_n$ before irradiation.

$$\chi_{mol}T = \frac{2Ng^2\mu_B{}^2}{k}\frac{140+91e^{7x}+55e^{13x}+30e^{18x}+14e^{22x}+5e^{25x}+e^{27x}}{15+13e^{7x}+11e^{13x}+9e^{18x}+7e^{22x}+5e^{25x}+3e^{27x}+e^{28x}},\ \chi = -J/kT$$

S_{Gd} : spin angular momentum of Gd ion

J : exchange interaction between Gd ion and Gd ion

Evaluation of the magnetic exchange interaction between Gd ion and carbene, $J_{Gd\text{-}carbene}$, and carbene-carbene, $J_{carbene}$-$J_{carbene}$, in [Gd(tta)$_3$(**4D1pyO**)]$_2$ after irradiation.

To estimate the values of $J_{car\text{-}car}$ and $J_{Gd\text{-}car}$, a rhombic four-spin system; $H = -J_{Gd\text{-}Gd}$ (S_{Gd1} S_{Gd2}) - $J_{car\text{-}car}$ ($S_{car\,1}$ $S_{car\,2}$) - $J_{Gd\text{-}car}$ (S_{Gd1} S_{car1} + S_{Gd1} S_{car2} + S_{Gd2} S_{car1} + S_{Gd2} S_{car2}, was applied to this spin system. The experimental data in the range of 150 – 30 K were analysed by a FIT-MART program.[28] To avoid the overparameterization, the $J_{Gd\text{-}Gd}/k_B$ value was fixed to -0.08 K, which was obtained by using the data before irradiation. The best fit gave $J_{car\text{-}car}/k_B$ = -8.9 K and $J_{Gd\text{-}car}/k_B$ = 2.4 K, respectively.

$S_{carbene}$: spin angular momentum of carbene,
S_{Gd} : spin angular momentum of Gd ion

$J_{Gd\text{-}Gd}$: exchange interaction between Gd ion and Gd ion
$J_{Gd\text{-}carbene}$: exchange interaction between Gd ion and carbene
$J_{carbene\text{-}carbene}$: exchange interaction between carbene and carbene

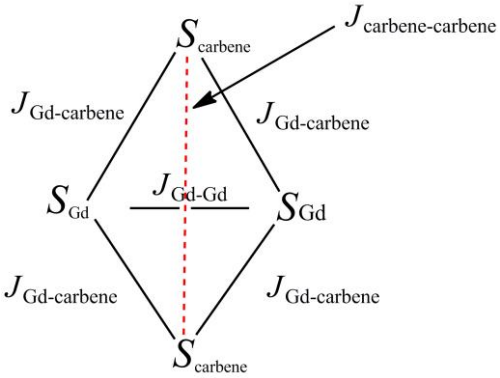

Extended Debye's model applied for the extraction of magnetic relaxation parameters

$$\chi' = \chi_s + (\chi_T - \chi_s)\left\{\frac{\{1+(\omega\tau)^{1-\alpha}\sin 1/2\alpha\pi}{1+2(\omega\tau)^{1-\alpha}\sin 1/2\alpha\pi+(\omega\tau)^{2(1-\alpha)}}\right\}$$

$$\chi'' = (\chi_T - \chi_s)\left\{\frac{(\omega\tau)^{1-\alpha}\cos 1/2\alpha\pi}{1+2(\omega\tau)^{1-\alpha}\sin 1/2\alpha\pi+(\omega\tau)^{2(1-\alpha)}}\right\}$$

Section 3. Materials and method

Bis{1,1,1,2,2,6,6,7,7,7-decafluoro-3,5-heptanedione}cooper(II) monohydrate, $Cu(dfhd)_2H_2O$;
To a solution of 1,1,1,2,2,6,6,7,7,7-decafluoro-3,5-heptanedione (924 mg, 3.0 mmol) in CH_3OH (1.0 ml) was added a solution of 1M NaOH water solution. After stirring for 5 min, a solution of $CuCl_22H_2O$ (255 mg, 1.5 mmol) was added and stirred for 10 min. The solution was extracted with EtOAc three times and the combined EtOAc solution was dried with $MgSO_4$. After evaporating of EtOAc solution, $Cu(dfhd)_2$ H_2O (620 mg, 0.9 mmol) was obtained as a bluish green solid in a 58% yield. m.p. 75 − 77 °C, IR (KBr disk) 1636 (νC=O), 1325 (νC−F), 1201 (νC−F), 1145 (νC−F), 1030 (νC−F) cm-1, UV-Vis (CHCl3) λmax = 693 (ε = 96) nm, Anal. Calcd for $C_{14}H_6O_5F_{20}Cu$: C 24.17, H 0.58%; found: C 24.09, H 0.59%.

$[Cu(tfac)_2$**NOpy₂**$]_n$ (**1a**)
Solutions of aminoxyl-dipyridine ligand **NOpy₂** (24 mg, 0.13 mmol) in $CHCl_3$ (2.0 ml) and $Cu(tfac)_2$ (46 mg, 0.13 mmol) in $CHCH_3$ (2 ml) were mixed and kept at rt for 2 days. Complex **1a** was obtained as single crystals of dark red plates (50 mg, 0.09 mmol) in a 72% yield. m.p. (dec.) 158 – 160 °C, IR (KBr disck) 1622 (νC=O), 1300 (νC−F), 1212 (νC−F), 1141 (νC−F) cm^{-1}, Anal. Calcd for $C_{20}H_{16}N_3O_5F_6Cu$: C 43.21, H 2.90, N 7.56%; found: C 43.04, H 2.98, N 7.66%.

$[Cu(hfac)_2$**NOpy₂**$]_n$ (**1b**)
Polymeric complex **1b** was prepared in a manner similar to the procedure for 1 by using $Cu(hfac)_2$ in place of $Cu(tfac)_2$. Complex **1b** was obtained as single crystals of dark red needles in a 60% yield. m.p. (dec) 205 − 208 °C, IR (KBr disk) 1647 (νC=O), 1255 (νC−F), 1212 (νC−F), 1143 (νC−F) cm^{-1}, Anal. Calcd for $C_{20}H_{10}N_3O_5F_{12}Cu$: C 36.19, H 1.52, N 6.33 %; found: C 36.21, H 1.56, N 6.44 %.

$[Cu(dfhd)_2$**NOpy₂**$]_n$ (**1c**)
Polymeric complex **1c** was prepared in a manner similar to the procedure for 1 by using $Cu(dfhd)_2H_2O$ in place of $Cu(tfac)_2$. **1c** was obtained as single crystals of dark red plates in a 65% yield. m.p. (dec) 250 − 255 °C, IR (KBr disk) 1653 (νC=O), 1330 (νC−F), 1218 (νC−F), 1197 (νC−F), 1169 (νC−F), 1147 (νC−F), 1119 (νC−F), 1029 (νC−F) cm^{-1}, Anal. Calcd for $C_{24}H_{10}N_3O_5F_{20}Cu$: C 33.37, H 1.17, N 4.86%; found: C 33.40, H 1.19, N 5.04%.

hfpip-X Derivatives; X = F, Cl, Cl_3, Br, I, F_3, F_5,

These ligands were prepared in a manner similar to the procedure for hfpip by using the corresponding substituted aniline derivative in place of aniline.

hfpip-F; Mp: 59-60 °C, ^{1}H-NMR (270 MHz, $CDCl_3$) δ 7.21 － 7.08 (m, 4H), 6.04 (s, 1H), ESI MS 324.0 [M + Na]+ , Anal. Calcd for $C_{11}H_6F_7NO$: C 43.87, H 2.01, N 4.65 %; found: C 43.90, H 1.84, N 4.79 %.

hfpip-Cl; Mp: 68-70 °C, ^{1}H-NMR (270 MHz, $CDCl_3$) δ 7.42 － 7.38 (d, J = 8.8 Hz, 2H), 7.21-7.18 (d, J = 8.7 Hz, 2H), 6.05 (s, 1H), ESI MS 340.0 [M + Na]+, Anal. Calcd for $C_{11}H_6F_6ClNO$: C 41.60, H 1.90, N 4.41 %; found: C 41.60, H 1.83, N 4.50 %.

hfpip-Br; Mp: 77-82 °C, ^{1}H-NMR (270 MHz, $CDCl_3$) δ 7.56 (d, J = 7.5 Hz, 2H), 7.14 (d, J = 7.5 Hz, 2H), 6.05 (s, 1H), FAB MS (in m-NBA matrix), 361 [M + H]+, Anal. Calcd for $C_{11}H_6F_6BrNO$: C 36.49, H 1.67, N 3.87 %; found: C 36.59, H 1.75, N 3.97 %.

hfpip-I; Mp: 71-75 °C, ^{1}H-NMR (270 MHz, $CDCl_3$) δ 7.75 (d, J = 8.8 Hz, 2H), 7.00 (d, J = 8.7 Hz, 2H), 6.05 (s, 1H), ESI MS 431.9 [M + Na]+, Anal. Calcd for $C_{11}H_6F_6INO$: C 32.30, H 1.48, N 3.42 %; found: C 32.39, H 1.44, N 3.51 %.

hfpip-F_3; Mp: 35-36 °C, ^{1}H-NMR (270 MHz, $CDCl_3$) δ 6.99-6.94 (m, 2H), 6.09 (s, 1H), ESI MS 360.0 [M + Na], Anal. Calcd for $C_{11}H_4F_9NO$: C 39.19, H 1.20, N 4.15 %; found: C 39.18, H 1.22, N 4.28 %.

hfpip-F_5; Mp: 115-116 °C, ^{1}H-NMR (270 MHz, $CDCl_3$) δ 6.21 (s, 1H), ESI MS 396.0 [M + Na]+, Anal. Calcd for $C_{11}H_2F_{11}NO$: C 35.41, H 0.54, N 3.75 %; found: C 35.63, H 0.61, N 3.96 %.

hfpip-Cl_3; Mp: 70-72 °C, ^{1}H-NMR (270 MHz, $CDCl_3$) δ 7.33 (s, 2H), 6.10 (s, 1H), ESI MS 407.9, 409.9, 411.9. [M + Na]+, Anal. Calcd for $C_{11}H_4F_6Cl_3NO$ /0.2 n-Hexane : C 36.29, H 1.70, N 3.47 %; found: C 36.38, H 1.67, N 3.52 %.

Co(hfpip-X)$_2$ Complexes;

These complexes were prepared in a manner similar to the procedure for Co(hfpip)$_2$ by using the corresponding substituted hfpip ligand. Co(hfpip-X)$_2$ complexes were obtained as red oils and used for the preparation of 1:1 complexes without further purification.

[Co(hfpip-X)$_2$(**NOpy$_2$**)]$_n$; X = H , F , F3 , F5 , Cl , Cl_3 , Br , and I .

These complexes were prepared by mixing the solutions of Co(hfpip-X)$_2$ and **NOpy$_2$** in suitable solvents in 1 : 1 ratio and then leaving the solution at low temperature (~ 0 °C).

[Co(hfpip-H)$_2$(NOpy$_2$)]$_n$, (2a) : novel compound

A solution of Co(hfpip-H)$_2$ (110 mg, 0.18 mmol) in acetonitrile (6 mL) and a solution of **NOpy$_2$** (32.9 mg, 0.18 mmol) in methanol (6 mL) were mixed. The solution mixture was kept at –3 °C for 2 days. The polymeric complex, **2a**, was obtained as dark red block crystals (73.6 mg). Mp (dec):

210-211 °C, Anal. Calcd for $C_{32}H_{20}N_5O_3F_{12}Co$: C 47.48, H 2.49, N 8.65 %; found: C 47.23, H 2.69, N 8.59 %.

[Co(hfpip-F)$_2$(NOpy$_2$)]$_n$, (2b) : novel compound

A solution of Co(hfpip-F)$_2$ (120 mg, 0.18 mmol) in acetonitrile (5 mL) and a solution of **NOpy$_2$** (36.0 mg, 0.19 mmol) in MeOH (5 mL) were mixed. The solution mixture was kept at 4 °C for 2 days. Complex, **2b**, was obtained as dark red block crystals (50.8 mg). Mp (dec): 252-256 °C, Anal. Calcd for $C_{32}H_{18}N_5O_3F_{14}Co$: C 42.73, H 2.02, N 10.90 %; found: C 42.60, H 2.01, N 11.13 %.

[Co(hfpip-F$_3$)$_2$(NOpy$_2$)]$_n$, (2c) : novel compound

A solution of Co(hfpip-F$_3$)$_2$ (242 mg, 0.31 mmol) in acetonitrile (10 mL) and a solution of **NOpy$_2$** (57.0 mg, 0.31 mmol) in CH_2Cl_2 (10 mL) were mixed. The solution mixture was kept at 4 °C for 2 days. Complex, **2c**, was obtained as dark red block crystals (66.6 mg). Mp (dec) > 300 °C, Anal. Calcd for $C_{32}H_{14}N_5O_3F_{18}Co$: C 42.03, H 1.63, N 7.85 %; found: C 41.90, H 1.54, N 7.63 %.

[Co(hfpip-F$_5$)$_2$(NOpy$_2$)]$_n$, (2d) : novel compound

A solution of Co(hfpip-F5)2 (94 mg, 0.11 mmol) in ethyl acetate (4 mL) and a solution of **NOpy$_2$** (20.5 mg, 0.11 mmol) in acetonitrile (4 mL) were mixed. The solution mixture was kept at –3 °C for 2 days. The polymeric complex, **2d**, was obtained as dark red block crystals (27 mg). Mp (dec): 240-242 °C, Anal. Calcd for $C_{32}H_{10}N_5O_3F_{22}Co$: C 38.85, H 1.02, N 7.08 %; found: C 39.03, H 1.10, N 7.08 %.

[Co(hfpip-Cl)$_2$(NOpy$_2$)]$_n$, (2e) : novel compound

A solution of Co(hfpip-Cl)$_2$ (140 mg, 0.20 mmol) in acetonitrile (4 mL) and a solution of **NOpy$_2$** (40.0 mg, 0.21 mmol) in $CHCl_3$ (4 mL) were mixed. The solution mixture was kept at 4 °C for 2 days. Complex, **2e**, was obtained as dark red platelet crystals (129 mg). Mp (dec): 210 °C, Anal. Calcd for $C_{32}H_{18}N_5O_3F_{12}Cl_2Co$ /0.25$CHCl_3$: C 42.65, H 2.03, N 7.71 %; found: C 42.35, H 1.99, N 7.90 %.

[Co(hfpip-Cl$_3$)$_2$(NOpy)$_2$]$_n$, (2f) : novel compound

A solution of Co(hfpip-Cl$_3$)$_2$ (90 mg, 0.11 mmol) in acetonitrile (5 mL) and a solution of **NOpy$_2$** (20.0 mg , 0.11 mmol) in acetonitrile (2 mL) were mixed. The solution mixture was kept at –3 °C for 2 days. The complex, **2f**, was obtained as dark red platelet crystals (80 mg). Mp (dec) > 300 °C, Anal. Calcd for $C_{32}H_{14}N_5O_3F_{12}Cl_6Co$ /CH_3CN: C 38.63, H 1.62, N 7.95 %; found: C 38.64, H 1.65, N 7.99 %.

[Co(hfpip-Br)$_2$(NOpy$_2$)]$_n$, (2g) : novel compound

A solution of Co(hfpip-Br)$_2$ (170 mg, 0.22 mmol) in acetonitrile (8 mL) and a solution of **NOpy$_2$** (41.0 mg , 0.22 mmol) in acetone (8 mL) were mixed. The solution mixture was kept at 4 °C for 2 days. Complex, **2g**, was obtained as dark red platelet crystals (90.5 mg). Mp (dec): 240 °C, Anal. Calcd for $C_{32}H_{18}N_5O_3F_{12}Br_2Co$ /0.5acetone: C 40.39, H 2.12, N 7.03 %; found: C 40.57, H 2.25, N 7.13 %.

[Co(hfpip-I)$_2$(NOpy$_2$)]$_n$, (2h) : novel compound

A solution of Co(hfpip-I)$_2$ (130 mg, 0.15 mmol) in acetonitrile (4 mL) and a solution of **NOpy$_2$** (28.0 mg , 0.15 mmol) in $CHCl_3$ (4 mL) were mixed. The solution mixture was kept at 4 °C for 2 days. Complex, **2h**, was obtained as dark red platelet crystals (80.6 mg). Mp (dec): 230 °C, Anal. Calcd for $C_{32}H_{18}N_5O_3F_{12}I_2Co$ /0.5$CHCl_3$: C 34.82, H 1.66, N 6.25 %; found: C 34.66, H 1.71, N 6.37 %.

4-oxo-4*H*-pyran-2,6-dicarboxylic acid (chelidonic acid)

To the 300ml of ethanolic solution of sodium ethoxide (68 g, 1 mol) was added to 144 ml of diethyl oxalate (1mol) and 38 ml of distilled acetone at room temperature. After heating at 70 °C for three hours on the oil bath, 100ml of H_2O and 200 ml of HCl aq. were added and heated at 70 °C for 14 hours additionally. The mixture solution was cooled to room temperature and then evaporated to c.a. 200 ml. Resulting beige solid was separated by the suction filtration and then washed by H_2O and acetone. 4-oxo-4*H*-pyran-2,6-dicarboxylic acid was obtained as pale-yellow solid in 50.0 % yield.
IR (KBr disk) 1747, 1728, 1640 cm^{-1}

4-hydroxypyridine-2,6-dicarboxylic acid (chelidamic acid)

25 g of chelidonic acid (136 mmol) was suspended to 100 ml of H_2O and cooled to 5 °C on the ice bath. 250 ml of 28% NH_3 aq. was added at 5 °C and the mixture was stirred at room temperature over night. 5 g of charcoal was added and the solution was heated under reflux for 30min, and then filtered through Celite® 545-RVS. The filtrate was evaporated to c.a. 200 ml under reduced pressure. 30 ml of HCl aq. was added, and the white precipitate was separated by the suction filtration. 20 g of 4-hydroxypyridine-2,6-dicarboxylic acid was obtained as a white solid in 80.4 % yield.
IR (KBr disk) 1714, 1616 cm^{-1}

diethyl 4-bromopyridine-2,6-dicarboxylate

To a petroleum ether solution of Br_2 (17.4ml, 336 mmol) was added to 32.0 ml of PBr_3 (340 mmol) in 40 ml of petroleum ether portionwise at room temperature. The resulting PBr_5 was separated by decantation. The mixture of PBr_5 and 15.2 g of chelidamic acid (80 mmol) was heated to 90 °C for three hours on the oil bath in the neat condition. After cooling to room temperature, 100 ml of $CHCl_3$

was added and the solution was cooled to 0 °C. 280 ml of distilled ethanol was thoroughly added over two hours, and the mixture was stirred at room temperature over night. Organic solvent was removed under reduced pressure and the crude product was purified by the silica gel column chromatography using dichloromethane/*n*-hexane as eluent solvents gave 12.0 g of diethyl 4-bromopyridine-2,6-dicarboxylate as a pale yellow solid (52.6 % yield).

4-bromo-2,6-bis(hidroxymethyl)pyridine

9.0 g of diethyl 4-bromopyridine-2,6-dicarboxylate (29.8 mmol) was dissolved to 200 ml of methanol. 8.4 g of sodium borohydride was added and the mixture was heated under reflux for two hours. After cooling to room temperature, 20 ml of HCl aq. was added and the precipitated inorganic salt was removed by filtration, then the filtrate was neutralized by $NaHCO_3$ aq. The pale yellow colored precipitate was separated and washed by small amount of H_2O. 5.7 g of 4-bromo-2,6-bis(hidroxymethyl)pyridine was obtained after drying under the reduced pressure. (87.7 % yield)

4-bromo-2,6-bis(methoxymethyl)pyridine

3.0 g of 4-bromo-2,6-bis(hidroxymethyl)pyridine (13.8 mmol) was dissolved to 100 ml of distilled THF at room temperature. 3.6 g of sodium hydride (90 mmol) and 6.7 ml of methyl iodide (110 mmol) were added, and the solution was stirred at room temperature over night. 50 ml of H_2O was added thoroughly and the organic layer was separated. Water layer was extracted by 30 ml of dichloromethane three times and the organic layer was combined, dried over $MgSO_4$. Removing the solvent gave 2.4 g of 4-bromo-2,6-bis(methoxymethyl)pyridine as a pale yellow solid.

(2,6-bis(methoxymethyl)pyridin-4-yl)(phenyl)methanol : novel compound

In a 200 ml three necked round-bottom flask, 1.23 g of 4-bromo-2,6-bis(hidroxymethyl)pyridine (5 mmol) was dissolved to 20 ml of distilled THF and was added to 6.3 ml of 0.95M EtMgBr in THF. After one hour of stirring at room temperature, 0.62 ml of benzaldehyde in THF was added and the solution was stirred over night. The reaction was quenched by adding 30 ml of H_2O and the water layer was extracted by 50 ml of dichloromethane three times. After removing the organic solvent under the reduced pressure, the crude product was purified by the silica gel column chromatography using dichloromethane/methanol as eluents.0.54 g of (2,6-bis(methoxymethyl)pyridin-4-yl)-(phenyl)methanol was obtained as a pale orange oil in 39.6 % yield.

^{1}H-NMR (270 MHz, $CDCl_3$) δ 7.38-7.27 (*m*, 7H), 7.77 (*t*, *J* = 8.0 Hz, 2H), 5.82 (*s*, 1H), 5.01 (*s*, 1H), 4.55 (*s*, 4H), 3.46 (*s*, 6H), ESI MS 296.1 $[M + Na]^+$,

(2,6-bis(methoxymethyl)pyridin-4-yl)(phenyl)methanone : novel compound

In a 50 ml round-bottom flask, 0.54 g of (2,6-bis(methoxymethyl)pyridin-4-yl)- (phenyl)methanol and was dissolved to 20 ml of chloroform and was added to activated MnO_2 (3.1 g, 37 mmol). The solution was heated under reflux for two hours on the oil bath and then cooled to room temperature. Organic layer was filtered through the Celite® 545-RVS. After removing the organic solvent, resulting yellow solid was purified by the silica column chromatography using dichloromethane/methanol. 0.37 g of (2,6-bis(methoxymethyl)pyridin-4-yl)(phenyl)methanone was obtained as a pale yellow oil. (69.0 % yield)

^{1}H-NMR (500 MHz, $CDCl_3$) δ 7.82 (*d*, *J* = 8.0 Hz, 2H), 7.63 (*t*, *J* = 6.3 Hz, 1H), 7.60 (*s*, 2H), 7.51 (*t*, *J* = 8.5 Hz, 2H), 4.65 (*s*, 4H), 3.50 (*s*, 6H), ^{13}C-NMR (125 MHz, $CDCl_3$) δ 195.5, 158.9, 146.1, 136.0, 133.5, 130.1, 128.6, 119.1, 75.18, 58.83, IR (KBr) 1672, 1596, 1371, 1118 cm^{-1}, HR-ESI MS 294.1119 (found), 294.1106 (calcd.) $[M + Na]^+$

4-(hydrazono(phenyl)methyl)-2,6-bis(methoxymethyl)pyridine : novel compound

In a 5 ml round-bottom flask, 82 mg of (2,6-bis(methoxymethyl)pyridin-4-yl)(phenyl)methanone (0.3 mmol) was dissolved to 1 ml of distilled DMSO and was heated to 60°C. After the addition of 310 mg of hydrazine monohydrochloride (4.5 mmol) and 0.15 ml of hydrazine anhydrous (4.5 mmol), the reaction mixture was heated to 90°C and stirred for 1 hour. The solution was cooled to room temperature and then poured into 5 ml of ice cold water. Resulting mixture was extracted with 10 ml of AcOEt three times. The organic layer were combined and back-extracted with 10 ml of H_2O three times and then dried over $MgSO_4$. Removing the solvents gave the 4-(hydrazono(phenyl)methyl)-2,6-bis(methoxymethyl)pyridine as an yellow oil (70 mg) in 81.2 % yield. This compound was used in next step without any further purification in this stage.

4-(diazo(phenyl)methyl)-2,6-bis(methoxymethyl)pyridine, L1 : novel compound

In a 10 ml Erlenmeyer flask, 4-(hydrazono(phenyl)methyl)-2,6-bis(methoxymethyl)pyridine (60 mg, 0.21 mmol) was dissolved to 3 ml of CH_2Cl_2 and was added to 360 mg of activated MnO_2. The reaction mixture was stirred at room temperature in the dark for 30 min. After completion of the reaction, insoluble solid was removed by the suction filtration through Celite® 545-RVS and the filtrate was evaporated to dryness under reduced pressure. **L1** was obtained as reddish oil (60 mg, 0.21 mmol, quant.)

^{1}H-NMR (500 MHz, $CDCl_3$) δ 7.45 (*t*, *J* = 7.8 Hz, 2H), 7.38 (*d*, *J* = 4.3 Hz, 2H) , 7.29 (*t*, *J* = 7.3 Hz, 1H), 7.12 (*s*, 2H), 4.52 (*s*, 4H), 3.47 (*s*, 6H), ^{13}C-NMR (125 MHz, $CDCl_3$) δ 158.3, 141.4, 129.5, 127.4, 127.2, 126.9, 119.1, 113.6, 75.46, 58.82, IR (NaCl) 2047, 1593, 1117 cm^{-1}, HR-ESI MS 306.1205 (found), 306.1218 (calcd.) $[M + Na]^+$

[Ln(hfac)$_3$L1] (Ln = Gd, Tb, and Dy) **: novel compound**

35 mg of Ln(hfac)$_3$ 2H$_2$O and 12 mg of **L1** was mixed in 4 ml of CH_2Cl_2 and 4 ml of *n*-heptane. After standing these solutions at 4 °C in the dark for 2 days, **[Ln(hfac)$_3$L1]** was obtained as reddish orange crystals.

IR (KBr disk) 2061, 1662, 1613, 1254, 1200, 1141 cm^{-1}, Anal. Calcd for $C_{31}H_{20}F_{18}GdN_3O_8$: C 35.07, H 1.90, N 3.96 %, found: C 35.16, H 2.08, N 3.79 %, Anal. Calcd for $C_{31}H_{20}F_{18}TbN_3O_8$: C 35.01, H 1.90, N 3.95 %, found: C 35.31, H 1.99, N 3.89 %, Anal. Calcd for $C_{31}H_{20}F_{18}DyN_3O_8$: C 34.90, H 1.89, N 3.94 %, found: C 34.96, H 2.08, N 3.79 %

4-Benzoylpyridine *N*-oxide

In a 50 ml round-bottom flask, 4-Benzoylpyridine (3.66 g, 20 mmol) was added to 8 ml of glacial acetic acid (140 mmol) and 7 ml of 30 % hydrogen peroxide (62 mmol). The solution was heated to 80 °C for three hours on the oil bath and then cooled to room temperature. 10 ml of water was added and excessive peroxide was quenched by sodium hydrogen sulfite. Resulting mixture was neutralized by sodium carbonate and extracted with 50 ml of CH_2Cl_2 three times. The organic layer were combined and dried over $MgSO_4$. After removing the solvents under reduced pressure, resulting pale yellow solid was re-crystallized from $CHCl_3$/*n*-hexane. 4-Benzoylpyridine *N*-oxide was obtained as a pale yellow block crystal (3.59 g, 18 mmol) in 90.2 % yield.

m.p. 110 – 112 °C, ^{1}H-NMR (500 MHz, $CDCl_3$) δ 8.27 (*d*, *J* = 6.5 Hz, 2H), 7.77 (*t*, *J* = 8.0 Hz, 2H), 7.73 (*d*, *J* = 7.0 Hz, 2H), 7.66 (*t*, *J* = 7.5 Hz, 1H), 7.54 (*t*, *J* = 7.0 Hz, 2H), ^{13}C-NMR (125 MHz, $CDCl_3$) δ 192.0, 139.3, 136.0, 133.3, 133.0, 129.6, 128.8, 126.9, IR (KBr disk) 1654, 1604, 1438, 1258 cm^{-1}, ESI MS 222.1 [M + Na]$^+$, Anal. Calcd for $C_{12}H_9N_1O_2$: C 72.35, H 4.55, N 7.03 %; found: C 72.15, H 4.52, N 7.11 %.

4-(hydorazono(phenyl)methyl) pyridine *N*-oxide : novel compound

In a 50 ml round-bottom flask, 4-Benzoylpyridine (3.0 g, 15 mmol) was dissolved to 20 ml of distilled DMSO and was heated to 60°C. After the addition of 5.2 g of hydrazine monohydrochloride (75 mmol) and 2.4 ml of hydrazine anhydrous (75 mmol), the reaction mixture was heated to 90°C and stirred for 2 hours. The solution was cooled to room temperature and then poured into 50 ml of ice cold water. Resulting mixture was extracted with 50 ml of $CHCl_3$ three times. The organic layer were combined and back-extracted with 50 ml of H_2O three times and then dried over $MgSO_4$. Removing the solvents gave the 4-(hydorazono(phenyl)methyl) pyridine *N*-oxide as a pale yellow solid (2.75 g, 12.9 mmol) in 85.6 % yield. This compound was used in next step without any further purification in this stage.

4-(diazo(phenyl)methyl) pyridine *N*-oxide; 4D1pyO : novel compound

In a 50 ml Erlenmeyer flask, 4-(hydorazono(phenyl)methyl) pyridine *N*-oxide (1.0 g, 4.7 mmol) was dissolved to 20 ml of CH_2Cl_2 and was added to 8.1 g of activated MnO_2 (84 mmol, ca. 90%). The reaction mixture was stirred at room temperature in the dark for 30 min. After completion of the reaction, insoluble solid was removed by the suction filtration through Celite® 545-RVS and the filtrate was evaporated to dryness under reduced pressure. Re-crystallization of the residual solid from $CHCl_3$/*n*-hexane gave **4D1pyO** as a reddish-purple block crystal (700 mg, 3.3 mmol) in 70.7 % yield.

m.p. 100 − 103 °C (dec.), ^{1}H-NMR (500 MHz, $CDCl_3$) δ 8.13 (*d*, *J* = 6.0 Hz, 2H), 7.48 (*t*, *J* = 7.8 Hz, 2H), 7.35-7.33 (*m*, 3H), 7.04 (*d*, *J* = 6.0 Hz, 2H), ^{13}C-NMR (125 MHz, $CDCl_3$) δ 130.5, 129.7, 129.4,

128.5, 127.9, 126.9, 126.4, 125.0, IR (KBr disk) 3108, 3069, 3032, 2044, 1497, 1480, 1235 cm^{-1}, ESI MS 234.1 $[M + Na]^+$,

3-Benzoylpyridine *N*-oxide

3-Benzoylpyridine *N*-oxide was obtained as pale orange oil in 92.0 % yield according to the same procedure used for 4-Benzoylpyridine *N*-oxide.

^{1}H-NMR (500 MHz, $CDCl_3$) δ 8.56 (*s*, 1H), 8.38 (*d*, *J* = 7.5 Hz, 1H), 7.81 (*d*, *J* = 8.0 Hz, 2H), 7.69-7.64 (*m*, 2H), 7.55 (*t*, *J* = 7.8 Hz, 2H), 7.43 (*t*, *J* = 9.8 Hz, 1H), ^{13}C-NMR (125 MHz, $CDCl_3$) δ 191.7, 141.7, 140.3, 136.7, 135.5, 133.9, 129.9 128.9, IR (NaCl) 1666, 1596, 1429, 1288 cm^{-1}, ESI MS 222.1 $[M + Na]^+$

3-(hydorazono(phenyl)methyl) pyridine *N*-oxide : novel compound

3-(hydorazono(phenyl)methyl) pyridine *N*-oxide was obtained as yellow solid in 65.9 % yield according to the same procedure used for 4-(hydorazono(phenyl)methyl) pyridine *N*-oxide.

3-(diazo(phenyl)methyl) pyridine *N*-oxide; 3D1pyO : novel compound

3D1pyO was obtained as purple oil in 66.7 % yield according to the same procedure used for **4D1pyO**.

^{1}H-NMR (500 MHz, $CDCl_3$) δ 8.14 (*s*, 1H), 7.96 (*d*, *J* = 6.5 Hz, 1H), 7.45(*t*, *J* = 7.8 Hz, 2H), 7.33-7.29 (*m*, 3H), 7.25 (*d*, *J* = 4.3 Hz, 1H), 7.07 (*d*, *J* = 8.0 Hz, 1H), ^{13}C-NMR (125 MHz, $CDCl_3$) δ 135.1, 134.2, 131.8, 129.9, 129.7, 128.9, 127.6, 126.4,125.9, 120.4, IR (NaCl) 3061, 2049, 1496, 1214 cm^{-1}, ESI MS 234.1 $[M + Na]^+$

[Ln(tta)$_3$4D1pyO]$_2$ 2CHCl$_3$ (Ln = Gd, Tb, and Dy) **: novel compound**

Ln(tta)$_3$ 2H$_2$O (0.04 mmol) and 4D1pyO (8.4mg, 0.04 mmol) were mixed in 10 ml of CHCl$_3$ and stirred for 10 minutes. Insoluble solid was removed by filtration and the filtrate was reduced to 5 ml under reduced pressure. After adding 5 ml of *n*-heptane, the solution was stored at 4 °C in the dark for 3 days. [Ln(tta)$_3$4D1pyO]$_2$ 2CHCl$_3$ was obtained as a red block crystal.

m.p. 118 − 120 °C (dec.), IR (KBr disk) 2049, 1308, 1230, 1185, 1139 cm^{-1}, Anal. Calcd for $C_{72}H_{42}F_{18}Gd_2N_6O_{14}S_6$: C 41.90, H 2.05 N 4.07 %, found: C 42.10, H 2.01, N 3.80 %, Anal. Calcd for $C_{72}H_{42}F_{18}Tb_2N_6O_{14}S_6$: C 41.83, H 2.05 N 4.07 %, found: C 41.98, H 2.21, N 3.78 %, Anal. Calcd for $C_{72}H_{42}F_{18}Dy_2N_6O_{14}S_6$ +1.5 $CHCl_3$: C 39.17, H 1.95 N 3.73 %, found: C 39.36, H 2.01, N 3.61 %

[Tb(tta)$_3$3D1pyO]$_2$ 4CHCl$_3$: novel compound

[Tb(tta)$_3$3D1pyO]$_2$ 2CHCl$_3$ was obtained as a red block crystal according to the same procedure used for [Ln(tta)$_3$4D1pyO]$_2$ 4CHCl$_3$.

m.p. 118 − 120 °C (dec.), IR (KBr disk) 2053, 1310, 1230, 1187, 1140 cm^{-1}, Anal. Calcd for $C_{72}H_{42}F_{18}Tb_2N_6O_{14}S_6$: C 41.83, H 2.05 N 4.07 %, found: C 42.11, H 2.07, N 3.89 %.

di(pyridine-4-yl)methanol

In a 200 ml three necked round-bottom flask, 4-Bromopyridine (6.8 g, 43 mmol) in dist. Et_2O was added to 31.5 ml of 1.65 M of *n*-BuLi (51.6 mmol) at -78 °C. The solution was stirred under nitrogen atmosphere for one hour on the acetone/dry ice bath and then warmed to room temperature. 100 ml of saturated NH_4Cl aq. was added and then the water layer was extracted by 50ml of $CHCl_3$ three times. The organic layer were combined and dried over $MgSO_4$. After removing the solvents under reduced pressure, resulting dark brown oily product was re-precipitated by Et_2O/*n*-hexane. Washing the obtained solid gave di(pyridine)methanol as a white solid (2.4 g, 13 mmol) in 30.0 % yield.

4,4'-(hydroxymethyl)bis(pyridine-*N*-oxide) : novel compound

In a 20 ml round-bottom flask, di(pyridine)methanol (1.8 g, 10 mmol) and tungstic acid (250 mg, 1 mmol cat.) was suspended to 7 ml of 30% H_2O_2 aq. at room temperature. The solution was heated at 70 °C for 15 hours on the oil bath and then cooled to room temperature. 1.0 g of activated MnO_2 was added in order to quench the excessive peroxide, and then the water layer was filtered through Celite® 545-RVS. If necessary, the water layer was additionally reduced by $NaHSO_3$ and then neutralized by $NaHCO_3$. Removing the water layer under the reduced pressure gave crude product as a white solid. This compound was used in next step without any further purification in this stage.

4,4'-carbonylbis(pyridine-*N*-oxide), K1(pyO)$_2$: novel compound

In a 100 ml round-bottom flask, crude di(pyridine-*N*-oxide)methanol and activated MnO_2 (9.7 g, 100 mmol) was suspended to 50 ml of chloroform and 10 ml of methanol. The solution was heated under reflux for two hours on the oil bath and then cooled to room temperature. MnO_2 and insoluble inorganic salts were separated through the suction filtration using Celite® 545-RVS. After removing the organic solvent, resulting yellow solid was purified by the silica column chromatography using dichloromethane/methanol. 1.8 g of K1(pyO)$_2$ was obtained as a pale yellow crystalline solid. (83.3 % yield in 2 steps)

^{1}H-NMR (500 MHz, $CDCl_3$) δ 8.29 (*d*, *J* = 6.5 Hz, 4H), 7.69 (*d*, *J* = 6.5 Hz, 4H) ^{13}C-NMR (125 MHz, $CDCl_3$) δ 187.5, 139.7, 131.0, 126.5, IR (KBr) 1654, 1604, 1255 cm^{-1}, ESI MS 239.2 [M + Na]$^+$

4,4'-(hydrazonomethylene)bis(pyridine-*N*-oxide) : novel compound

In a 20 ml round-bottom flask, **K1(pyO)$_2$** (216 mg, 1 mmol) was dissolved to 5 ml of MeOH and was heated to 60°C. After the addition of 68.5 mg of hydrazine monohydrochloride (1 mmol) and 0.16 ml of hydrazine anhydrous (5 mmol), the reaction mixture was heated to 90°C and stirred for 4 hours. The solution was cooled to room temperature and then stood under -30 °C room over night. The precipitate was separated by filtration and was washed by a portion of cold methanol. 4,4'-(hydrazonomethylene)bis(pyridine-*N*-oxide) was obtained as a pale yellow crystalline solid (170 mg, 73.9 % yield). This compound was used in next step without any further purification in this stage.

4,4'-(diazomethylene)bis(pyridine-*N*-oxide), D1(pyO)$_2$: novel compound

In a 20 ml Erlenmeyer flask, 4,4'-(hydrazonomethylene)bis(pyridine-*N*-oxide) (105 mg, 0.46 mmol) was dissolved to 5 ml of CH_2Cl_2 and 1 ml of methanol was added to 1.0 g of activated MnO_2 (10 mmol, ca. 90%). The reaction mixture was stirred at room temperature in the dark for 30 min. After completion of the reaction, insoluble solid was removed by the suction filtration through Celite® 545-RVS and the filtrate was evaporated to dryness under reduced pressure. Purification of the residual solid by the aluminum column chromatography using dichloromethane/methanol gave **D1(pyO)$_2$** as a reddish solid. Re-crystallization from $CHCl_3$/methanol gave a single crystal suitable for the X-ray analysis (95 mg, 91.3 % yield)

^{1}H-NMR (500 MHz, CD_3OD) δ 8.31 (*d*, *J* = 4.5 Hz, 4H), 7.51 (*d*, *J* = 5.5 Hz, 4H) ^{13}C-NMR (125 MHz, $CDCl_3$) δ 140.8, 140.7, 132.4, 123.0, IR (KBr) 2060, 1490, 1234 cm^{-1}, HR-ESI MS 251.0543(found), 251.0545 (calcd.) $[M + Na]^+$

[{Ln(tta)$_3$}$_2$(D1(pyO)$_2$)]$_n$ *n*CH_2Cl_2 *n*PhCN (Ln = Gd, Tb, and Dy) : novel compound

In a 4 ml test tube, 2 ml of CH_2Cl_2/methanol (9 : 1) solution of **D1(pyO)$_2$** (1.5 mg, 0.0066 mmol) was thoroughly mounted onto the suspension of Ln(tta)$_3$ 2H_2O (11.3 mg, 0.013 mmol) in benzonitrile. After two weeks, [{Ln(tta)$_3$}$_2$(**D1(pyO)$_2$**)]$_n$ *n*CH_2Cl_2 *n*PhCN was obtained as yellow-orange colored crystals.

m.p. 118 − 120 °C (dec.), IR (KBr disk) 2067, 1665, 1540, 1308, 1230, 1188, 1141 cm^{-1}, Anal. Calcd for $C_{67}H_{39}Cl_2F_{18}N_5O_{14}S_6Tb_2$: C 39.04, H 1.91 N 3.40 %, found: C 39.23, H 2.00, N 3.51 %,

Chapter 9. References

(1) Kahn, O. Molecular Magnetism; Wiley-VCH Publishers: Weinheim, Germany, **1993**.

(2) Daniel, L; DiVincenzo, D. *Phys. Rev. A*, **1998**, *57*, 120-126.

(3) Mannini, M.; Pineider, F.; Sainctavit, P.; Danieli, C.; Otero, E.;Sciancalepore, C.; Talarico, M.; Arrio, M.-A.; Cornia, A.; Gatteschi, D.;Sessoli, R. *Nat. Mater*, **2009**, *8*, 194−197.

(4) Sato, O.; Tao, J.; Zhang, Y. Z. *Angew. Chem., Int. Ed*. **2007**, *46*, 2152 − 2187.

(5) Kinoshita, M.; Turek, P.; Tamura, M.; Nozawa, Y.; Shiomi, D.; Nakazawa, Y.; Ishikawa,M.; Takahashi, M.; Awaga, K.; Inabe, T.; Yusei, M. *Chem. Lett*. **1991**, *20*(7), 1225-1228.

(6) Fujita, I,; Takui, Y.; Kinoshita, T.; Itoh, K.; Miko, F.; Sawaki, Y.; Izuoka, A.; Sugawara, T.; Iwamura,H. *J. Am. Chem. Soc*. **1990**, *112*, 4074-4075.

(7) Caneschi, A.; Gatteschi, D.; Renard, J.;Rey, P.; Sessoli, R. *Inorg. Chem*. **1989**, *28*, 2940−2944.

(8) (a) Gatteschi, D.; Sessoli, R.; Villain, J. *Molecular Nanomagnets*; Oxford University Press: New York, **2006**. (b) Caneschi, A.; Gatteschi, D.; Sessoli, R. *J. Am. Chem. Soc*. **1991**, *113*, 5873-5874. (c) Christou, G.; Gatteschi, D.; Hendrickson, D.N.; Sessoli, R. *MRS Bull*. **2003**, *25*, 66−71. (d) Aubin, S. M. J.; Dilley, N. R.; Pardi, L.; Krzystek, J.; Wemple, M. W.; Brunel, L.-C.; Brian Maple M.; Christou, G.; Hendrickson, D. N. *J. Am. Chem. Soc*. **1998**, *120*, 4991−5004. (e) Brechin, E. K.; Boskovic, C.; Wernsdorfer, W.; Yoo, J.; Yamaguchi, Y.; Sanudo, E. C.; Concolin, T.; Rheingold, A. L.; Ishimoto, H.; Hendrickson, D. N.; Christou, G. *J. Am. Chem. Soc*. **2002**, *124*, 9710−9711. (f) Murugesu, M.; Habrych, M.; Wernsdorfer, W.; Abboud, K. A.; Christou, G. *J. Am. Chem. Soc*.**2004**, *126*, 4766−4767. (g) Ishikawa, N.; Sugita, M.; Wernsdorfer, W. *J. Am. Chem. Soc*. **2005**, *127*, 3650−3651. (h) Ishikawa, N.; Sugita, M.; Ishikawa, T.; Koshihara, S.; Kaizu, Y. *J. Am. Chem. Soc.* **2003**, *125*, 8694–8695.

(9) (a) Jiang, S. D.; Wang, B. W.; Sun, H. L.; Wang, Z. M.; Gao, S. *J. Am. Chem. Soc*. **2011**, *133*, 4730– 4733. (b) Jiang, S.-D.; Wang, B.-W.; Su, G.; Wang, Z.-M.; Gao, S. *Angew. Chem., Int. Ed.* **2010**, *49*, 7448– 7451.

(10) (a) Clérac, R.; Miyasaka, H.; Yamashita, M.; Coulon, C. *J. Am. Chem. Soc*. **2002**, *124*, 12837–

12844. (b) Miyasaka, H.; Miguel, J.; Yamashita, M.; Clérac, R. *Inorg. Chem.* **2009**, *48*, 3420– 3437. (c) Caneschi, A.; Gatteschi, D.; Lalioti, N.; Sangregorio, C.; Sessoli, R.; Ventur, G.; Vindigni, A.; Rettori, A.; Pini, M. G.; Novak, M. A. *Angew. Chem., Int. Ed*. **2001**, *40*, 1760– 1763. (d) Kajiwara, T.; Nakano, M.; Kaneko, Y.; Takaishi, S.; Ito, T.; Yamashita, M.; Igashira-Kamiyama, A.; Nojiri, H.; Ono, Y.; Kojima, N. *J. Am. Chem. Soc.* **2005**, *127*, 10150– 10151. (e) Caneschi, A.; Gatteschi, D.; Lalioti, N.; Sangregorio, C.; Sessoli, R.; Ventur, G.; Vindigni, A.; Rettori, A.; Pini, M. G.; Novak, M. A. *Angew. Chem., Int. Ed*. **2001**, *40*, 1760–1763. (f) Lescouëzec, R.; Vaissermann, J.; Ruiz-Pérez, C.; Lloret, F.; Carrasco, R.; Julve, M.; Verdaguer, M.; Dromzee, Y.; Gatteschi, D.; Wernsdorfer, W. *Angew. Chem., Int. Ed*. **2003**, *42*, 1483–1486.

(11) Koga, N.; Karasawa, S. *Bull. Chem. Soc. Jpn*., **2005**, *78*, 1384–1400.

(12) (a) Kanegawa, S.; Karasawa, S.; Maeyama, M.; Nakano, M.; Koga, N. *J. Am. Chem. Soc*. **2008**, *130*, 3079−3094. (b) Yoshihara, D.; Karasawa, S.; Koga, N. *J. Am. Chem. Soc*. **2008**, *130*, 10460−10461.

(13) (a) Sano, Y.; Tanaka, M.; Koga, N.; Matsuda, K.; Iwamura, H.; Sano, Y.; Drillon, M. *J.Am. Chem. Soc*. **1997**, *119*, 8246–8252.

(14) Kanegawa, S. Thesis fot the Doctor of Science, **2008**, Kyushu university.

(15) (a) Giacovazzo .C (Ed.), Fundamentals of Crystallography, second ed., Oxford University Press, **2002** (b) Zehnder . M, Neuburger. M, P.von Matt, Pfaltz , A, *Acta Crystallogr., Sect. C*, **1995**, *51*, 1109-1112.

(16) (a) Estes, W. E.; Gavel, D. P.; Hatfield, W. E.; Hodgson, D. J. *Inorg. Chem*. **1978**, *17*, 1415−1421. (b) Hayashi, H.; Karasawa, S.; Koga, N. *J. Org. Chem*. **2008**, *73*, 8683−8693. (c) Stamatatos,T.C,; Vlahopoulou, G.; Raptopoulou,C.; Psycharis,V.; Escuer,A.; Christou,,G.; Perlepes,S. *Eur. J. Inorg. Chem*. **2012**, *19*, 3121-3131.

(17) (a)Karasawa, S.; Yoshihara, D.; Watanabe, N.; Nakano, M.; Koga, N. *Dalton Trans*. **2008**, 1418−1420. (b)Liu, Y.-H.; Cheng, Y.-C.; Tung, Y.-L.; Chi, Y.; Chen, Y.-L.; Liu, C.-S.; Peng, S.-M.; Lee, G.-H. *J. Mater. Chem* **2003**, *13*, 135−142.

(18) (a) van Koningsbruggen, P. J.; Kahn, O.; Nakatani, K.; Pei, Y.; Renard, J. P.; Drillon, M.; Legoll, P. *Inorg. Chem*. **1990**, *29*, 3325–3331. (b) Pardo, E.; Ruiz-García, R.; Lloret, F.; Faus, J.; Julve, M.;

Journaux, Y.; Delgado, F.; Ruiz-Pérez, C. *Adv. Mater*. **2004**, *16*, 1597–1600. (c) Ferrando-Soria, J.; Pardo, E.; Ruiz-García, R.; Cano, J.; Lloret, F.; Julve, M.; Journaux, Y.; Pasán, J.; Ruiz-Pérez, C. *Chem. Eur. J*. **2011**, *17*, 2176–2188. (d) Pardo, E.; Ruiz-García, R.; Lloret, F.; Faus, J.; Julve, M.; Journaux, Y.; Novak, M. A.; Delgado, F. S.; Ruiz-Pérez, C. *Chem. Eur. J*. **2007**, *13*, 2054–2066.

(19) (a) Toma, L. M.; Lescouëzec, R.; Lloret, F.; Julve, M.; Vaissermann, J.; Verdaguer, M. *Chem. Commun*. 2003, 1850−1851. (b) Liu, T.; Zhang, Y.-Z.; Kanegawa, S.; Sato, O. *J. Am. Chem. Soc*. **2010**, *132*, 8250−8251.

(20) Wang, Y.-Q.; Zhang, X.-M.; Li, X.-B.; Wang, B.-W.; Gao, E.-Q. *Inorg. Chem*. **2011**, *50*, 6314−6322.

(21) (a) Manson, J. L.; Huang, Q-z.; Lynn, J. W.; Koo, H.-J.; Whangbo, M.-H.; Bateman, R.; Otsuka, T.; Wada, N.; Argyriou, D. N.; Miller, J. S. *J. Am. Chem. Soc*. **2001**, *123*, 162−172. (b) Miller, J. S.; Manson, J. L. *Acc. Chem. Res*. **2001**, *34*, 563−570. (c) Manson, J. L.; Kmety, C. R.; Epstein, A. J.; Miller, J. S. *Inorg. Chem*. **1999**, *38*, 2552− 2553. (d) Takagami, N.; Ishida, T.; Nogami, T. *Bull. Chem. Soc. Jpn*. **2004**, *77*, 1125−1134. (e) King, P.; Clérac, R.; Anson, C. E.; Coulon, C.; Powell, A. K. *Inorg. Chem*. **2003**, *42*, 3492−3500.

(22) Wang, X.-Y.; Wang, Z.-M.; Gao, S. *Inorg. Chem*. **2008**, *47*, 5720−5726.

(23) (a) Rinehart, J. D.; Fang, M.; Evans, W. J.; Long, J. R. *Nat. Chem*. **2011**, *3*, 538– 542. (b) Rinehart, J. D.; Fang, M.; Evans, W. J.; Long, J. R. *J. Am. Chem. Soc.* **2011**, *133*, 14236– 14239. (c) Demir, S.; Zadrozny, J. M.; Nippe, M.; Long, J. R. *J. Am. Chem. Soc.* **2012**, *134*, 18546−18549. (d) Meihaus, K. R.; Corbey, J. F.; Fang, M.; Ziller, J. W.; Long, J. R.; Evans, W. J. *Inorg. Chem.* **2014**, *53*, 3099– 3107.

(24) (a) Karasawa, S.; Kumada, H.; Koga, N.; Iwamura, H. *J. Am. Chem. Soc.* **2001**, *123*, 9685–9686. (b) Karasawa, S.; Koga, N.; *Polyhedron* **2003**, *22*, 1877–1882. (c) Karasawa, S.; Koga, N.; *Polyhedron* **2001**, *20*, 1387–1389. (d) Morikawa, H.; Imamura, F.; Tsurukami, Y.; Itoh, T.; Kumada, H.; Karasawa, S.; Koga, N.; Iwamura, H. *J. Mater. Chem*. **2001**, *11*, 493–502. (e) Kanegawa, S.; Karasawa, S.; Nakano, M.; Koga, N. *Chem. Comm*., **2004**, 1750–1751.

(25) (a) Pinsky, M.; Avnir, D. *Inorg. Chem*. **1998**, 37, 5575−5582. (b) Casanova, D.; Cirera, J.; Llunell, M.; Alemany, P.; Avnir, D.;Alvarez, S. *J. Am. Chem. Soc*. **2004**, 126, 1755−1763. (c) Cirera, J.; Ruiz, E.; Alvarez, S. *Chem. −Eur. J*. **2006**, 12, 3162−3167.

(26) (a) Costes, J.-P.; Dahan, F.; Dupuis, A.; Laurent, J.-P. *Inorg. Chem.***1997**, *36*, 4284-4286.

(27) (a) Eliseeva, S. V.; Ryazanov, M.; Gumy, F.; Troyanov, S. I.; Lepnev, L. S.; Bünzli, J.-C. G.; Kuzmina, N. P. *Eur. J. Inorg. Chem*. **2006**, 4809- 4820. (b) Yi, X.; Bernot, K.; Pointillart, F.; Poneti, G.; Calvez, G.; Daiguebonne, C.; Guillou, O.; Sessoli, R. *Chem. Eur. J*. **2012**, *18*, 11379– 11387. (c) Yi, X.; Calvez, G.; Daiguebonne, C.; Guillou, O.; Bernot, K. *Inorg. Chem.* **2015**, *54*, 5213– 5219. (d) Pointillart, F.; Le Guennic, B.; Golhen, S.; Cador, O.; Ouahab, L. *Chem. Commun*. **2013**, *49*, 11632–11634. (e) Pointillart, F.; Le Guennic, B.; Cauchy, T.; Golhen, S.; Cador, O.; Maury, O.; Ouahab, L. *Inorg. Chem*. **2013**, *52*, 5978– 5990. (f) Han, T.; Shi, W.; Zhang, X. P.; Li, L. L.; Cheng, P. *Inorg. Chem.* **2012**, *51*, 13009-13016.

(28) (a) Pointillart, F.; Golhen, S.; Cador, O.; Ouahab, L. *Eur. J. Inorg. Chem*. **2014**, 4558– 4563. (b) Pointillart, F.; Le Gal, Y.; Golhen, S.; Cador, O.; Ouahab, L. *Chem.Eur. J.* **2011**, *17*, 10397– 10404. (c) Pointillart, F.; Le Guennic, B.; Maury, O.; Golhen, S.; Cador, O.; Ouahab, L. *Inorg. Chem.* **2013**, *52*, 1398– 1408.

(29) Ishida, T.; Murakami, R.; Kanemoto, T.; Nojiri, H. *Polyhedron.* **2013**, *66*, 183-187.

(30) (a)Morikawa, H.; Karasawa, S.; Koga, N. *Appl. Magn. Reson*. **2003**, *23*, 507– 515. (b) Koga, N.; Ishimaru, Y.; Iwamura, H. *Angew. Chem., Int. Ed*. **1996**, *35*, 755–757.

(31) L. Engelhardt, C. Garland, C. Rainey, A. Freeman, *FIT-MART* project. Department of Physics and Astronomy, Francis Marion University, Florence, South Carolina 29501, USA.

(32) (a) a) Bernot, K.; Bogani, L.; Caneschi, A.; Gatteschi, D.; Sessoli,R. *J. Am. Chem. Soc*. **2006**, *128*, 7947−7956. (b) Bogani, L.; Sangregorio, C.; Sessoli, R.; Gatteschi, D. *Angew. Chem., Int. Ed*. **2005**, *44*, 5817-5821.

(33) Baeyer, A.; Villiger, V. *Ber*. **1899**, *32*, 3625-3633.

(34) Koga, N.; Ishimaru, Y.; Iwamura, H. *Angew. Chem., Int. Ed.* **1996**, *35*, 755– 757.

(35) *Crystal Structure 3.5.2* : Crystal Structure Analysis Package, Rigaku and Rigaku/MSC (**2000-2003**). 9009 New Trails Dr. The Woodlands TX 77381 USA.

(36) *Bruker SAINT Version 7.6A Software Reference Manual*; Bruker AXS, Inc.; Madison, WI, **2007**.

List of Publications

1. Preparations, Crystal Structures, and Magnetic Properties of N,N-Dipyridylaminoxyl as a New Magnetic Coupler and Its One-Dimensional Cobalt(II) Chains
Kensuke Murashima, Takeaki Watanabe, Shinji Kanegawa, Daisuke Yoshihara, Yuji Inagaki, Satoru Karasawa, and Noboru Koga, *Inorg. Chem.*, **2012**, *51*, 4982-4993.

2. Influence of diamagnetic chelating ligand (L) on spin exchange coupling in heterospin chain complexes, $[Cu(L)_2NOpy_2]_n$
Kensuke Murashima, Satoru Karasawa, Kenji Yoza, Noboru Koga, *Polyhedron*, **2013**, *66*, 188-193.

3. 3- and 4-(α-Diazobenzyl)pyridine-N-oxide as Photoresponsive Magnetic Couplers for 2p - 4f Heterospin Systems: Formation of Carbene-Tb^{III} and Carbene-Dy^{III} Single-molecule Magnets
Kensuke Murashima, Satoru, Karasawa, Kenji Yoza, Yuji Inagaki, and Noboru Koga, *Dalton. Trans.*, **2016**, *submitted*.

4. Molecular Structures of One-dimensional Ln^{III} Complexes Linked with Di(pyridine-*N*-oxide)diazomethane and their Magnetic Properties after Irradiation
Kensuke Murashima, Satoru Karasawa, and Noboru Koga, *in preparation*.

The author was involved in the following research as a technical advisor.

5. 1-D, 2-D, and 3-D Heterospin Complexes Consisting of 4-(N-tert-Butyloxylamino)pyridine (4NOpy), Dicyanamide ion (DCA), and 3d Metal Ions; Crystal Structures and Magnetic Properties of $[M^{II}(4NOpy)_x(DCA)_y(CH_3CN)_z]_n$: M^{II} = Mn, Co, Ni, Cu, and Zn.
Hiraku Ogawa, Koya Mori, Kensuke Murashima, Satoru Karasawa, and Noboru Koga, *Inorg. Chem.*, **2016**, *55*, 717-728.

Acknowledgement

This work was supported by a scholarship of the Japan Society for the Promotion of Science (JSPS). The author thanks to JSPS for their cordial funding supporting the present work for three years.

The present work has been carried out under the supervision of Professor Noboru Koga at the Graduate School of Pharmaceutical Sciences, Kyushu University. The author would like to express his best gratitude to him for his ardent direction and helpful suggestions through the work.

The author is sincerely grateful to Dr. Satoru Karasawa at the Graduate School of Pharmaceutical Sciences, Kyushu University for his continuous interest and the accurate indication about this work.

The author is greatly indebted to Dr. Takeyuki Akita at the Graduate School of Pharmaceutical Sciences, Kyushu University for his kind encouragement and valuable suggestions.

The author acknowledges Dr. H. Shirakawa at the National Institute of Advanced Industrial Science and Technology and Mr. T. Ota of IQUANTUM Co. LTD. for the SQUID measurements below 2 K and Dr. K. Yoza of Bruker AXS Co.LTD. for useful discussion on X-ray crystallography and Dr. Y. Inagaki for the EPR spectra measurement at the cryogenic temperature, and professor Dr. O.Sato for the technical cooperation about the photo irradiation.

The author also wishes to thank to Dr. Daisuke Yoshihara for his polite and genial direction as an elder researcher.

The author is thankful to all the members of Koga's laboratory at the Kyushu University for their valuable assistances and kind friendships.

Finally, the author would like to devote his ultimate gratitude for his family for their constant and helpful encouragement through a long time at the Kyushu University.